Universitat Autònoma de Barcelona

Measurement of the invariance of the speed of light observing the active galactic nucleus Mkn421 with the MAGIC Telescope[1]

Javier López Muñoz
Universitat Autònoma de Barcelona
Departament de Física
Edifici Cn, UAB
E-08193 Bellaterra (Barcelona)

July 3, 2006

supervised by

Manel Martínez
IFAE
Edifici Cn, UAB
E-08193 Bellaterra (Barcelona)

[1]Ph.D. Dissertation

A mi amor,
por que su valentía
me ha enseñado
como recorrer este camino.

Contents

List of Figures

List of Tables

Chapter 1

Introduction

The work presented in this Thesis is situated at the crossroads between two fields of modern science, γ-ray astronomy and fundamental physics. The motivation for this Thesis is the study, from an experimental point of view, of possible signatures of a Quantum formulation of Gravity using astronomical observations. The modern Very High Energy (VHE) γ-ray detectors have already played an essential role in providing experimental data for such kind of measurements, which have lead to remarkable results. In this Thesis, we study how to bring one step farther this kind of measurement within the VHE γ-ray experimental astronomy. This is done by using one of the most active emission periods shown by the Active Galactic Nuclei Markarian 421 in the last years observed by MAGIC Telescope.

γ-ray Astronomy

γ-ray astronomy is included in the young field of astroparticle physics, field that started with the discovery of cosmic rays in 1912 by the physicist Viktor Hess using his famous flying balloon experiment. Since then, cosmic ray physics has evolved dramatically both theoretically and experimentally. Today, experimental astroparticle physics use data coming from balloons, satellites and different kinds of ground based detectors.

Astronomy with γ-rays deals with the most energetic radiation emitted by astronomical sources. The non-thermal behaviour shown by the spectrum of this radiation motivates the belief that γ-rays production involves acceleration, interaction and decay of highly relativistic particles. The interest in the study of the cosmos by using γ-ray is based on the interesting properties of these particles. Being neutral particles, γ-rays are not deflected by interstellar and intergalactic magnetic fields, thus pointing back to their original source. Moreover, γ-rays carry time and energy information from their generation process, making them messengers not only of the highly relativistic populations that produced them, but also of the astronomical environments where they come from. Therefore, γ-ray astronomy is the most adequate tool to study non-thermal processes in the universe, from the neighbourhoods of very compact objects like black holes in AGNs or micro-quasars to the collision of shock waves with the interstellar medium in supernova remnants.

Despite its interest, γ-ray astronomy is one of the youngest branches of astroparticle physics. The reason for the late exploration of this promising high energy regime was due to the fact that cosmic γ-rays get absorbed by the Earth's atmosphere. Hence, γ-ray astronomy could not be developed until it was possible to send detectors above the

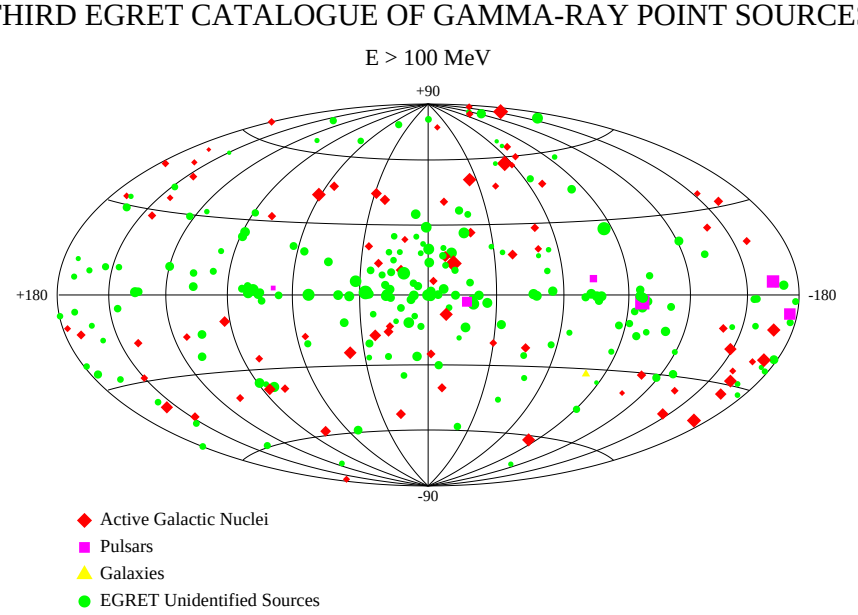

Figure 1.1: The EGRET map of the sky in γ-rays in galactic coordinates.

atmosphere using either balloons or satellites. First γ-ray detectors carried into orbit, like the ones placed on the Explorer-XI satellite in 1961, picked up less than 100 cosmic γ-rays. Since this pioneering experiment, a handful of increasingly more powerful detectors were launched to space. However, it was not until the 1990s that photons of the MeV-GeV energy range became useful to study the universe in this energy regime, with the launch of the Compton Gamma-Ray Observatory (CGRO) satellite. This satellite was equipped with a set of powerful γ-rays instruments, among which there was the EGRET detector, which covered the energy band for γs between MeV to GeV. The Third EGRET Catalog contains 271 detections with high significance, including pulsars, solar flares, blazars, radio galaxies, normal galaxies and around 170 yet unidentified sources. In figure 1.1 the EGRET all-sky map and the sources reported in its final catalog (see reference [1]) are shown.

Today, γ-ray astronomy done with satellites continues its expansion. The already operating INTEGRAL satellite is a space-based γ-ray observatory, which has on board instruments dedicated to optical, X-rays and γ-rays observations. It is also planned to launch in the near future a satellite called AGILE (Astro rivelatore Gamma a Immagini LEggero), entirely dedicated to high-energy astrophysics. This will cover the energy range from tens of KeV to 50 GeV. However, the satellite that is expected to change the perspective of astrophysics in the GeV energy domain in the near future is GLAST [2, 3], which will be launched by the end of 2007. For GLAST, the LAT instrument on board is such that after one week of observations, it is expected to reach the same sensitivity and coverage as that reached by the whole decade of earlier EGRET operations.

Despite the interesting results obtained from satellites for low-energy γ detection, this technique is not adequate for the High energy γ regime. Due to the limited detector areas placed in satellites and the exponentially decreasing energy spectra expected for γ-rays sources, the sensitivity for such detectors in the GeV domain is limited by very low statistics. This situation has motivated the development of alternative techniques which

could extend the γ-ray astronomy to higher energy domains. In this sense, the pioneering work of the Whipple collaboration [4] in the late 1980's was the beginning of ground-based detection of very high energy γs, with the detection of γs of several hundreds of GeVs coming from the first TeV source, the Crab Nebula. For this purpose, the Whipple Telescope used the so-called Imaging Atmospheric Cherenkov (IAC) technique, which is based in the detection of the Cherenkov photons emitted by the secondary charged particles that are produced when a high energy γ-rays enters the atmosphere. Although considerable effort has been applied to the development of alternative techniques for ground based detection of very high energy γ-rays (such as solar arrays like STACEE [5], air-shower particle detectors like MILAGRO [6], etc.), there are yet no competitive detection techniques with respect to IAC Telescopes.

During the 1990s, a first generation of IACTs (Whipple, the HEGRA array, CAT, etc.) operated, observing γ-rays between a few hundred GeV to several TeV. This old generation of IACTs discovered a handful of TeV sources, both galactic and extragalactic ones, settling the technique as a new window to the universe. In the last decade, there has been a new set of projects with the goal of constructing a new generation of IACTs, which would increase the old telescopes sensitivities and reduce the existing energy threshold, in order to close the gap with the satellite observations. Several of these new telescopes are still in development or just started taking data, such as the VERITAS array [7] or the upgrade of the existing CANGAROO array [8]. At present, two new generation IACTs are already in operation: the HESS telescopes array [9], which started nominal observations in 2003, and the MAGIC Telescope [10], that started one year later.

MAGIC is a 17 meter diameter reflector single telescope designed and built with the goal of reaching the lowest energy threshold among the new generation IACTs. This technical requirement was motivated by the aim to close the energy gap between 10-300 GeV, still observationally unexplored. MAGIC also had the aim of being able to perform follow-ups of the prompt emission of Gamma-Ray Bursts (GRBs), thus having to combine an ultralight structure with a large number of technical innovations to carry out fast repositioning. The Thesis presented in this document has been developed within the MAGIC collaboration.

During the last two years, the starting of the new generation IACTs operation has produced a large push in the GeV-TeV astronomy. By 2003 the number of confirmed VHE sources had crept up to 12 during more than 20 years of observations. Since then, the number of sources has almost tripled. In figure 1.2 the number of detected sources in the TeV energy domain at 2005 is shown. This catalogue of sources claims 32 sources, including 6 unidentified objects, two consolidated populations of galactic VHE emitters (Pulsar Wind Nebulae and Supernova Remnants), one binary pulsar, one microquasar, a region of diffuse emission, and eleven AGNs.

Quantum Gravity

The two most revolutionary theories from the last century are Quantum Mechanics and Special Relativity. At different moments of last century both theories were the seed for the development of two of the most successful fundamental theories in Physics, the Standard Model of particle physics and the General Relativity. Decades of experimental research has proven that the Standard Model is extremely successful describing the behaviour of fundamental particles, being possible in this description to neglect Gravity due to the large difference in strength between it and the other fundamental interactions. By the

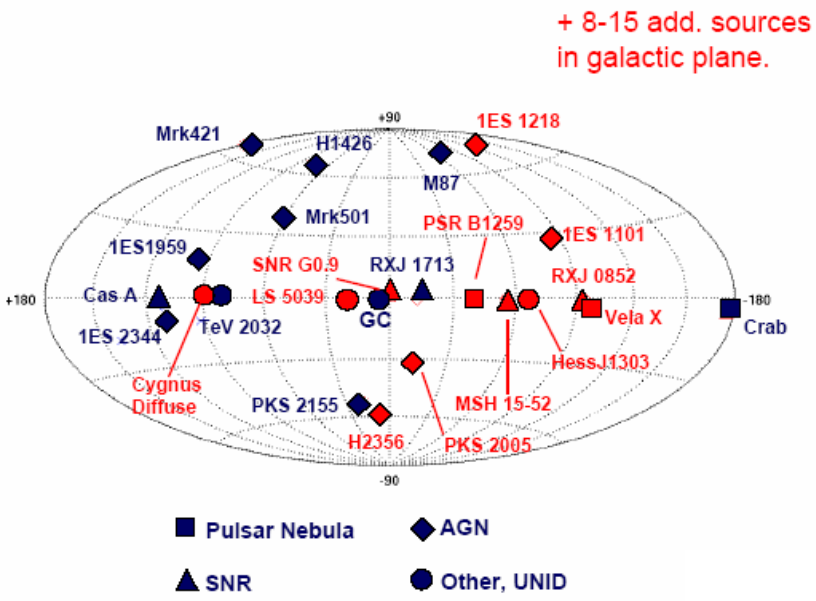

Figure 1.2: The Very High Energy γ-ray sky in 2005. Not shown are 8 more sources discovered by HESS in a survey of the galactic plane. Red symbols indicate the most recent detections, brought during 2004 and 2005 by the last generation of IACTs: HESS and MAGIC. Figure extracted from reference [11].

other hand, General Relativity has shown to be also extremely precise in the description of the motion of objects in the universe, from planets to galaxies, being in this case possible to neglect any Quantum mechanic behaviour of these macroscopic objects. Early since the formulation of these two theories, there has been a continuous theoretical effort in order to harmonize Gravity and Quantum mechanics in a Quantum formulation of Gravity. The theoretical pursuit of this formulation has provided a rather large set of candidates for being the Quantum Gravity theory, among which nowadays the most popular ones are String theory and Loop Quantum Gravity. However, none of these theories can be taken yet as truly scientific theories, in the sense that they do not make predictions which could falsify them.

Even though the Quantum formulation of Gravity has been a problem studied for more than 50 years and has proposed theoretical environments where such a theory might be necessary, it does not exist yet a single experimental result which needs a Quantum formulation of Gravity for its interpretation. Traditionally, this caused certain scepticism in part of the scientific community about the possibility that such a theory might never be necessary. In fact, the considered impossibility of obtaining experimental results with sensitivity up to the Planck mass, which is the natural energy scale for the unification of Gravity with the other already explained forces of nature, supports this sceptical view.

However, in the last decade there has been a big interest in the scientific literature about the possibility of using VHE astronomical observations to test new physics beyond Special Relativity. VHE astronomical observations provide data about the most energetic processes ever measured from Earth. For some of the particles involved in these processes, their energies are orders of magnitude bigger than the ones accessible in the most powerful

particle accelerators at Earth. Moreover, the cosmological distances that the messengers from these processes, i.e. γs, have to travel to arrive to us could amplify any residual Quantum Gravity effect. This fact makes these messengers good vehicles to prove fundamental aspects of current physic theories, such as a possible Quantum behaviour of space-time.

Based on these ideas, a set of astronomical observations has been used to look for a possible signature of new Physics. Most of these measurements are based in testing the invariance of the Lorentz symmetry as one of the main postulates of Special Relativity. Among these experiments, the pioneering proposal is the measurement of the invariance of the Speed of Light using Gamma Ray Bursts (GRB) observations. The main idea behind this proposal was to measure a possible time shift with respect to energy for very sharp time structures observed in GRBs. A positive observation of such an effect could be interpreted as an energy dependence of the speed of γs, violating in such a way the Lorentz symmetry.

Even though existing measurements on this possible effect have already constrained it, none of them has been able to be sensitive up to the Planck scale which, as it has been aforementioned, is the natural scale for Quantum Gravity. Despite last years tremendous advances in the measurement of the invariance of the Speed of Light, better experimental data and new measurement techniques are still needed in order to reach sensitivities up to the Planck scale.

1.1 Contents of this Thesis

The aim of this Thesis is the measurement of the invariance of the Speed of Light with respect to energy, using as the source of photons the observations done by MAGIC of Markarian 421 during the Spring of 2004. Following this goal, the problem has been addressed in several steps, which are presented in the several chapters in this Thesis. These chapters have the following contents.

In chapter 2 a brief introduction to the Imaging Air Cherenkov technique is given. A description of the different parts of the hardware of the MAGIC Telescope is also included, with a special emphasis in the Camera and Calibration system, as the author of this Thesis collaborated actively in its assembling, testing, installation and on-site maintenance of the whole Camera and Calibration systems.

In chapter 3 the slow control of both the Camera and the Calibration systems is presented. This is the major technical contribution of the author to the design and construction of MAGIC. The author shared the responsability of the design, development, test, installation and maintenance of the Camera and Calibration control system. The work of the author included both software and hardware developments, particularly regarding the use of standard industrial protocols, such as CANbus, for the remote control of the functionalities of the mentioned telescope systems which includes the HVs regulation and monitoring, the DCs monitoring, the calibration pulser box configuration setting, among others.

In chapters 4 and 5 the observation done by MAGIC of Markarian 421 during Spring 2004 is analysed. The first of these chapters shows the part of the analysis used for selecting γs from the whole detected sample of events obtained by MAGIC. This analysis is done in several steps, going from the reconstruction of the image recorded by the telescope of the air shower produced by the cosmic ray in the atmosphere, to the selection of the γ candidates among these recorded images using the simulation of the Telescope

response. The second of these chapters explains how magnitudes, like the energy of the γ-rays detected, are reconstructed. With this information the fundamental tools to understand the source observation, like the energy spectrum or the time light curve, are described and reconstructed.

The author has performed the complete analysis for the Markarian 421 data sample during the Spring of 2004. This includes constructing all the necessary tools to study the real performance of the telescope during that period. This was particularly important, both for the present work and the MAGIC collaboration, due to the fact that the telescope was in commissioning phase on that period. Some parts of the analysis tools particularly developed for this Thesis are part of the Standard Analysis of MAGIC. This is the case of the algorithm used to reconstruct the position of the source based on the star field of view as observed by the MAGIC camera. The author has also developed several parts of the analysis chain used in this Thesis, such as the whole set of tools used for the reconstruction of the spectrum and light curve.

In chapter 6, the measurement of the invariance of the Speed of Light is presented. The measurement is presented in the context of the current experimental results and phenomenological frameworks existing in the literature. Due to the reduction in the energy threshold of new IACTs like MAGIC, the impact in the measurement of a new observational scenario where farther sources can be detected, is explored. This study has been already published before the completion of this Thesis. Within the framework of this study, a new method for the measurement of the invariance of the speed of light is proposed. The most significant contribution of this method, compared with previous existing ones, is the fact that it is able to use all the information contained in every single γ detected, therefore enhancing the sensitivity of the measurement. Along the chapter, this new approach is studied in detail in order to scrutinize its potential and possible limitations. In addition, the method is compared with previous existing ones. To conclude this chapter, the method is applied to the Markarian 421 analysed observations to perform a real measurement of the studied phenomenon.

Finally, chapter 7 presents the summary and conclusions of the Thesis, which has implications in both the fields of Very High Energy γ-ray astronomy and Quantum Gravity.

Chapter 2

The MAGIC Telescope

In this chapter, the detection technique used by Imaging Air Cherenkov Telescope (IACT) to indirectly detect γ-rays entering the Earth atmosphere is described. For that purpose, the main features of Extended Air Showers (EAS) are briefly commented, stressing the differences between EAS induced by primary γ-rays and the much more numerous EAS induced by charged cosmic ray (CR) nuclei, which represent the main source of background for these telescopes. The detection of EASs by IACTs via the Cherenkov radiation produced in EASs is explained. Finally, a technical description of the MAGIC Telescope, the detector on which the experimental part of this Thesis is based on, is presented. Special emphasis in the description of the telescope camera and calibration system, on which construction and development the author has been particularly involved, is done.

2.1 Detection principles of IACTs

An Imaging Atmospheric Cherenkov Telescope is a ground-based instrument which detects Cosmic Rays (CR). Detection is done not by direct observation like in satellites but by the indirect observation of the effects CR produce when entering in the atmosphere. When an enough energetic CR (> 1 GeV) hits de atmosphere, an Extended Air Showers (EAS) develops. The primary CR particle interacts with the molecules and ions of the atmosphere, thus producing new particles which in their turn interact with other atmospheric particles, starting a cascade effect. The number of particles in the shower increases quickly till it reaches a maximum, due to the fact that the energy of the primary particle is distributed among the cascade and at some point, particles do not have enough energy to produce new ones. When the mean energy among the particles in the EAS falls below the production threshold, losses of energy through ionization and Compton scattering became the dominant process and some time after this point the shower dies out. During their travel down the atmosphere within the EAS, secondary particles could have velocities above the speed of light in the air, hence the charged particles among these emit light as Cherenkov radiation. IAC telescopes use the Cherenkov light produced by EAS as the signature to detect the primary Cosmic Rays.

Cosmic Rays are mainly ionized atomic nuclei (approximately 98%, from which 87% are protons, 12% alpha particles, and 1% heavier elements such as C, N, O, Fe), electrons (approximately 2%) and a very small fraction γs and neutrinos [12]. All these particles are emitted by a diversity of astrophysical objects and some of them reach the Earth. Despite being a very small fraction of the whole spectrum of CRs, only the mentioned

neutral particles (γ-rays and neutrinos) are suitable candidates to do real astronomy. This is because the charged fraction of CRs interacts with the interstellar and intergalactic magnetic fields, thus becoming deflected. As a result, the distribution of the charged fraction of CR is isotropic. From all the CR radiation entering the Earth atmosphere, only the small flux of neutral CRs points back to their origin, which is an essential characteristic to do astronomy. Hadronic Cosmic Ray physics is a very interesting and active branch in Astroparticle physics. However, it lacks the information of their origin sources, which need to be investigated by other king of messengers like γ-rays.

Of crucial importance to γ-ray astronomy is the fact that hadronic and electromagnetic showers differ, thus providing a possibility to differentiate among signal (i.e. γs) and background (i.e. hadronic) CRs. In the following paragraphs, both sorts of showers will be described.

2.1.1 Electromagnetic Showers

Electromagnetic showers can be started with a high energy γ-ray or electron, developing a shower that contains mostly electrons, positrons and photons.

When the primary particle is a γ-ray, the strong Coulombian interaction with an atmospheric nucleus produces the emission of a virtual photon that ends in an $e^{\pm}$ pair. Both the electron and positron became accelerated in the presence of the strong coulomb fields of the atmospheric nuclei, emitting new photons by bremsstrahlung radiation. If the energy of these secondary γ-rays is still high enough, they produce again $e^{\pm}$ pairs, that can be followed by further bremsstrahlung radiation. This process continues, decreasing the mean energy of the particles in the shower until the critical energy threshold E_c is achieved (about 80 MeV for $e^{\pm}$ in air) and the energy losses by ionization of the surrounding atmospheric molecules became the dominant factor.

If the primary incident particle is an electron or a positron, the shower develops in the same way, just starting the cascade by bremsstrahlung radiation. Electron induced showers are an irreducible background to γ-rays showers detection. However, their flux is much lower than the background produced by hadronic showers.

In electromagnetic showers there is also a muonic and hadronic component. They are produced by $\mu^{\pm}$ pair production and by hadronic photo-production respectively. Nevertheless, none of these two components are expected to be significant in EM showers detected by Cherenkov telescopes due to the small cross-sections for these processes (e.g. 1.5 mb for hadronic photo-production in air) compared with $e^{\pm}$ pair production (i.e. 500 mb).

The result of the whole process of an electromagnetic shower is, therefore, a shower of photons, electrons and positrons. Interestingly, the shower is strongly collimated in the incident direction due to the relativistic energies of the particles involved. The main process that broadens the shower transversely is multiple scattering and, in second order, the deflection of the charged particles by the Earth magnetic field. In figure 2.1 are shown two schemes of an electromagnetic and an hadronic shower respectively.

2.1.2 Hadronic Showers

Hadronic showers are induced by high energy cosmic ionized nucleus (mostly protons and nucleus of helium) hitting the atmospheric nucleus and developing a shower with an hadronic core of pions, kaons and lighter nucleons (see figure 2.1), together with non negligible electromagnetic and muonic shower components. About 90% of all secondary

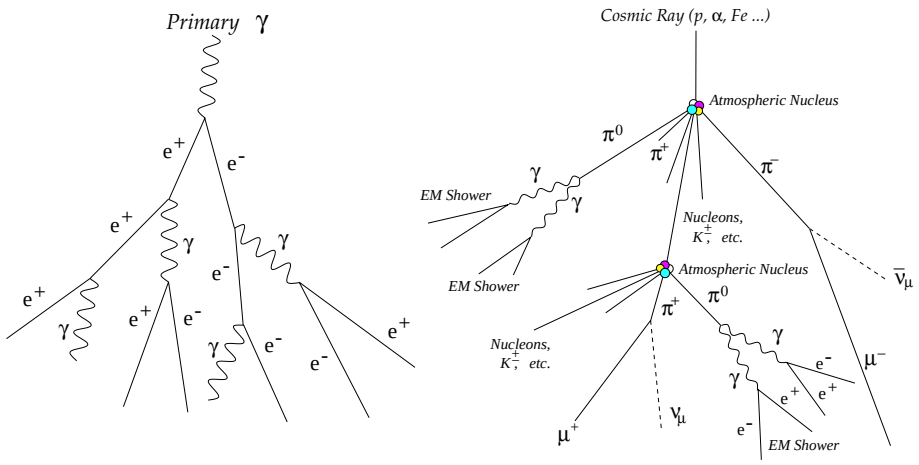

Figure 2.1: Sketch of the structure and the interactions present in an EAS, induced by a cosmic γ-ray (left) and by a charged cosmic nucleus (right).

particles produced in the hadronic core of the shower are pions, out of which 2/3 are charged pions and 1/3 neutral pions. π^0 has such a very short lifetime ($\tau \sim 10^{-16}$ s) that almost instantly decays, in most of the cases into two photons ($\pi^0 \longrightarrow \gamma + \gamma$). Both the resulting high energy photons will initiate, on their turn, an electromagnetic sub-shower, so with each hadronic interaction, approximately one third of the energy goes into the electromagnetic component of the shower. On the other hand, secondary charged pions and kaons may decay into muons and neutrinos generating a muonic component of the shower. Muons only lose their energy via ionization or decay through the channel $\mu^{\pm} \longrightarrow e^{\pm} + \nu_e(\bar{\nu}_e) + \bar{\nu}_\mu(\nu_\mu)$, thus releasing an additional fraction of energy into the electromagnetic component of the shower. Muons and neutrinos also prevent another fraction of energy, around a 5%, from being absorbed by the atmosphere [13]. This is due to the fact that the muon lifetime ($\tau = 2.2 \times 10^{-6}$ s) is about two orders of magnitude higher than that of the pion and kaon ($\tau \sim 10^{-8}$ s), and, as many muons are produced with very high energy in the upper layers of the atmosphere, frequently they have high enough Lorentz factors to reach the Earth surface before decaying.

Hence the three components of a hadronic EAS are the hadronic core built up from high energy nucleons and mesons which usually re-interact and mostly become electrons and positrons whose energy is mostly dissipated through ionization, the electromagnetic sub-showers originated from π^0 decays, and a fraction of nearly non-interacting muons and neutrinos. The most numerous particles in a hadronic shower are, therefore, positrons and electrons.

Despite having similar composition than electromagnetic showers, there are important differences among the two sorts of EAS (see figure 2.1). Hadronic showers are broader than electromagnetic ones. The main reason is that the lateral spread of hadronic showers is caused by the transverse momentum get by the secondary hadrons in the hadronic interactions, which is meaningfully larger than the scattering angle generated from multiple scattering, the process that causes lateral spread in electromagnetic showers. In addition, the nuclear interaction lengths of hadrons in air are almost double than the radiation length for bremsstrahlung and the interaction length for $e^{\pm}$ pair production ($\xi_{nuclear} \sim 83\ g/cm^2$, $\xi_{brems} \sim 37\ g/cm^2$, $\xi_{pair} \sim 47\ g/cm^2$), forcing the starting point and the max-

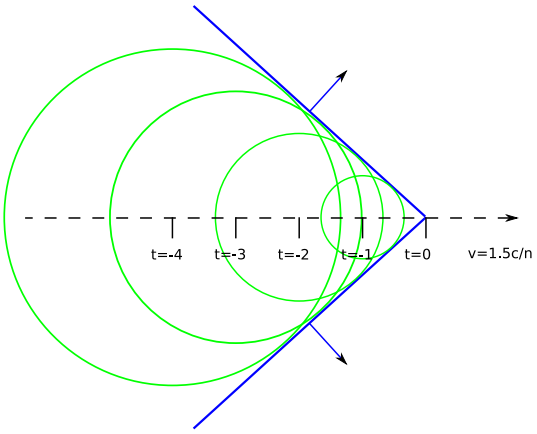

Figure 2.2: Sketch for the propagation of Cherenkov light derived from Huygens principle. The radiation emitted by a particle moving in a medium can cause constructive interferences that generate a shock wave if the particles travels faster than light. The front wave propagates in a direction that depends on the velocity of the particle.

imum of the shower of hadron-induced EAS to occur deeper in the atmosphere than in the case of a γ-ray induced shower of the same initial energy.

Afterwards, these discrepancies between electromagnetic and hadronic induced EAS will be used by IACTs in order to disentangle for a given shower its origin and in such way be able to select among the whole set of detected EAS the ones induced by cosmic γ-rays.

2.1.3 Cherenkov light produced by an EAS

Whenever a charged particle travels through a insulator medium with a speed $v = \beta c$ that exceeds the speed of light in that medium (i.e. $v > c/n$, where n is the refractive index of the medium), light is emitted. This light emission is called Cherenkov radiation.

When a charged particle travels in a medium, it disrupts the local electromagnetic field. The effect of the electromagnetic field of the charged particle is the polarization of the electrons in the surrounding atoms and molecules of the medium. Photons are emitted as the insulator's electrons restore themselves to equilibrium after the disruption has passed [1]. For charged particles with low velocities there is not a Cherenkov effect because the emitted photons interfere destructively due to the symmetrical distribution of charge on the medium. However, when the disruption (i.e. the charge particle) travels faster than the emitted photons themselves travel, the photons interfere constructively, intensifying the observed radiation (see figure 2.2).

This process is similar to the one produced by supersonic objects travelling in the air. The sonic waves that travel slower than the supersonic body produce a shock front. In an equivalent way, the Cherenkov emission produces a shock-wave behind the charged particle as this one crosses the medium. The wavefront propagates at a fixed angle $\theta_{\check{c}}$ with respect to the trajectory of the particle, due to the fact that the light emitted from different points along the particle trajectory add coherently just for a certain angle (see

[1] In a conductor, the electromagnetic disruption can be restored without emitting a photon

scheme **c** of figure 2.2). This Cherenkov angle can be deduced from only geometrical considerations as follows

$$\cos\theta_{\check{c}} = \frac{\frac{c}{n}\cdot\Delta T}{\beta c\Delta T} = \frac{1}{\beta n} \tag{2.1}$$

Due to the fact that β is by definition smaller than 1, the maximum angle of Cherenkov emission is observed for ultra-relativistic charged particles and is given by the expression 2.2.

$$\cos\theta_{\check{c}}^{max} = \frac{1}{n} \tag{2.2}$$

The fact that Cherenkov radiation is only produce by charge particles with a minimum energy (i.e. $v > c/n$), produces an Cherenkov energy threshold which is show in expression 2.3.

$$E_{\check{c}}^{thr} = \frac{m_0c^2}{\sqrt{1-\beta_{min}^2}} = \frac{m_0c^2}{\sqrt{1-(1/n)^2}} \tag{2.3}$$

where m_0 is the rest mass of the charged particle.

From the previous equations, it is seen that the Cherenkov emission angle and the energy threshold for Cherenkov emission are not constant values along the path of the shower, as the refractive index depends on the density of the medium, which in the case of the atmosphere changes with altitude. An accurate modelization of the atmosphere is a rather complex problem. However, in any model of the atmosphere a good approximation is that the density of air decreases with altitude, then the refractive index also decreases with altitude.

Regarding the energy threshold for Cherenkov emission, it is higher in the upper layers of the atmosphere and decreases as the EAS develops on, as n decreases with height. It is also the case that nearly all the Cherenkov light in an EAS is produced by the secondary electrons and positrons, as they are an overwhelming fraction of the particles in the shower and, being the lightest charge particle produced, they are more likely to be above the threshold of Cherenkov emission. For instance, at 10 km the Cherenkov energy threshold for electrons is still below the critical energy which indicates the shower maximum ($E_c \sim 83$ MeV), so most of the electrons and positrons still emit Cherenkov radiation when the electromagnetic EAS is already dying out. Muons from hadronic EAS can also emit a non negligible fraction of the Cherenkov light and occasionally produce a fake light distribution of a γ-ray induced shower.

Regarding the maximum angle of Cherenkov emission, it is smaller at the beginning of the shower than in the shower tail, again due to the change of n_h with height. Interestingly, this height dependence of the angle is responsible for a characteristic enhancement of the Cherenkov light density that arrives at a certain position in the ground [2]. As can be seen in Figure 2.3, the light emitted by shower electrons and positrons at different heights reaches the ground at approximately the same distance from the axis of the shower. From EAS simulations it is shown that the ring structure, called hump, typically occurs for radius between 100 and 130 m from the center of the Cherenkov light pool. Nevertheless, due to multiple scattering the trajectories of secondary $e^{\pm}$ are slightly deviated from the

[2]The Cherenkov light at the ground is the superposition of all the light emitted in cones integrated over the whole shower longitudinal path.

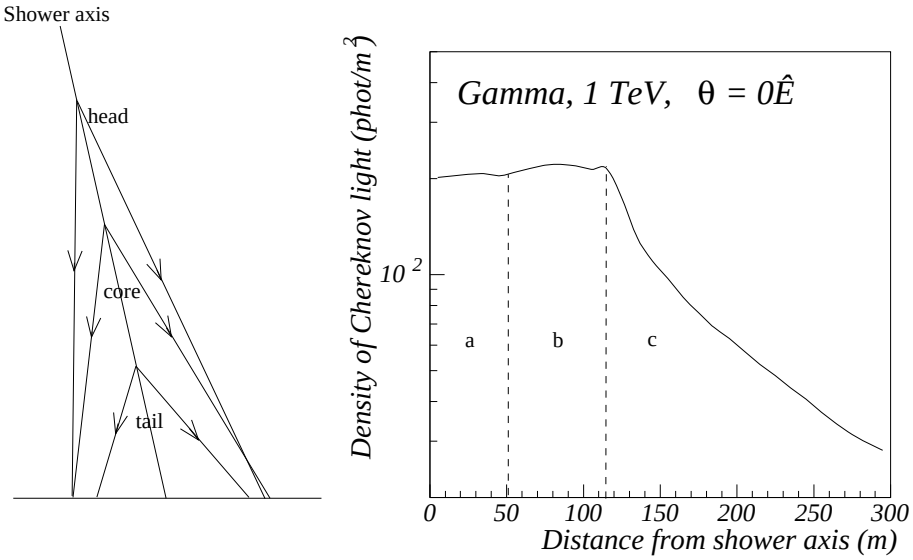

Figure 2.3: Schematic view of a shower with different Cherenkov angles at different altitudes is shown in left figure. In the right figure the lateral distribution of Cherenkov photons from the shower axis is shown. The region (a) closer to the impact of the shower axis collects the light principally from the shower tail, while the region up to about 120 m from the shower axis is dominated by light coming from the shower core. Light produced by the shower halo particles contributes to region (c). Figure extracted from reference [14]

trajectory of the primary γ-ray, the hump produced in real EAS is somehow spread out. For hadron-induced EAS, the hump structure is even less visible as $e^{\pm}$ directions are even more dispersed due to the high transverse momentum kick of nuclear interactions and $e^{\pm}$ scatter away from the shower axis.

Differences in the shower development between a hadron-induced and a γ-induced EAS result not only in differences in the shape of the Cherenkov light distribution at ground level, but also in time structure differences. Air showers develop practically at the speed of light, resulting therefore in very short Cherenkov flashes. Typically the front of Cherenkov photons produced in an electromagnetic EAS arrives at the ground in 2-5 ns, whereas hadronic showers have a wider time spread (10-15 ns) due to the development of many electromagnetic sub-showers. Both shape and time pattern differences can be used to distinguish between hadronic or electromagnetic showers with a sensitive enough ground-based instrument.

For detection purposes, it is also necessary to know the spectrum of the Cherenkov light radiated in an EAS. Cherenkov radiation shows a continuous spectrum with a frequency cut-off in the X-ray band. This characteristic, together with the fact that higher frequencies (shorter wavelengths) are more intense in Cherenkov radiation, explains that most Cherenkov radiation is in the ultraviolet spectrum decreasing along the visible region. This is why visible Cherenkov radiation is observed to be brilliant blue.

Nevertheless, the spectrum observed at ground level is quite different from the emitted one due to the interactions of the Cherenkov photons with the air molecules along their travel through the atmosphere. The observed spectrum peaks at around 330nm, as a result of the different attenuation processes that Cherenkov photons suffer in the atmosphere.

The most important processes are listed bellow.

1. Absorption in the Ozone layer, mainly in the upper part ($\gtrsim$ 10 km) of the atmosphere. Practically all photons with wavelength lower than 290 nm are absorbed through this process ($O_3 + \gamma \rightarrow O_2 + O$).

2. Rayleigh scattering, which occurs on polarizable molecules with sizes smaller than the photon wavelength. If the atmospheric conditions are good, this is the process responsible for most of the Cherenkov light attenuation from 15 to 2 km above sea level, with a cross section $\propto \lambda^4$.

3. Mie scattering, which takes place on polarizable molecules with sizes comparable or larger than the photon wavelength, basically aerosol particles present in the atmosphere. Its effect is especially important when atmospheric conditions are not optimal (i.e. if there is dust, pollution, clouds, fog, etc).

4. Absorption by H_2O and CO_2 molecules, only important for photon wavelengths above 800 nm. These wavelengths are outside the sensitive range of the photosensors which are typically used for Cherenkov detection.

2.1.4 Common remarks for IACTs detection technique

Imaging Air Cherenkov Telescopes are formed by the same basic elements than almost all kind of ground-based telescopes. First, the steer system which is used to track the astronomical source being observed. Due to the rotation of the Earth the sources seems to move along the sky making necessary to move the telescope continuously to follow the observed source. Second, the mirror surface which collects the light, in that case, from the light pool produced by the Cherenkov radiation emitted by the secondary particles in the EAS. And third, a camera formed by light detectors placed in the focal plane to collect the reflected Cherenkov photons. In IACTs, the light detectors need very rapid time response (of the order of ns) due to the narrow time window in which light coming from the showers is concentrated. Using slower photodetectors will introduce unnecessary integration of noise in the measurement making the detection less sensitive. Traditionally, and in most of the present IACTs, photomultiplier tubes (PMT) have been used to convert the incident Cherenkov photons into electric pulses, despite higher sensitivity light detectors such as Hybrid PhotoDetectors (HPD), Avalanche PhotoDiodes (APD) or Silicon Photomultipliers (SiPM) are under study.

The term 'Imaging' in the IACT name comes from the reconstruction of the EAS development shape in this technique. The main reason for this reconstruction is the aim of distinguish between electromagnetic induced EAS from hadronic induced ones. In this sense, pixelization with enough granularity in the photodetectors camera is required in order to be able to distinguish signal (i.e. electromagnetic showers) from a continuous background (i.e. hadronic showers) by imaging. As shown in figure 2.4, the image formed in the camera of photosensors is a geometrical projection of the atmospheric shower. As has been previously mentioned, Cherenkov photons emitted at different heights reach the telescope mirror dish with different angles and, therefore, will be focused on different (relative) positions in the camera of the telescope. As a consequence, the image contains information of the longitudinal development of the EAS which can be reconstructed, allowing us to know the number of particles emitting Cherenkov light as a function of the height in the atmosphere.

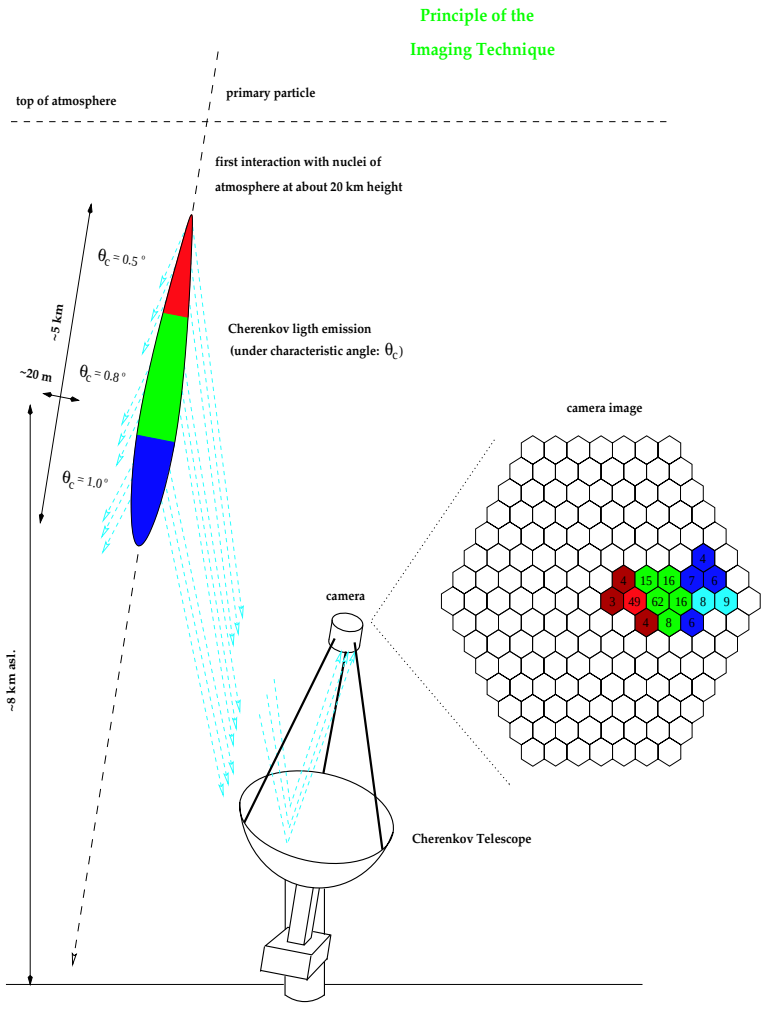

Figure 2.4: Sketch of the principle of the Cherenkov technique through the formation of the image of an EAS in an IACT pixelized camera. The numbers in the figure correspond to a typical 1 TeV γ-ray induced shower. Figure extracted from reference [15].

The Cherenkov technique relies on the shower development information that is contained in the images formed in the telescope camera to infer the characteristics (energy, incident direction and particle type) of the particle that originated the EAS. The total amount of light contained in the image is the main estimator of the energy of the primary particle. Despite energy losses through ionization are 3 or 4 orders of magnitude bigger than the energy lost in form of Cherenkov radiation, the ratio between both energy losses is in first order constant, so a measurement of the Cherenkov light provides a good estimation of the total energy absorbed by the atmosphere, which acts as a calorimeter for the detector. It is in this sense that in IACTs the atmosphere is considered part of the detector instrument.

To characterize an IACT, two important parameters are required which are its sensitivity and energy threshold. Sensitivity of an IACT is defined as the minimum detectable γ-ray flux in a given number of observation hours. The energy threshold of the telescope is the minimum energy of the primary particle to which the telescope is able to disentangle

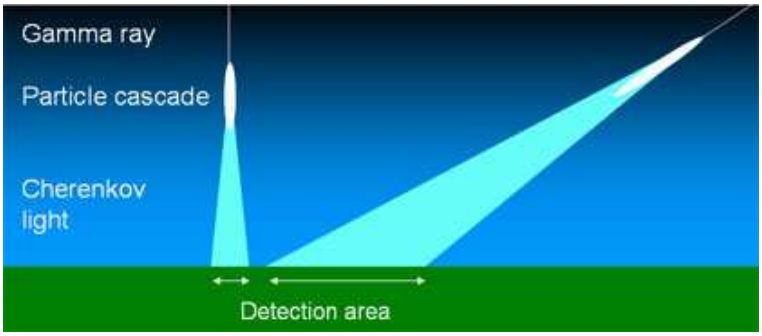

Figure 2.5: Collection area dependence with Zenith angle sketch. Figure extracted from reference [16].

the signal from the background. Both sensitivity and energy threshold are not constant parameters for a given telescope, due to the fact that they are strongly influenced by the amount of dispersion (i.e. density) of the Cherenkov light at the observation level (i.e. ground level). For example, observational conditions like the Zenith angle for the observed source might produce a change in the light density at ground. For the same primary cosmic ray, equivalent amount of Cherenkov photons will be produced for any Zenith angle. However, due to geometrical reasons, this number of photons is projected in a bigger surface at ground level (see figure 2.5) producing a lower photon density.

The spread of Cherenkov light has two counteracting consequences. On one hand, the light spread allows the IACT to detect EASs over a large range of impact parameters, from around 30 to 150 m.[3] This provides IACTs with huge collection areas (of the order of 10^5 m^2) which turn into high sensitivities in comparison with γ-ray detectors mounted on satellites, whose dimensions are clearly limited by space-launching requirements to $\sim$ 0.01 - 1 m^2. On the other hand, the dilution of the Cherenkov radiation over a large light pool makes its detection more difficult, forcing the use of large collecting mirror areas and very high sensitivity photodetectors, to be able to detect the EAS induced by the γ-rays of the lowest energy achievable by this technique (just few GeV). Implicitly, this means that an IACT is able to recognize γ-ray induced showers only for energies above a given threshold (E_{th}). As the number of Cherenkov photons is proportional to the energy of the primary γ-ray, the energy threshold is basically limited by the size of the collection mirror area and the sensitivity of the photodetectors.

From this discussion it is clear that although the sensitivity of IACT grows when observing at high zenith angles (due to the increase on collection area), the energy threshold of the telescope increases as the Cherenkov light spreads in a larger area.

Only two years ago, the lowest energy threshold [4] reached with an IACT had been the one obtained by the Whipple telescope, of about 300 GeV. Nowadays, a new generation

[3] Although the efficiency of detection of showers with impact parameters larger than $\sim$ 150 m is quite low, the large amount of showers arriving with these larger impact distances makes them to be still a significant fraction of the total amount of detected showers.

[4] The conventional definition of E_{th} for IACTs is the energy for which the differential γ-ray rate distribution peaks. This definition makes the parameter E_{th} dependent on the slope of the γ-ray spectrum of the source. Therefore, a reference astronomical object or standard candle needs to be used for an unambiguous definition of E_{th}. For northern hemisphere telescopes, the source most widely chosen as reference is the Crab Nebula pulsar.

of Cherenkov telescopes are significantly lowering the energy threshold. Both the HESS array and the MAGIC telescope have already reached the level of 100 GeV. The goal of the MAGIC collaboration is to achieve even further progress in pushing down the energy threshold, as its mirror reflector area is substantially larger than the one of any other existing IACT.

In the following sections of this chapter a brief description of the different parts of the MAGIC telescope will be provided.

2.2 The MAGIC Telescope

MAGIC Telescope stands for Major Atmospheric Gamma Imaging Cherenkov Telescope, and it is one of the latest generation IACTs. Characteristic of MAGIC is its 17-m diameter reflector dish that turns it into the largest Cherenkov telescope ever. The location of MAGIC is the Roque de los Muchachos Observatory, in the Canary island of La Palma (at a latitude of 28.8° North, longitude of 17.9° West, and 2200 m above sea level), which belongs to the Instituto de Astrofísica de Canarias (same location where the HEGRA stereoscopic system of Imaging Atmospheric Cherenkov Telescopes was installed). This location is considered to be one of the best observation sites in the northern hemisphere. [5]

The initial ideas of the project were developed during 1995 [17] and the detailed Technical Design Report [18] was ready in 1998. The large amount of the funds was granted at the end of the year 2000, allowing the starting of the construction of the telescope in September 2001. After two years of construction work the official inauguration of MAGIC was in October 2003, despite the first Cherenkov images were recorded already in March that year. The commissioning phase of the telescope started right after the inauguration and was concluded one year later, at the beginning of autumn 2004. Since then, the telescope is running in normal operation mode, with only technical accesses during full moon periods between data taking shifts. MAGIC is an international collaboration of physicists and technicians from 17 institutions based in 10 different countries (Germany, Spain, Italy, Switzerland, Poland, USA, Armenia, Finland, South Africa and Bulgaria).

Technically and experimentally, MAGIC represents a challenge by introducing technological innovations and testing new techniques never used before in the field of IACTs. The main reason for this focus on improvement is the goal of the experiment: to cover with high sensitivity the unexplored energy gap between 10 GeV and 300 GeV in γ-ray astronomy. Doing so requires a significant lowering of the energy threshold with respect to contemporary instruments. With photosensor with high efficiency detecting Cherenkov photons and the world-wide largest collecting mirror area, an E_{th} close to 30 GeV is the ultimate target for MAGIC.

In the following subsections the most relevant elements of the MAGIC Telescope will be described, with major emphasis in the description of the telescope camera and calibration system, on which construction and development the author has been particularly involved.

2.2.1 The telescope frame, reflector mirror dish and drive system

One of the main goals pursued by the MAGIC Telescope was to be able to reposition to any direction in the sky in less than one minute. This requirement was needed in order to allow for follow up observations of the prompt emission of Gamma-Ray Bursts (GRB)

[5] In fact, due to good atmospheric quality, low human-made light background and good weather, it became the European Northern Observatory (ENO).

after an alert from an X-ray or γ-ray satellites. To achieve this goal, the inertia of the moving parts of the telescope need to be as low as possible, especially the mirror frame.

MAGIC supports its mirror dish with a three layer structure made of low-weight carbon fiber-epoxy tubes joined by aluminium knots.[6] Carbon fiber is rigid enough and at the same time provides MAGIC with low enough inertia. The current fast mode the telescope can be moved to the two most distant position of the sky in less than 100 seconds. Whereas the average time needed to move between two random positions in the sky is around 40 seconds. These values are for the present commissioned steering mode however the design of the steering system still allows some place for improvement. The structure also guarantees wind resistance up to 170Km/h and stability for complete ice coverage up to 3 cm thickness.

The frame design follows the concept of a pre-existing 17-m solar collector which was already built and tested few years ago as part of the German solar power research program. The reflector of MAGIC is an octagonal-shaped tessellated mirror dish of 236 m^2. The overall curvature of the reflector is parabolic to minimize the spread in the arrival times of the Cherenkov photons at the camera plane. The focal length to diameter ratio, f/D, is about 1. This ratio provides high optical quality to the images at the camera, ensuring that the effect of the optical aberrations in the shower images remains smaller than the pixel size.

The telescope reflector is composed of 964 mirror elements of 49.5 $\times$ 49.5 cm^2 area each, 892 of them grouped in 4-element panels and the rest in 3-element panels located at the rim of the reflector dish. The curvature of the individual mirror elements is spherical and due to the overall parabolic shape of the reflector, their focal length increases gradually (from 17 to 18 m) when moving out from the center of the dish. The construction of these individual mirror elements can be considered another of the technical innovations adopted by the MAGIC Telescope, being lighter, more resistant and cost effective than conventional glass mirrors typically used by IACT. The base of each mirror element is made of an aluminium box filled by an aluminium honeycomb structure, to be light enough but with the required rigidity. The 5 mm thick mirror front plate surface is polished and shaped with diamond milling and afterwards quartz coated to protect it against ageing and scratches. The final assembly weights less than 4 kg. The mean reflectivity in the range of interest for the Cherenkov spectrum ($\sim$ 300-650 nm) is about 85% and the roughness of the mirrors surface is below 10 nm. 90% of the light of a parallel incident beam is collected in an area smaller than a small pixel of the MAGIC camera [19]. Each mirror panel is equipped with an internal heating system to prevent dew and ice formation.

Another novel technique related to the reflector surface has been introduced in the MAGIC Telescope. Despite the frame being rigid enough, the huge structure suffers from residual deformations when moving from one to another position. To correct their influence, an Active Mirror Control (AMC) system has been developed. Each mirror panel has been equipped with a switchable laser pointer. The signal from this laser is monitored by a CCD camera and used as a reference to know the actual position of the mirror panel. To adjust the position of the mirror to the nominal one, two stepping motors are used, tilting the panel in both directions. The readjustment operation of the whole reflector surface is remotely controlled, being automatically performed in less than 3 minutes.

Due to the high pointing accuracy required, the large dimensions of the MAGIC

[6]The weight of the combined frame and mirror dish is less than 20 tons, being the total final weight of the telescope about 64 tons.

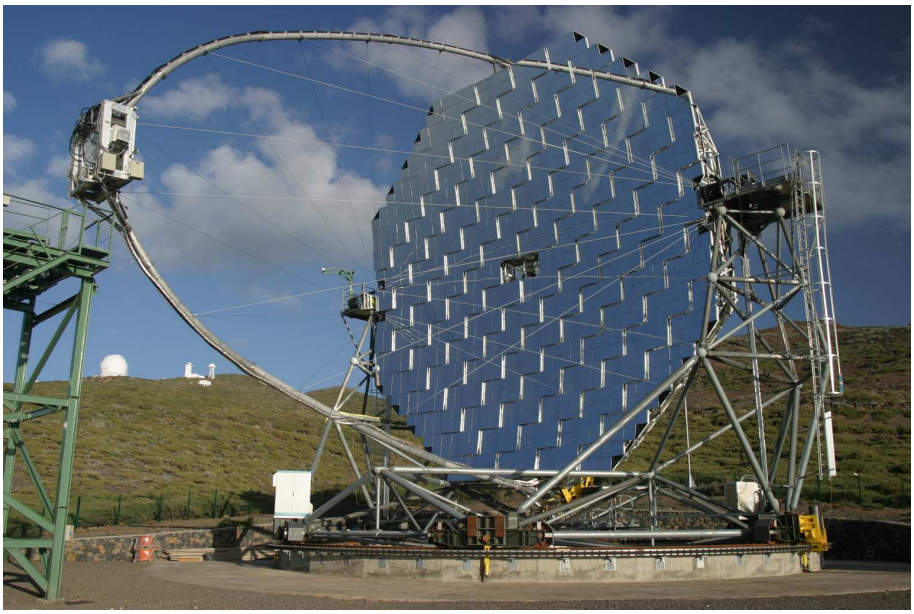

Figure 2.6: The MAGIC Telescope at "El Roque de los Muchachos" site in the canary island of La Palma.

telescope and the fast repositioning goal, the drive system of the MAGIC Telescope has also been a major challenge. The azimuth axis of the telescope is equipped with two 11 kW motors, while the elevation axis has a single motor of the same power. The position of the telescope is measured in the mechanical frame by three absolute 14-bit shaft encoders. This configuration allows the measuring of the telescope position with an accuracy of about 0.02 degrees. By using a CCD camera mounted on the reflector frame, it has been established that the telescope tracks to better than a 1/10 of a pixel size [20].

2.2.2 The Camera

The camera is a crucial element in the performance of an IACT, having a strong influence in both energy threshold and sensitivity of the telescope. Regarding the first parameter, the camera is the device where Cherenkov photons are collected and converted to photoelectrons [7] (phe), so its efficiency strongly affects the energy threshold of the telescope. Regarding the second one, γ/background separation power is highly dependent on the quality of the shower images recorded in the camera, so it also directly influences the sensitivity of the telescope.

Historically, IACT cameras were designed with a single PMT. Today, arrays of a few hundred of pixels are common. Last years improvements in the detection technique can mainly be attributed to the achievement of finer pixelization, allowing an increase of efficiency in the important differentiation between hadron and gamma showers. Finer pixels have also implied an improvement in the trigger efficiencies for γs, in the angular resolution, in the γ/h separation, and also some modest noise reduction by limiting the image to its minimal necessary size. In turn, also the energy resolution is slightly improved

[7] A photoelectron is the e^- emitted when a photon interacts with the sensitive part of a given photosensor.

due to the better determination of the shower maximum location, particularly for low energy events.

Lowering the E_{th} of an IACT can be achieved by constructing large mirror area reflectors (i.e. more Cherenkov light is collected). This is rather expensive and complicated, from the technical point of view. In MAGIC, the mirror area has been increased up to an affordable size and in addition the conversion efficiencies from Cherenkov photons to photoelectrons have been improved in the camera PMTs. Moreover, non-sensitive regions (dead areas) in the camera have bee reduced by using dedicated light concentrators.

An optimal IACT camera should be able to register both low energy and high energy showers with comparable efficiency. These two requirements imply counteracting demands to the camera design. On one hand, high energy showers emit more light and produce more extended images in the camera, due to the fact that they develop along larger depths in the atmosphere (up to $\sim 1.5°$). In this sense, only a large field of view (FOV) camera ensures full containment of the higher energy showers images ($\sim 4\ °$ ø FOV for $E_\gamma \lesssim 10$ TeV). This is particularly important due to the fact that the information of any shower tail is particularly useful to improve the γ/h separation and the energy and angular resolution of the telescope. The benefits from a bigger FOV are also related with better sensitivity for studying γ-ray emission from extended objects, such as Galactic SNRs which can have an angular extension larger than one degree. On the other hand, images from low energy showers (sub-100 GeV) are smaller so they demand a finer pixelization at least in the central region of the camera. A small pixel size also helps to reduce of the light of the night sky (LONS) background. This allows to reduce the trigger threshold preset on the discriminator level, which in turn implies a reduction in the E_{th} of the telescope. However, due to the high cost of each photosensor, the final layout of the camera is always a compromise between a large FOV and a finer pixelization.

Camera layout

The chosen design for the camera of the MAGIC Telescope has also been designed taking into account the requirement of a minimum weight for the telescope to allow a fast repositioning. For this reason, most of the trigger and readout electronics were not housed inside the camera but in the central data acquisition building, located 100 m away from the telescope. A part from minimizing the weight and size of the camera, to separate the electronics increases heat dissipation and reduces pickup noise, due to the fact that the electronics of the final processing signal are really noisy systems. Additionally, this design allows reducing substantially the complexity of the camera, thus simplifying its maintenance and repairs. This is particularly important as the camera is the element of the telescope that is more difficult to access.

The layout of the camera is schematically shown in figure 2.7. Due to the necessary compromise between telescope performance for both high and low energy events, and cost, the hexagonal detecting area was split into two regions: an inner part, segmented in 396 hexagonal finer pixels[8] of 0.1° angular diameter ($\sim$ 30 mm ø at the camera plane), which covers up to 2.1° (2.3°) ø FOV for the short (long) hexagonal camera axis; and an outer part with 180 hexagonal bigger pixels of 0.2° angular diameter ($\sim$ 60 mm ø at the camera plane), to cover up to 3.5° (3.8°) ø FOV. The trigger region consists only of the central 325 pixels, as described in Section 2.2.3.

[8]The central pixel is left empty and is currently equipped with a higher sensitive photodetector devoted to optical studies.

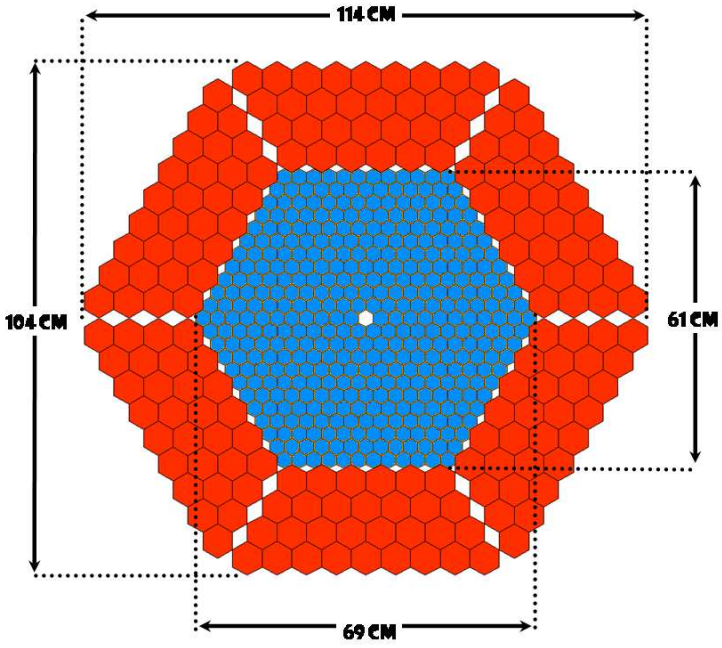

Figure 2.7: Scheme of the MAGIC camera layout. The inner region (in blue) is equipped with 0.1° ø FOV pixels to get a better sampling of the low energy showers. The outer region (in red) is segmented in 0.2° ø FOV pixels. The whole camera FOV is 3.5-3.8° in diameter.

The MAGIC camera configuration allows, with the finer inner pixels, a good sampling of the small images that are produced by low energy γ-rays, which is the main detecting goal of MAGIC. Although the shower tails of the larger images will be mapped into the outer region which is equipped with large pixels, the quality of the images of the higher energy showers is not substantially deteriorated, as the light density is also larger. The total cost and complexity saved with respect to a uniform segmentation of the camera with finer pixels accounts on 540 photodetectors and all the elements of their corresponding readout channels.

From the layout of the MAGIC Telescope camera it has to be highlighted also another interesting element: the plate of light concentrator cones in front of the photodetector pixel matrix. Light concentrators provide three important benefits. First, they ensure a nearly 100% active area camera by minimizing the dead space between photosensors. With an entrance of hexagonal shape, these light concentrators allows for a perfect compactness of the camera pixels, while their output window of circular shape perfectly couples to the round active area of the PMTs. With this low-cost plate, photon detection efficiency of the PMT camera increases the by about 50%. Second, an enhancement of the probability of photon double cathode crossing, thus improving the QE of the PMTs by $\sim$ 15%. For some incident angles of the photon reaching the light collector, they can cross twice the sensitive area of the cathode, hence the effective QE increases. Actually, the design of the light collectors is thought to improve the double crossing feature. And third, the

Figure 2.8: Front view of the MAGIC Telescope camera. Several parts of the camera can be observed in this photograph: the protecting plexiglass window, the light concentrators collect the incident light onto the camera photosensors as well as other most exterior elements like the camera lids.

plate rejects a large fraction of the light coming with an incident angle larger than the one defined by the last ring of mirrors of the main reflector; which reduces the level of background light in the camera. MAGIC light concentrators are made of a plastic material covered with aluminized Mylar foil of $\sim$ 85% reflectivity.

Finally, the entire camera (light concentrators, photosensors and other electronic) are protected from the environmental conditions by a 2 mm thick window made of UV transmitting plexiglass. Both sides of the plexiglass window are slightly reflective ($\sim$4%) so its overall transmission is 92%.

The described elements conforming the MAGIC camera can be seen in a photograph of the front part of the camera, in figure 2.8.

Camera focus distances

The camera can be shifted along the telescope axis to the reflector to set different focus positions. The camera runs along four guides and it is fixed to its position with two nuts, one at each side of the camera. Using the right wrench one can manually shift the camera along the guides.

The most important positions defined along this axis are three. First, focusing to infinity by definition is produced when the camera is placed at the focal plane (i.e. 17

m away from the reflector). At this position the stars should have the minimal spread, actually, this spread defines the reflector Point Spread Function. Second, when the camera is 3 cm further away from the reflector (i.e. 17.03 m away from the reflector). For this position the reflector focuses objects that are 10 km away into the camera plane. This is the distance to a typical shower and cosmic ray data are taken at this position. And third, when the camera is 30 cm further away than the focus the reflector focuses objects that are 1 km away into the camera plane. This is approximately the distance from the telescope to the nearby highest altitude site place, El Roque de los Muchachos. A lamp installed in this area is used to re-align manually the telescope mirrors once every two or three months.

The Photosensors

Several photo-sensors were considered for installation in the MAGIC camera: photomultiplier tubes (PMTs), hybrid photo-multipliers (HPDs) and avalanche photodiodes (APDs). Although HPDs and APDs offered higher quantum efficiencies, the restricted size of the active area and high prices of such devices would have made a deep impact into the total cost of the telescope. Hence, the option of using a special production of PMTs satisfying all MAGIC requirements was adopted and we left the possibility of using HPDs for the camera of the second upgraded MAGIC telescope.

The PMTs were produced in a dedicated R&D cooperation with the English company Electron Tubes (ET) in order to design a model of PMT which fulfills all the requirements of the MAGIC telescope. The most important characteristics required for the PMTs were several. Low gain ($\lesssim 2 \times 10^4$) compared to typical PMTs to avoid that light of the night sky (LONS) induces photoelectron rates in excess of a few hundred MHz. The main reason for this requirement is the aim of observing during moderate moon and in such a way increase the duty cycle for the MAGIC telescope. Good time resolution with a pulsed FWHM close to 1 ns in order to which improves the γ-ray / h separation and reduce the noise generated by the LONS. Wide dynamic range up to 5×10^3 to detect the largest expected signals ($\sim 5 \times 10^3$ phe per camera pixel for a $\sim$ 10 TeV γ-induced shower), and still resolve signals of just few $\gtrsim$ phe. Good QE in the range of wavelengths of the showers Cherenkov light. Single photoelectron response to allow a single calibration of the detection chain. And finally, low after-pulse rate to avoid limiting the minimum trigger threshold setting for individual PMTs.

The outcome of this collaboration was the design and construction of the new ET9916A (25 mm ø) for the inner pixels and ET9917A (38 mm ø) for the outer pixels of the MAGIC Telescope. Technically, these PMTs have two distinguishing features from conventional PMTs that make them follow the necessary requirements: a hemispherical photocathode (PhC) and a dynode system with only 6 stages in circular-focused configuration.

Compared to the flat entrance window of conventional PMTs, the main advantage of a hemispherical-shaped photocathode is twofold: first, a higher aperture solid angle which provides better light collection inside the light cones; second, as the produced photoelectrons travel roughly the same distance between the photocathode and the first dynode, there is a reduced time jitter. Regarding the 6-stage dynode system, with this design it is easier to obtain a low gain and also low interdynode time spread but maintaining good interdynode electron collection efficiency, in comparison with typical 10 or 12-stage photomultipliers. As a result, these PMTs are capable to produce signals with rise times as short as $\sim$ 700 ps and FWHM $<$ 1-1.2 ns (see reference [21]).

The hemispherical shape of the photocathode has been found to have an additional advantage: for some incident angles, photons cross the photocathode twice. In this sense, if the photon is not absorbed in the first crossing it still has a second chance of being absorbed at the other side of the hemispherical sensitive area. Therefore, double-crossing photons have a higher probability to create a photoelectron and hence be detected by the PMT. The QE enhancement due to this double crossing effect can be as high as 20%. Once this effect was known and characterized, the design of the light concentrator cones was adapted to maximize the number of photons which suffer double crossing.

The photocathode of the ET9116A and ET9117A type PMTs is bi-alkali with enhanced green sensitivity. Its uniformity and its Quantum Efficiency [9] (QE) as a function of the wavelength of the incident light have been measured in detail in reference [22]. Results show that the mean QE exceeds 20% in the 330 - 470 nm range, achieving 25% at the peak, which makes them adequate for the expected Cherenkov photon spectrum range. A further substantial enhancement of the effective QE of the PMTs used in MAGIC was achieved by coating manually the PMT photocathode with a light scattering lacquer mixed together with a wavelength shifter [23]. After this improvement, the mean QE improves up to 23%, with a peak value arriving close to 30%.

By increasing the HV difference between the photocathode and the first dynode the single photoelectron response improves, but also the probability of after-pulsing. After detailed studies [21], the configuration that maintains the after-pulsing rate below a reasonable level and allows, up to a certain degree, the single photoelectron response is 3 : 1 : 1 : 1 : 1 : 1 (from cathode to anode). It was also found that further increasing the HV difference in the fifth and sixth dynode by 50 V increases the dynamic range of photoelectrons to 510^3. The first five amplification stages (HV_{C1}, HV_{12}, ..., HV_{45}) are powered through a main HV power supply. HV_{C1} is fixed to 360 V by using two Zener diodes and HV_{12},... and HV_{45} are all equal and regulated individually for each pixel. The last two dynodes need an independent power supply in order to get a high current and maintain the voltage difference even when there is a large electron multiplication. The voltage between D5 and the anode ($HV_{56} + HV_{6A}$) is fixed actively using the so-called Active Load power supply to 350 V . The voltage between D6 and the anode is set by an independent power supply to 175 V.

Signal transmission

As it has been mentioned before, the decision of housing the main readout electronics outside the camera had major advantages. Camera maintenance and a light and small-size camera which reduces oscillations and the need of heavy telescope counter-weights (a requirement for fast telescope movements). The lack of trigger and acquisition systems in the camera helps reducing the pickup noise which affects to the PMT analog signals. Moreover, the heat dissipation inside the camera is lowered, and a cheaper and lighter cooling system can be used. The electronic pixel chain is modular, allowing for further updates on the trigger system of FADC system without modifying the camera (upgrading tests can be easily made in observation nights).

However, it presented also a major problematic related with the substantial distortion and attenuation that the PMT pulses suffer when they are transmitted through a 150 m long coaxial cable to the data acquisition building. Signal transmission is, then, a

[9] Quantum efficiency is the percentage of photons hitting the photo-sensitive surface that will produce an photoelectron.

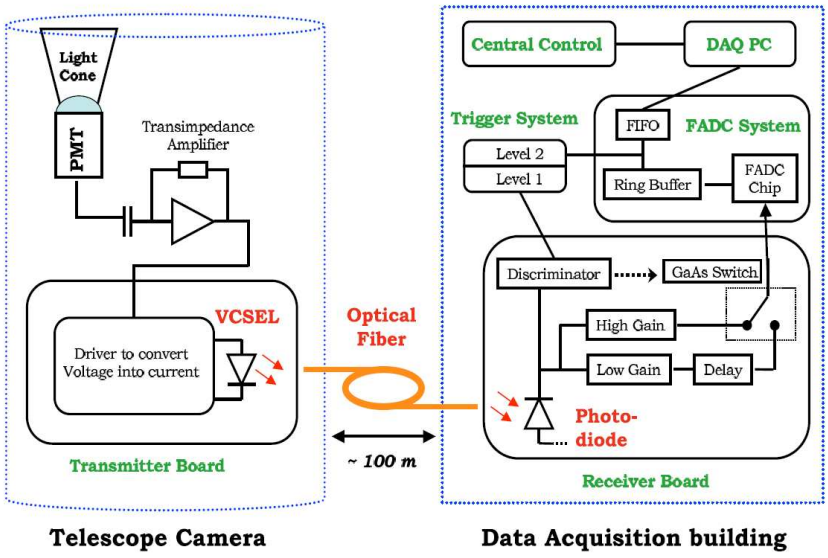

Figure 2.9: Scheme of the signal flow and the data readout in the MAGIC Telescope. Figure extracted from reference [25].

major challenge for MAGIC, taking into account that a distortion of a few ns of the fast Cherenkov optical flashes can significantly reduce the efficiency of the time coincidence based trigger. In this sense, it was decided to drive the transmission of the PMT signals through optical fibers [10], due to the fact that through them the degradation of analog signals is significantly lower than in coaxial cables. The use of optical fibers for the signal transmission has also additional advantages, such as forbidding the crosstalk between different channels (which in practice are typically packed very close to each other in their way to the data acquisition building) and avoiding the influence of external electromagnetic interferences. It is also the case that optical fibers are much lighter and allow individual channels to be packed more compactly.

The use of optical fibers implies that the electrical PMT pulses have to be converted into light pulses. To do so, members of the MAGIC and VERITAS collaboration joined efforts in 2000 to built successfully an optical link system with VCSEL drivers (Vertical Cavity Surface Emitting Laser) to transmit PMT pulses [26]. The use of VCSELs instead of Light Emitting Diodes (LEDs) or other conventional lasers was a technical innovation. This innovative system was then used to transmit the signals of the 111 PMTs located in the outer ring of the camera of the WHIPPLE telescope through 50 m long optical fibers to the main station [27]. Unfortunately, unexpected instabilities in gain and noise performance, attributed to the mode "hopping" in the VCSELs, appeared in many of the channels of the optical link system making the WHIPPLE collaboration decided not to include the signals of the channels transmitted by optical fibers into their data analyses.

Regarding MAGIC, an extensive study on a particular VCSEL [11] was carried out in order to reduce the effect of these performance problems. The above mentioned insta-

[10] The idea of using optical fiber for the signal transmission was first proposed and developed by the AMANDA collaboration [24].

[11] Type HFE4080-321 from Honeywell

bilities were characterized so that by modifying slightly the design of the system these instabilities where far below the statistical fluctuations of the PMT signals. In addition, detailed quality checks were carried out for each single VCSEL, and all those lasers not fulfilling the strict requirements to be used in MAGIC were rejected. The details of these studies, as well as the final performance of the optical link system used in MAGIC is reported in [25].

As a result of all these technical studies, a final scheme of the signal transmission system was proposed (see figure 2.9). The pulsed signal after the preamplifier stage goes through a coaxial cable with gold-plated SMA connector to the Transmitter Boards, also inside the camera. Each Transmitter Board contains 18 VCSELs being used 36 (25 for the inner camera and 11 for the outer) for the transmission of the whole set of pixels and keeping around 10% of spares. In the Transmitter Boards the voltage signal from the PMT is converted into current signals which modulate the current flowing through the VCSEL, hence modulating the light output signal. Due to AC coupling at the input of the board, the constant light produced by the constant forward current (bias current) flowing through the VCSELs is not amplified; only short PMT pulsed signals are amplified and transmitted to the rest of the acquisition chain. Finally, the optical fibers bring the light signals to the control house, where the optical receivers are installed. Each receiver board contains 8 channels to perform the light-to-electric signal conversion. Once the optical pulses have been converted to electrical pulses, they are split in two branches; one (the so-called trigger signal) goes to a discriminator (located in the same receiver board) which is part of the trigger system. The other branch (so-called FADC signal) goes to the FADC system, where electric pulses are digitized. The details for these two systems are explained in some detail in the following sections.

2.2.3 The Trigger system

As it has been aforementioned the optical signals from the whole set of pixels arrive to the acquisition building and are reconverted by photo-diodes into electrical pulses in the so-called *receiver boards*. The trigger decision is actually done using these electrical pulses.

The trigger system of the MAGIC camera only considers the signals coming from the innermost 325 pixels (out of 397 inner pixels). As shown in figure 2.10, the trigger pixels are grouped in 19 overlapping macrocells of 37 pixels each. [12]

The whole trigger system is segmented into several stages or levels, called Level 0, Level 1 and Level 2 trigger.

- *L0T*: The level 0 trigger is located within the receiver boards and acts on each individual PMT signal. The analog pulse of each channel passes through a discriminator which compares its amplitude with a tunable threshold. If the amplitude exceeds the threshold, the discriminator produces a square pulse of adjustable width (normally set to 6 ns). The discriminator threshold level is set by an 8 bit DAC that is controlled by the computer running the Central Control program. This allows the discriminator thresholds to be tuned remotely and changed during data taking according to the needs of the observation (e.g., observations of extragalactic sources, with a lower level of LONS than galactic ones, allowed for discriminator thresholds to be lower and increase the sensitivity).

[12] Actually one pixel (out of the 37) is not wired to the trigger logic.

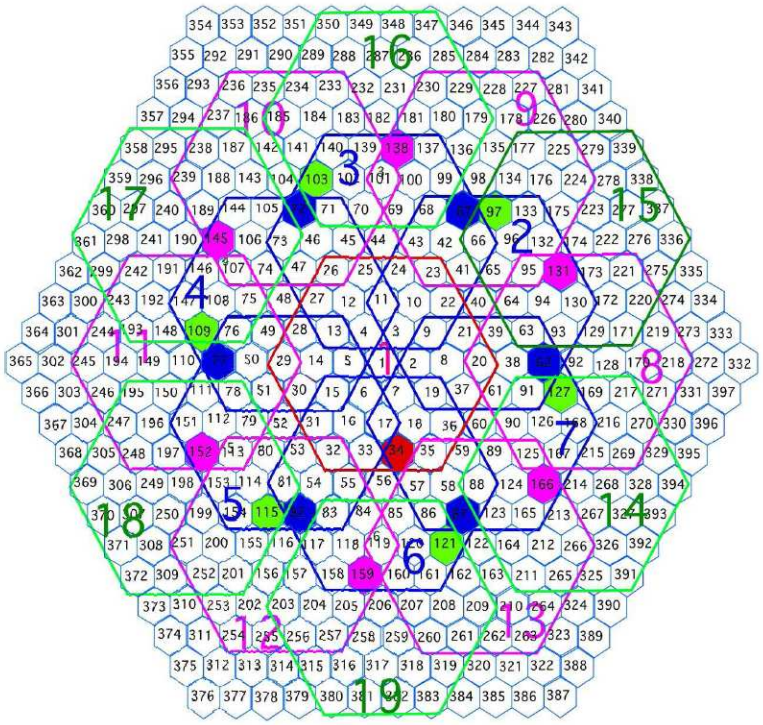

Figure 2.10: The trigger macrocells in the inner region of the MAGIC camera.

- *L1T*: The level 1 trigger searches for coincidences of neighbour pixels in each defined macro-cell. The signals coming from the discriminators of the receiver boards are sent to each of the 19 *L1T* boards, one for each overlapping trigger macrocells. The boards perform a logic combination of input signals to look for clusters of 2, 3, 4 or 5 next-neighbour pixels occurring in a short time interval (few ns). The multiplicity of the cluster of neighbour pixels can be set by the Central Control program, thus remotely modified during telescope operation. With multiplicities larger than two, a second condition is required, conforming the so-called closed-packed configuration: each pixel contributing to the trigger must have a minimum of two fired next-neighbours. This configuration helps to reduce the rate of triggers caused by muons. The overlapping of the trigger macrocells ensures that any 5 close-compact next-neighbours is at least full contained in one macro-cell.

  The *L1T* configuration which is used typically for normal data taking is four closed-packed pixels. However, due to the fact that the lowest energy showers can be partly rejected by this trigger level, other configuration selections are currently under study.

- *L2T*: The level 2 trigger is widely programmable and can perform a 'digital analysis' of the shower image , reducing the trigger rate to a value that can be processed by the Data Acquisition System (DAQ). *L2T* can a rough topological analysis of the event based on number of pixels, shape and orientation of the digital image[28]. The level 2 allows MAGIC to perform a true online pattern recognition of the images, which increases the background rejection at the trigger level.

  It should be mentioned that the *L2T* has also a prescaler board to scale down the

number of triggers in order not to overcome the maximum continuous acquisition rate of 1 kHz allowed by the DAQ system in normal operation conditions. This might be a very valuable feature when performing observations at very low E_{th} ($\leq$ 30 GeV), as it is planned for some gamma ray emitting pulsars, and specially, in the case of possible observation GRBs, where the trigger rate might go up to several kHz.

Despite currently the *L2T* is not performing the digital analysis of the shower images, there are ongoing studies to optimize the use of this feature.

The individual pixel rates of the channels included in the trigger region are monitored using 100 MHz scalers and these values are used to dynamically regulate the discriminator thresholds for each individual pixel. This Individual Pixel Rate Control (IPRC) acts only on pixels that are affected by stars brighter than 4m. In normal observation, the global trigger rate is about 250 Hz for extragalactic sources (standard pixel threshold) and about 200 Hz for galactic sources (increased pixel threshold). According to the full MC simulation of MAGIC this rate corresponds to a trigger threshold around 60 GeV .

2.2.4 The Data Acquisition system

As has been previously mentioned, the second branch of the analog signal coming from each pixel is sent to the Flash Analogic-to-Digital Converter (FADC) system. The DAQ system of the MAGIC Telescope consists on 18 crates of 4 FADC boards and a dual processor PC running a multi-threaded C++ readout program in a Linux operative system. Each FADC board digitizes the signals coming from 8 channels.

While still in the receiver board, the analog FADC signal is duplicated again into a *high-gain* and a *low-gain* channel. The high-gain signal is amplified by a factor of 10 whereas the low-gain signal is delayed by 50 ns. If the high-gain signal exceeds a preset threshold, a switch is actuated and the delayed low-gain signal is added right afterwards the high-gain. This procedure substantially extends the dynamic range of the 8-bit FADCs. The combination of both signals with different gains is continuously digitized at 300 MHz by the FADC channel and stored in ringbuffers.

The level 2 trigger directly communicates with the FADC system and enables the acquisition of the data whenever an event passes all the trigger system levels. When a level two trigger arrives at the FADC chips, they stop digitizing. The position of the signal in the ringbuffer is determined and 30 time-slices of 1 byte (15 for the high gain and 15 for the low gain) are written into the 512 kBytes FiFo buffer for each pixel. The readout of the ring buffer can be performed at a maximum rate of 80 Mbytes/s, thus resulting in a dead time of less than 1 μs (less than 0.1% dead time at the design trigger rate of 1 kHz). Both the time and trigger information for each event is recorded by dedicated digital modules which are read out together with the FADC boards.

The final step of data acquisition is data recording. The FADC digitized pulse is reorganized and formatted into the standard raw event data format and saved to a RAID disk system at a rate up to 20 Mbytes/s. The typical amount of data generated in one night of data-taking ups to 150 GBytes of rawdata. On daytime, this data is transformed into a compressed format and written to tape for data storing. During normal telescope operation, the complete readout program running in the DAQ PC is controlled remotely via TCP/IP by the Central Control.

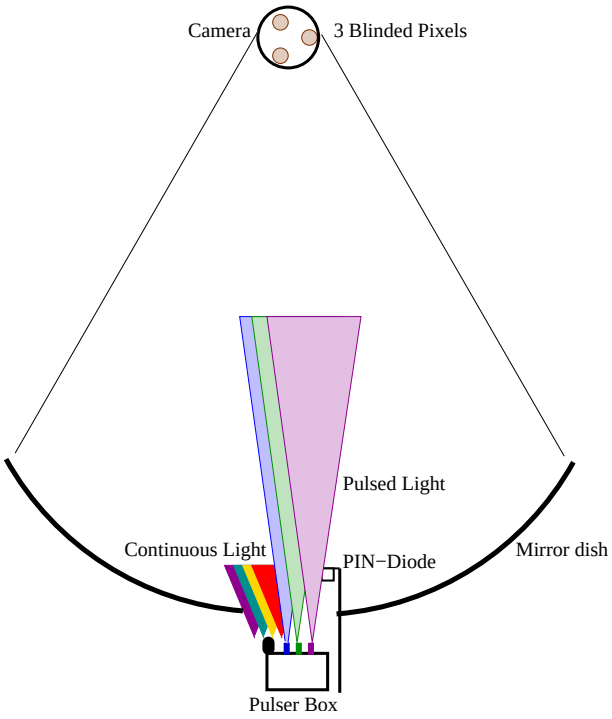

Figure 2.11: Scheme of the componets of the calibration system. Figure obtained from reference [30].

2.2.5 The Calibration system

The final output of the detection chain is given in FADC counts by the DAQ system. Integrated charge expressed in counts has no physical meaning and cannot be directly used for the description of the shower image. Hence FADC counts must be converted into photons which have physical connection with the EAS produced by the primary particle. In order to reconstruct the number of photons from the digital information it is necessary to calibrate the camera and the readout chain with respect to the incident light flux. Therefore, the calibration of the telescope has a main two-fold aim: to determine the response of the readout chain to equal inputs and to determine the conversion factor between the number of recorded FADC counts and the number of incident photons for each individual pixel (relative and absolute calibration, respectively).

To do so, the MAGIC collaboration built a dedicated calibration system for the absolute light flux calibration of the PMT Camera [29, 30]. This calibration system provides fast light pulses at different wavelengths and variable intensity in order to calibrate the whole dynamic range of the camera photosensors and their readout chain.

The main components of the MAGIC calibration system are shown in figure 2.11 and explained in the following paragraphs:

- *The pulser box*: This is the 'heart' of the calibration system and it is placed in front of the camera in the center of the telescope mirror dish. The pulser box houses pulsed LEDs providing ultra-fast light pulses in three different colours: 370 nm (UV LEDs), 460 nm (blue LEDs) and 520 nm (green LEDs). The LEDs are arranged in 16 slots with 1, 2 or 5 LEDs of the same type, slots that can be switched on independently.

The combination of firing different slots together makes possible to produce a range of intensities of a factor greater than 300 in order to calibrate the whole dynamic range of the camera and the readout chain. The light pulses produced have about 3-4 ns FWHM duration, which is nearly as short as the Cherenkov light flashes reaching the individual pixels from the air showers, making the calibration an equivalent condition than for real observation. At the same time, a continuous light source in four different colours (i.e. red, blue, green and ultraviolet) and variable intensities, with the purpose of simulating and calibrating the PMTs response for different conditions of background light, such as different levels of light in the night sky, the presence of the moon or stars in the camera FOV, etc.

- *PIN-diode*: This device is a photodiode that exhibits an increase on its electrical conductivity as a function of the intensity and wavelength of the incident light, with overall detection efficiency very close to 100%. The PIN diode is calibrated with a ^{133}Ba source. The PIN-diode are used in order to measure the absolute quantity of photons contained in the individual calibration pulses, thus allowing absolute calibration of the telescope.

- *Blind pixels*: With the same function than the PIN-diode, the calibration system has installed also the so-called 'blind pixels', which are a tree pixels located at the camera which operates in single photon mode. Technically, each of these 'blind pixels' is non-coated inner-size PMTs placed in the outermost ring of the camera. Their Quantum Efficiency is well known because they were accurately measured at lab. The term 'blind' comes from the fact that the illumination is attenuated in the PMT range of wavelengths by using a diaphragm and a filter. As it will be discussed later in the calibration methods, these characteristics allow the blind pixel to resolve single photons which make possible to measure the absolute flux for known diaphragm and filter attenuation factors.

In figure 2.12 pictures of the different parts of the calibration system are shown.

In addition to these parts of the calibration system, there exist a set of service systems closed related with the calibration system. For example, a sophisticated trigger system which allows to pulse the LEDs at almost any frequency up to 4.5 kHz, or the remote control for the different parts of the calibration system. These points of the calibration system are explained in more detail apart (see section 3) being part of the technical contribution of the author.

Calibration methods

As has been mentioned, the MAGIC calibration includes a relative calibration and an absolute calibration, which run as follows. The relative global calibration is essential in order to equalize the response of different channels when subjected to the same input signal. The complexity of the readout chain for each pixel makes it natural that the signals obtained from different pixels are not directly comparable [13]. The general flat-fielding tries on one hand to optimize the dynamic range of the camera by equalizing the dynamic

[13] For instance, the PMTs are, to a certain extend, hand-made devices from which a sizeable spread on the quantum efficiency, the photo collection efficiency and other characteristics is expected; the electrical to optical conversion of the signal in the VCSELs is also expected to be slightly different for different channels, etc

Figure 2.12: Picture of the main components of the MAGIC calibration system. The top picture shows a front view of the *pulser box* when installed in the central part of the reflector dish. Whereas the bottom left picture shows the on of the *blind pixels* installed in the camera and the the bottom right the *PIN diode* installed around one meter in front of the *pulser box*. Notice that in this last picture it is possible to see the MAGIC camera in the rear part of the picture.

range of all channels, and on the other, to make the response of the trigger homogeneous in the whole trigger area. This procedure is done periodically, with intervals of several months in order to correct changes in the hardware of readout chain.

On the other hand, an absolute calibration is also needed in order to convert the signal recorded by a pixel in FADC counts to the physical quantities related to the flux of photons incident onto the camera. The calibration system of the MAGIC telescope provides three independent methods to perform this absolute calibration:

- The *Blind Pixel method* compares the signal in the camera pixels with the response of the aforementioned blind pixels', which being illuminated through a diaphragm and a filter receive an attenuated signal. Whereas the 'normal' pixels detect strong signals when illuminated with the calibration pulser box, the 'blind pixel' can see just few photoelectrons, actually in mean value they detect less than one photoelectron. The distributions of FADCs counts expected for a PMT in single photoelectron conditions is a set of peaks each of them corresponding to one, two, etc photoelec-

trons. By analyzing this single phe spectrum recorded by the blind pixel, the mean number of photoelectrons produced in the photocathode can be estimated and used, together with the known QE, pixel geometry and diaphragm and a filter receive attenuation, to compute the mean number of photons arriving from the calibration pulses per unit area.

- The *PIN diode method* compares the signal in the camera pixels with the one measured by a Positive-Intrinsic-Negative diode (PIN diode) located at 110 cm distance from the pulser box. By monitoring the light pulses emitted by the calibration pulser, the mean number of photons that arrive per unit area onto the camera plane can be estimated from the number of phe generated in the PIN-diode, its QE, the LED emitted light spectrum and the geometry of the system.

- The *Excess Noise Factor* or *F-Factor* method, used traditionally by Cherenkov telescopes to perform their absolute calibration. The Excess Noise Factor (F) of any detector with some gain describes noise added by the detector to the input signal during the amplification. The F-Factor of any electronic device is then simply defined as:

$$F = \frac{(Signal/Noise)_{input}}{(Signal/Noise)_{output}} \tag{2.4}$$

  The method applied to PMTs is based in two characteristics: first, on the fact that F-Factor for PMT could be assumed as a good approximation to be constant, and second that the intrinsic noise of the input signal is known due to the poissonian behaviour for the number of photoelectrons produced. For PMTs with a known F-Factor (F) and analysing the output signal of each pixel, one can extract the average number of phe impinging on the first dynode of each PMT.

The advantage of the F-Factor method, compared with the other two, is its simplicity and robustness. However, a disadvantage is that it does not implicitly include the QE and phe collection efficiency of the PMTs (which can vary from one PMT to another) nor the transmission efficiency of the light guides, whereas the Blind Pixel and the PIN-diode methods do. Therefore, the F-Factor method measures the number of phes arriving to the first dynode of the PMTs and the other two methods measure the photon flux.

Note that such a calibration system provides three independent methods (containing different systematic errors) for the calibration of the camera; two methods measure the photon flux and a third one measures the number of phes arriving to the first dynode of the PMTs. This design increases the reliability in the calibration procedure, and allows monitoring possible variations in the performance of the pixel chain, as well as in the different light measuring devices of the calibration system.

Chapter 3

Camera and Calibration Slow Control

The IFAE group, where the author developed this Thesis, has had several responsibilities in the construction of the MAGIC Telescope. One of the major responsibilities among them was the development, from the initial design to the final installation on site, of the slow control for the Camera and Calibration systems. The aim of this chapter is to introduce with some detail these control systems which is the main technical contribution of the author of this Thesis to the development of the MAGIC Telescope. In particular, the author shared the responsibility of the design, development, test, installation and maintenance of the Camera and Calibration control system. Among these tasks, the author was the main responsible for the development of the the part of the system that steers the functionalities of the hardware controlled via the CANbus, which includes the HVs regulation and monitoring, the DCs monitoring and the calibration pulser box configuration setting, among others. In addition, the author participated in the camera instrumentation, electronics testing and improvements prior to its installation into the telescope, as well as having a leading role in the development of the trigger system used by the Calibration system. After the camera on-site installation, special tests and maintenance has also been carried out to assure the nominal performance of the whole system.

This chapter is partially based on the technical papers [31, 32, 33] where the author has actively participated.

3.1 Central Control

The slow control of the MAGIC Telescope has the purpose of allowing the remote control of the Telescope hardware by a human operator as well as in an automatic manner. The present situation of the slow control makes possible a minimal intervention of the operators, leading most of the decision-making during data taking to an automatic control.

The philosophy of the slow control of the MAGIC Telescope is based on a central control program (CeCo) which steers functional units which correspond to the independent subsystems of the telescope. CeCo knows in every moment the state of each subsystem of the telescope and takes the right action for every combination of subsystem states. In this sense, the CeCo does not manage directly the details of every subsystem but receives from the subsystem control systems a summary of the necessary information to take the global decision about the whole system. Together with this decision-making system, the

CeCo provides the main Graphical User Interface (GUI) to operate the telescope during the daily observations.

The main subsystems of the MAGIC telescope are the standard present in any detector equivalent to MAGIC, that is, the drive system, the Active Mirror Control, the Camera and Calibration, the trigger, the DAQ and some other smaller but not less important subsystems.

The communication between the different telescope subsystems (e.g Camera and Calibration control systems) and CeCo are done either via standard TCP/IP socket connections or NFS file system. This technical characteristic of the MAGIC slow control allows running all the communications over the standard internal network of the telescope site, thus avoiding the building of a new communication structure. However, this characteristic also makes the system sensitive to possible external attacks from the Internet. This possible danger has been taken into account very seriously in the design and implementation of the internal network, making a big effort to guarantee its safeness.

The main part of the CeCo program is written using Labview 6i whereas small parts, like the responsible of the TCP/IP communication, is written using plain C and the standard system libraries of the Operating System.

3.2 Camera & Calibration Control

The slow control of the camera (i.e. CaCo) can be addressed from two points of view: the software and the hardware used in the control. From the point of view of the software, the CaCo is based on a similar philosophy than the Central Control. There exists a central program (called *Guagua*) which controls a set of dedicated camera subsystems programs (called *drivers*). From the point of view of the hardware, many parts of the camera hardware give 'services' to the 'heart' of the system which are the PMTs. Among these services, there is the low and high voltage supply and the cooling of the camera. In the following paragraphs both the software and hardware dimensions of the slow control of the MAGIC camera are explained in detail, making special emphasis in those in which construction and design the author of this Thesis has had a leading role.

3.2.1 Hardware related with CaCo

Before entering in the discussion of the different parts of the camera control hardware, it is necessary to introduce a general idea present in most of the subsequent explanations, which is the internal division of the camera hardware in six sectors. The camera of MAGIC is built on a hexagonal geometry (e.g. the light collectors, the whole camera itself, etc), chasing the simplest, more compact and closest to a circular symmetry solution. This hexagonal camera is split into 6 triangular units called sectors (see figure 3.1), which are the basic hardware units of the camera. Each of the sectors is provided with a *mother board*, which is an electronic PCB that does not process any of the signals but provides the wiring for the 'services' necessaries to the PMTs to work, such as the low and high voltages to all the pixels, communication lines for monitoring purposes, etc. In the next paragraphs, a detailed discussion of these different 'services' is included

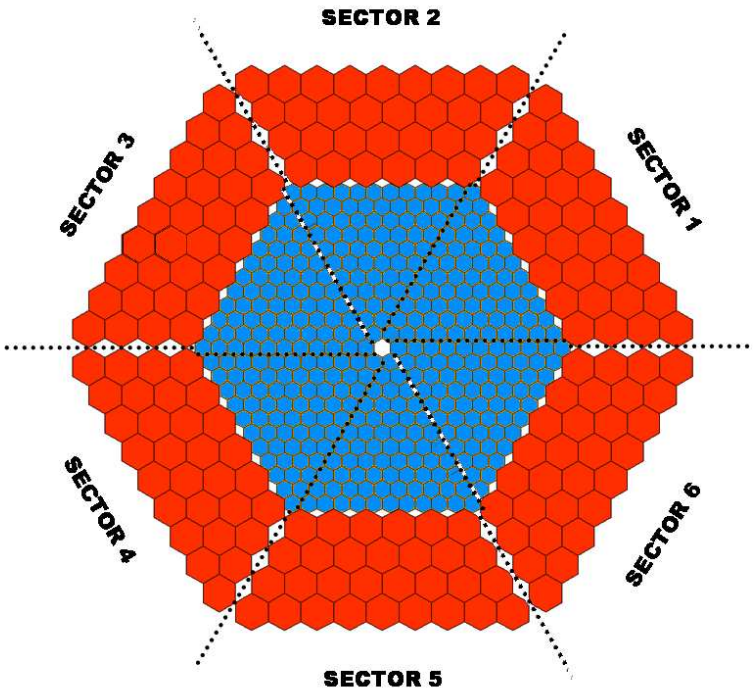

Figure 3.1: Scheme of the MAGIC camera layout split in sectors. The sectors are the first natural division of the camera due to the segmentation of the hardware according to them. The six sectors are equal replicas from the hardware point of view.

Communication protocols

Another necessary introduction is the discussion about the communication protocols used in the CaCo. The hardware in this system is accessed through basically two communication buses and protocols, CANbus and RS-485.

1. CANbus is an industrial multi-node serial bus developed for the automotive industry and nowadays widely used in many areas. The advantages of this bus are: its high level of reliability transferring data even in very electromagnetically adverse environments, the theoretical almost 100% sustained occupancy of the bus and the possibility of using very long communication lines (up to 1 km). The main disadvantage is the small bandwidth of the bus. However, this disadvantage does not represent a problem for CaCo because of the small amount of data necessary to be sent through the slow control of the camera. The CaCo system used two CANbus lines of about 200 meters long with a total of 16 nodes, which controls the whole high voltage supply sequence, the whole anode DC current monitoring as well as many of the calibration system functionalities.

   At computing level, the CANbus lines are connected to two PCI 'CAN_PCI2' boards from JANZ Company.

2. RS-485 bus keeps many similarities with CANbus (e.g. multi-node, serial, differential (long lines), etc.). The main reason to choose RS-485 instead of CANbus for some parts of the camera control is the wide spread use of RS-485 for the control of autonomous Programmable Logic Controllers (PLCs). These controllers are small computers used for automation in industrial processes, such as control of machinery on factory assembly lines. The main difference from other computers is the special input/output arrangements, making PLCs very practical to connect to sensors and actuators. The use of PLCs powered by batteries is optimal in the control of very critical systems that cannot rely on external computing control systems.

   In the camera control, two RS-485 lines of about 200 meters long are used to communicate two autonomous PLCs. Through these lines and with the Modbus protocol, critical systems like the cooling system of the camera, the camera lids, the camera low voltage power supplies and other auxiliary camera subsystems are controlled.

   At computing level, the physical RS-485 lines are connected to a Meilhaus ME-9000/4 PCI card which can control up to 4 RS-485 lines.

The whole on site computing system for the MAGIC Telescope (e.g, internal network, telescope subsystems control, etc.) is based in the Open Source operation system Linux. In particular, it is based on a modified version of the Linux distribution SuSe 7.2 with kernel version 2.4.16. The decision of using Linux as the main OS made the selection of the computing bus controller boards a demanding job, being at that moment few companies the ones that produce drivers for their products in Linux. However, the decision taken about the supplier companies has proven to be correct, with not even a single problem with their controllers in around 4 years of daily use on the MAGIC site.

PMTs HV supply and regulation

The MAGIC camera has a sophisticated supply of high voltage which is completely automatized. The setting of the HV is based on two stages: first, a general high voltage is produced in the control house [1] and sent to the camera to power all the PMTs; second, each PMT has dedicate electronics that regulates (i.e. reduces) the previous general high voltage to the requested for that particular pixel.

The general high voltage is produced by two commercial power supplies (PS) placed in the electronic room of the control house and send to the camera using two special coaxial cables of 150 meters. Each of the high voltage power supplies provides up to 300 Watts (i.e. 600 Watts adding both) distributed in a maximum voltage of 2000 V and a current of 150 mA. [2] These independent lines power the two halves of the camera (sectors 1, 2, 6 and sectors 3, 4, 5; as labelled in figure 3.1). The control of the supplies could be done by direct access via a screen/keyboard placed in these devices or by remote control trough RS-232 serial protocol. A photograph of these power supplies is shown in figure 3.2. In order to be able to control the HV supply through the CANbus lines, a commercial electronic translator RS-232 to CANbus from IXXAT Company is used (i.e model 'CANlink CAN/RS-232 Gateway').

[1] The control house is the building which hold most of the auxiliary services of the MAGIC Telescope, as the trigger, the DAQ, the computing, etc. In addition, the control house is where the operators control the telescope during data taking. This building is placed 100 meters away from the telescope.

[2] During the writing of this Thesis it has taken place the installation of a new single HV power supply for the whole camera with a power of 3000 Watts. The installation of this new supply will avoid problems with the gain of the PMTs produced by future ageing effects.

HV power supply

Medium voltage power supplies

Figure 3.2: High and medium voltage power supplies front photograph. The top figure shows the view of the HV power supply where the screen/keyboard for the manual control can be observed. The botton figure show the 360V Active Loads (right box) and the 175V PS (right box). The cabling going out from these power supplies is used for voltage and current monitoring purposes done by the CaCo.

In addition to the general high voltage, the so-called medium voltages are also produced in the control house. As explained in section 2.2.2 the last two dynodes in the PMTs are powered by dedicated power supplies. The fifth dynode is powered by an Active Load at 360 V, which main difference with a normal PS is that it is able not only to give power but to consume it in case it is necessary, in order to maintain the voltage. Whereas the last dynode is powered by a normal power supply of 175 V (see figure 3.2). There exist two Active Loads and medium voltage PS which power the two halves of the camera in the same way than the high voltage lines.

Once the high and medium voltages are produced and sent to the camera, it is necessary to regulate the high voltage necessary for each pixel. A dedicated electronics (called

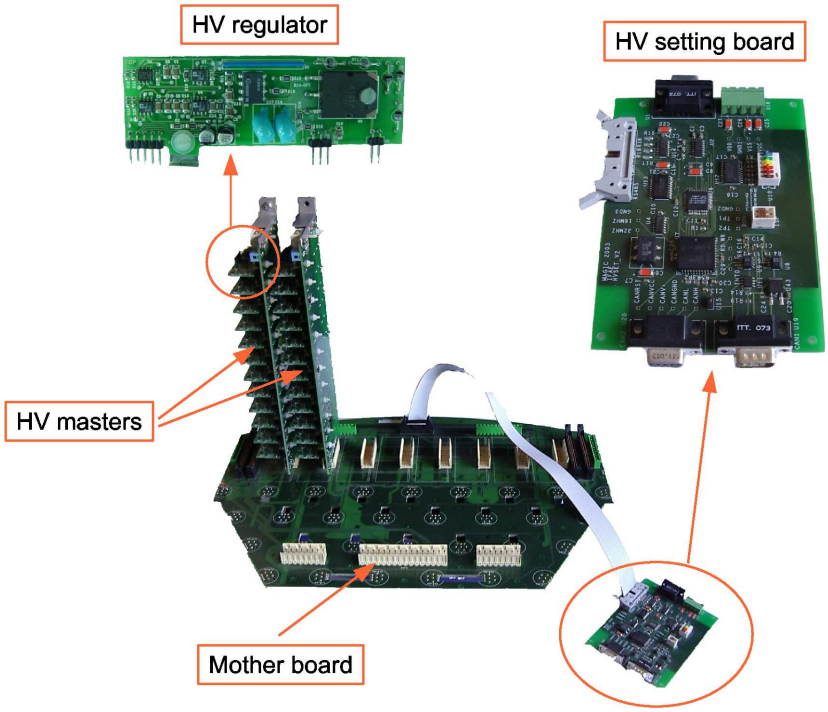

Figure 3.3: PMTs HV regulation set-up. This figure shows the main hardware elements used in the camera control for the regulation of every PMT high voltage. These elements are the *mother board*, the *HV masters*, the *HV regulators* and the *HV setting* board. In the figure a real photograph of the laboratory set-up, used to test the components installed in the camera, is shown. Due to requiremens of the mechanics of the camera, the *mother boards* are physically composed by two parts. In the picture, just the outer part of this board is shown. The view of the *mother board* shown in the picture is the rear part, the PMTs are connected into the front part.

HV regulators) were designed for that purpose. These electronic devices, based in power MOSFET technology, are able to reduce a given high voltage up to 1400 V, being the reduction proportional to a given input voltage. The photocathode of every PMT is connected through the mother board to one *HV regulator*, making possible to produce independently the requested HV for any single pixel.

The *HV regulators* are hold in groups of 12 by the so-called *HV master* (i.e. there are 48 *masters* for the whole camera). The *masters* boards act as the interphase between the regulators and the whole control system, providing to its correspondent *HV regulators* the general high voltage (which they take from the *mother board*) as well as the reference voltage to make the HV reduction. These reference voltages are produced in the *masters* boards by 12-bits DAC, thus with a precession of 0.5 V (i.e. 2000 $V/2^{12}$).

The DACs of all the *HV masters* are accessible through a serial bus connected to the *mother boards* through the *HV masters*. To control all these DACs a dedicated electronic board called *HV setting* which incorporates a serial bus, among other things, together

with a CANbus controller was developed. This board in connected in DC-chain with all the *mother boards*, providing to the CaCo PC the control of any single PMT HV via CANbus. In figure 3.3 it is shown a laboratory test set-up for the regulation of high voltage which follows the same scheme than the one used the camera.

PMTs HV & DC currents monitoring

Most of the data flow within the camera control is due to the monitoring of the high voltages and the anode DC currents. Both informations are necessary for the right operation of the CaCo: HV measurements give the system the online knowledge of any possible problem with the HV setting, whereas the DC monitoring gives fundamental information for the integrity of the PMTs, due to the fact that large DC currents could damage them. Additionally, the information from the PMT DCs could be used in the offline analysis, being a direct optical measurement of the light conditions during data taking (e.g. atmospheric conditions, moon, bright stars in the observed field of view, etc.)

Due to the symmetrical requirements for the monitoring of HVs and DCs, both measurements are integrated in the whole control system using the same scheme and electronics. The measurement of the anode DC currents is integrated in the base of each of the PMTs, providing this information to the *mother board*. The HV measurement is done in the *HV regulators*, making accessible this information first to the *HV master* and from here also to the *mother board*. Concerning the dynamic range, the anode DC currents can be read up to 30 μA, while the HVs can be measured up to 2000 V. The readout of these two measurements is done by the so-called *multiplexor board* (see figure 3.4). Each of these boards is able to measure either the DC or the HV for the 96 pixels of one sector. The *multiplexor board* contains a tree of multiplexors that make possible to measure the 96 channel using one single 12-bits ADC present in the board. To send this information to the control system, each of these boards contains a CANbus controller making possible to plug them into one of the two CANbus lines.

As a summary, 12 *multiplexor boards* are used to monitor the whole set of HVs and DCs of the camera (2×6 sectors). All of them communicate with the camera control PC using one of the two CANbus lines, being the scheme of the CANbus lines the same used for the high and medium voltages (i.e 1, 2, 6 sectors for one line and 3, 4, 5 for the other one).

Calibration Control: Pulser box settings & trigger

The calibration is not considered part of the camera system. Nevertheless, from the point of view of the slow control, that system shares many resources with CaCo (e.g. CANbus lines, AC power, etc), being here the natural place to explain it. The integration of the Calibration system in the camera control system was motivated by the existence of many services on the telescope for the camera hardware which could include rather straightaway the necessities of the calibration.

The slow control of the calibration system could be divided into two main parts. On one hand, all the settings for the configuration of the pulser box are controlled remotely using the Camera CANbus lines. Many possible configurations are available for the calibration pulser box: 16 slots with LEDs emitting light in three different wavelengths can be selected. Moreover, 4 different continuous light (CL) sources with different colours as well as the emission intensity for the selected colour can be set. All these settings are controlled using the same kind of board used in the regulation of the HV voltages

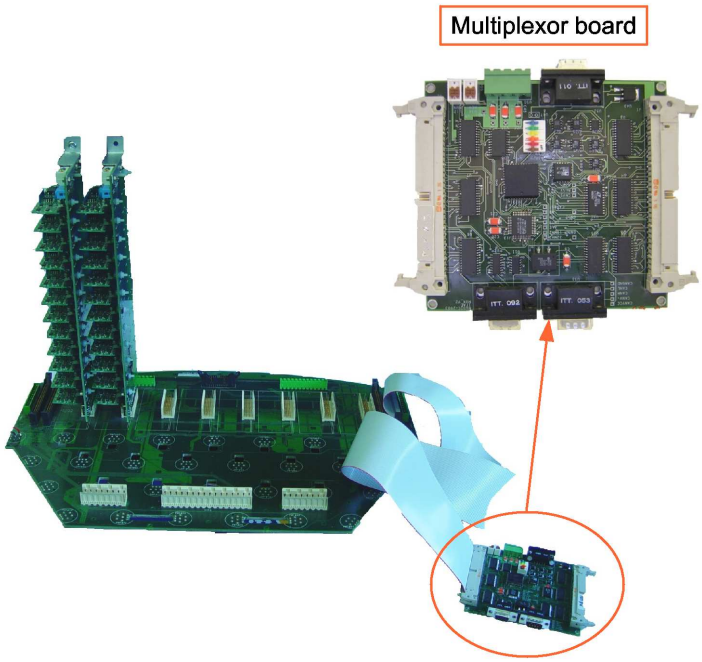

Figure 3.4: *Multiplexor board* laboratory set-up. In the figure a photocompsition of the laboratory set-up used to test the HVs and DCs monitoring chain is shown. In the photograph just one *multiplexor board* is shown whereas in the camera two are installed, one per HVs and another for DCs monitoring. Moreover, just one flat-cable is connected to the *board* in this picture whereas actually two of these cables are necessary to bring the 96 channels for each of the two *multiplexor boards* in each sector.

inside the camera (i.e. *HV setting* board). This multi-purpose board, in addition to the CANbus controller and the serial bus, includes also a DAC. That characteristic makes this device optimal for the control of the pulser box. The serial port can be used to send as binnary information which of the slots and the CL sources are needed, and the DAC can easily be used to steer a variable current source to produce the desired emission level of the CL source. Thus, by using this device, all the functionalties of the calibration are accessible through the standard CANbus lines of the CaCo system.

By the other hand, the calibration system has a dedicated trigger system for firing the flashes at the pulser box. The production of these triggers is done at the control house and sent afterwards to the pulser box in the centre of the mirror dish using an optical fibre, in order to avoid interferences.

The calibration trigger is generated using a Meilhaus ME-1400B input/output PCI card which contains 6 digital counters and 48 digital I/O channels, both with 16-bits precision. The digital input/output lines are connected to the DAQ system making possible to stamp digital information in every event. That characteristic is used to stamp for calibration event the configuration setting requested (i.e. LEDs slots fired, CL source, etc.).

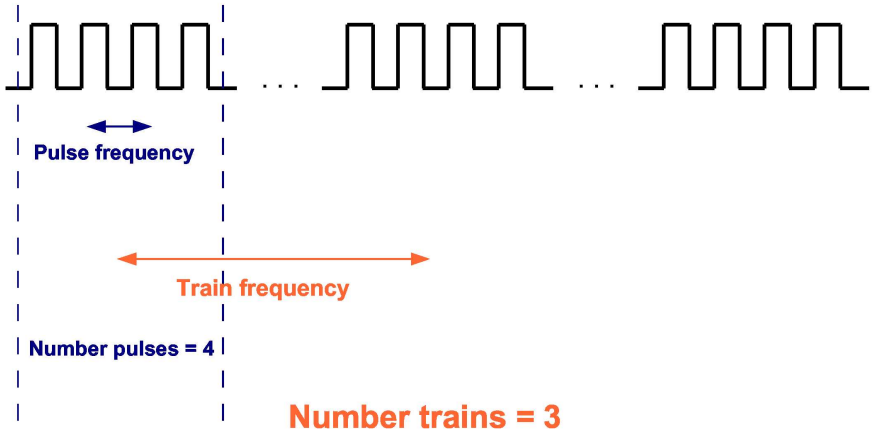

Figure 3.5: Calibration trigger pattern sketch. In this picture a graphical representation of the 4 free parameters which can be set by the CaCo system are shown.

Having this information attached to the event is very convenient for the off-line analysis of the calibration information. The collection of digital counters are used to produce the desired trigger pattern. Those counters are able to produce different sets of digital clocks (i.e. periodic square functions) and gates (i.e. digital '1' during a certain time window), where either the frequency of the clocks and the duration of the gate could be select via the PC. Combining all these digital signals, the calibration trigger system is able to produce a rather sophisticated trigger pattern. The pattern consist of a train of pulses where the frequency of the train, the frequency of the pulses, the number of pulses within on train and the number of trains can be selected. [3] The maximum frequency possible with this system is of 1 MHz where the minimum is less than 10^{-3} Hz. In figure 3.5 a sketch of a typical trigger pattern is shown.

The calibration trigger system is connected directly with the *L2* trigger of the telescope. This makes possible to fire the whole DAQ system from the camera control. In fact, this characteristic of the calibration trigger system is used by MAGIC to produce the so-called 'pedestal' events, also called 'random triggers'. These events are empty because the trigger that fires the system is not due to any signal in the PMT camera but forced by the *L2T*. Pedestal events are used to know the response of the complete readout chain to a zero signal. For more details about the use of the pedestal events in the analysis presented in this Thesis see section 4.1.1.1.

PLC controlled camera subsystems

The modularity, autonomy, and robustness of the control via a PLC have offered a way to control some of the most critical subsystems of the camera. Dedicated programs running in PLCs are developed to steer these critical subsystems. This makes that CaCo accesses their functionalities through simple commands send to the PLCs by the RS-485 bus.

[3] Due to the digital nature of the counters not a continuum the frequencies or number of pulses are possible.

In the following paragraph a brief description of the most important camera subsystems controlled by PLCs are explained. For a more detailed explanation about them see reference [34].

- *Camera lids*

  The camera entrance that faces the telescope mirror collector is protected from daylight with two light-and-water tight lids. As the PMTs can be damaged if they are exposed to too bright illumination, during data taking it is needed to remotely control a fast closing of the camera lids in case a sudden increase of the pixels DC current occurs (e.g. due to the accidental illumination of the reflector by a passing car). For this and any other situation that could require a fast action over the lids, the central control of the telescope can access the PLC that controls the motors and send the appropriate order to it: open, close or stop. A manual operation of the lids was also implemented to allow an easy opening/closing without using the central control program when a technical camera access is needed.

- *Cooling system*

  The goal of the cooling system is to regulate the temperature inside the camera with two main purposes: to ensure a stable temperature during data taking (within $\pm$ 1 degree) to minimize the temperature dependent fluctuations of some of the devices of the readout chain (e.g. the VCSELs for the analog transmission of the signal), and to control the temperature in general to avoid extremely high temperatures which could simply damage some of the camera electronic components but also to avoid too low temperature, to prevent for water condensation inside the camera.

  During data taking, 800 Watts of heat are dissipated inside the camera including both high and low voltage consumption. [4] The cooling system of the MAGIC camera consists in a water-based system with S-shaped copper tube which runs along the external lateral wall of the camera and acts as a heat-cool exchanger. At ground level, there is a 200 l tank filled with glycolate water, to avoid freezing problems, which feeds the pipeline that goes up to the camera. The water of the tank can be cooled or heated depending of the needs with either a refrigerator unit connected to the tank or using a 2400 Watts resistor placed inside the tank. Finally, a set of fans installed inside the camera homogenize the inside temperature and make more efficient the heat-cool exchange.

  The cooling system is completed with a set of temperature and relative humidity (RH) sensors installed at three different positions in the camera (at the center, close to one optical link transmitters, and close to the camera wall). The camera control system sets the working conditions for the cooling but is the PLC who takes the decisions to keep the desired temperature inside the camera.

In addition to these two subsystems, a set of non-critical ones are also controlled by programs running in the PLCs. The most important one among them is control of the low voltages for the electronics inside the camera which includes all the electronics for the PMTs, the HV regulator chain, the optical transmission of the signal, etc. The PLCs

[4] The medium voltages being produced at the control house does not dissipate heat inside the camera. Despite the high voltage it is also produced in the control house, the *HV regulators* reduce the general high voltage by dissipating inside the camera the power as heat.

are also used to control some auxiliary LEDs installed in the camera frame (which are used as spatial references by systems of the telescope like the Active Mirror control or the StarGuider [5]) and the switching *on/off* of the voltages for the calibration pulser box, among others.

3.2.2 Camera control software

The software of the camera control can be divided into two layers. The first layer is the responsible of the communication with the hardware. That part of the software is divided in units called *drivers* which, each of them, is responsible for the access to the functionalities of a different subsystem of the camera. The *drivers* have the objective of hiding the complexity of accessing the hardware for the layer of the CaCo on top of them. That means that the *drivers* have encoded inside all the functionality of the different subsystems of the camera both those to perform actions with the hardware as well as those to monitor the available information.

The second layer of the software is the one responsible of the communication with the users (through a Graphical User Interphase), the communication with the central control and the responsibility of taking the decisions let by the central control to be taken at the CaCo level. This part of the camera control software is called *Guagua*.

Camera control *drivers*

The *drivers* of the camera control are written in C++. The decision of using an Object Oriented (OO) programming language matches very much with the requirements of the system. The functionalities present in the camera system many times are almost equivalent for many camera subsystems (e.g. HVs and DCs monitoring) making the inheritance present in OO an optimal solution. In addition, many of the different elements of the control system are repeat (e.g. *multiplexor boards*), making their representation is the software as objects very convenient. The decision to take C++ over all the existing OO languages was motivated by the straight inclusion of C/C++ in Linux with access to many system libraries in the native language.

The communication between the *drivers* and the following layer of the CaCo system (i.e. the *Guagua*) is done through *pipe* files. These special files are the standard way used in Linux to open communication between separate running programs. They consist of special files where programs can write and read with the advantage respect to normal files that both programs can keep opened the *pipe* while they are writing and reading and in addition the Operation System could alert each of the programs if the other one is 'listening'.

The structure of the *drivers* is standardized, having the same structure for all of them. Each *driver* is continuously listening the so-called command *pipe* which is used by the *Guagua* to send the actions to be performed by the *driver*. Thus, the actions done by the *drivers* are never done autonomously but externally driven. On the other hand, the monitoring work performed for each subsystem is done periodically by sending a standardized report through a second *pipe*. For each subsystem, it is defined which are the magnitudes to be monitored and these are sent, in form of a fixed reports, to the

[5] The StarGuider is a system of the telescope which uses a CCD camera placed in the mirrors dish center for recording the star field of view rear the PMT camera. With this measurement, the camera LEDs as a reference and star catalogs, the StarGuider system is able to measure the pointing position of the telescope.

Guagua at a regular frequency as long as the *driver* is running. Making an equivalence with the previous idea, the monitoring of the subsystems is an autonomous process done by the *drivers*.

The camera and calibration control system has 10 subsystems controlled by their corresponding *drivers*. A list of these *drivers* with a short explanation about their functionalities is included in the next paragraph. The subsystems can be divided into those controlled using the CANbus and those controlled by RS-485 lines. In addition, there is one subsystem that controls the production of the calibration trigger pattern which is neither controlled by any of these buses but directly by an I/O PCI card installed in the CaCo PC.

RS-485 *drivers*:

- *LV*: The responsibility of this subsystem is switching on/off and monitoring all the low voltage supplies which power the camera electronics. This includes several supplies of +5V, +12V and -12V with currents that go from 1 to 10 amperes for the different voltages.

- *COOLING*: The cooling of the camera is actually controlled by a program inside the PLC. The role of the cooling *driver* is first, the setting of the working parameters of the cooling (e.g. the inside temperature of the camera, the range of tolerance around that temperature, etc.) and second, the monitoring of all the sensors related with the cooling. This subsystem readout a rather large set of sensors which includes 3 temperature and 2 relative humidity (RH) sensors inside the camera, one temperature and one RH sensor in the LV box as well as pressure sensors for detecting obstruction or leakage in the water circuit.

- *LIDS*: This subsystem is the responsible for the opening and closing of the lids that cover the front part of the camera. In addition to these actions, the lids can be stopped at any moment in case of necessity. The system is instrumented with sensors that tell whether the lids are at the opened or closed position. In an equivalent way to the cooling, the real control of the movement of the lids it is done by a program running inside the corresponding PLC. This *driver* is responsible of the communication with that PLC, making the access to the functionalities given by the PLC program transparent for the *Guagua*.

It is important to remark that the programs inside the PLCs responsible of the control of the hardware of these subsystems have been designed and developed at IFAE as part of the Camera and Calibration slow control system (see reference [34] for more details).

CANbus *drivers*:

- *HVPS*: The main responsibility of this *driver* is to ramp up and down the high voltage power supply. For a given requested voltage, this program takes care of ramping the high voltage PS in predefined voltage steps in orther to allow any existing capacity in the camera to have time to get charged (or discharged). In addition, it takes care of the settings of the power supply like the maximum current allowed before triping, etc. This *driver* reports the working high voltage and current consumption for both power supplies. As it has already been mentioned in this

chapter, the power supply is controlled using RS-232, despite it is plug to one of the CANbus lines through a RS-232 to CANbus translator.

- *DCMON*: 6 *multiplexor boards*, one per sector, are controlled through the CANbus lines by this subsystem. It is a monitor dedicated *driver* which reports the anode DCs currents for the 576 installed PMTs on the camera.

- *ALMON*: This subsystem is also a dedicated monitoring one providing the voltage and current for the medium voltages power supplies (i.e. 360 V Active Load and 175 V PS). It is controlled through a slightly modified *multiplexor board* through the CANbus.

- *HVCTR*: This *driver* has many similarities with the *DCMON* one. In fact, most part of the code of this *driver* is done deriving classes from *DCMON* ones. 6 *multiplexor boards* plus 1 *setting board* pluged to the CANbus are used to regulate and monitor the HVs for the whole camera.

- *CALIB*: This *driver* takes care of the pulser box settings as part of the calibration control system. Inside the pulser box there is a slightly modified *setting board*, through which all the functionalities of the box (i.e. pulser LED slots and CL source) are remotely controlled. In its present state, no monitoring is available for the pulser box hardware. However, future plans include introducing readout of certain magnitudes inside the box, such as the temperature or values of certain voltages. The introduction of these changes in the present system from the point of view of the software is straightforward by the addition of a new node in the CANbus.

As a summary of these *drivers* it can be remarked that there exist 16 CANbus nodes connected to 2 different physical lines which control a plethora of different subsystems functionalities, most of them related with the setting and monitoring of the PMTs magnitudes.

I/O PCI *driver*:

- *CALIBIO*: This subsystem is the one in charge of the production of the calibration trigger pattern. Using the frequency, number of events and train specified by the *Guagua*, the *driver* set the 6 digital counters and the 48 digital I/O to produced the required pattern.

The normal reporting frequency for the *drivers* is of one second, although subsystems like the *DCMON* is pushed to the maximum frequency allowed by the bandwidth supplied by the CANbus lines. The mean frequency achieved for this *driver* is of the order of 6 Hz. The reason for measuring the DCs with the maximum possible frequency is motivated by the aim of using this data for off-line studies, such as the measurement of low frequency oscillations of the camera position, oscillations produced by the drive system during repositioning, using the star field viewed by the PMTs.

The automatic reports produced by each of the *drivers* are recorded to disk by CaCo. All these reports contains a time stamp with milliseconds precision with the date they were produced. That makes possible an off-line merging of all the slow control information with the shower image events recorded by the standard readout chain of MAGIC. The

combination of all this information allows the use of the CaCo data in the standard MAGIC shower image analysis, such as the use of the star field measured by the PMT DCs and star catalogs for the calculation the pointing position of the telescope. This information could be essential for the analysis in case of mispointing of the drive system, as it will be shown in next chapter.

Before finishing this review of the CaCo *drivers* it is important to remark one of their most important characteristics which is that many subsystems controlled by independent 'programs' (i.e. *drivers*) share common resources, in particular the communication buses. This particularity of the system was addressed by designing the *drivers* to be multi-threading programs, using the standard Linux system library for that purpose (i.e. *<pthread.h>*). By using threads, a program is able to split itself into two or more simultaneously running tasks, which share common resources. Therefore, all the *drivers* which share the same bus run inside a common program as independent threads. When different threads share a resource that can only be accessed in a sequential way, such as the bus, it is necessary to arbitrate this access using 'semaphores'. Due to the fact that the pthread library includes functions that allow a thread to 'freeze' the rest of threads running in the same program, these functions can be used for that "semaphoring" purpose. When a *driver* (i.e. thread) needs to access the bus, it freezes the others *drivers*, ensuring a 'lonely' access to the bus. As soon as the *driver* ends using the bus, it unfreezes the rest of threads.

Camera control GUI & decision-making

The responsibilities of the *Guagua* program are two-fold. First, it has to act as the GUI of the CaCo system. This means that it has to deal with the actions requested either by the central control or by a human operator. The CaCo system has been designed to provide the user a simple interface to the camera and the calibration functionalities, hiding the complexity of these actions either at the *Guagua* or the *driver* level. In addition, the *Guagua* has to provide the available information about the system to these two agents, via TCP/IP to the central control and via the GUI to the human operation. In figure 3.6 it is shown the front panel of the *Guagua* during a normal operation of MAGIC. In particular, this screenshot shows the state of the *Guagua* during an observation of Crab Nebula.

Additionally to the external actions requested to the *Guagua*, it has an autonomous decision-making system in order to deal with situations where rapid actions are needed because of the presence of some risk for the hardware (e.g. strong illumination of the camera) or situations where the recipe to recover the problem are well known (e.g. communication lost with some of the HV power supplies). This decision process is based on the evaluation of the status of every controlled subsystem using the reports sent periodically by each of the *drivers*. Using this information, the *Guagua* constructs the global state for the Camera and Calibration system and decides which actions to take, if necessary, according to the corresponding state. For a more detailed explanation about the *Guagua* program see reference [35].

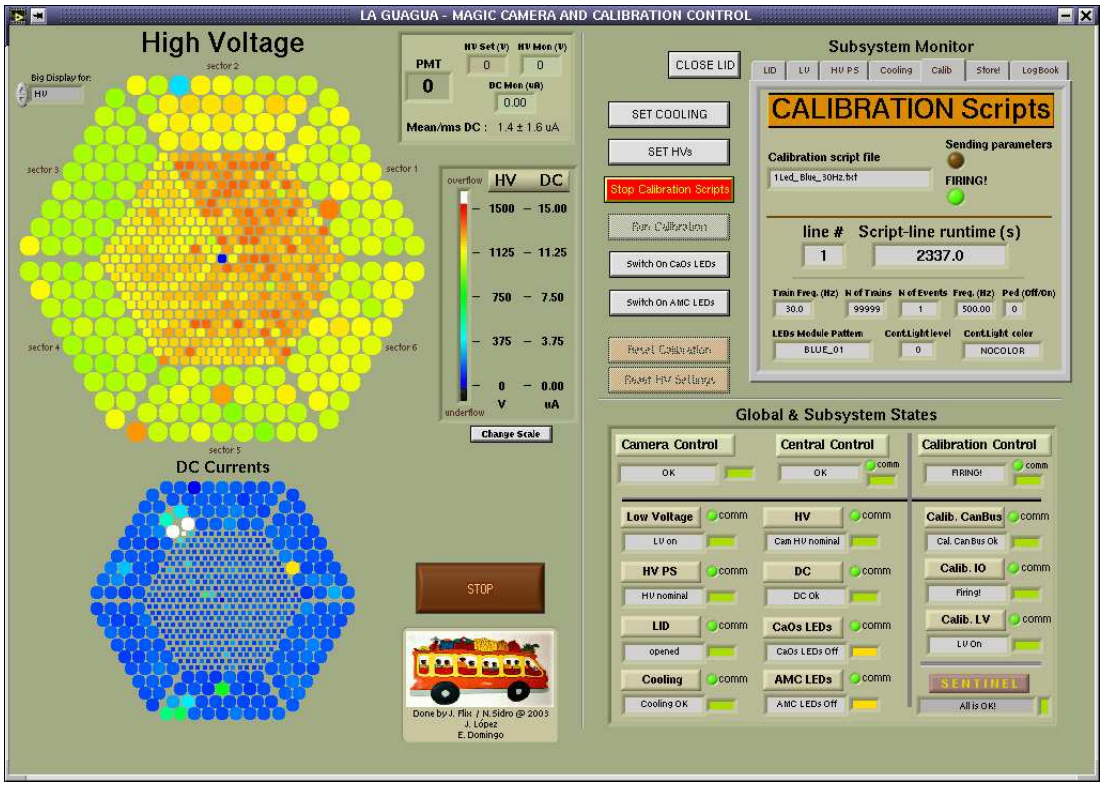

Figure 3.6: Camera and Calibration control Graphical User Interphase. In the left side of the panel there are represented two cameras with the values for the HVs and DCs for each of the 576 PMTs. In the botton left 'camera' there can be observed the two brightest stars in the Crab Nebula field of view (i.e. Tau ζ and Tau 114), as they are seen in the DCs of the PMTs. In the top right part of the panel the monitored magnitudes for the rest of the camera subsystems is available, whereas in the botton right the states for the different subsystems as well as the global state for CaCo are displayed. This figure is extracted from reference [35].

Chapter 4

Shower Image Analysis

The aim of the analysis presented in this chapter is the measurement of the number of γs detected for the studied sources. For this purpose, the different parts of the analysis performed to the raw events recorded by MAGIC are shown. This includes steps like the reconstruction of the shower image, the selection of the data samples and the γ selection using the MAGIC Monte Carlo simulation. The results coming from these analysis will be used in the following chapter to show the distribution of the number of γs both in time and energy intervals.

4.1 Shower image reconstruction

The first step in IACTs data analysis is the reconstruction of the shower image. This is a process based on the calculation of a set of parameters which tries to characterize the images recorded by the camera produced by the Cherenkov photons coming from EAS. The process of shower image reconstruction includes the following steps: the determination of the number of photons detected by each pixel, the selection of the pixels which belong to the shower image and the calculation of the image parameters. In the following sections, a detailed explanation of all these steps is shown, making special emphasis in the analysis presented in this Thesis.

4.1.1 Signal reconstruction

In every event, the electric pulse produced by the complete analog chain is digitized and recorded for each pixel. The first step in the analysis of an event is the reconstruction of this signal for each pixel. This process mainly consists of two parts: the determination of the pedestal level suitable for this pixel and the subsequent extraction of the signal.

4.1.1.1 Pedestal subtraction

In any digitized measurement, the subtraction of the pedestal level is a simple but fundamental part of the signal reconstruction. The pedestal is an artificial bias added to the analog signal before the digitization. It ensures that regardless any possible negative fluctuation, the recorded signal is well inside the dynamic range of the FADC. Moreover, adding a pedestal, the reference point (i.e. the zero of our measurement) is recorded together with the real signal.

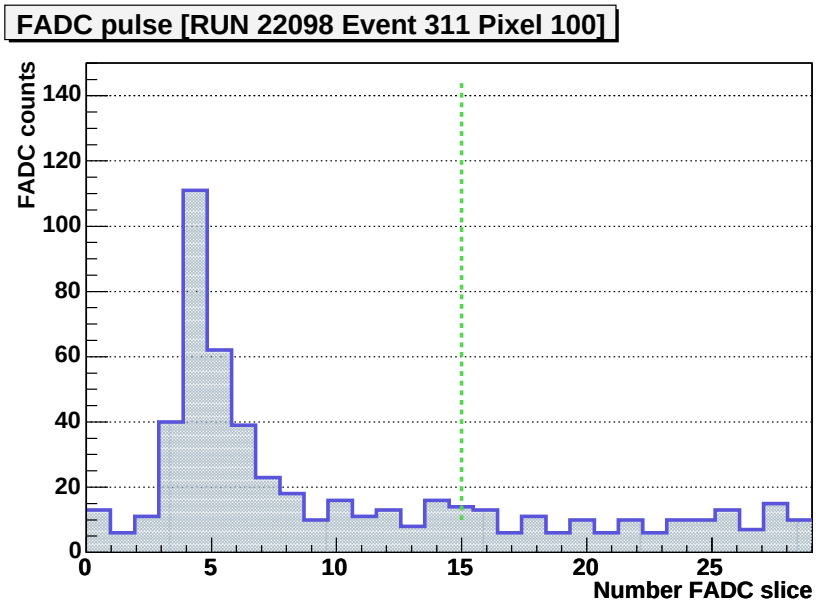

Figure 4.1: Digitized PMT pulse from a real cosmic shower. The vertical dashed line visually splits the FADC slices measured with high and low gain branches.

In order to recover the original signal coming from the analog chain of the telescope, this pedestal level has to be calculated and subtracted from any recorded digitized signal. By definition, any part of your digitalized sample where there is no signal is a measurement of the pedestal level. However, in any 'empty' signal sample there are the fluctuations coming from the noise contribution (e.g. either electronic, NSB, etc.) together with the pedestal level. For this reason, it is necessary to make a statistical analysis of a minimum number of pedestal measurements in order to obtain an accurate mean value for the pedestal level.

The pedestal for this analysis can be calculated in two different ways:

- from a dedicated pedestal run where all the events recorded are 'empty' (the trigger system is fired randomly especially for this purpose).

- directly from the shower events. For this calculation it can be used a very convenient particularity of the MAGIC DAQ. As it was explained in the description of the telescope (see section 2.2.4), the DAQ have two amplification branches: high and low gain. There is an electronic switch in charge of changing the branch going to be digitized. After digitizing the 15 hi-gain samples, the switch changes the branch for digitizing the 15 low-gain samples. Nevertheless, this switch is fired only if the signal is above a certain discriminator level, hence for signals below that level all 30 samples are hi-gain samples. This fact makes possible to use the so call low-gain samples (actually hi-gain samples) of small signals to measure the pedestal level for all pixels while normal data is being taken.

  In figure 4.1 it can be seen a real digitized cosmic pulse including both signal and pedestal.

The first method is only used in dedicated or special studies, as it will be shown

later, like the pedestal and NSB level measurement before a calibration run. The second method is the one used in the standard analysis due to the fact that it is able to measure the pedestal level with large statistics and almost synchronously with the event it is going to be applied to.

4.1.1.2 Signal extraction

The aim of the signal extraction is to get the integrated charge and arrival time of the digitized electric pulse produced by the analog chain, although only the charge is used in the presented analysis. Several algorithms have been developed in the MAGIC collaboration in order to optimize the resolution in both charge and time reconstruction. For a complete description and performance discussion for all the algorithms used in MAGIC see reference [30].

The most widely-used integrated charge extraction algorithms by the collaboration are briefly explained below:

1. **Sliding window**: For a given window of FADC time slices it searches the position which maximizes the sum of the contents inside the window. This sum is the result of the signal extraction.

2. **Spline**: This algorithm consist of the interpolation of the FADC contents using a cubic polynomial function. Then, the position of the maximum is computed and the integral in a window with a raise and a fall time with respect to the maximum is given.

3. **Digital filter**: In this method the extracted signal is calculated as the weighted sum of n consecutive FADC slices. The aim of using weights is to give more importance to the FADC slices where most part of the signal is contained, hence where the signal to noise ratio is larger. In this way, the effect of the noise contamination on the extracted signal is reduced. These weights are determined by taking into account the expected pulse shape, known by the pulse shaper and from MC simulation. Because the position of the pulse is not known, a sliding window is also required in this method. For a more detailed explanation of this algorithm see reference [36].

In the analysis presented here, the *spline* extractor with raise and fall times both of 0.5 time slices has been applied. Despite this one not being the extractor with best resolution and bias behaviour, it is one of the best (just after the digital filter). Moreover it has the ability of reconstructing the signal even when the pulse is close to the edges of the FADC digitization window, which is not the case for other extractors. During the period analyzed in this study, the mean position of the pulses moved few times, reaching in the worst case the second FADC time slice.

4.1.2 Calibration

As it has been shown in previous sections, the signal recorded by the telescope is stored in FADC counts. Integrated charge expressed in counts has no direct physical meaning and can not be straightforwardly used for the description of the shower image. Hence FADC counts must be converted into photons which have physical connection with the EAS produced by the primary particle. Moreover, from a practical point of view, this conversion is necessary because the integrated charge for two pixels illuminated with the

same light flux will be different because of the different pixel chain gains (i.e. PMT gain, analog transmition gain, etc.). Hence the calculation of any image parameters must use signals in terms of photons, which is the physical meaningful magnitude in this case.

MAGIC built a calibration system for the absolute light flux calibration of the PMT Camera based on independent and redundant methods (see section 2.2.5) [1]. This absolute light calibration consists of the determination of the conversion factors between the number of recorded FADC counts and the number of incident photons for each individual pixel.

4.1.2.1 Excess Noise Factor

For the calibration in this analysis it has been used the so-called *Excess Noise Factor* or *F-Factor* method, which converts the FADC counts in number of electrons hitting the first dynode of the PMT (i.e. photoelectrons). As it was explained in the section 2.2.2 the number of photons and photoelectrons (*phes*) are related by the *Quantum Efficiency* [2], which is known in average for the PMTs installed in the camera.

The Excess Noise Factor of any detector with some gain describes how the response function differs from a perfect amplifier. In other words, it gives the amount of noise added by the detector to the input signal during the amplification. In this method, the *F-Factor* is defined as the relation between the noise-to-signal fraction at the output over the one at the input of the amplification (see equation 4.1).

$$F = \frac{(Noise/Signal)_{output}}{(Noise/Signal)_{input}} \tag{4.1}$$

In the case of PMTs the noise-to-signal relation at the input is known because the number of *phe*s produced in the photocatode follows the Poisson statistics (i.e. noise-to-signal at input $= \sqrt{N_{phe}}/N_{phe}$. Then, the *F-Factor* relates this mean number with the mean distribution of the signal after the amplification.Represention the mean and the standard deviation of this distribution as Q and σ respectively, the *F-Factor* can be expressed as shown in the next equation.

$$F = \frac{\sigma/Q}{\sqrt{N_{phe}}/N_{phe}} = \frac{\sigma/Q}{1/\sqrt{N_{phe}}} \tag{4.2}$$

From this formula it can be seen that the mean N_{phe} for PMTs with known F factors can be obtained from the charge distribution (i.e. mean and variance) produced by a constant incident light flux. This opens the possibility to use dedicated samples of data with controlled incident flux to find calibration constants (i.e. the relation between mean charge and N_{phe}).

First of all it is important to remark that the excess noise factor F for the MAGIC PMTs was calculated in the lab with a small subsample of the ones installed in the camera, obtaining a value of 1.15 ± 0.02 [23].

From the practical point of view, dedicated pedestal and calibration runs were used to find the calibration constants. Runs with 5000 pulsed calibration events produced by light pulsers with the same colour and intensity were produced. A previous pedestal run with

[1] For a deep and complete study about the performance of the different parts and the calibration system as a whole see reference [30].

[2] For correctness it should be taken into account the collection efficiency of the first dynode. But this factor most of the time is "misunderstandingly" included in the Quantum Efficiency.

1000 random triggers was always taken just before each calibration run. The same signal extraction method applied to the data was used for the calibration data which lets the charge distribution for monochromatic calibration events. In good approximation, this charge distribution is a Gaussian with mean value $< Q >$ and variance σ_Q^2. It is important to remark that the measured charge has the pedestal already subtracted, hence $< Q >$ is the mean charge produced by the calibration events. Nevertheless, due to this pedestal subtraction, σ_Q^2 is the addition of two variances: the calibration events intrinsic one and the pedestal events variance. Finally, with all this information the number of *phe* can be derived from the calibration and pedestal events charge distributions (see formula 4.3).

$$N_{phe} = \frac{< Q >^2}{\sigma_Q^2 - \sigma_{ped}^2} F^2 \tag{4.3}$$

Hence the corresponding calibration factors can be seen in formula 4.4.

$$CF = \frac{N_{phe}}{< Q >} = \frac{< Q >}{\sigma_Q^2 - \sigma_{ped}^2} F^2 \tag{4.4}$$

Identification and treatment of bad pixels

In any observation with MAGIC it is very likely that among the 576 pixels of the readout chain, few of them present some kind of hardware malfunction. The problem can be found in any of the different parts of the pixel (e.g. PMT, analog transmition, etc.), making them unsuitable for the analysis. The calibration is a perfect tool to recognize these pixels. Pixels with very low mean $< Q >$, too large variance or non-Gaussian charge distribution for calibration runs are labelled as *bad* pixels. These tagged pixels are treated in a special way in order not to bias the shower image calculation. The signal, pedestal and pedestal RMS for the *bad* pixels are interpolated using the measured values for the neighbour pixels (excluding those tagged also as unsuitable). Then these pixels with their new contents are once again included in the standard analysis data chain.

4.1.3 Image cleaning

Image cleaning is absolutely necessary in analysis based on image momenta like the one used in this study. It will be shown in the next section that most of the parameters used in the analysis of the shower images are based on the momenta of the Cherenkov photon distribution in the camera plane up to order n^{th}.

Image cleaning is an algorithm used to keep, for the subsequent image analysis, only those pixels that contain a 'substantial' amount of the shower information. This is necessary because the images recorded by the DAQ contain, together with the shower image, a non negligible noise contribution from the NSB. If all pixels were used in the momenta computations, the information obtained will be related to the noise contribution rather than to the shower (i.e. signal) one. Because of that, the image cleaning selects those pixels with a signal-to-noise ratio high enough to assure that the distortion of the image parameters due to the noise is negligible.

4.1.3.1 Cleaning Algorithms

The image cleaning algorithm used consists of two loops over the pixels comparing the signal with two cleaning levels. In the first loop, the pixels with a signal greater than the

highest cleaning level are kept and labelled as *core* pixels of the event. In the second loop, those pixels next neighboured to a *core* pixel and with a signal above the lowest cleaning level are also kept and labelled as *boundary* pixels. This part of the cleaning algorithm is common for the two basic cleaning algorithms used in the collaboration, namely *Absolute* and *Scaled* image cleanings. They differ in the way the cleaning levels are determined. For the first one, two constant numbers of *phe*s are set as cleaning levels. In the second, the cleaning levels are computed for each pixel as $N_{1,2}$ times the mean pedestal RMS (i.e. noise level) of that particular pixel.

The main advantage of *Scaled* cleaning is that it retains as much as possible of the image in order to have the largest amount of information about the shower compared with the *Absolute* cleaning. Nevertheless, *Scaled* cleaning depends on the pedestal RMS, which is actually a measure of the NSB and the starlight. Therefore the image parameters depend on the night sky and weather conditions, which make the combination of data more difficult. Moreover, when using the *Scaled* cleaning, the noise level in the Monte Carlo simulation should be set carefully equal to the one in the data analysed samples. That makes also the MC vs. data comparison much more complex than for the *Absolute* cleaning.

In this study, as it will be shown later, the comparison between the MC and data plays a fundamental role due to the fact that the telescope was not under well known conditions at the beginning of the commissioning phase. It has been necessary to study these conditions in order to produce a satisfactory simulation of the data. It is for this reason that the *Absolute* image cleaning has been used with *core* and *boundary* cleaning levels of 10 and 5 *phe* respectively. This a conservative image cleaning taking into account that the mean pedestal RMS for inner pixels is around 1 *phe*, which means a cleaning level 10 sigmas [3] from the NSB noise level in case of *core* pixels.

4.1.4 Image parameters

Image parameters [4] are the variables used to describe the shower image. As it has been shown in the description of the detection principles of EAS by IACTs, the shower image in the PMT camera is the lateral view of the shower development. The aim in the definition of the parameters is to find out differences in the development in the atmosphere among γs and Hadrons. For this reason many of the parameters used are based on n^{th} order momenta of the shower image.

Many image parameters have been defined in the literature and inside the MAGIC collaboration. They can be divided in two types: those describing the shape of the shower image, which are independent of the source position on the camera, and those depending on the assumed source position. A small description for the ones used in this analysis is presented below. However, before stating these definitions, two technical remarks are needed. First, just the pixels selected during the image cleaning are used in the image parameters calculation. Second, in the momenta calculation the pixel position in the camera are weighted by the measured number of photoelectrons for this pixel.

[3] This value is correct for the galactic sources analysed with the conditions presented before.

[4] Also known as Hillas parameters in honour of Prof. Michael Hillas, who was the first one proposing this kind of image analysis for IACTs.

Source-position independent parameters

- ***size*** is the total signal collected in the image and it is measured in units of photoelectrons. This parameter is related to the number of Cherenkov photons (i.e. secondary particles) produced by the EAS. For this reason, and due to the fact that the atmosphere is used in IACTs detection technique like a huge calorimeter, *size* keeps direct information about the Energy of the primary.

- ***mean x & mean y*** are the center of gravity (CGO) coordinates of the image. They are very convenient parameters for the finding of inhomogeneities in the camera sensitivity.

- ***width & length*** are the half width and half length shower image and they are defined to keep $length \geq width$. They provide information about the lateral and longitudinal development of the EAS. Hence they are expected to be different for γs with respect to Hadrons, being useful for their separation.

- ***conc*** is the fraction of *phes* contained in the two brightest pixels, is terms of *phes*, with respect to the complete *size*. It gives information about the core of the EAS.

- ***leakage*** is the fraction of *phes* contained in the two last pixel rings of the camera. It gives information about how much of the image is contained in the camera. Large values of leakage means that a big part of the shower image has not been detected by the camera, hence in that situation all the other image parameters (e.g. *size*, *length*, etc.) could give wrong values which have to be used carefully.

- ***asym*** is the vector between the image center of gravity and the brightest pixel. It gives information about the asymmetry of the phe distribution along the major axis. It points to the part of the shower corresponding to the maximum development and helps to discriminate between the shower's head and tail.

Source position depending parameters

- ***dist*** is the distance between the CGO and the source position on the camera. For a given energy and zenith angle (ZA) of the primary, *dist* depends on the shower impact parameter.

- ***m3long*** is the third moment of the image along the shower image major axis. It keeps information about the head/tail of the shower image. It is defined as positive when the head of the image points to the source position. γs are expected to point to the source position while Hadrons are isotropically distributed. For that reason this parameter is useful in the γ-Hadron separation.

- ***alpha*** is the angle between the major shower axis and the direction determined by both the image CGO and the source position on the camera. In a similar way than the previous parameter, *alpha* is expected to be small for γs and flat distributed for Hadrons. *Alpha* is the image parameter with the largest γ-Hadron separation power.

For an illustration of the geometrical meaning of some of the image parameters described before, see figure 4.2.

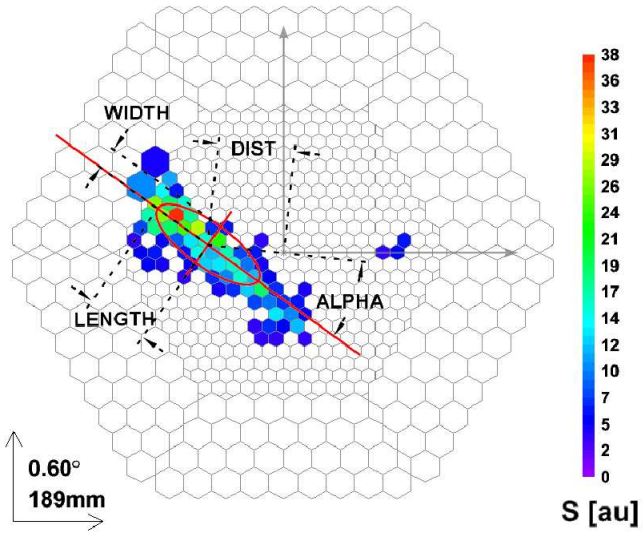

Figure 4.2: An illustration of the geometrical meaning of some image parameters. The charge of the pixels is expressed in *phe*. In the image, only the content of the pixels which survive the image cleaning is drawn, being the rest of the pixels blank. In the calculation of the image parameters drawn in the figure the source position is assumed to be the camera center.

4.1.5 Source tracking mispointing

It has been shown in previous section that many image parameters depend on the assumed source position on the camera. Therefore the knowledge of this position is vital for a correct calculation of these parameters, hence for the correct interpretation of the shower image.

In the normal operation of the telescope the position of the source is kept fix in the camera center [5]. Unfortunately, during the period being analysed in this study the steering system was being finely tuned and for this reason all observations had a non negligible mispointing. Furthermore, the alt-azimuthal mount of MAGIC makes all the sky objects focused on the camera (e.g. stars, the source position) rotate around the camera center while the telescope is tracking. The consequence for the combination of these two factors is that the source position on the camera is moving along all the observation time. For this reason a method to measure continuously the source position synchronously with the data taking was mandatory. A method for that purpose was developed and used by the author for the complete set of data presented in this Thesis, which is presented below.

4.1.5.1 Source position from star field on the camera

As it has been explained in the chapter about the slow control (see section 3.2.1) the anode currents (i.e. DC currents) of PMTs, among many other telescope subsystems

[5] This is the traditional observation mode and the first used by the MAGIC Telescope. However it also exists an alternative observation mode called "Wobble mode" where the source is observed in a fix off-axis position on the camera. For a discussion about observations in "Wobble mode" see reference [37]

information, are recorded simultaneously with the FADC data. DC currents, on the contrary to normal PMTs readout (sometimes called AC readout), measure the continuous illumination of the camera. Hence they contain, besides other continuous light sources, the star field as it was seen by the camera synchronously with shower data taking. On the other hand, from astronomical catalogs it can be deduced the star field as it should be seen by the MAGIC camera at any moment during the tracking of any source. Joining the information coming from these two sources, it is possible to find the actual source position by comparing the measured and expected star field.

Based in these ideas the method to calculate the pointing position of the telescope was developed. A brief explanation of the algorithm designed and used in this method is presented bellow.

1. **DC inter-calibration**. In data taking the global gains for the complete electronic chain are set as similar as possible for all the channels. This process is called *Flat-Fielding* and it has a two-fold aim. On one hand, it tries to optimize the dynamic range of the camera by equalizing the dynamic range of all channels. On the other, to make the response of the trigger homogeneous in the whole trigger area. Actually, each electronic channel has several parts (e.g. PMT, optical transmitter, etc.) with individual gains which may differ from channel to channel. For that reason to achieve the *Flat-Fielding*, the different gains in a channel must compensate each other. In the present design of MAGIC the PMT gain, through the HV setting, is the one used for this purpose. Therefore, during normal operation of the telescope each PMTs have different HV settings, which mean different PMTs gains.

   Camera images built with the DC currents are distorted due to the unbalance photo-tube gains. In order to solve this problem, a relative DC current inter-calibration is performed. For that purpose special runs called Continuous Light Runs are taken. In these runs the camera is homogeneously illuminated with one of the different continuous light sources installed in the calibration box. Using the DC currents measurement for these runs, it is possible to calculate an inter-calibration constant in order to correct the different gains effect. These constant is nothing else than the factor between of the DC current for a given pixel over the mean value of all pixels.

   Something to remark is that PMT HV settings are very precise and stable. Therefore any Continuous Light Run taken under the same HV configuration is suitable for inter-calibrate DC currents data. In the present analysis just one Continuous Light Run was used for the complete data set.

2. **Star finding**. Once the calibrated DC current image is finished, a star catalog is used to find the stars inside the field of view of the camera. In that process two issues must be taken into account. First, PMTs installed in the camera are not sensitive to all kind of star brightness. Hence just those stars with brightness above 7 magnitude has been selected in this analysis. Second, the expected positions of the stars on the camera are calculated supposing the telescope is actually tracking the source. This means that in the case a mispointing occurs, the expected and actual stars position must differ. Then for each star in the list, from the brightest to the faintest, the real position on the camera is searched in a circle around its expected one with a 2D dimension Gaussian fit.

3. **Source finding**. The source finding algorithm is based on finding the coordinates transformation which convert the expected star position to the actual ones. This

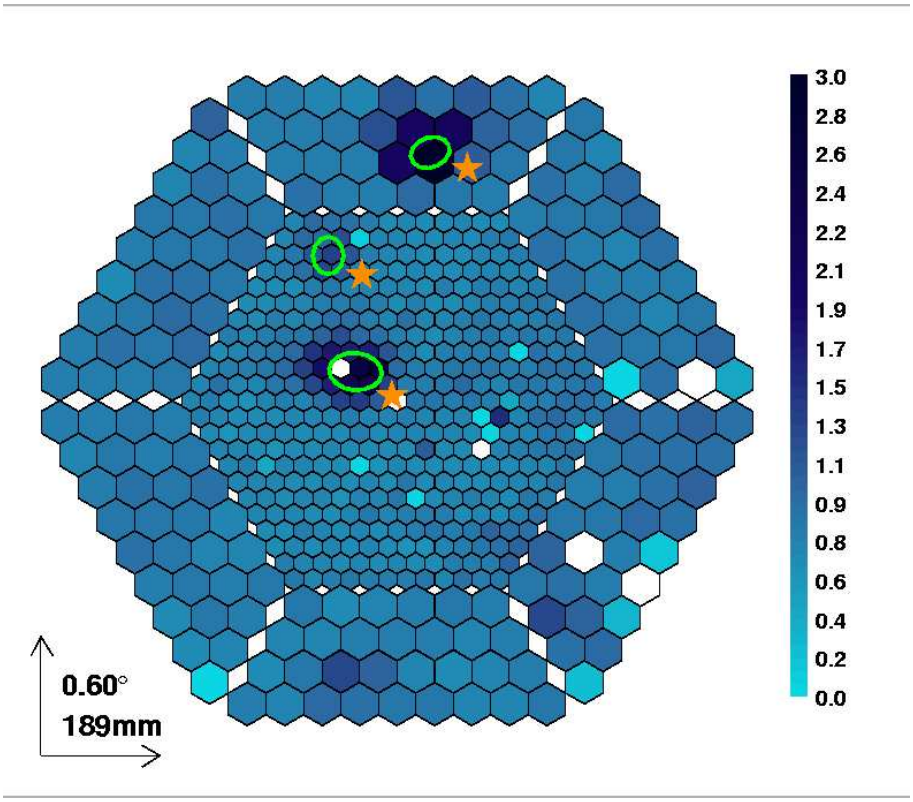

Figure 4.3: Mkn421 stars field of view seen for the MAGIC camera. The camera image is composed by the DC currents of each PMTs expressed in microamperes. The stars UMa 51, SAO 62385 and UMa 49 (sorted from the closest to the camera center to the farthest) can be seen in the camera. The five-peaked stars are the expected positions for stars and the circle are the one sigma contour of the gaussian fits. From this image it can be observed that the measured positions for the stars are left-up shifted from the expected ones. The conclusion is that Mkn421 is not in the camera center but is also left-up shifted.

transformation, composed of a translation and a rotation, is calculated using minimization numerical methods. Once this transformation is found, it is applied to the center of the camera (i.e. expected source position) to find the actual source position.

For an example of the algorithm applied to the star field of view of Mkn421 see figure 4.3.

This source position algorithm has been applied to all the data analysed in this Thesis. Mispointing values up to 0.3 deg has been observed for several nights. In figure 4.4 it is shown the calculated source positions for one Mkn421 observation night where it can be seen the typical evolution of the mispointing during the observation.

In the movement of the measurement of the source position in the camera plane presented in previous figure there can be observed a clear trend which is a general round movement around some point close to the camera center. That kind of movement is due to the Alt-Az mount of MAGIC that makes the sky objects projected in the camera plane

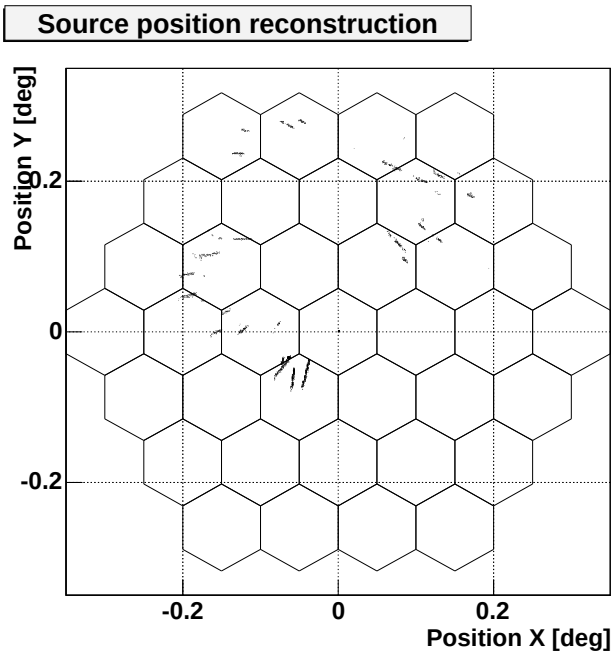

Figure 4.4: Source position on the camera calculated using the star field for Mkn421 observation during 21th April 2004. In the figure just the first three rings of pixels has been drawn. The black dots represent each of the source position measurements.

to rotate around the pointing position.

During this chapter there will be shown some tests about the performance of this pointing measurement method (see section 4.5.2).

4.2 Data sample selection.

In this study the recorded data by MAGIC for Mkn421 during March and April of 2004 have been the aim of the analysis. Moreover, a Crab Nebula observation in March 2004 in coincidence with the Mkn421 sample has been analysed too as a reference source. Crab Nebula is the northern VHE γ-Astronomy standard candle because it is the strongest steady source in the northern hemisphere. For this reason it is used by the IACTs telescopes as a calibration source. In this analysis, as it will be seen in next sections, it has been used to test the performance of the analysis in several points.

Those observations were performed doing a traditional *On* and *Off* schedule. After the source was observed for a certain time (*On* observation), the same path in the sky done by the source was observed again, obviously without observing any source (*Off* observation). In that way the *Off* observation is a pure background sample virtually taken in the same conditions of the *On* sample: weather, telescope performance (due to the time proximity of both samples), zenith angle range, etc. This similarity in the conditions of both samples is essential because, as it will be shown later in next sections, the *Off* data is used in this analysis as a background sample ideally comparable to the background component of the *On* sample. In the analysis based on *On* and *Off* observations, the *Off* sample is used to estimate the background (i.e. all events coming from non-γ particles) remaining in the

On sample after the analysis.

Before starting with the analysis of the data sample it has been necessary to select a subsample which fulfils a certain number of quality checks. Those checks guarantee that the operation of the telescope during the observation were done under nominal conditions. The aim is for the data taken to be under known and similar observational conditions, making possible to join all the different subsamples and to reconstruct the primary information from the image analysis following the same criteria.

Those checks and tests are explained in more detail later on this section. Moreover there is a table with a summary of the complete selected and excluded data with short explanation for the excluded nights or subsamples at the end of this document in appendix A.

4.2.1 Atmospheric conditions monitoring

As it was explained in the section about the detection principles of IACTs (see section 2.1) the atmosphere plays a fundamental role in the detection of air showers. IAC Telescopes record the Cherenkov light produced by the secondary particles of EAS. The atmospheric conditions affect the development of the shower, the transmition of the Cherenkov light, etc. It is in this sense that the monitoring of this conditions are mandatory for the understanding and subsequent reconstruction of the recorded information.

Following the previous statements, in the detection process of EAS with IACTs the atmosphere can be seen as part of a detector together with the ground telescope. Therefore both parts, telescope and atmosphere, have to be understood and monitor in order to be able to extract reliable results from the recorded data.

Atmospheric extinction

Optical telescopes are even more sensitive to bad atmosphere conditions than Cherenkov telescopes. They need to monitor carefully these conditions because the atmosphere acts as a lens previous to their optical system. MAGIC can profit the accurate monitor of the atmosphere done by the neighbour optical telescopes placed in the observatory. The Mercator telescope [38], a hundreds of meters distant to MAGIC, measures and make public the extinction of the atmosphere over the observatory every night. Atmospheric extinction can be understood as the gradual dimming of light as it passes through the atmosphere and therefore the Mercator measurements can be used to monitor the quality of the sky transparency. For a more detailed explanation of the extinction coefficients measurements in *El Roque de los Muchachos* see reference [39].

For each of the nights studied in this study, the Mercator extinction measurement has been checked in order to select only those data samples with good optical atmospheric conditions. In figure 4.5 you can see an example of the Mercator extinction measurement for one of the nights analysed. Moreover the distribution of the extinction measurements for all the nights selected for this study is shown. It can be seen that most of the nights (i.e. the standard atmospheric conditions) have extinction measurement below 0.25 kV (this represents 3 standard deviations from the mean extinction value). In this study any night with measurements above this limit has been rejected for the subsequent analysis.

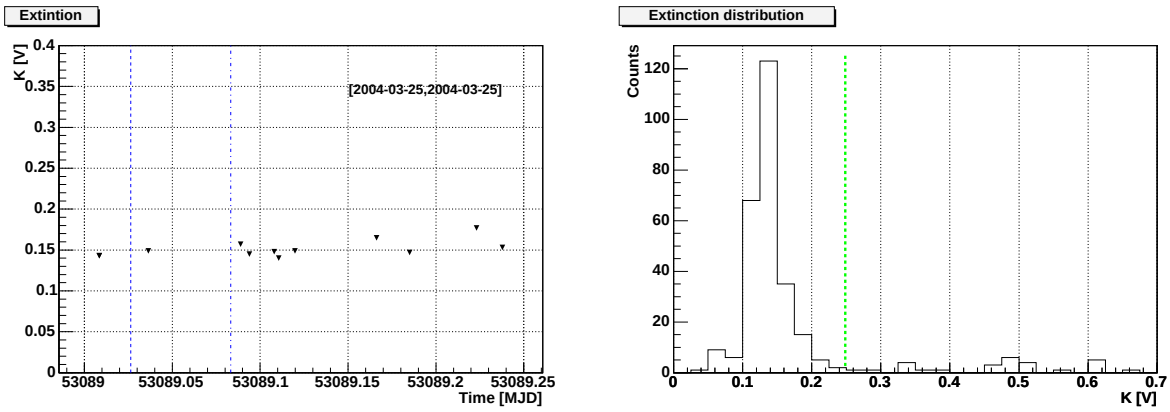

Figure 4.5: Mercator extinction measurement for analysed observations during March and April 2004. The left figure shows the extinction measurements for Mkn421 observation during 25th of March 2004 where the vertical (blue)dashed lines show the starting and ending Modified Julian Day of the observation. In the right figure the extinction distribution for the complete set of nights of the selected observation analysed in this study is shown. In this figure the (green)dashed vertical line shows the limit used to select the nights with 'good' atmospheric conditions.

4.2.2 Cosmic-rays rate stability

There is not evidence of time variability in the flux of hadronic cosmic rays hitting the Earth's atmosphere for the energy range of MAGIC. Therefore, under similar atmospheric and telescope conditions, MAGIC should record the same hadronic cosmic rays rate. This allows using this rate as a good parameter to monitor the overall observation conditions stability, both atmospheric and telescope ones.

Before comparing the cosmic rate for different nights it is necessary to have one extra thing into account. The cosmic rate depends on the zenith angle; therefore, the comparison must be done for the same zenith angle intervals. The rate dependence on the zenith is a combination of two effects. First, the observed rate is the integral rate above the trigger energy threshold. Moreover, that threshold depends on the zenith angle the telescope is pointing at. As a result, the trigger rate inherits the zenith dependence from the energy threshold. Second, the rate is the flux times the telescope effective area (see section 5.1.3.2) which due to geometrical reasons grows/ungrows with the zenith angle.

The hadronic cosmic rate has been computed for all data runs of the nights with extinction measurements good enough for observation. Together with the run by run cosmic rate calculation, the rate was also calculated in larger time intervals where the most probable value (peak value) instead of the mean value was selected. This value has been used as an estimator of the expected rate for that particular time interval. The runs with a rate more than 3 sigmas away from this reference rate were discarded from the analysis. In figure 4.6 it is shown an example for the hadronic cosmic rate for one night observation with the marked runs to be discarded.

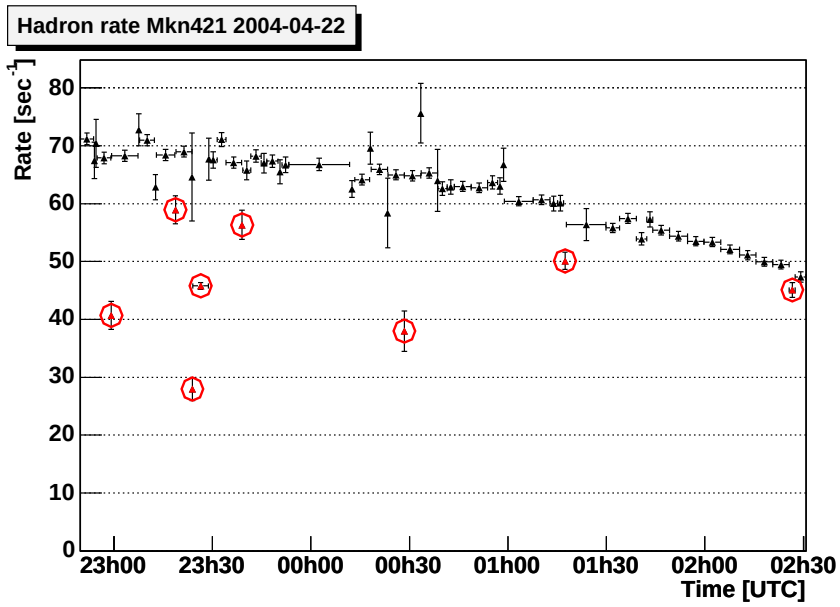

Figure 4.6: Mean hadronic cosmic rate ($size > 200phe$) for every run in Mkn421 observation during 22th of April 2004. The runs discarded for the analysis (those with a rate more than 3 sigmas away from the expected rate) are marked with a (red)circle. The evolution of the rate seen in the figure is due to the change with time of the zenith angle during the observation of the source.

4.2.3 Image parameters comparison

The last and most sensitive test to check the similarity of the observational conditions, both atmospheric and telescope response, for different data samples are the image parameters themselves. Like in the hadronic cosmic rate case, the distributions of Hillas parameters depend on *size* and the zenith angle for similar observational conditions, hence they might be comparable in similar *size* and zenith angle ranges.

Special interest has the comparison between the *On* and *Off* samples due to the fact they are going to be compared in order to see a possible excess in the *On* sample. Only *Off* samples with very similar conditions than the *On* sample being analysed can be used in the background estimation. In order to guarantee compatibility between *On* and *Off* it has been compared every *On* night with the addition of all the *Off* going to be used in the estimation, and vice-versa. The comparison was made for the distributions of the basic image parameters (*size*, *width*, *length*, etc.) which afterwards in the analysis will be used either for the γ-selection or primary information reconstruction. In figure 4.7 it is shown an example of the image parameters comparison for Mkn421 *On* and *Off* samples used in this study, for one night.

Camera response homogeneity

The distribution of events in the trigger region on the camera plane is expected to be uniform. However, it has been observed that some regions of the camera show a lower number of events than others. These inefficiencies can be related to trigger macro-cells misbehaviour, pixels with a wrong response or even completely dead, etc, and produce

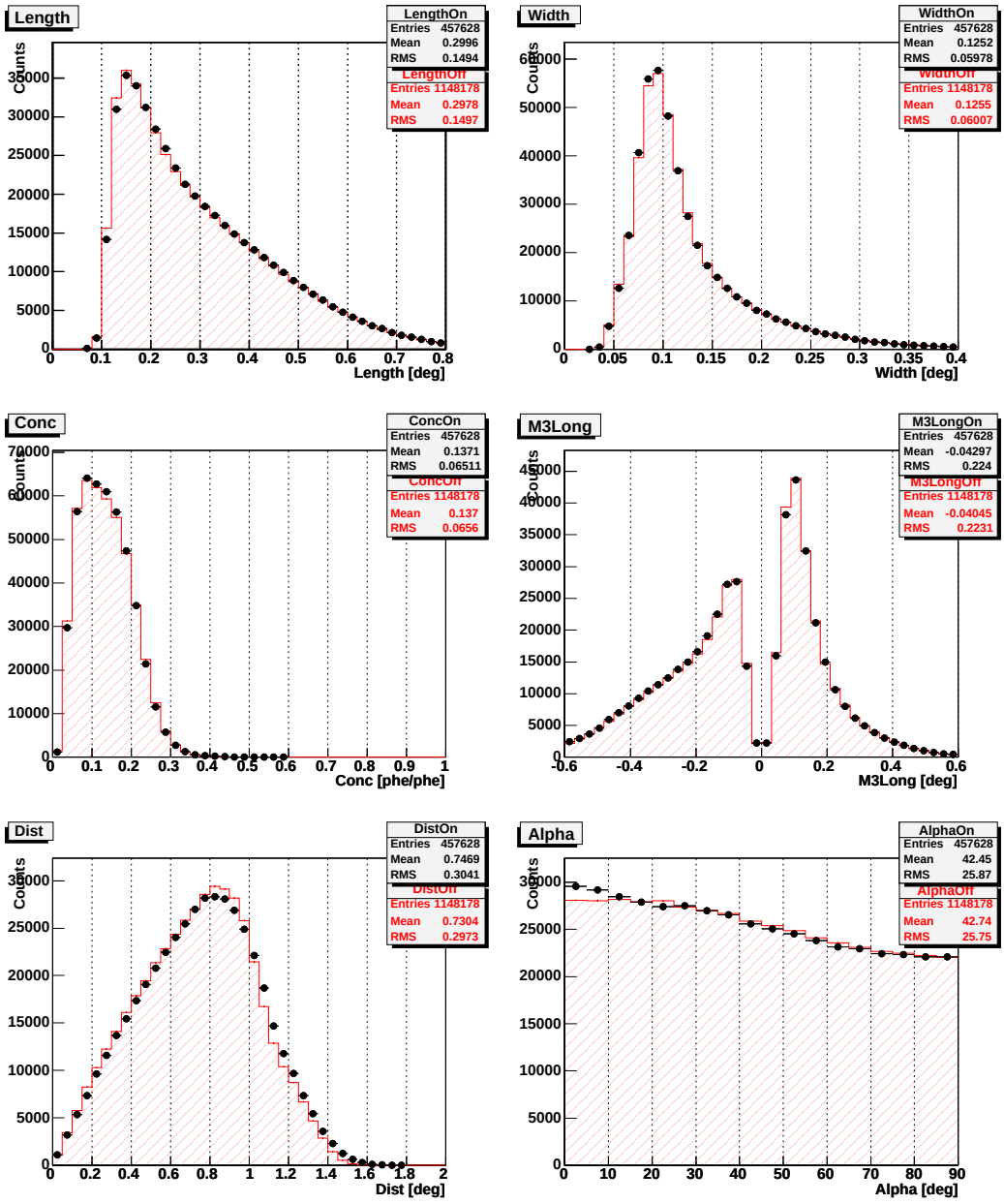

Figure 4.7: Hillas parameters comparison between Mkn421 *On* sample of 22th of April with OffMkn421-II *Off* sample for *size* above 200 *phes*. The *On* sample is drawn as black dots and the *Off* as red dashed histograms. For each image parameter both histograms have been normalized to have the same area. Most image parameter distributions are comparable within errors but for the low values of the *alpha* distribution. This discrepancy are due to the γs which can be seen even with a simple *size* cut.

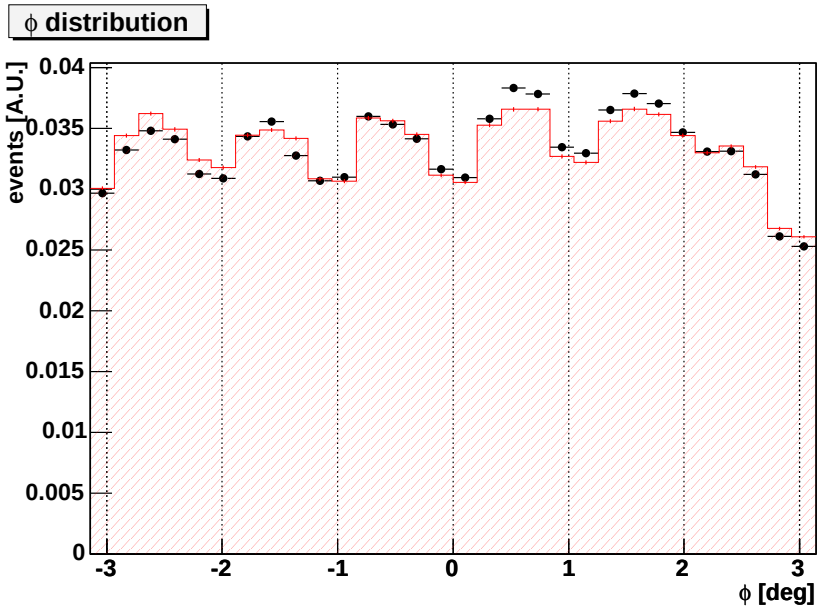

Figure 4.8: Comparison between *On* and *Off* Mkn421 samples from April 2004 for the ϕ distributions. The *On* sample is drawn as black dots and the *Off* as red dashed histograms. Both distributions are computed for events with *size* above 200 *phes*.

inhomogeneities in the response of the camera. These inhomogeneities could produce distortions in the image parameters distributions because images near those regions could be truncated. To guarantee the equality between *On* and the *Off* samples it has been tested that any possible inhomogeneity were stable in time in order to affect in the same way both samples. In addition, a big inhomogeneity in the camera could produce a wrong calculation of the flux for a given observation. Even in the case that this inhomogeneity affects in the same way *On* and the *Off* samples, which would ensure a correct treatment of the background in the *On* sample, the number of γs reconstructed will be less than the expected one.

The center of gravity of the shower image is a perfect tool to test this possible inhomogeneities of the camera. In figure 4.8 it is represented the distribution for the ϕ angle which is defined as the angle between the x axis of the MAGIC camera and the line formed by the camera center and the center of gravity. In this figure it can be observed a good agreement in the distribution of events between the *On* and *Off* samples of Mkn421 in April. It important to remark that the periodic shape that appears in the ϕ distribution is due to the "star" shape of the trigger area (see section 2.2.3). Despite this trigger induced shape, no big inhomogeneities are present in any of the two samples. The same kind of study has been performed for all the analysed sources arriving to the same kind of conclusions.

4.2.4 Data samples

To conclude this section in table 4.1, it is presented a summary of the most basic information of the remaining samples after the selection performed in this section. A final remark is that the complete observed samples for Crab Nebula and Mkn421 covered larger ZA

windows that the finally used in this analysis. The ZA ranges have been set in order to guarantee the matching between *On*, *Off* and MC samples.

SOURCE	DATES	ZENITH	OBS. TIME
Crab	19,21 March	30° *to* 50°	110 min
OffCrab	19,21 March	30° *to* 50°	130 min
Mkn421-I	19,21,25 March	8° *to* 23°	196 min
OffMkn421-I	16,21,25 March	8° *to* 23°	82 min
Mkn421-II	19,21-25 April	8° *to* 44°	728 min
OffMkn421-II	20-22 April	8° *to* 44°	350 min

Table 4.1: Selected data samples summary. This table contains the dates, zenith angle range and observation time for each of the studied data samples.

4.3 MAGIC Monte Carlo simulation

For the understanding of the results of the MAGIC Telescope, a complete simulation of the telescope response is mandatory. As it will be shown in the next sections, either the selection as γ-like candidate or, even more important, the reconstruction of the information of the primary γ-ray for an event, are based on this simulation.

The analysis presented in this study has been performed using the standard simulation package of the MAGIC collaboration. This software has been developed by members of the collaboration during the last years, including in the simulation the knowledge gained across the design, construction and commissioning of the telescope. The simulation package has been done in a modular approach which takes into account the development of air showers in the atmosphere, the reflection of the light by the mirrors, the response of the camera and the readout electronics. In next section a brief description of the main parts of the simulation are presented. For a more detailed discussion about the MAGIC Monte Carlo simulation see reference [40].

4.3.1 MAGIC Monte Carlo description

The simulation program of MAGIC is composed by three main modules: *MMCS* (in charge of the simulation of the primary particle), the *Reflector* and the *Camera*.

MMCS

To simulate extensive air showers (EAS) the well known tool CORSIKA (version 6.014 [41, 42]) was used. This program simulates the parameters for the primary particle, the interaction of that primary, γs or hadrons, with the nuclei of the atmosphere as well as all the secondary particles interactions produced in the EAS. During the development of the EAS, all the charged particles with velocity above the speed of light in the atmosphere are simulated to produce Cherenkov light. As result of this program, the full information about all the produced Cherenkov photons which may hit the ground is available: their position, direction, wavelength, height of the production and production time.

A summary of the main parameters of the air showers production used in this analysis is presented.

1. U.S. standard atmosphere model with curved geometry is used.

2. For the correct use of the Monte Carlo in the analysis, both spices of particles, γs and hadrons, have been simulated. Samples with around $45 \cdot 10^6$ γs, $25 \cdot 10^6$ protons and $9 \cdot 10^6$ nuclei of Helium [6] have been used in this study. From these produced particles around $400 \cdot 10^3$ γs and $14 \cdot 10^3$ hadrons triggered the system in the simulation.

3. Zenith angle have been simulated for γs with a flat distribution in $cos\theta$ in bins of 0.01 covering the complete data range from 0° to 50° degrees. While hadrons were simulated isotropically in 5° semiaperture cones centered at values of $cos\theta = 1.00$, 0.99, etc. covering from 0° to 30° degrees in zenith. Azimuth angles were simulated for showers coming from the South ($\phi = 0°$) and the East ($\phi = 90°$) with the same number of events at each one.

4. The energy simulation were done using a pure power law in the expected energy range of the MAGIC Telescope. From 10 GeV to 30 TeV for γs, and from 30 GeV up to 30 TeV for hadrons with spectral indexes of 2.6 for γs, and 2.75 and 2.62 respectively for protons and helium.

5. A core axis position is simulated in a circle up to a distance of 400 meters for hadrons and 300 meters for γs from telescope center.

Reflector

The *Reflector* program takes the Cherenkov photons from the output of the previous program and simulate three main steps: atmospheric absorption, reflection on the mirrors and tracking to the camera plane. In the first step the photon is traced from were it was emitted till the ground, taking into account the atmospheric effects Rayleigh, Mie scattering and the absorption by the ozone. After that, the possibility of the photon to hit the mirrors dish is checked. Then the absorption of the photon by the mirrors, taking into account the dependence with the photon wavelength, is calculated according with a mean value of the real reflectivity measurements done at lab with real mirrors. Finally, the reflection is simulated assuming a perfect spherical mirror and the photon is tracked to the camera plain. Whenever a reflected photon is found to lie within the camera limits, the program writes its relevant parameters to the reflector output file.

Camera

The previous two steps of the simulation are very CPU and disk space demanding. For that reason, these two steps are not run locally for each study but centrally done by a special group in the collaboration. In this sense, the *Reflector*'s output already produced is later run locally in the *Camera* program with the specific parameters needed for the different studies. For this reason the *Camera* program not only simulates the behaviour of the real camera but some other characteristics which may differ for each study or period, such as: the diffuse NSB, stars in the field of view, mispointing, size of the reflector area or the point spread function. Moreover, from the point of view of the camera behaviour, the

[6] The ratio between the protons and Helium nuclei used in the work is the one to reproduce the known cosmic-rays composition as publish in the reference [43, 44]

electronic noise, light guide performance, photo multiplier gains and quantum efficiencies, trigger pulse shapes, trigger rules and FADC digitalization are simulated.

Here there are the main parameters used in the *Camera* program for this work. Most of the values used in this simulation were set to measurements done with the real hardware at the beginning of the commissioning phase in winter 2003-2004.

1. Trigger response was set to the actual conditions of the real data taking of the telescope. The trigger multiplicity and topology was set to 4 close-compact next neighbours with a minimum overlap of 0.25 ns above the discriminator threshold of 4 mV. The single photoelectron at the input of the discriminator was simulated as a Gaussian of 2ns FWHM and 1 mV of amplitude.

2. The photon conversion in the camera plane to photoelectrons in the 1^{st} dynode of the inner PMTs is 0.183 phe^-/photons and for the outer PMTs 0.122 phe^-/photons. These values are the integration of the mean PMTs QE weighted by the MC wavelength distribution of Cherenkov photons. These values are the integral value of the QE of the PMTs but the dependence with the wavelength of the incident photons used was obtained averaging the measurement of the QE of some PMTs in the lab before being installed and shipped with the camera to the telescope site. The gain from phe^- to FADCs counts was 7.8 FADC counts/phe^- for inner PMTs and 3.2 counts/phe^- for outer PMTs.

3. The diffuse NSB was set according to measurements performed in the MAGIC site for sources far enough to the galactic plane and it was of 0.130 phe^-/ns for the small(inner) PMTs and 0.347 phe^-/ns for the large ones.

4. The reflector surface was reduced to agree with the actual conditions of the period when the analysed data was taken. During these periods there were $15m^2$ of uninstalled mirrors.

5. Finally the PSF for the reflector has been set to 25mm and 20mm respectively for the March and April data. These values have been obtained from a dedicated study performed in this Thesis. For the details of this study see section 4.6.

One very important thing to remark is that the output of the *Camera* is the same as the one of real data. This makes possible to use exactly the same analysis programs (signal extraction, calibration, image cleaning, etc.) for Monte Carlo than for real data. The analysis presented in previous sections was applied to the MC samples to obtain the expected image parameters distributions for each type of primary particle. In figure 4.9 can be observed a comparison between some basic Hillas parameters distributions between simulated γs and Hadrons.

Finally, the complete MC samples have been split in three statistical equivalent samples, two *Train* samples and one *Test* sample. In the following sections (and chapters) MC samples will be used for different purposes. In order not to bias some of the calculations, statistical independent samples will be needed. Just as an example, MC γs are used for the γ-selection in this analysis and afterwards the efficiency of this selection is computed for the flux calculation using also MC γs. These two steps of the analysis need different MC samples to avoid introducing a bias in the efficiency calculation.

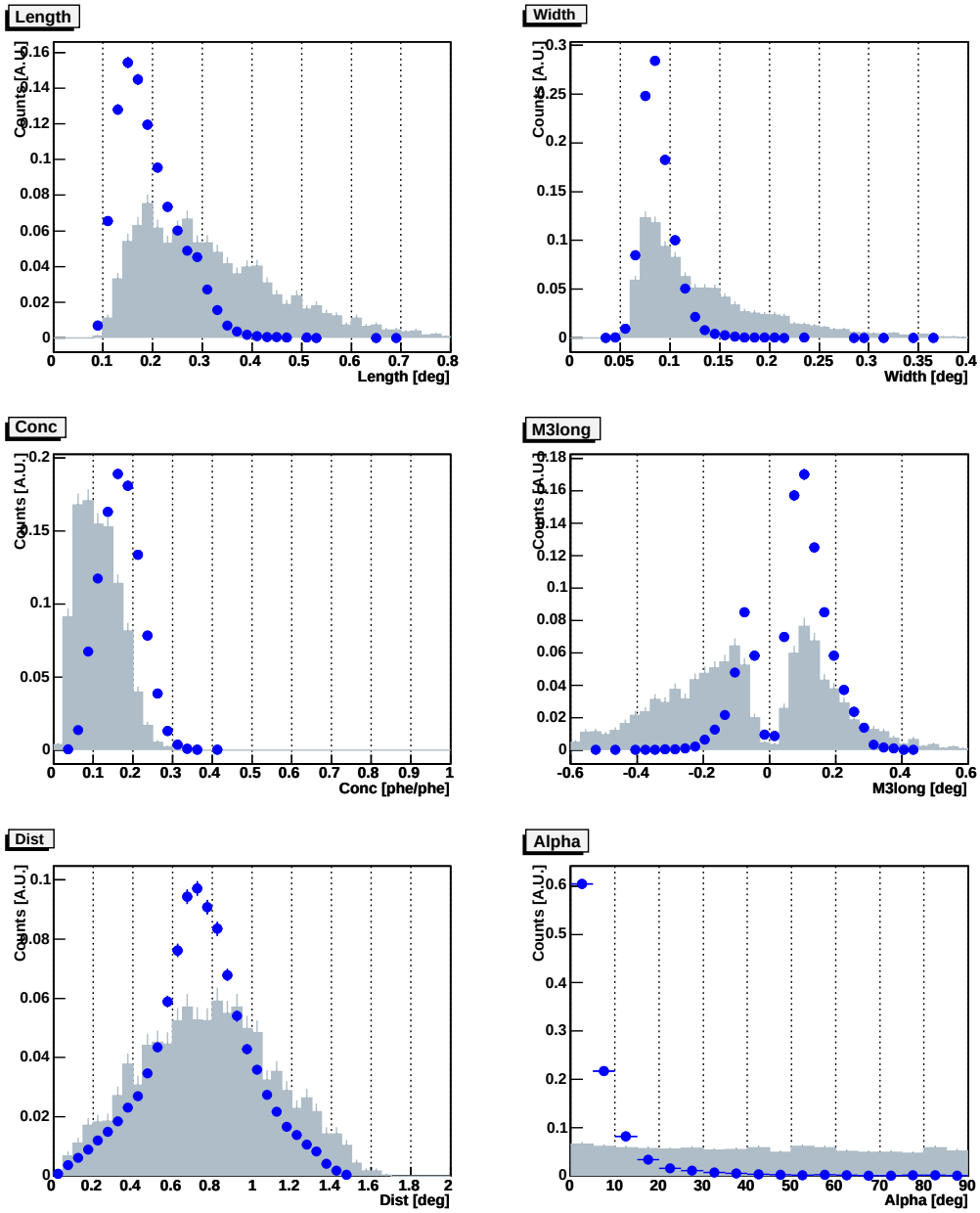

Figure 4.9: Comparison of the distributions for basic image parameters between simulated MC γs (blue dots) and protons (light blue filled histogram), for *size* above 200 *phes* and zenith angle between 0° and 30°. From the different figures it can be observed that the main differences are that γs are slimmer (i.e. lower *width*, *length*) and point to the source position (i.e. positive *m3long* and low *alpha* value).

4.4 γ/Hadron separation

One of the key points of the analysis with IACT data is the selection of γ-ray candidates from the full sample of events. These kind of signal/background classification processes are nowadays very common in many experimental branches of Physics with well established and tested mathematical methods and algorithms.

In the case of IACTs, this classification is called γ/Hadron separation and has a special importance because, in normal conditions, only 10^{-3} of the recorded events comes from a γ-shower [7].

In this section the two methods used in this analysis are going to be explained. It is important to remark that these two methods differ very much from each other. While the first one is a very powerful method based on statistical learning called *Random Forest*, the second is a very simple method just used to crosscheck the results of the first one.

4.4.1 Quality cuts

Before starting with the γ/Hadron separation methods it is necessary to introduce some special cuts just used to clean the data samples for already known background events (such as spark events) or to limit the parameters space to help the selection methods in their work.

4.4.1.1 Filter static cuts

In this section some static cuts used in the analysis are going to be explained and listed below. They are used to limit the parameter space in regions which are wanted to be excluded. After the list of static cuts, a table with the values for these cuts is shown (see table 4.2).

1. ***size* & *ncore***: A minimum *size* and number of core pixels were used to guarantee that reconstructed images have a minimum of information in order to have meaningful image parameters.

2. ***dist***: Upper and lower cuts are applied to *dist*. The lower cut on *dist* is applied because images with too small impact parameters yield showers that are too round and too close to the center of the camera (bad definition of *alpha*), which lead to a very difficult γ-Hadron discrimination. The trigger region does not cover the whole camera. For this reason hadrons with large *dist* (i.e outside the trigger region) could only trigger the system if they point to the camera center. This fact makes the *alpha* distribution for hadrons to rise for low values when events with *dist* above the trigger region are considered. In order to keep the hadron *alpha* distribution as flat as possible, an upper cut in *dist* is applied. This last constrain makes more realible the background estimation done using the *Off* sample.

3. ***cdist* & *leakage***: The variable *cdist* is defined as *dist* but taking as reference point the center of the camera instead of the source position on the camera. In the case of no mispointing both image parameters have the same meaning. But in the present case, with a sizeable mispointing, this second cut is very convenient. The upper

[7] This number is for the Crab Nebula flux integrated above 300 GeV. For other sources or energy ranges this value might be different.

limit in *cdist* and *leakage* are used to remove showers that are excessively affected by a limited camera size and that are truncated at the border.

VARIABLE	CUT_{min}	CUT_{max}
ncore	6	
size	$160phe$	
dist	0.3°	$0.75^\circ + 0.45^\circ \cdot \log\left(\frac{size}{100phe}\right)$
cdist		1.2°
leakage		0.4°

Table 4.2: Filter static cuts summary.

4.4.2 Random Forest

Random Forest (RF) [45] is the main γ-Hadron separation method used in the analysis presented in this study. *Random Forest* can be used for two things: the classification of events and an approximation to a continuous function that depends on some event's variables. Those two capabilities allow, respectively, the enhancement of signal/background and the estimation of some magnitude of the event not directly measured. *Random Forest* is an statistical learning method [8] (like Neural Network, etc.) which means that uses samples of examples to be trained. In orders words, it is able to develop a functional dependence just using examples of the "correct" behaviour.

In previous sections it was seen that MAGIC MC simulation provides the expected "correct" (signal/γs) behaviour and the "incorrect" (background/Hadrons) behaviour. Therefore, the addition of the learning capabilities of *RF* with the Monte Carlo simulation of the telescope becomes a very powerful tool in the selection and reconstruction of the shower images.

In the subsequent explanations, for simplicity, it will be addressed the problem of classification in categories only. However, everything explained can be extrapolated for the function approximation using *Random Forest*. The reader interested in more details can consult the already quoted references and references therein.

4.4.2.1 Random Forest algorithm

Before being able to explain how *Random Forest* works it is necessary to define and describe another concept called *decision tree* (hereby just *tree*). A *tree* is a set of rules (or said in others words, a set of if/elses) which for a given set of variables is able to give you a unique solution (that solution can be a category or a continuous value).

A *RF* is the combination of a large number of *trees* (in the case of this analysis is 100) where the final classification is calculated averaging the independent classifications done for each tree.

[8] For an introduction to statistical learning methods, including *Random Forest*, with application to physics experiments, in particular MAGIC, and with a comparative study among statistical learning methods and classical algorithms see reference [46].

A *Random Forest* has two main processes: the training and the subsequent classification of events. For a clearer understanding of these processes, they are going to be explained in the inverse order they actually happen in practice.

Classification process

A graphical example of a simple classification problem to illustrate the operation of the *Random Forest* is used in the following explanations.

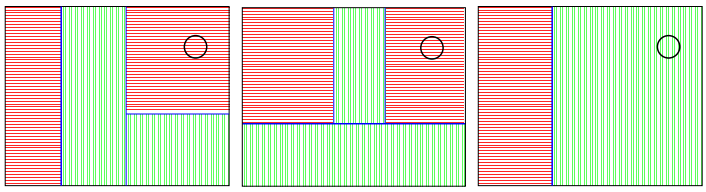

Figure 4.10: Example of *Random Forest* classification.

In figure 4.10 a graphical representation of a *RF* is shown. As it can be seen the *RF* has as inputs 2 variables (i.e. dimension, represented as the x and y axis of the square), it is composed by 3 trees and can classify the events in 2 categories which are 'red' and 'green'. In the figures the classification is represented by dashed areas with green vertical lines or red horizontal lines. This means that for any event within a dashed area, the given tree makes a classification for this event as the color for this area (i.e. 'red' or 'green'). In the example presented in the previous figure, the event is classified as $red(horizontal)$ by the first tree, $red(horizontal)$ by the second and $green(vertical)$ by the third. The final classification is by voting then the event is classified as $red(horizontal)$.

This example is a very simple idealization of a *Random Forest* but explains the basic mechanism of the classification process. *Random Forest* can be seen as a classification method that divides the hypercube of the N-dimension space of variables in small N-dimension hypercubes assigned to one of the possible categories of the classification. Any event that lays in one of these hypercubes is classified with the corresponding label.

Random Forest training

As in all statistical learning methods, the "heart" of the classification method is the training. In the case of *Random Forest*, each tree is trained independently but following the same algorithm.

The training for a *tree* is performed following the next steps. First, from the complete train sample a randomly selected subsample of the same size is chosen, allowing repetition. Selection with repetition means that each time an event is chosen from the complete train sample, it is not discarded for the subsequent selections. Therefore, just due to probability, some events could be selected more than one time. This selection process is called *Bagging* and it modifies the training sample for each *tree*, guaranteeing some degree of independence between them but keeping the same distributions probabilities for the variables space, hence solving the same classification problem. In statistical learning theory it has been proved that *Bagging* improves the classification performance of the algorithms.

Once the new training sample for the *tree* is ready, the rules for the classification have to be found. To find these rules the following steps are done.

1. First a subspace of variables of size n (in the case of this analysis 3) is randomly selected from the complete list of variables.

2. For each of those subspace variables, the optimal cut has to be found. For that purpose, it is necessary to find the cut for this variable that separates the most the categories. Several algorithms can be used for that step but the so-called *Gini-index* is the one applied in the MAGIC *Random Forest* implementation. For a given cut, the *Gini-index* is a magnitude that quantifies the separation of two set of points (i.e. two distributions) with respect a given variable. When both sets of points are completely separated by the cut it values '1' and when they are completely mixed it values '0'.

   From the practical point of view, for each variable the events are sorted according to its value and the *Gini-index* is computed for each of these events. The *Gini-index* measures the inequality between the two categories below and above the event value. Therefore the event with maximum *Gini-index* gives the cut which maximizes the separation of categories (i.e. the optimal).

3. Once n optimal cuts are computed, the one with higher *Gini-index* among them is used to separate the training sample in two parts (i.e. hyper-cubes), for those events bellow the cut and those above.

This process is recursively repeated for each new created subsample. It continues until a created node is entirely composed of events of the same category or the total number of events is smaller than a minimum number. This minimum number is used to avoid over-training of the *tree*, in other words, to avoid the *tree* to have nodes which reflect statistical fluctuations of the sample and not real trends of the categories. Those final nodes are called terminal nodes and are the ones used in the classification process. Once a node is set as terminal the category with the larger representation in the node is chosen as the category of the node.

In the following discussion how to use the previous graphical example to show the training process for a *Random Forest* is shown.

In figure 4.11 it can be seen the training for the previous example. It shows, from left to right, the 3 steps performed in the training of the first tree. The first figure show the *Bagging* selected training subsample. In the second the first rule is found. It has been selected the x variable and the optimal cut has been found leading a terminal $red(horizontal)$ node. In the last figure the second rule can be observed. It is chosen again the x variable and divided the node in one terminal $green(vertical)$ node and another terminal node because has 2 events which is the minimum allowed number in that particular example. The training for the rest of trees can be explained in a similar way.

4.4.2.2 Random Forest in this analysis

After the brief introduction about how a *Random Forest* works, now it is going to be explained how it has been used in this analysis from a practical point of view.

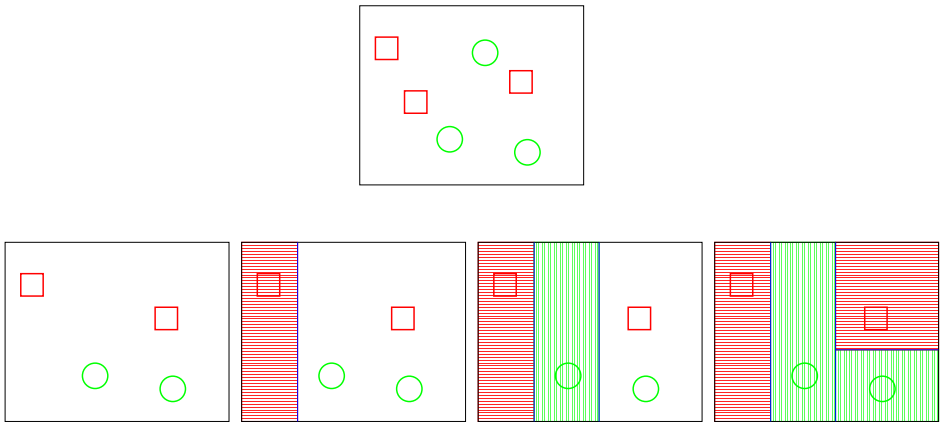

Figure 4.11: Example of *Random Forest* training.

First of all, a very important remark is that the *Random Forest* used in the analysis was not a category classification one but it produces as output a continuous variable called *Hadronness*. This variable has a range from 0 to 1 and the *RF* was trained to give 0*s* for γs and a 1*s* for Hadrons. Naturally, the distribution of *Hadronness* for both categories (γs and Hadrons) covers the complete range (0-1) but they tend more to 0 for γs and to 1 for Hadrons. The complete coverage of the range for both samples is expected due to the fact that the two samples are not orthogonal in the variables space: actually, they are quite similar in some regions. There will always be Hadron events that look very much like a γ and viceversa. In that way *Hadronness* becomes a very useful tool for the γ-Hadron separation because for each event a single cut in that variable is enough. Moreover, tighter or looser *Hadronness* cut may produce samples with more or less efficiency (ϵ) and purity.

$$\epsilon = \frac{N_{selected\_signal}}{N_{total\_signal}} \tag{4.5}$$

$$Purity = \frac{N_{selected\_signal}}{(N_{selected\_signal} + N_{selected\_background})} \tag{4.6}$$

This freedom of choice may be very convenient regarding the particular necessities of each analysis.

The second important remark is about the samples used for training the *RF*. Monte Carlo simulated γs have been used as the signal sample. Nevertheless, the sample used for the background has not been Monte Carlo Hadrons but real *Off* data of the source going to be analysed. This is the optimal solution because *Off* data, by definition, contains all the possible kinds of background (e.g. Hadrons, muons, NSB, etc.). Therefore, if *On* and *Off* samples are compatible, the *RF* are trained with a pure and virtually identical background sample.

Variables used in the *Random Forest*

The variables used as input for the *Random Forest* are traditional image parameters. They have been selected according to the degree of discrepancy between γs and Hadrons

in the Monte Carlo (see figure 4.9). The parameters selected are *size* (actually log(*size*)), *width*, *length*, *dist* and *m3long*. In a first version of the analysis, *conc* was included in the list of parameters due to the difference between MC γs and Hadrons. Nevertheless, after a deeper investigation during the development of this Thesis it was found that the addition of this parameter to the selection gives worse results. In section 4.7 it can be seen the disagreement between the Monte Carlo simulation with the real data. It was explored the addition of extra image parameters to the *RF*, which yielded marginal improvements. The reason for that behaviour is that the remaining parameters are correlated with the already used ones. Therefore, the *RF* is unable to extract new information from them.

Even being *alpha* the variable showing biggest differences between γs and Hadrons, it is not used in RF because the *alpha* distribution is the main tool for signal/background subtraction (see section 4.4.3), which is essential to estimate the remaining background in the *On* sample after all the cuts (that is, to know the number of signal events). Moreover, the inclusion of *alpha* in the *Random Forest* will only improve using a simple static cut in *alpha*, in case that there exist correlations among *alpha* and the other image parameters used in the *RF* which in good approximation is not the case.

Due to how *trees* work, the cuts applied to one of the variables most of the times depend on cuts applied to the rest of them. From a practical point of view this can be seen as if cuts applied to a single variable were not static but dependent on the rest of variables. It is important to remark that the parameterization of this dependence is found during the training by the *Random Forest* without any a priori bias. That is very convenient for analysis like the one presented here, where the dependences between the variables are very complex and many times difficult to parameterize correctly.

This characteristic of *Random Forest* opens the possibility to introduce variables not for selection but to give the rest of cuts dependence in such a variable. Actually, *size* has been introduced in the *RF* to be used in such way.

It is expected for γs and Hadrons to have different *size* distributions which is a direct consequence that both have different energy spectra. *RF* could use these differences in order to distinguish between γs and Hadrons. Nevertheless, for a correct use of the *Random Forest*, the signal sample used to train it (in our case MC γs) must have the same energy (i.e. *size*) distribution than the sample to be analysed. However, the energy distribution of the source analysed is one of the things wanted to be measured. Moreover, MAGIC is pioneering in its energy range, thus meaning that none of the previous measurement can be used as input. For all these reasons *size* it is used just as a dependence variable, not a separation variable, in this selection method.

From the technical point of view, the use of *size* as just a dependence variable, it is done by applying a conceptually simple trick. It consists in making the signal and the background training samples to have the same *size* distribution. The Monte Carlo γs are simulated with the Crab Nebula energy spectra [9] which is the standard candle for VHE γ-Astrophysics. Before training the *Random Forest*, a random selection of events from the *Off* sample is done in order to leave the *size* distribution of the γs sample statistically equal to the *Off* one going to be use for the training. That process ensures that the *Random Forest* will not use the *size* to separate the signal and background samples due to the fact that both have the same distribution.

[9] Actually a power law with 2.6 spectral index is simulated. This corresponds to the VHE part of the Crab Nebula energy spectra but that is not true for the rest of the wavelengths.

Hadronness cut optimization

As it has been explained before, the Hadronness variable allow to choose the "selection" level once the *Random Forest* has been trained. In this analysis the selection of that level is based on the maximization of the *Quality Factor* which is proportional to the sensitivity (it measures how well the background has been suppressed while enough signal events have been kept). This factor it is defined by the equation 4.7.

$$Q = \frac{\epsilon_{\gamma s}}{\sqrt{\epsilon_{Hadrons}}} \tag{4.7}$$

Where $\epsilon_{\gamma s}$ is the efficiency of the Hadronness cut for γs and $\epsilon_{Hadrons}$ for Hadrons. However, whatever the value of the *Hadronness* cut obtained with this maximization, it is only considered when the $\epsilon_{\gamma s}$ for this cut is above 80%. When this is not the case, the *Hadronness* cut which gives an efficiency of 80% in the one chosen. This is done to guarantee that a big enough number of γs is kept in the selection. In addition, by requiring this minimum efficiency, the *Hadronness* cut is set in a region of the efficiency curve (see figure 4.12) where the slope is not too steep. To have the *Hadronness* cut in a non very steep region is essential because otherwise small discrepancies between data and MC could lead to big systematic errors in the calculation of the efficiency. In other words, the difference between the real efficency of the cut and the one calculated with the Monte Carlo could be very large.

The two conditions mentioned before, that are selecting enough γs and having an *Hadronness* cut in a non very steep region, are fundamental for the subsequent parts of the analysis, such as the calculation of the spectra or the light curves (see chapter 5).

To enhance the separation power of the *Random Forest*, the optimization process has been performed for several *size* bins. Figure 4.12 shows the results for the optimization of the *Hadronness* cut for the *Random Forest* trained for the selection in the Mkn421-II data sample. From this figure it can be observed that the optimization in different *size* bins is completely necessary due to the very different behaviour of the *Random Forest* for different *size* values.

4.4.3 On/Off background subtraction

As it has been pointed out in previous sections, after applying quality and hadronness cuts, the application of the cut in *alpha* is still left. The exclusion of this variable in the standard γs selection process (i.e. *Random Forest*) is due to the fact that the *alpha* distribution is used in the determination of the remaining background contamination in the already selected *On* data sample, hence the number of γs.

Number of Excesses

From a practical point of view, the number of γs is estimated with the number of excess events in the *alpha* distributions (so-called *alpha* plot) for *On* and *Off* samples after cuts. It has been shown that the *Off* sample should be a pure background 'virtually' equal to the *On* sample. Hence the difference between both distributions has to be the contribution from γs. Moreover, as it was seen from the MC, γs are expected to peak for low values of *alpha* while background has a flat distribution. Hence the two distributions should agree for large *alpha* values where just background events are expected. However, they might differ for low *alpha* values where on top of the background, signal events should show-up.

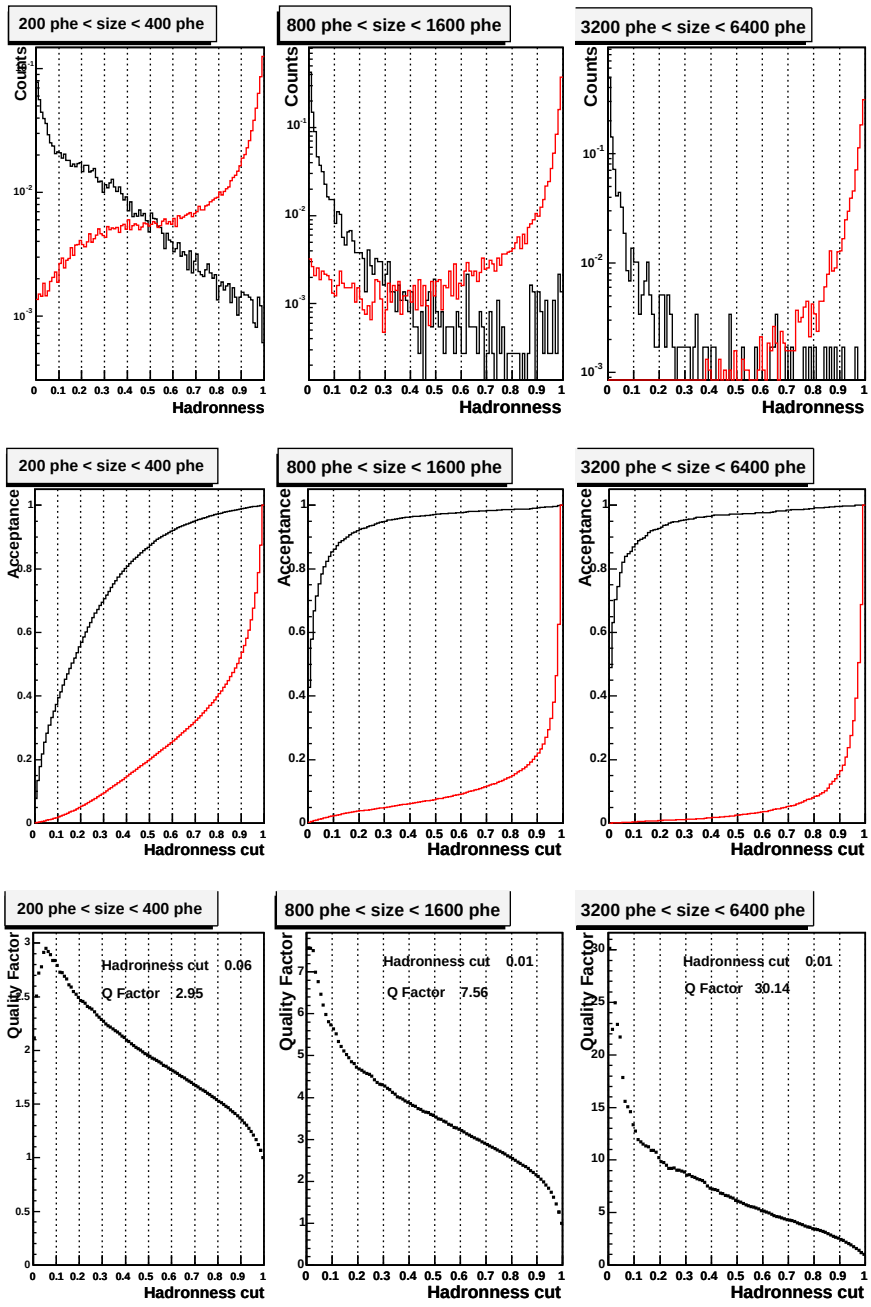

Figure 4.12: Optimization of the *Hadronness* cut in different *size* bins. This optimization has been done with the *RF* using MC γs (black histogram) and *Off* events from the *Off* Mkn421-II sample (red histogram). The different columns are for different *size* bins. In the top row are shown the *Hadronness* distribution for γs and Hadrons, while in the second and third rows the efficiency and the *Quality Factor* for a given *Hadronness* cut are shown.

Following this argumentation, two regions could be defined in the *alpha* plot: the signal region (below the *alpha* cut), which actually is composed of γs and Hadrons; and the background region, for high *alpha* values, where just background events are expected. In this analysis the signal and background regions are defined for *alpha* between 0° and 15° and between 30° and 80° respectively.

Then the number of γs is calculated from the number of *On* events in the signal region (i.e. N_{On}) minus the estimation of the number of background in the signal region (i.e. N_b). This number of background by construction is proportional to the number of *Off* events in the signal region (i.e. N_{Off}).

There are several ways to compute this normalization between N_b and N_{Off} (from now on α). The ideal way would be by the ratio between effective observation times.

$$\alpha = \frac{T_{On}}{T_{Off}} \tag{4.8}$$

but during *On* and *Off* observations the weather conditions and/or the telescope performance may vary slightly, leading to small differences in the distribution of their image parameters, hence the efficiency of the cuts might be slightly different. In that case the ratio of the observation times leads to a wrong normalization after applying cuts. In order to solve this problem it can be computed this normalization by the ratio between the number of events located in the background region of the alpha plot after applying cuts.

$$\alpha = \frac{N_{On}^{Background\_region}}{N_{Off}^{Background\_region}} \tag{4.9}$$

In this study the normalization between the *On* and *Off* is done using formula 4.9. Finally, the number of excesses is calculated using equation 4.10

$$N_{execess} = N_{On} - \alpha N_{Off} \tag{4.10}$$

Significance

The significance gives the probability that a given number of excess could not have occurred by statistical fluctuations of the background. Most of the times this probability is expressed as the equivalent number of standard deviations (i.e number of σs) taking the distribution of the number of excesses as Gaussian.

For the estimation of this significance in γ-ray astronomy the straight derivation from the N_{excess} over its standard variation was used in the past (see equation 4.11).

$$N_\sigma = \frac{N_{On} - \alpha N_{Off}}{\sqrt{N_{On} + \alpha^2 N_{Off}}} \tag{4.11}$$

However Li and Ma [47] made a critical examination of the methods used in the analysis of γ-ray experiments to estimate the statistical significance for observations. They proved using Monte Carlo studies that previous formula underestimated the significance of a positive signal taking the null result as hypothesis. As a conclusion, they proposed a formula to correctly evaluate the statistical significance of a positive result. In this analysis the formula 17 from the Li & Ma paper (see equation 4.12) is used.

$$N_\sigma = \sqrt{2\left\{N_{On}\ln\left[\frac{1+\alpha}{\alpha}\left(\frac{N_{On}}{N_{On}+N_{Off}}\right)\right] + N_{Off}\ln\left[(1+\alpha)\left(\frac{N_{Off}}{N_{On}+N_{Off}}\right)\right]\right\}} \tag{4.12}$$

4.4.4 Scaled Hillas cuts

The first, and most basic, γ/Hadron separation method used in the Imagining Air Cherenkov Astrophysics field was called "supercuts" [48] and were a set of constant cuts applied to the basic Hillas parameters *width*, *length*, *dist* and *alpha* derived from a MC simulation. The main problem of this approach was that due to the step power of the energy distribution for the known γ-ray sources, these cuts were optimized for the most probable energies, hence for images of low energies. This fact leads to a poor selection of images from γ-showers of medium-high energies.

In order to solve this problem several approaches were developed. One of them, called "Dynamical supercuts" [49], proposes the cuts applied to the Hillas parameters to be not constants but functions of variables like *size* or zenith angle. Another solution, technically slightly different but conceptually the same, was the so-called "Scaled Hillas". This approach keeps the cuts constant but defining a new set of Hillas parameters: the standard ones normalized with a parameterized function of the mean dependence of that parameter with the set of desired variables.

In this analysis a very simple approach has been adopted for this separation method. Constant cuts were applied to less dependent variables like *dist* and *alpha* and Scaled Hillas were defined to *width* and *length*, which have proved to be the variables with more separation power after *alpha*. The parameterized function used was a first order polynomial for both *width* and *length*. These parameterizations were obtained from MC γ (PSF 25mm) simulation with the following results.

$$ScaledWidth = \frac{width}{5.05\cdot 10^{-3} + 2.90\cdot 10^{-2}\cdot \log(size)} \tag{4.13}$$

$$ScaledLength = \frac{length}{-1.08\cdot 10^{-1} + 1.06\cdot 10^{-1}\cdot log(size)} \tag{4.14}$$

Once the new scaled parameters are defined it is necessary to optimize the cuts by the maximization of some quantity that gives the maximum separation power. In this method this is done by the maximization of the quantity $(Number of Excesses)*(Significance)^2$ for an *On-Off* train sample. In such a way the optimization algorithm not only maximizes the significance, i.e. the γ-Hadron separation, but also keeps a reasonable number of excess events.

Figure 4.13 shows the value of the $N_{Excess} * \sigma^2$ for different values of the cuts in ScaledWidth and ScaledLength for Crab-I sample (see appendix A). It has been used to optimize the Scaled Hillas cuts leading to the following ones.

$$ScaledWidth < 1.3$$
$$ScaledLength < 1.4$$

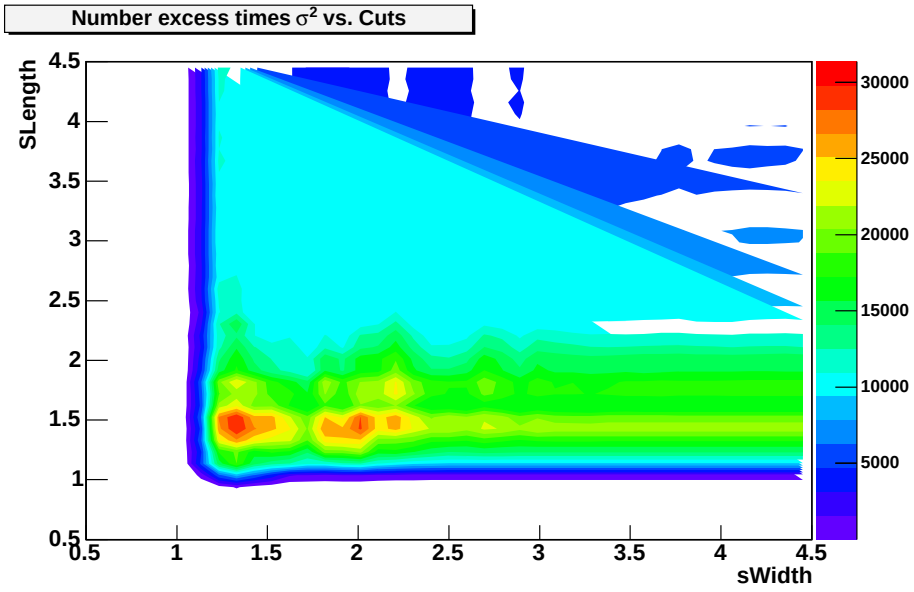

Figure 4.13: $(Number\ of\ Excesses) * (Significance)^2$ vs. Scaled Hillas cuts for Crab-I sample.

As it was explained before in this chapter, the objective of this method was to complement the *Random Forest* capabilities using a simple but powerful enough alternative method. The advantages of this extra method with respect to *RF* are several: simplicity, speed and, the most important one, which is the MC simulation independence. This last characteristic allows an indirect way to test the MC simulation. For example, an incompatible *Number of Excesses* obtained in the same sample by both methods could indicate a problem in the MC of γs, The comparison of both methods will be discussed with more detail in following sections. Obviously, the disadvantage of the Scaled Hillas cuts is the lower separation power compared with the *Random Forest*.

4.5 Sky Map

As it has been shown in this chapter, the analysis based on the *alpha* distribution has the requirement of knowing a priori the position of the source in the camera plane. This requisite could be fulfilled for observation of point like sources such as AGNs, where the position on the sky is well known from observations in other wavelengths. However, this is not the case for extended sources such as SNRs or sources with generally poorly known position like GRBs. To treat these cases, an alternative analysis method to reconstruct individual γ-ray direction called *disp* [50, 51] were developed for IACTs.

In the study presented in this Thesis both analysed sources are point-like source. Nevertheless, this method is a perfect tool to test the mispointing correction applied to the data. In the next paragraph the *disp* method implementation done in the MAGIC collaboration is introduced.

4.5.1 The *disp* method

The *disp* method was first used by the Whipple collaboration and it has been adapted to the MAGIC telescope by members of the collaboration. For a detailed explanation see reference [52].

The idea behind this method is that the source position of the primary γ-ray should lie on the major axis of the Hillas ellipse that parameterizes the shower image. The distance between this position and the center of gravity of the image is what is defined as the *disp* parameter. It is expected that shower images which are closer to the source position in the camera are more roundish, while showers which are further away from this position are more elliptical. For this reason it was proposed to use the "ellipticity" of the shower image to derive the source position along the ellipse major axis. In formula 4.15 it is written down the original expression used for the calculation of *disp*.

$$Disp = \xi \left(1 - \frac{Width}{Length}\right) \tag{4.15}$$

In previous equation the parameter ξ is calculated using a MC γs sample.

Due to the different features of the MAGIC Telescope compared with the predecessor IACTs, such as its parabolic reflector and its lower energy threshold, it was adopted a more general parameterization (see equation 4.16).

$$Disp = A(size) + B(size) \cdot \left(\frac{Width}{Length + \eta(size) \cdot leakage}\right) \tag{4.16}$$

This new parameterization includes a second order polynomial dependence of the A, B and η parameters on the logarithm image *size*. It was also included a correction term in *Length* to account for images truncated at the edge of the camera, similarly to the correction introduced for the CT1 HEGRA telescope [53]. As in the previous case, the functions A, B and η have been optimized using the MC γs sample. In the following equations can be found the values for the optimal parameterization.

- For events with no *leakage*

$$\begin{aligned} A &= 0.923 + 0.707 \cdot (\log(size) - 2) - 0.381 \cdot (\log(size) - 2)^2 \\ B &= -0.634 - 0.862 \cdot (\log(size) - 2) + 0.333 \cdot (\log(size) - 2)^2 \end{aligned}$$

- For events with *leakage*

$$\begin{aligned} A &= 1.42 + 0.0188 \cdot (\log(size) - 2) - 0.0104 \cdot (\log(size) - 2)^2 \\ B &= -5.67 + 1.82 \cdot (\log(size) - 2) - 0.0576 \cdot (\log(size) - 2)^2 \\ \eta &= 12.6 - 1.85 \cdot (\log(size) - 2) - 0.769 \cdot (\log(size) - 2)^2 \end{aligned}$$

Once the *disp* value and the line where the arrival position lies are known for a given event, the direction along this line is the only unknown magnitude. In order to disentangle between the two possible solutions, the *asym* image parameter has been used. This parameter allows in most cases to determine the head-tail of a shower image.

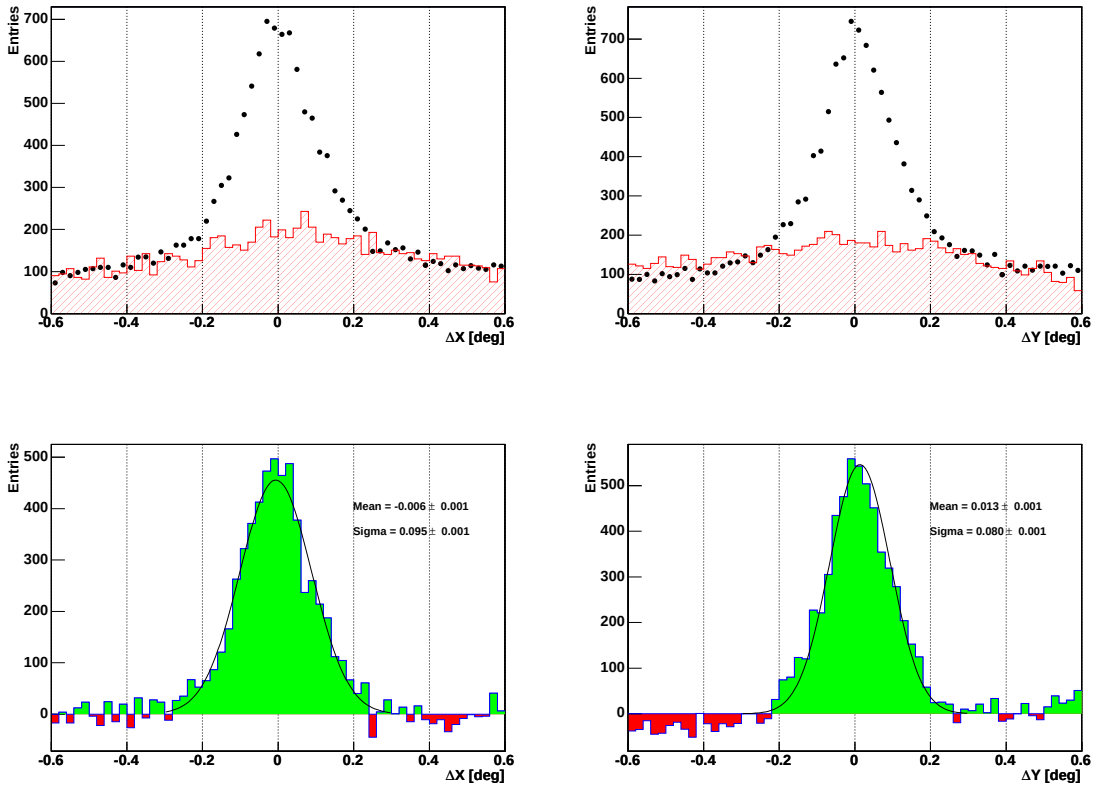

Figure 4.14: Distribution of differences between the source position calculation using the *disp* and the field of view stars methods. Left figures represent the projection in the x axis of the camera system whereas right ones show the y axis projection. The upper plots show the *On* (black dots) and *Off* (red shaded histogram) distributions. The bottom histogram shows the difference between the *On* and *Off* distributions (green-red solid histogram).

4.5.2 Mispointing correction vs. *disp*

The *disp* method has been used in this Thesis for two different things. The first one consists in the test of the mispointing correction applied to the data. To do this, it has been compared the arrival positions obtained from *disp* with the source position computed for each event with the stars field of view (see section 4.1.5.1). The distribution for the difference between these two source position calculations for the Mkn421-II sample are represented in figure 4.14. In case of having a bias in the mispointing calculation it should show-up in this test as a shifted center of the distributions. The mean values for both distributions are within less than 0.01 deg, which is a tenth of the diameter of an inner camera pixel. The first conclusion from this test is that the mispointing correction does not have any bias that could affect the standard analysis performed in this Thesis. In addition, the width of these distributions is the combination of the resolution of both source position calculation methods. Both distributions shows a σ of the order of 0.1 deg which is compatible with the expected resolution for the *disp* method for the *size* cut used in the test (see reference [52]). The conclusion is that the resolution of the mispointing

calculation should be much less than 0.1 deg in order to not affect the width distributions.

The second result from the *disp* method is the sky map for the analysed sources in sky coordinates *Right ascension* and *Declination* (see figure 4.15). In the production of this sky map each arrival position on the camera calculated with *disp* is transformed into sky coordinates. To do this, a reference point on the camera which sky coordinates are known is necessary. In normal operation this position generally is the center of the camera, which sky position is known because it is the point in the sky being tracked by the steering system. Due to the problems with the steering system explained in previous sections, this information is no longer credible and an alternative reference point is needed. In the sky map presented before, the source position was calculated using the stars field of view as reference point, assigning the known Mkn421 sky coordinate to the given source position on the camera.

4.6 Tuning PSF for Monte Carlo simulation

Before showing the results of this chapter it is necessary to present the specific study performed in order to measure the point spread function for the two periods analysed in this Thesis.

One of the new developments done for MAGIC has been the Active Mirror Control system which adjusts the reflector during data taking to keep its parabolic shape (see AMC section 2.2.1). This new advantageous feature of MAGIC demands a carefully monitoring of the reflector performance, in particular of the Point Spread Function (PSF). The PSF can be defined as the flux distribution due to diffraction in the image of an ideal point-like source as seen by the telescope optics. In other words, it represents the goodness of your reflector to keep differentiated the image on the focal plane of close points situated on the focus. From now on in this document, PSF will be used not for the complete flux distribution but for the "width" (i.e. sigma) of the distribution.

The PSF is a key parameter in the performance of the telescope. Having a good optics response (i.e. a small PSF) is essential for MAGIC goals for two reasons. First, the Cherenkov photon density that arrives to the ground for EAS is converted by the reflector in a new photon density in the focal (i.e. camera) plane. Larger reflector PSF produces lower Cherenkov photon density on the camera. For the present design of the trigger, it can be seen that it fires the telescope when a cluster of pixels is above a certain photon density. Moreover, low energy showers produce lower photon densities, hence this low energy events are triggered depending on the reflector PSF value. In other words, a large PSF increases the energy threshold, whose reduction is the main goal for the construction of the MAGIC telescope. Second, the IACT technique is based on the discrimination between γs and hadrons using the image parameters, that is, the shower image shape. When the reflector blurs the shower image due to the PSF it makes both kind of shower images to look more similar. Therefore, large PSF makes γ-hadron separation less efficient.

During the periods of time analysed in this Thesis several interventions were performed to set the AMC system in nominal working conditions. Due to that fact, the value of the PSF changed some times during these months. Actually, during February 2004 there was a rather big adjustment of the system to improve its performance. For this reason, it has been studied the PSF response for the two periods analysed in order to set the correct value in the MC simulation used in the analysis.

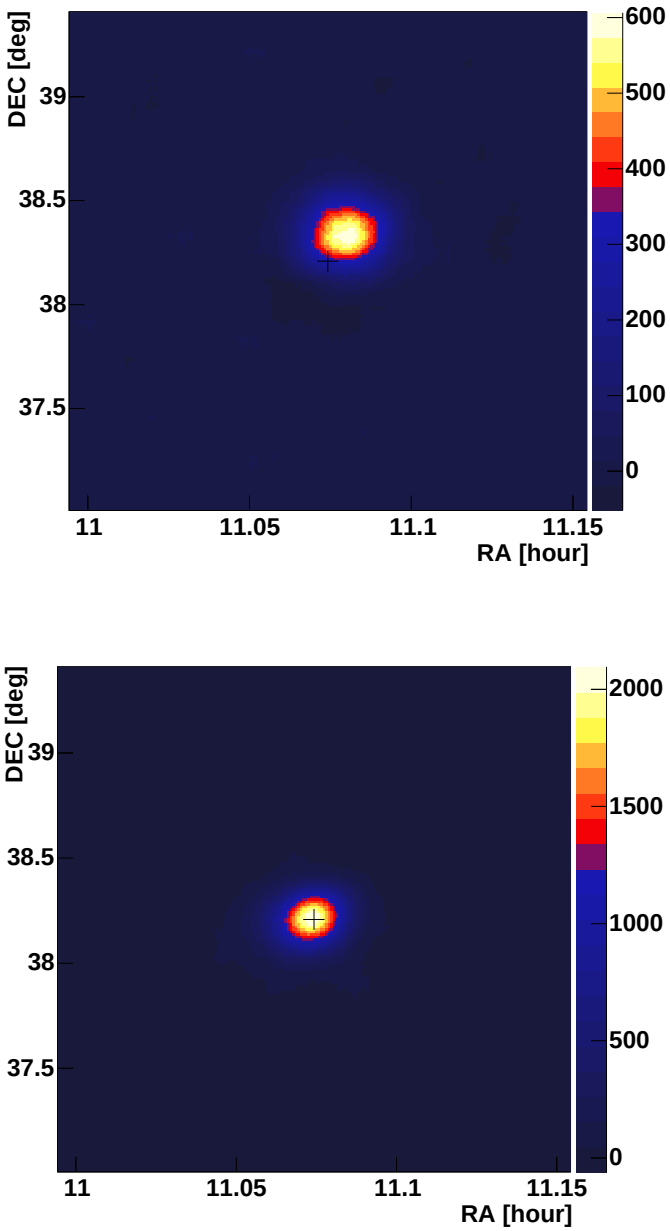

Figure 4.15: Sky map of excess events calculated with the *disp* method for the Mkn421-II sample. The top figure represents the sky map assuming that Mkn421 is in the center of the camera. Due to this wrong hypothesis the central cross in this case marks the position of the center of the camera instead the position of Mkn421. The bottom figure represents the sky map calculated once the mispointing is corrected using the stars in the field of view. In this case the central cross marks the sky coordinates of Mkn421.

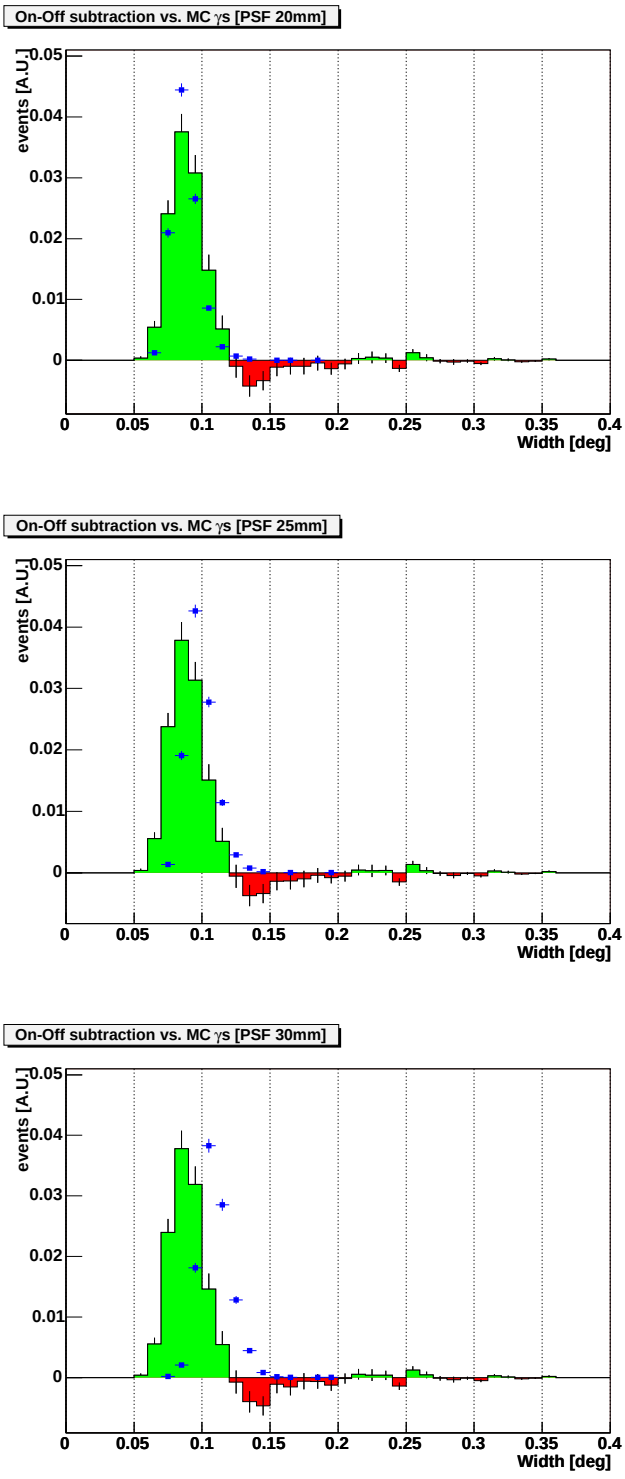

Figure 4.16: Comparison for *width* distribution between several MC γs with different PSF and real *On-Off* data. Mkn421 of 25th April 2004 sample has been used for the real γs distribution. This distribution from data is compared with MC simulations with values of PSF of 20mm, 25mm and 30mm. The blue dots represents the MC γs while the solid histograms show the *On-Off* subtraction for real data.

4.6.0.1 Comparison between real excesses and Monte Carlo.

The strategy followed in the estimation of the PSF consists in the comparison for the *width* distribution between γ events extracted from data with several MC γs simulated with different values for the PSF (actually 20mm, 25mm and 30mm). The image parameter chosen for the comparison has been *width* because it is one of the parameters most sensitive to the PSF value of the reflector. Then, the PSF estimated for a given period was taken from the Monte Carlo γs which best compared with the real data.

For the selection of the real γs, the Scaled Hillas cuts, explained in the previous section, has been applied. Using this selection method it is guaranteed that the distributions obtained from *On-Off* subtraction has no bias due to the use of a certain Monte Carlo in the selection. This would not be the case if Random Forest were used. In addition to the Scaled cuts, a cut in *alpha* lower than 6° has also been applied.

The *width* distribution for the real γs is obtained using a similar receipt than the one used in the calculation of $N_{excesses}$. Using just the scaled cuts, an *alpha* plot is built for the real data. From this plot, following the procedure explained in section 4.4.3, the normalization between the *On* and the *Off* samples and the number of excesses are obtained. Finally, the *width* distribution for real γs is obtained from the subtraction of the *On-Off*, taking into account the normalization found. Then the obtained distribution is compared with the MC ones. The MCs samples have been selected using the same set of cuts applied to the real data and have been normalized according to the number of excesses.

In figure 4.16 it is shown the results for the comparison between data of the Mkn421-II sample with several MCs. From this study it can be deduced that the best estimation for the PSF for April 2004 was of $20mm$. Similar study was performed for March 2004 data obtaining a value of $25mm$.

4.6.0.2 *Random Forest* for different Monte Carlo conditions

An additional test has been performed in order to prove that the estimation for the PSF is not just the best option between the set of simulated values but the one in the real data. This test consist in the comparison of the behavior of the *Random Forest* between real data an MC γs. This test is very sensitive to differences between data and MC because it takes into account the distributions for all the image parameters used in the *RF* as well as all the correlations between them.

The three available MC γs have been used to train a different *Random Forest* each. In this training the same *Off* sample has been used. Then, this different *RF* have been used to analyze the same *On* sample which has been selected for this particular study. For each of the MCs, it has been calculated the number of excesses for *Hadronness* cuts applied in regular intervals. From this part of the analysis it has been obtained the $N_{excesses}$ as a function of the *Hadronness* cuts. Moreover, for the given MC, the same analysis has been applied to the test sample of the corresponding MC γs, obtaining the efficiency (ϵ) for the applied cut. By definition, the magnitude $N_{excesses}/\epsilon$ should be a constant for any applied cut if the MC is an accurate enough description of the data.

In figure 4.17 it is presented the $N_{excesses}/\epsilon$ curves for the three MC presented in the previous section. From this test it can be concluded that the MC γs of 20mm is a very good description of the Mkn421 data of April. Just for a *Hadronness* cut below 0.1 could be observed significative discrepancies from the expected behavior which for largest values is below 20%.

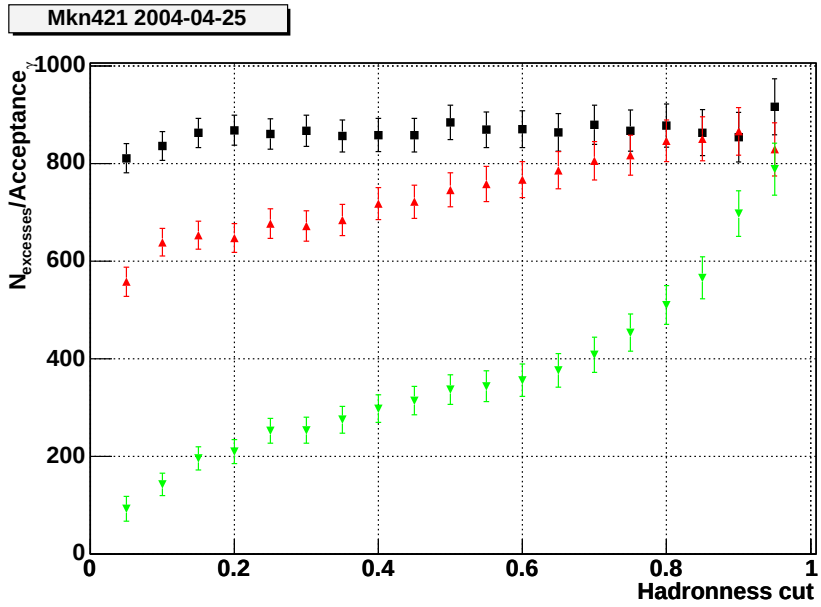

Figure 4.17: $N_{excesses}/\epsilon$ for Mkn421 during 25th of April as a function of the *Hadronness* cut. Three different *Random Forest* trained with MC γs with PSF values of 20mm (black squares), 25mm (red up-triangles) and 30mm (green down-triangles) have been used. Note that the points in each curve are highly correlated between them.

4.7 Shower image analysis results

To finalize this chapter, two results obtained from the analysis presented are going to be shown. The first one is the comparison between data and MC for the image parameters used in the γ-Hadron selection. The second one is the measurement of the number of γ-rays detected for the selected sources, which was remarked as the aim for this analysis at the beginning of this chapter.

For the comparison between data and MC, the same approach explained in the previous section about the estimation of the PSF value has been applied. In this case the comparison was performed using MC with 20mm PSF and Mkn421-II data (see figure 4.18 for the results). From these first results, several conclusions could be obtained. First, most of the Hillas parameters are in good agreement between data and MC with the exception of the *conc* distribution. The agreement between data and MC confirms the result for the PSF in April obtained in the previous section comparing the behaviour of several *Random Forests* over real data. Regarding the *conc* distribution, an extra test was done to support the observed disagreement for this parameter between data and MC. Two *RF* were trained using the same data and MC but with the difference that one had *conc* in the list of variables used for discrimination and the other had not (see figure 4.19). From these results it is clear that *RF* behaves better in real data when *conc* parameter is not used for discrimination. The only plausible conclusion is that this parameter is not well described by the MC simulation. Further studies are needed in order to understand this misbehaviour which are beyond the scope of this Thesis. A second conclusion comes from the accurate agreement for the *alpha* distribution. This image parameter is very sensitive to possible mispointing, then any remaining bias or error in the mispointing correction

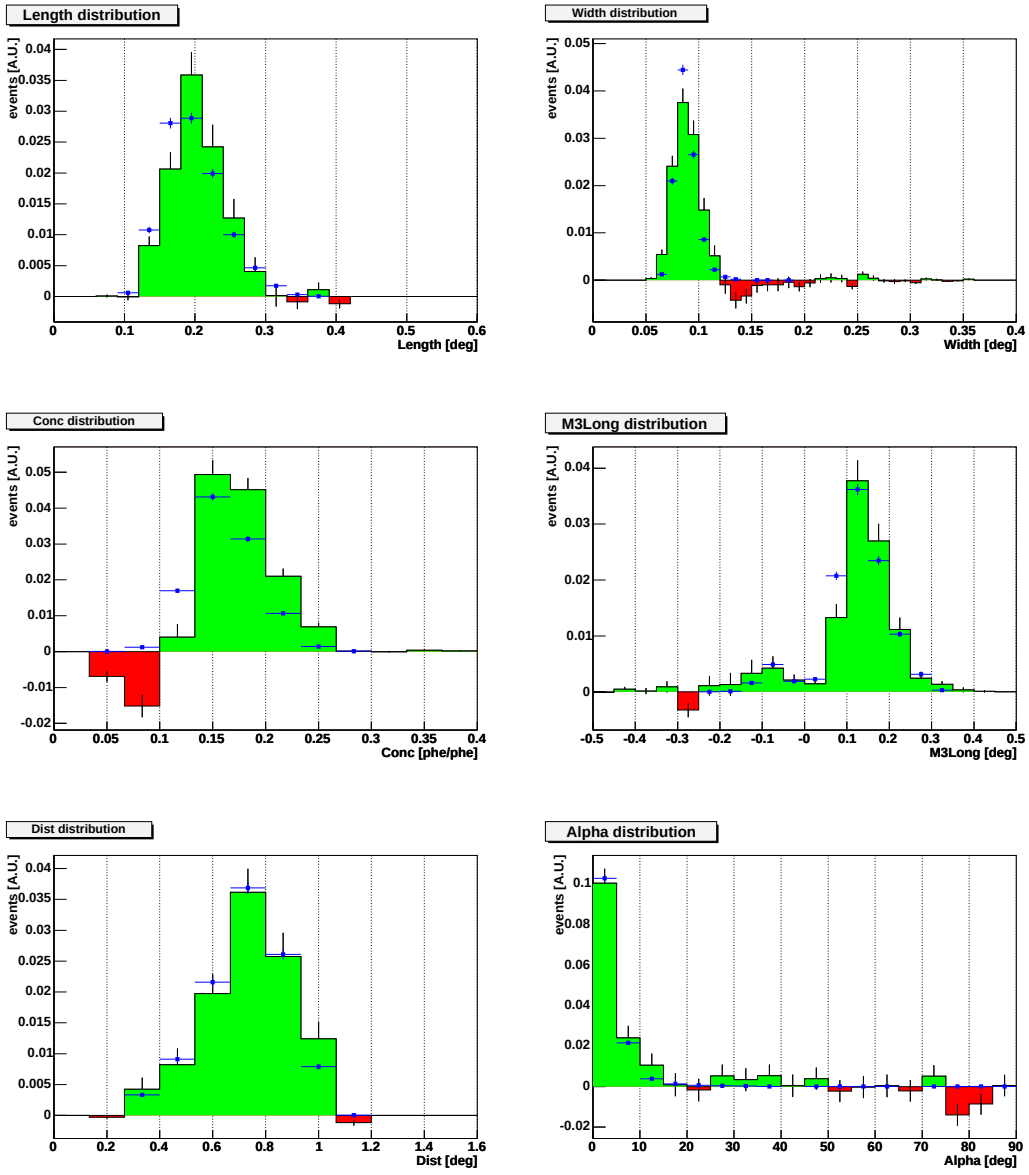

Figure 4.18: Comparison for the basic image parameter distributions between MC γs and real *On-Off* data. For the excess distributions Mkn421 during 25th of April has been used. MC γs with PSF 20mm are used for comparison. The blue dots represent the MC γs while the solid histograms show the *On-Off* subtraction for real data.

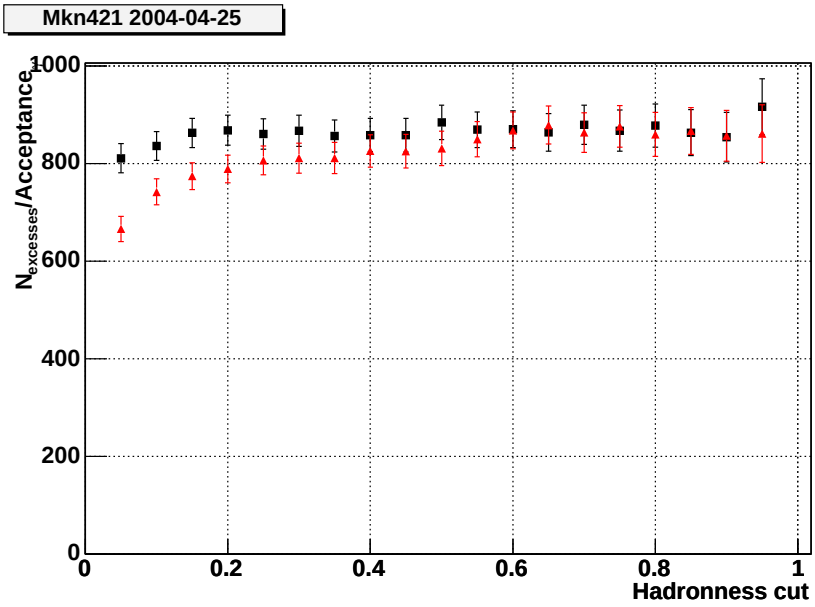

Figure 4.19: $N_{excesses}/\epsilon$ for Mkn421 during 25th of April as a function of the *Hadronness* cut for *Random Forest* with and without *conc* image parameter. The *RF* without *conc* parameter included is represented by (black)squares whereas the one with is drawn as (red)up-triangles. Both *RF* has been trained using the same *Off* sample and the MC γs with 20mm PSF value.

should be observable in this comparison.

To finish the present chapter, the global *alpha* plots for Crab Nebula and Mkn421 samples are shown in figure 4.20. The *size* cut applied in these plots ($size > 200phe$) is close to the lower limit where the analysis is still sensitive. Therefore it has been tried to maximize the $N_{excesses}$ at the expense of the significance of the signal. This has been done because the aim of showing the strength of the Mkn421 emission compared to the steady emission of Crab Nebula during the spring of 2004. To summarize from this chapter the most important results, together with the main observational conditions, for each of the data samples are shown in table 4.3.

SOURCE	ZENITH	OBS. TIME	N_{excess}	N_σ
Crab	30° *to* 50°	110 min	694 ± 80	8
Mkn421-I	8° *to* 23°	196 min	1601 ± 133	12
Mkn421-II	8° *to* 44°	728 min	11322 ± 244	43

Table 4.3: Summary of the results for the analysed data samples. The first three columns show the data sample name, the zenith range and the observational time for that samples, whereas the last two show the number of excesses and number of sigmas obtained for each sample.

Taking into account the observation times of both sources it can be concluded from the number of excesses obtained for each source that Mkn421 had, during this period, an

emission few times the Crab Nebula flux. The proper flux calculation for both sources will be shown in next chapter.

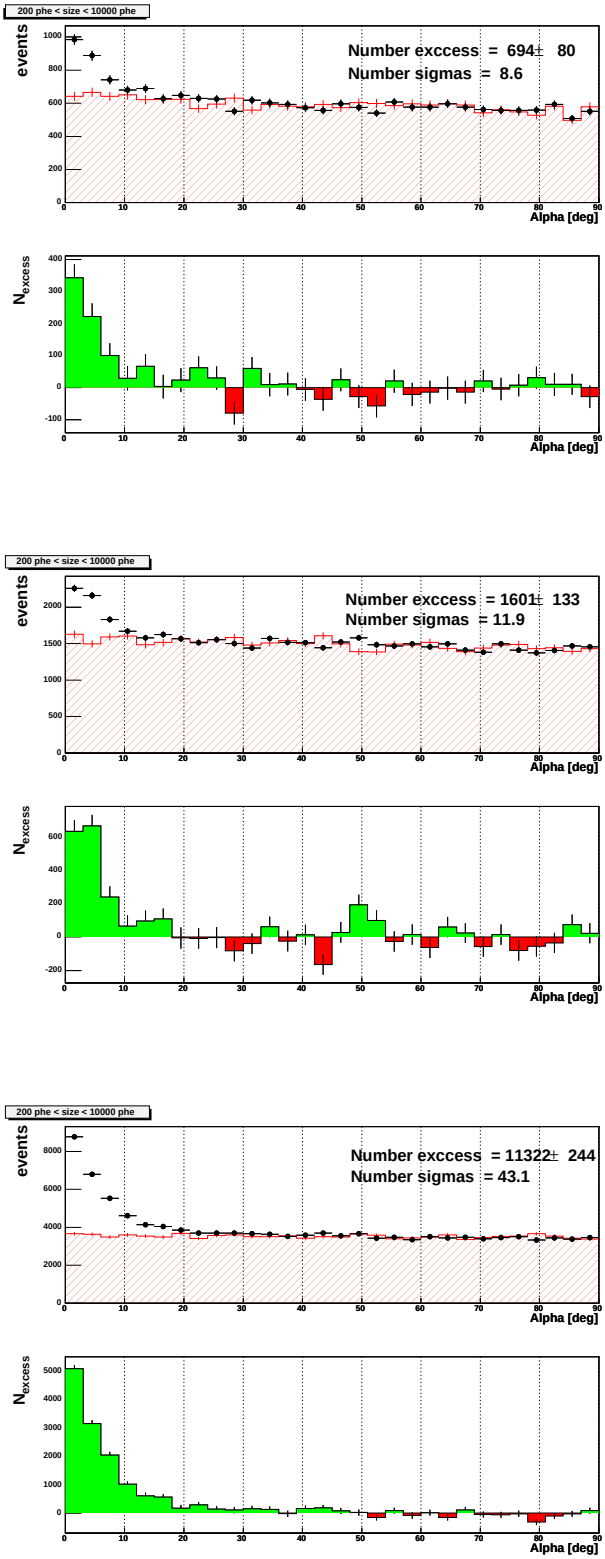

Figure 4.20: *Alpha* plots for Crab Nebula and Mkn421 global samples with *size* cut above 200*phe*. The upper figure shows the Crab Nebula results whereas the medium and bottom ones show the Mkn421-I and Mkn421-II respectively.

Chapter 5

Mkn421 Spectrum and Light Curve

The physical magnitudes that can be measured for γ-rays are direction, energy and arrival time [1]. In point-like sources, like the ones analysed here, the direction is fixed and known, leading the last two quantities as the only relevant information. The energy *spectrum* (or *differential flux*) and the *light curve* of a source contain information about the γ-ray distribution in terms of energy and time, respectively. In the following, the different steps performed for the calculation of the energy *spectrum* and time *light curve* are described. Along the chapter, the results of the Markarian 421 (Mkn421) during the spring of 2004 flare are also presented. This is not only to illustrate with real data the different steps being done in the analysis, but also will serve as the input for the calculation of the speed of light invariance that will be the presented in the following chapter.

In order to guarantee that the quality of the data being used was good enough for the mentioned calculations, an energy spectrum analysis has been done, in addition to the light curve analysis necessary for the subsequent parts of this Thesis. The energy spectrum analysis is also relevant in the framework of the MAGIC collaboration due to the fact that this is the first data taken with the telescope. Subsequent measurements of the Mkn421 source have been recently published in [54]. In this work, coherence between results obtained in the analysis presented and already known results for the Mkn421 source have also been used as an indicator of the goodness of the analysis done.

5.1 Energy spectrum

The *differential flux* is defined as the number of γs per unit energy, time and area coming from a given source and arriving to the Earth, and is given by the formula 5.1.

$$\frac{dFlux_\gamma}{dE} = \frac{dN_\gamma}{dt \cdot dA \cdot dE} \tag{5.1}$$

It can be understood as the probability density function of the number of γs in terms of energy. From the practical point of view, like in any other probability density measurement, it is computed in energy bins. This measurement needs information from both

[1] Actually, also the polarization of the γ could be measured. However in the IACTs this measurement is nowadays not possible due to the indirect detection of the γ-rays.

real and MC data. From the real data, the rate of excesses (i.e. γ-candidates) is obtained, while the *effective collection area* of the detector is computed using the Monte Carlo. Moreover some so-called *spill-over* (or *unfolding*) coefficients have to be computed using the MC, in order to correct the migration of events between energy bins due to the non-zero energy reconstruction resolution and the non-symmetrical energy distribution. In all these calculations it has to be taken into consideration the zenith angle dependence of these quantities, thus performing the calculation separately in zenith angle bins.

The calculation of the energy spectrum is described by the formula 5.2.

$$\frac{dFlux_{\gamma}(E^i)}{dE} = \left\langle \frac{\Delta N^i_{Excess}(E^i,\theta^j)\cdot U^i(E^i,\theta^j)}{\Delta E^i \cdot T_{eff}(\theta^j)\cdot A_{eff}(E^i,\theta^j)} \right\rangle_{\theta^i} \tag{5.2}$$

All quantities, including the differential flux, are calculated for each energy (E^i), ZA (θ^j) or both kind of bins (E^i,θ^j) according to the dependences of each quantity. Each of the differential flux calculations for the different zenith angle bins is an equivalent and independent measurement, due to the fact that the source flux does not depend on the ZA of the observation. Then the final differential flux is the combination of the measurements for the different zenith angle bins.

5.1.1 Energy estimation

On the contrary to the arrival time, the energy of a detected γ-ray is not directly measured by IACTs. However, this energy is an essential parameter for the EAS development, hence for the image characteristics (see section 2.1). The energy can be estimated using the shower image parameters presented in the previous chapter. In this analysis the energy reconstruction has been done using a parameterization, details of which will be shown along this section.

5.1.1.1 Image Parameters used in the parameterization

As it has been previously pointed out, IACTs use the atmosphere as a calorimeter for the detection of γ-rays. Therefore, the *size* of the image is the parameter with more information about the primary energy because it denotes the observed light yield produced by EAS.

A part from *size*, there are two more image parameters used to make second order corrections, especially for high energy showers. The first relevant parameter is *dist*. This parameter keeps information about the impact parameter of the primary γ-ray. This knowledge is important because the impact parameter gives information about the position where the telescope lies in the pool of Cherenkov light for a particular primary. The light collection (i.e. *size*) for a given γ-ray depends on this position and it is especially important beyond the so-called hump, which is the border of the light pool where the light density decreases very rapidly. Moreover, the finite dimension of the MAGIC camera plays an important role for high energy showers due to the fact these images are not completely contained in the camera. The *leakage* parameters have been taken into account in order to do a correct estimation for γ-ray with large energy.

Finally, it has been necessary to take into consideration the geometrical effect in the shape of the shower images due to the observation at different zenith angles. The light pool for a shower is the density of Cherenkov photons in the ground produced by the EAS. For the same EAS the characteristics of the light pool depends on the ZA for pure

geometrical reasons. As it has been said before, the *size* is nothing else than the part of the light pool collected by the reflector and focused into the camera. For this reason a correction based on the $\cos(\theta)$ is used in the estimation.

Even though other parameters are very convenient for the selection of the γ-candidates, they add very little information to the parameters list already mentioned, so they have not been introduced in the energy parameterization presented here.

In the formula 5.3 it can be seen the parameterization used for the energy estimation.

$$E_{Reco} = (p_0 + p_1 \cdot \sqrt{size} + p_2 \cdot size + p_3 \cdot size^2 + p_4 \cdot dist + p_5 \cdot leakage + p_6 \cdot leakage^2) \cdot \left(\frac{1}{\cos(\theta)}\right)^2 \tag{5.3}$$

It is necessary to remark that a constant p_0 has been added to the parameterization in order to allow a possible offset in the estimation.

5.1.1.2 Parameterization optimization

Once it has been decided the *Ansatz* for the energy estimation, it is necessary to determine the method going to be used for the optimization of the parameters $\{p_i\}$. In the current analysis the simple *Least Square Method* was used. This method consists on the minimization, for a given train sample, of the sum of the squared difference between the estimated and the real energy. Obviously the MC γs was used as the train sample in this process. The problem simplifies considerably in the case of a linear parameterization like the one used here. In that case the method essentially reduces to a system of linear equations which can be solved analytically, as it will be shown in the following paragraphs.

The *Ansatz* used in the estimation can be expressed as $E_{Reco} = p_i \cdot Hillas^i$ where $Hillas^i$ is the set of Hillas parameters used in the parameterization [2]. Crossed up-down indexes represent in the present calculation the sum over all the values for the given index. Using this formulation, the sum over all the events of the squares of $E_{Reco} - E$ for all the events can be written down as follows.

$$S = \sum_k ((p_i \cdot Hillas^i)_k - E_k)^2 \tag{5.4}$$

The finding of the values for the parameters $\{p_i\}$ which minimize the expression 5.4 is just a mathematical problem which is solved as it is shown in next expression.

$$\frac{\partial S}{\partial p_j} = 2 \cdot ((p_i \cdot Hillas^i)_k - E_k) \cdot (Hillas_j)^k = 0 \tag{5.5}$$

By definition, this system of linear equations has the same number of unknowns than equations, so it can be solved using a Gaussian elimination algorithm. From the practical point of view, the problem is easier to be solved if the linear equations are expressed in terms of matrices and vectors. The solutions are shown in equation 5.6.

$$p_j = \left[(Hillas^T)^l_k Hillas^k_j\right]^{-1} \cdot (Hillas^T)^l_k \cdot E^k \tag{5.6}$$

In the method presented, the energy distribution of the train sample plays an essential role on the determination of $\{p_i\}$. The method minimizes the whole sample giving the

[2] Actually, in the real calculation $Hillas^i$ are the set of Hillas parameters over the $\cos(\theta)^2$ correction.

same weight to each of the events. In this sense, in optimizations where the train sample have steep energy distributions, the parameterization will be more tuned for low energies which are the most probable energies. In order to have some control about the importance of the different energy ranges in the optimization process it is possible to introduce energy dependent weights for each event in the minimization, leading to the following solution for $\{p_i\}$.

$$p_j = \left[(Hillas^T)^l_k Hillas^k_j\right]^{-1} \cdot (Hillas^T)^l_k \cdot E^k \cdot (E^k)^{weight} \tag{5.7}$$

The equation 5.7 is then a more general solution which actually includes the particular solution presented in equation 5.6 (i.e. $weight = 0$).

5.1.1.3 Energy reconstruction resolution and bias

The *Least Square Method* optimizes both the resolution and the bias of the energy reconstruction. Since resolution and bias are equal to the standard deviation and the mean of $(E_{Reco} - E_{True})/E_{True}$ respectively (E_{True} refers to the real energy of the MC event), it can be inferred that the magnitude minimized in the optimization is proportional to the addition in quadrate of both quantities (i.e. $\sum(E_{Reco} - E_{True})^2 \propto (\sigma^2_{(E_{Reco}-E_{True})} + \mu^2_{(E_{Reco}-E_{True})})$). This property of the optimization method is very convenient because not just a small resolution should be requested to the energy reconstruction but also a linear behaviour which is measured by the bias.

Both magnitudes, bias and resolution, have been estimated for the presented parameterization. They have been defined as the mean and the sigma of the distribution of the variable $(E_{True} - E_{Reco})/E_{True}$. A Gaussian fit has been used to calculate those quantities excluding from the fit possible tails. These calculations have been performed in several energy bins in order to have the resolution and the bias as a function of the energy.

Before deciding the final parameterization the effect of introducing weights depending on the energy has been explored. In figure 5.1 the comparison of the bias, resolution and the variance (defined as the squared sum of both magnitudes) are shown for different values of the energy dependent weights. From this comparison it can be observed that a weight equal to $E^{0.6}$ shows the best behaviour for the bias. Nevertheless, the introduction of these weights produces a slightly worse resolution for lower energies. Looking at the variance, the conclusion is that the net effect for this weight value is an improvement for very large energies (above 3 TeV) and slightly degradation for energies below 500 GeV, in addition with a more linear behaviour for most part of the studied energy range. The previous presented results have been produced with the MC simulation with 20mm PSF. However, an analogous study has been performed for the 25mm PSF Monte Carlo with similar results with the only difference of a worse energy resolution in few percentages.

The parameters $\{p_i\}$ have been computed using an energy dependent weight of $E^{0.6}$. The final values for the different parameters are shown in table 5.1 while the results obtained for the resolution and bias are presented in figure 5.2. These results show a bias smaller than 10% and a resolution of the order of 25% for energies from $400GeV$ to $4TeV$.

The bias of the energy reconstruction shows divergences from linearity at both edges, low and high energies, for any set of parameters $\{p_i\}$ used. These two non-linearities can be explained by two different effects. The behaviour at high energies is due to the fact that the corrections introduced in the parameterization through *dist* and *leakage* are not enough to compensate the partially contained high energy showers on the camera. The low energy lost of linearity is due to the effect of the energy threshold. The *size*

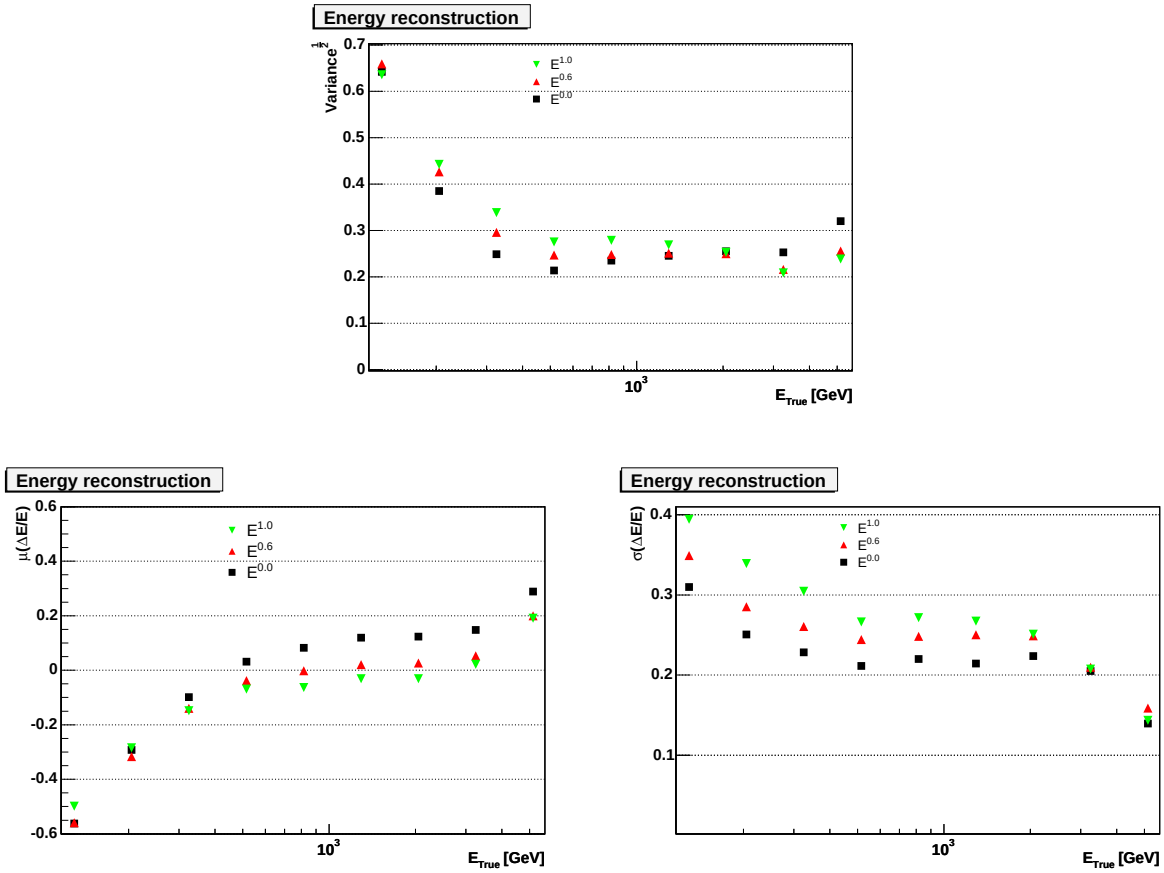

Figure 5.1: Energy reconstruction bias and resolution for several energy dependent weights. The upper figure shows the square root of the variance defined as $bias^2 + resolution^2$. The bottom-left and bottom-right figures represent bias and resolution respectively. Three different values of energy dependent weights are presented, $E^{0.0}$ (black)squares, $E^{0.6}$ (red)up-triangles and $E^{1.0}$ (green)down-triangles. All these results have been produced using the MC simulation with 20mm PSF.

distribution for shower images with energies close to the energy threshold is biased due to the fact that shower images with an increase in the number of Cherenkov photons by statistical reasons trigger (or get selected by the analysis) more than statistical *size* decreased showers. In that scenario the deviations for the *size* cannot be compensated by the parameterization and, as result, the observed bias becomes negative.

5.1.2 Excess rate distribution

To calculate the excess event rate distribution versus energy is the first step for the *spectrum* calculation. From the previous chapter it can be obtained the number of excesses for each energy and zenith angle bin. However, it is necessary to compute the effective observation time to compute the excess rate distribution.

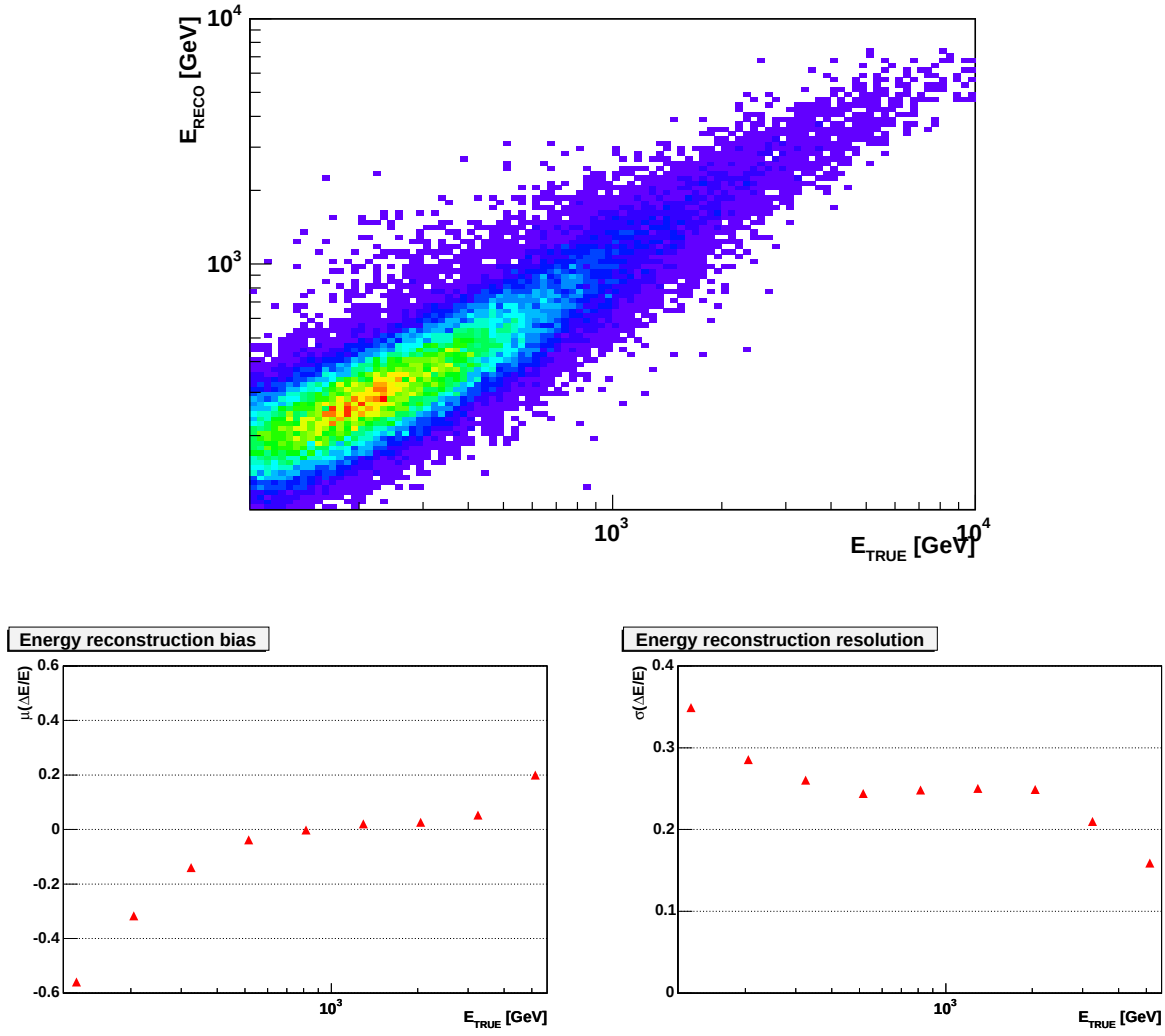

Figure 5.2: Energy reconstruction resolution and bias for $E^{0.6}$ weight. The upper figure shows the dependence between E_{True} and E_{Reco} whereas the bottom-left and bottom-right figures are the bias and the resolution, respectively. These results have been produced with the MC sample with 20mm PSF.

p_0	-48.3	GeV
p_1	4.02	$GeV \cdot phes^{-\frac{1}{2}}$
p_2	0.323	$GeV \cdot phes^{-1}$
p_3	$-8.04 \cdot 10^{-6}$	$GeV \cdot phes^{-2}$
p_4	0.486	$GeV \cdot deg^{-1}$
p_5	-45.8	GeV
p_6	$3.43 \cdot 10^4$	GeV

p_0	-12.1	GeV
p_1	4.41	$GeV \cdot phes^{-\frac{1}{2}}$
p_2	0.340	$GeV \cdot phes^{-1}$
p_3	$-8.51 \cdot 10^{-6}$	$GeV \cdot phes^{-2}$
p_4	0.272	$GeV \cdot deg^{-1}$
p_5	-680	GeV
p_6	$4.75 \cdot 10^4$	GeV

Table 5.1: Energy estimation parameters. The two sets of parameters for Monte Carlo with 20mm (left table) and 25mm (right table) PSF values are shown.

5.1.2.1 Effective observation time

Any real detector has a certain time after the detection of an event, called dead time, while it is not able to record any new events. Several causes may produce this dead time but in the case of MAGIC it is due to the need of the system to fully record the detected event.

For a correct calculation of any flux (i.e. rate), the effect of these lost events during the dead time has to be corrected. In IACTs it is performed using the concept of *effective observation time* (T_{eff}). This effective time compensates the reduction in the measured rate produced by the dead time. Therefore, by definition of T_{eff}, the rate computed using this time and the actual detected number of events ($N_{actual\_detected}$) has to be the same than the original rate it would be detected in case the detector had no dead time.

$$Rate = \frac{N_{actual\_detected}}{T_{eff}} \tag{5.8}$$

Looking the other way around equation 5.8, it can be shown one of the possible definitions for the effective observation time (see equation 5.9).

$$T_{eff} \equiv \frac{N_{actual\_detected}}{Rate} \tag{5.9}$$

If we are calculating the rate of excess events, the previous equation by itself could seem useless because it uses for the calculation of an unknown quantity (T_{eff}) the actual magnitude to be measured ($Rate$). However, the effective time for the excess rate calculation can be performed using the cosmic rate. The T_{eff} computed using this rate should be the same for hadrons or γs because they are simultaneous. Moreover, using the comic rate increases the available statistics, then reducing the error in the effective time error measurement.

The only ingredient left for the T_{eff} calculation is the measurement of the actual cosmic rate. A particularity of the time distribution for cosmic rays can be used for the measurement of this rate, which is that the number of cosmic rays (i.e. γ-rays) arriving for a given time window follows a Poisson distribution. This means that, by definition, the elapse of time between two consecutive cosmic rays follows an exponential distribution with slope equal to the actual cosmic rate (i.e. $Prob(\Delta t) \propto \exp^{-Rate \cdot \Delta t}$). For real detectors the distribution for Δt keeps the exponential shape for values bigger

than the dead time, although the distribution is truncated for values of the order of the dead time. Then the actual rate can be measured fitting the real distribution of Δt just taking care of selecting the fitting region far enough from the beginning (i.e. dead time region) of the distribution. Therefore, once the actual cosmic rate is known, the effective observation time can be computed as it is shown in the equation 5.9.

5.1.2.2 Energy and Zenith angle binning

As it has been pointed out at the beginning of the chapter the differential flux distribution, hence all the different parts of the flux calculation included the rate distribution, is measured in energy and Zenith angle bins. The selection of the number and the width of such bins is a compromise between the need of enough bins for the correct description of the dependencies with energy and ZA in the flux calculation and the demand of wide bins to keep enough statistics in each of them.

The energy bins have been chosen to have the same size in logarithm scale. This is completely necessary in order to keep enough statistics for medium-large energy bins and keep statistical errors reasonably small. The small number of events for large energies is due to the rapid decrease of flux with energy (e.g. following a power-law) for most of the observed sources in the IACTs energy range. In addition to the first requirement, the energy bins have been chosen at least to be bigger than the energy resolution for that particular bin. This tries to reduce the effects of the migration of events between energy bins, an effect which is going to be explained in some detail in the following paragraph.

The zenith angle bins have been chosen with equal size in the cosine of ZA. This decision is based on the fact that most of the dependencies in the analysis with the ZA are geometrical effects due to the projection of the Cherenkov light pool on the ground, thus depending on $\cos(\theta)$. The size of these bins has been chosen to be of the order of 0.1 in $\cos(\theta)$. However, ZA bins have not been possible to be fixed at exactly this value for all data samples because the ZA ranges for each of them are different and obviously not always multiple of 0.1.

The rate for the Mkn421-II sample is shown in figure 5.3. A couple of ideas should be stressed from the previous figure. The first one is that the energy threshold, defined as the energy where the differential rate is maximum, grows with the Zenith angle. The threshold obtained from this figure is the analysis energy threshold which is analogous to the trigger energy threshold but for the γs that can be separated from the background. In table 5.2, the analysis energy thresholds for the lower ZA bins of each of the data sample are written down.

SOURCE	ZENITH	ENERGY THRESHOLD
Crab	30° *to* 42°	360 GeV
Mkn421-I	8° *to* 23°	180 GeV
Mkn421-II	8° *to* 26°	200 GeV

Table 5.2: Analysis energy thresholds for the different data samples. These values correspond to energy threshold for the lowest zenith bin used in this analysis of each data sample.

Moreover, the rate for energies well above the threshold also grows for larger ZA.

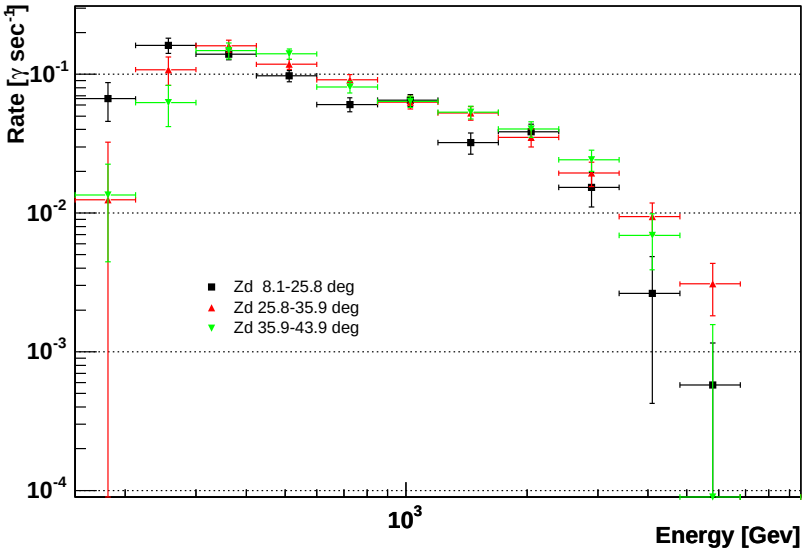

Figure 5.3: *Rate* calculated for Mkn421 during the 23th of April 2004. Three different Zenith angles bins are drawn as different set of points (see legend for the Zenith angle ranges for each bin). Each of the drawn points represents the mean value for the rate computed within the given zenith and energy bin. The horizontal lines for the drawn points represent the width of the energy bin.

These two behaviours are expected and were introduced and explained in the description of the IACTs detection technique (see section 2.1).

5.1.3 Monte Carlo derived information

Once the differential rate of excess events is computed from the data, some extra ingredients are left to compute the *spectrum* as it has been shown in equation 5.2. All the remaining parts of the calculation are computed using the Monte Carlo data because these magnitudes contain information about the sensitivity of the telescope and behaviour of the analysis rather than information about the observed source.

5.1.3.1 Spill-over correction factors

As a consequence of the non perfect energy reconstruction, the excess rate distribution in terms of the energy is the convolution of the real event rate with the energy estimation resolution and bias. This effect always happens when a certain probability distribution is calculated in terms of a magnitude with a certain reconstruction (or measurement) resolution. In the case presented in this Thesis, this effect is not a minor one due to the fact that in the measurement of very steep distributions like the energy spectrum, the migration of events from low energy to large energy bins could be quite large. The *spill-over* coefficient tries to correct this effect using the Monte Carlo simulation. The idea behind this correction is to allow knowing which fraction of the events measured within a reconstructed energy bin has actually the real energy within this bin.

The spill-over correction coefficient for a given energy bin is the fraction between the number of events with E_{True} within this bin over the number of events with reconstructed energy within the same energy bin (see equation 5.10). Both numbers of events are computed from the MC events that survive the same selection process applied to the real data.

$$U(E^i, \theta^j) = \frac{N^{selected}_{E_{true}}(E^i, \theta^j)}{N^{selected}_{E_{Reco}}(E^i, \theta^j)} \tag{5.10}$$

5.1.3.2 Effective collection areas

The effective collection area connects the differential excess rate with the differential flux as it can be seen in equation 5.11.

$$\frac{dFlux_\gamma}{dE} = \frac{\frac{dRate_\gamma}{dE}}{A_{eff}} \tag{5.11}$$

As it has been pointed out in different occasions before, IACTs detect cosmic rays indirectly using the atmosphere as part of the detector. The telescope is sensitive to detect γ-rays in a volume of the atmosphere along the observation direction of the telescope. The effective collection area can be seen as the projection area around the telescope observation axis where it is sensitive for detecting γ-rays. From the mathematical point of view the A_{eff} is the 'area integral' of the probability for the telescope to detect γ-rays for a given impact parameter, energy and zenith angle observation (see equation 5.12).

$$A_{eff}(E, \theta) = \int_o^\infty Prob(E, r, \theta) \cdot 2\pi r dr \tag{5.12}$$

Calculating this probability is a very complex problem, due to the fact that different factors such as γ-ray EAS development, the detector sensitivity and performance, etc. have to be taken into consideration. For this reason, Monte Carlo simulated data has been used to solve it. From the practical point of view this probability is computed, in energy and ZA bins, as the fraction of the number of events which triggers in the MC simulation over the number of simulated events. Once the probability is known, the integral in equation 5.12 can be solved leading to the expression used to calculate the effective collection area (see equation 5.13).

$$A^{trigger}_{eff}(E^i, \theta^j) = \frac{N^{trigger}(E^i, \theta^j)}{N^{simulated}(E^i, \theta^j)} \cdot \pi \cdot (r^2_{up} - r^2_{low}) \tag{5.13}$$

In this formula r_{up} and r_{low} are the maximum and minimum impact parameter simulated in the Monte Carlo sample used for the calculation.

Selection efficiency

The effective collection area described in previous paragraphs is the trigger collection area. This area gives information about the sensitivity of the telescope to trigger the events. Nevertheless, the excess rate used for the calculation of the differential flux is computed after a γ-candidates selection. Then the effective collection area must be corrected by the inefficiency of the γ selection process.

The selection efficiency is nothing else than the percentage of events selected from the samples of events that have triggered the system.

$$\epsilon^{\gamma}(E^i, \theta^j) = \frac{N^{selected}(E^i, \theta^j)}{N^{trigger}(E^i, \theta^j)} \tag{5.14}$$

Then, to calculate the differential flux the effective collection area used is the multiplication of both quantities as it is shown in equation 5.15.

$$A_{eff}(E^i, \theta^j) = A_{eff}^{trigger}(E^i, \theta^j) \cdot \epsilon^{\gamma}(E^i, \theta^j) \tag{5.15}$$

In figure 5.4 it is shown the different Monte Carlo derived magnitudes used for the calculation of the *differential flux* of the Mkn421 data sample. From these figures it can be observed that the typical trigger effective area is of the order of hundred of thousands square meters in the plateau, hence for central energies in the *spectrum* energy range. It is also remarkable that the efficiency of the analysis is rather large. It is of the order of 50% in this central part of the *spectrum*. As it was pointed out before in this Thesis, large selection efficiencies reduce the systematic errors due to disagreements between data and Monte Carlo. Obviously, selection efficiency falls for low and high energies. For low energies, this happens due to the filter static cuts explained in previous chapter (i.e. *size*, *dist*, *alpha*, etc). Whereas for high energies, the reduction of the efficiency is due to the problems of leakage in the camera for high energy showers.

The differential flux calculation presented in previous paragraphs is actually the measurement of the mean value for each of the selected energy bins.

$$\frac{dFlux_{\gamma}^{i}(E)}{dE} = \frac{1}{\Delta E} \cdot \int_{E^i}^{E^{i+1}} \frac{dFlux_{\gamma}}{dE} \cdot dE \tag{5.16}$$

Before going on with the presentation of the *differential flux* results, it is going to be explained how the flux mean measured in each energy bin has been represented in the final *differential flux* plot.

5.1.3.3 Where to stick the data points

The usage of histograms for the calculation of probability density functions (e.g. energy spectrum) always leads to the measurement of the mean value for each histogram bin. Nevertheless, it is a common practice to present this measurement as the *p.d.f* for a particular point (i.e. E^i) within the bin. The most used point in the literature to represent this measurement is the mean value within the bin for the given probability density (see equation 5.17). This point is also called barycentre.

$$E^i = \overline{E^i} = \frac{1}{\Delta E} \cdot \int_{E^i}^{E^{i+1}} E \cdot \frac{dFlux_{\gamma}}{dE} \cdot dE \tag{5.17}$$

The previous expression cannot be computed using the actual *differential flux* because this magnitude is in fact being measured in this process. Nevertheless, from the practical point of view the baricenter can be computed just averaging the energy for all the events which lay in the given energy bin.

In reference [55] is presented a discussion about the correctness of using this particular point. The conclusion is that it is correct in the case the probability density can be expressed using polynomials. This requirement is just maintained in measurements either

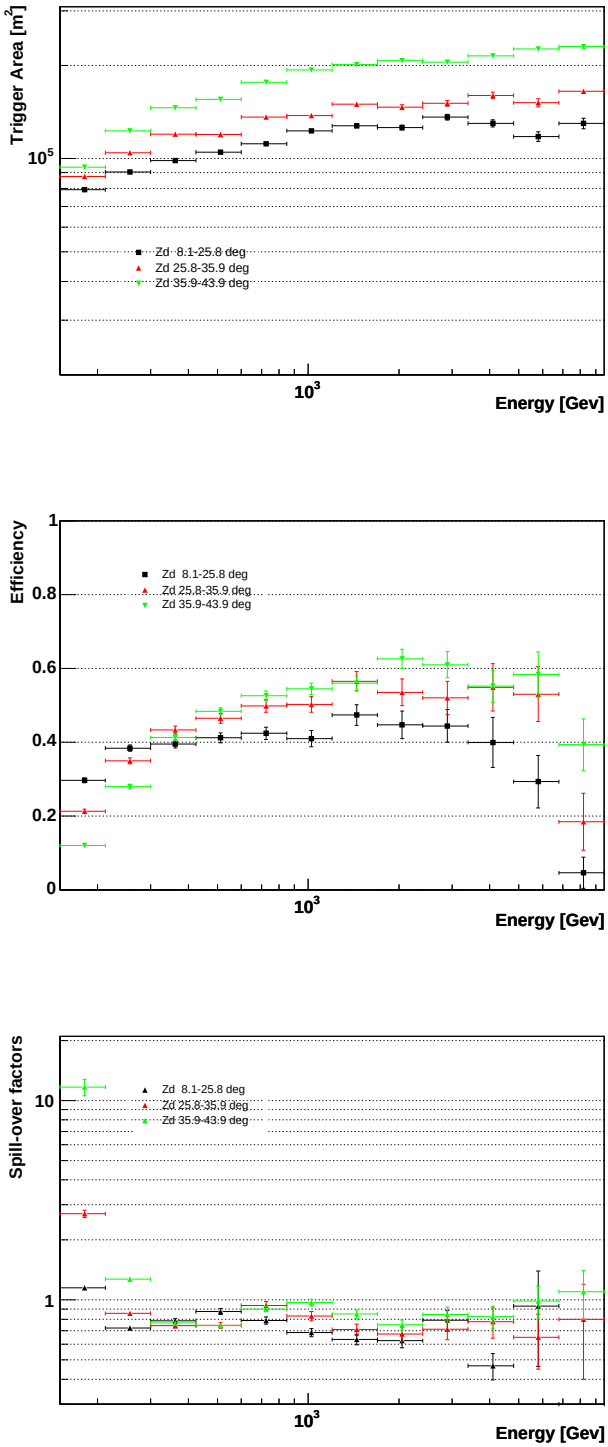

Figure 5.4: Monte Carlo derived magnitudes for the *differential flux* calculation using MC with 20mm PSF. These magnitudes are used for calculation of the *flux* for Mkn421-II data sample. The effective trigger area (up figure), the selection cuts efficiency (middle figure) and the spill-over correction factors (bottom figure). The horizontal lines for the drawn points represent the width of the energy bin.

with polynomial probability densities or those which use small bins where any probability density can be linearly approximated using Taylor series. As a consequence of the rapid variation in terms of energy of the spectrum, its measurement is performed in logarithmic energy bins in order to keep enough statistics for last bins. The scenario of logarithmic bins was studied in the referred paper, concluding that the difference between the p.d.f value for the barycentre and the mean p.d.f value in the bin are sizable, especially for the largest bins. In the paper it is shown that this effect already leads in the literature to wrong results when fitting the probability densities using the barycentre as the reference point.

Once arrived to the conclusion that the use of the barycentre for representing the measured spectrum is not correct, in the paper it is proposed to use the actual value of the energy for which the spectrum is equal to the mean value within the bin (see equation 5.18) [3].

$$\frac{dFlux_\gamma(E = E^i_{lw})}{dE} = \frac{1}{\Delta E} \cdot \int_{E^i}^{E^{i+1}} \frac{dFlux_\gamma}{dE} \cdot dE \tag{5.18}$$

Obviously this equation cannot be solved, since the energy spectrum is unknown, being indeed what is wanted to be measured. However, a reasonable ansatz can be assumed making the calculation of E^i_{lw} possible either numerically or analytically. Obviously now the spectrum results depend on this ansatz. However, it is going to be shown in next paragraphs that all the MC derived quantities depend on an energy spectrum ansatz. It will also be explained how it has been dealt with this dependence for the point position calculation together with the other MC quantities.

5.1.3.4 Common remarks for MC derived magnitudes

From the practical point of view, there is a couple of common remarks for all the Monte Carlo derived quantities computed in this analysis which are listed below.

1. In the calculation of these quantities the MC subsample *Test* is used for all of them. This Monte Carlo subsample has not being used in any of the optimizations processes necessary for the analysis (e.g. *Random Forest*, energy reconstruction, etc.). The use of this independent subsample is necessary to guarantee that the obtained MC results are not biased by the utilization of events used in optimization processes.

2. The values obtained in these calculations depend on the energy spectrum of the used MC sample [4]. Actually, for the correct use of all these quantities the spectrum of this MC sample has to be the same of the data. Since the spectrum of the data is what it is being measured, all these MC derived quantities are computed recursively. The algorithm to measure the spectrum is then as follows. First, the rate of excess events is computed and is kept without change during the subsequent steps. The different MC dependent quantities are computed with the original spectrum of the MC. Then, the resulting spectrum is fitted using a χ^2 approach with an ansatz function using the set of pair of points formed by $(\frac{dFlux_\gamma(E^i)}{dE}, E^i_{lw})$. Once the results of the fit are known, this information is used to recalculate the MC based

[3] In the paper the proposed point is referred as x_{lw} in relation with the fact of using *large width* bins.
[4] A power law with a spectral index of 2.6 (see section 4.3.1)

quantities again and recalculate the spectrum. This procedure continues until the difference between the values obtained for the fit for two consecutive iterations are less than one tenth the statistical errors of the fit.

Systematic errors

In the measurement of the *differential flux* there could be sources of systematic uncertainties which affect the reconstruction of the energy and the calculation of the flux level for a given energy. Although it is difficult to know all the systematic uncertainties that can affect the final results, at least with the present understanding of the telescope, one can nevertheless make in most cases reasonable guesses to get a coarse estimate:

- **Atmospheric transmission**: Atmospheric conditions are still not directly monitored during data taking. There exists a project within the collaboration to monitor the atmosphere conditions during data taking using a LIDAR, however this project is still in development. At present, the monitoring done by the optical telescopes in *El Roque de los Muchachos* is used for the selection of good conditions nights (see section 4.2.1), however the variations in the monitoring results among these good nights are not simulated in the MC. In the MC simulations, a standard atmospheric model is used, that can slightly differ from the real observation conditions producing an uncertainty in the estimation of the real flux. This estimated uncertainty can be as high as 15%.

- **Calibration in absolute scale**: The calibration system can introduce systematic errors that are still completely not understood at the moment. Among other effects, the light outcome from the calibration system can vary due to temperature drifts. In addition, the F-factor method may as well introduce a systematic error due to the poor knowledge of the PMTs signal-to-noise ratio. Moreover, the QE might differ between individual pixels about 5%. A conservative uncertainty in the charge-to-phe conversion factors is estimated to be about 10% [30].

- **Causes of Cherenkov photon losses**: The mirrors reflectivity is on average 85% in our MC data. This number agrees quite well with the lab measurements. However, the photon losses in the whole optical system of MAGIC were evaluated with a dedicated study of the muon rings images [56]. As a result, the overall global factor between expected number of photons from MC and the one observed for the data was used to tune the MC simulations. Nevertheless, this muon study was done in a slightly different period than the one used in the analysis presented in this Thesis. An uncertainty of the whole Cherenkov photons collection is possible because of a different level of dirt, dust, small degradation of the mirrors, etc, than in the muon analysis. All these effects might result in light loses not bigger than 5%.

- **Camera (trigger) inefficiency**: We have seen that the distribution of events in the camera is not completely homogeneous. The trigger inefficiency compared due to the inhomogeneities of the camera response is estimated comparing to the Monte Carlo to be around 10%

- γ **selection efficiencies**: The selection and the efficiencies calculated using the Monte Carlo for the γ selection can be as well a source of systematic uncertainty.

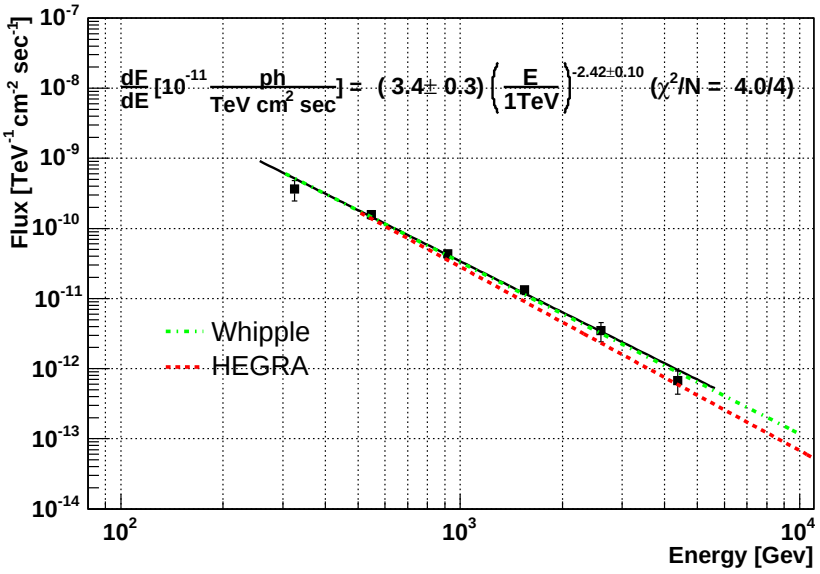

Figure 5.5: *Differential flux* measurement for Crab Nebula during March 2004. The solid line represents the best fit of the data points assuming a power-law. The vertical error bars represent the statistical errors for each energy bin. The fit results written down in the figure just show the statistical errors of the fit. In the figure there are drawn the spectra measured for Crab Nebula by Whipple and HEGRA collaborations [57, 58].

This systematic error has been investigated by changing the *Hadronness* cut in section 4.6 leading a maximum uncertainty in the efficiency of $\delta\epsilon_\gamma$ 20% which can be directly translated to an error in the flux estimation.

The total systematic error for the period of data analysed in this Thesis is roughly estimated to be 30% in the estimation of flux level. The evaluation of the systematic error on the spectral index implies knowledge of the energy dependence of the errors listed above. The systematic uncertainty on the spectrum slope has been estimated to be at least of the order of 0.2 [19]. This is a coarse and conservative estimation of the systematic errors that can affect the data. These are the values that today the MAGIC collaboration quotes on all their results, although, a robust analysis to estimate the systematics is certainly needed. The dominant systematic uncertainties are the atmospheric model used in the MC simulations (15%), the γ selection efficiencies (20%), camera (trigger) inefficiency (10%), and absolute light conversion (calibration) (10%) error.

5.1.4 Spectrum results

Before measuring the Mkn421 spectrum during the spring of 2004 it is necessary to check the correct reconstruction of the Crab Nebula spectrum for a coincident period of time. Crab Nebula is the strongest steady TeV source known. This makes possible to use Crab Nebula as the standard candle for IACTs, hence it is used as a reference source to check compatibilities between telescopes and between periods of time within the same telescope.

The *differential flux* for the data sample of Crab Nebula gathered during March 2004 has been measured following the procedure explained in previous sections. The obtained

	THIS THESIS	WHIPPLE	HEGRA
F_0	$3.4 \pm 0.3_{stat}$	$3.2 \pm 0.17_{stat} \pm 0.6_{syst}$	$2.83 \pm 0.04_{stat} \pm 0.6_{syst}$
α	$2.42 \pm 0.10_{stat}$	$2.48 \pm 0.06_{stat} \pm 0.04_{syst}$	$2.62 \pm 0.02_{stat} \pm 0.05_{syst}$
E_{RANGE}	250 GeV to 6 TeV	500 GeV to 8 TeV	500 GeV to 80 TeV

Table 5.3: Crab Nebula spectrum fit result compared with Whipple and HEGRA measurements. The results shown in the table correspond to a power-law fit with formulation $dF/dE = F_0 \cdot (E/TeV)^{-\alpha} \cdot 10^{-11} \cdot \gamma \cdot TeV^{-1} cm^{-2} sec^{-1}$. The last row shows the energy range used for each of the measurements. The results from the other telescopes have been obtained from references [57, 58].

spectrum is shown in figure 5.5. This result has been fitted assuming a power-law and they are shown in table 5.3 together with previous measurements obtained by Whipple and HEGRA collaborations.

The measurement for Crab Nebula obtained in this Thesis is compatible within one standard deviation with the analysis of Crab Nebula performed by the Whipple collaboration and it is at two standard deviations from the measurement done by the HEGRA collaboration. The plausible reason for the bigger discrepancies with HEGRA results could be the different energy ranges between both measurements. The measurement performed in this Thesis is closer in energy to the IC peak of Crab Nebula, expected close to 100 GeV. In the IC peak the spectrum is expected to become softer than for very large energies like the ones studied in the HEGRA measurement. In this context, the better coincidence with Whipple is consistent because of the closer coincidence in the studied energy ranges.

One final remark is that the Crab Nebula measurement presented here is performed with a minimal data set, which leads to very limited results. Moreover, the analysed Crab Nebula data does not cover the complete ZA range of the analysed Mkn421 data, making impossible an exactly equivalent check of the behaviour of the telescope and the analysis for the Mkn421 conditions. The used data sample for the Crab Nebula analysis was the only one available for the corresponding Mkn421 data period, which was the only Crab Nebula data with similar telescope conditions with Mkn421 data. Even though all these inconveniences, it has been possible to perform a measurement in agreement with previous results from other IAC Telescopes giving an additional confirmation of the right behaviour of the analysis presented in this Thesis.

Mkn421 spectrum

For variable sources like blazars (e.g. Mkn421) the calculation of the spectrum as the average over a long time period is not the best approach. The averaging could hide interesting phenomena like large changes in the flux level or even changes in the shape of the spectrum. Mkn421, in the IACTs energy range, has already shown this kind of phenomena in many occasions in the past (see references [59, 60]). In these studies about Mkn421, a correlation between the level of the *integral flux* and the spectrum shape was observed. In order not to average data subsamples with different spectral shapes, the data sample has been divided according to their flux state. In figure 5.6 the daily mean integral flux for the March and April of 2004 can be observed (see section 5.2.1 for a

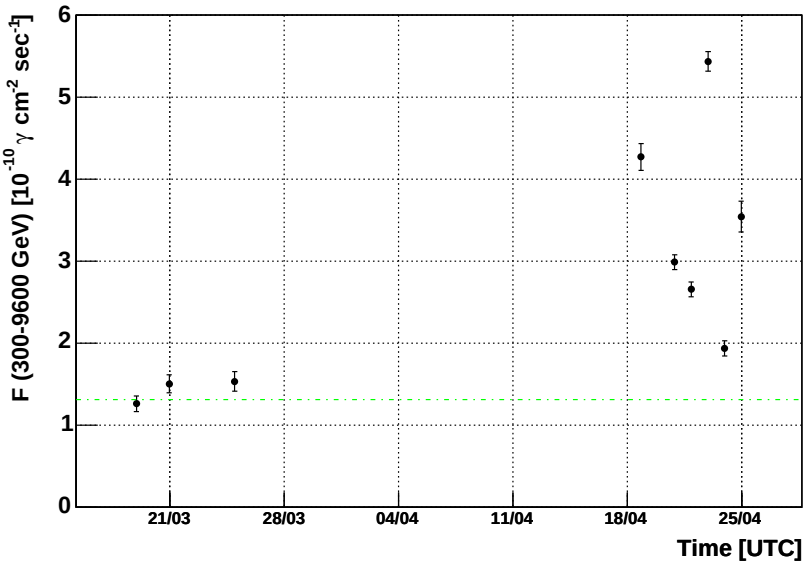

Figure 5.6: Daily average *integral flux* for Mkn421 during the spring of 2004. The (green) dashed line represents the *integral flux* for Crab Nebula integrated in the same energy range. For the Crab Nebula *integral flux* value the measured spectrum from the analysis of this Thesis has been used.

detailed explanation about the integral flux calculation procedure).

Following the results shown in the previous figure, the different nights have been divided into three subsets. Those nights with an average *integral flux* below $2 \cdot 10^{-10}\gamma \cdot TeV^{-1} \cdot cm^{-2}sec^{-1}$ (low state), those above $4 \cdot 10^{-10}$ (high state) and the nights between these two flux levels. The energy spectrum has been computed separately for each of them and the results are shown in figure 5.7. The measured spectra has been fitted assuming a power-law with an exponential cut-off and the results for all activity states are summarized in the table 5.4

From these measurements, a clear change in the spectra shape depending of the activity state of the source is observed. Low state shows softer slope plus lower energy cutoff than high state. This behaviour in Mkn421 has been observed in many occasions by other IAC Telescopes (see references [59, 60]).

In order to study in more detail the variation of the spectral shape for different activity states, daily averaged *differential flux* were calculated. For that purpose, it is necessary to chose a magnitude that quantifies the change in the shape of spectrum and look for a dependence with the mean integral flux. Traditionally several quantities has been used for that purpose, in this Thesis the energy cutoff has been chosen. Due to the high correlation between the slope and the cutoff in the fit, the slope was fixed to the intermediate value $\alpha = 1.85$. This was done in order to see the change in the spectrum shape just though a possible change in the energy cutoff value. The results of the daily average spectrum for the change of the spectral shape are shown in figure 5.8.

From the previous figure a clear correlation between flux activity level and the hardening of the spectrum can be observed. Event though this study has been done using the energy cutoff of the spectrum, it is not possible to assure that the observed correla-

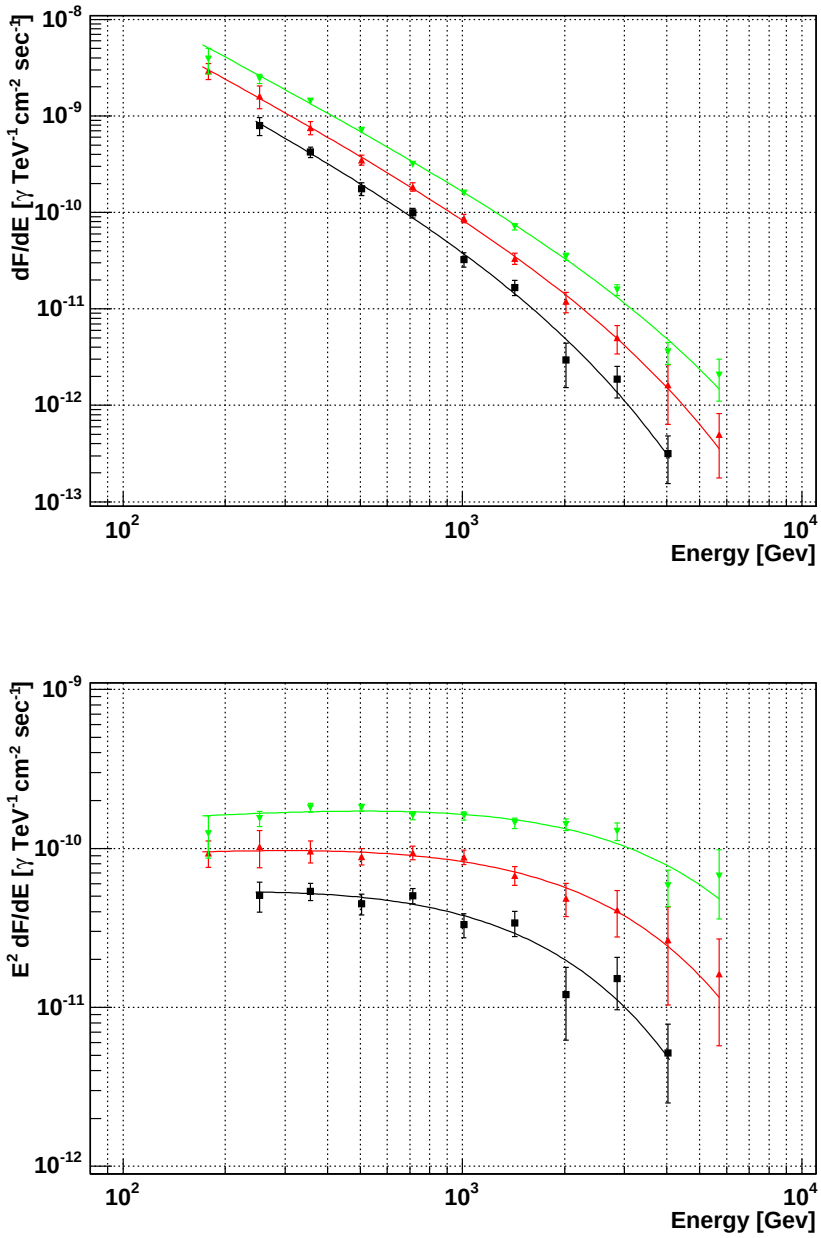

Figure 5.7: *Differential flux* measurement for Mkn421 during the spring of 2004. The complete sample has been divided into three subsamples according with their daily mean *integral flux*. The (black)squares correspond to the average spectrum for the nights in low state, (red)up-triangles for nights in medium state and (green)down-triangles for high state nights (actually only the night of 23th of April arrive to this flux level). The *differential flux* is shown in the top plot whereas the *differential flux* times the square of the energy (i.e. SED) is shown in the bottom plot.

	LOW STATE	MEDIUM STATE	HIGH STATE
F_0	$8.1 \pm 2.4_{stat}$	$13.2 \pm 2.8_{stat}$	$22.6 \pm 2.3_{stat}$
α	$1.83 \pm 0.24_{stat}$	$1.86 \pm 0.16_{stat}$	$1.84 \pm 0.09_{stat}$
E_{cutoff}	$1.3 \pm 0.4_{stat}\ TeV$	$2.1 \pm 0.8_{stat}\ TeV$	$3.1 \pm 0.8_{stat}\ TeV$
χ^2 (N $d.o.f$)	5.2 (6 $d.o.f$)	1.8 (8 $d.o.f$)	9.0 (8 $d.o.f$)

Table 5.4: Fit summary results for Mkn421 spectra in several activity states. The results shown in the table correspond to a power-law with an exponential cutoff fit with formulation $dF/dE = F_0 \cdot (E/TeV)^{-\alpha} \cdot exp(-E/E_{cutoff}) \cdot 10^{-11} \cdot \gamma \cdot TeV^{-1} cm^{-2} sec^{-1}$.

tion is between the flux activity state and the energy cutoff, due to the aforementioned correlation between the energy cutoff and the spectrum slope in the fit. Actually, an equivalent correlation between the spectrum slope and the activity state could have being found if the energy cutoff would have been fixed instead of the slope. The real conclusion of this study is observation of a dependence between the activity state and the spectral shape for Mkn421. For the observation of Mkn421 during the Spring of 2004 done in this Thesis, the hypothesis of a constant spectral shape has a probability of less than 1.3‰ (see figure 5.8).

5.2 Light Curve

During the study of the energy spectrum of Mkn421 it has been shown that the emission changed with time. In particular it has been shown that just in the period of time analysed in this Thesis, the changes in the daily average *integral flux* for consecutive nights were up to a factor three. The study of the evolution of the emission with time for Mkn421 in epochs of high activity can be done in time intervals shorter than one night. Actually, with emission levels like the one observed for Mkn421 during the spring of 2004, it could be done in intervals of few minutes.

In this section it is going to be presented how *light curves* are computed in this Thesis. *Light curves* are nothing else than the *integral flux* evolution with time. In addition to the calculation of this magnitude, a set of specific tests for the consistency of the measured *light curves* are presented.

5.2.1 Light Curve calculation procedure

The definition of the *integral flux* for a given energy range is the integral of the *differential flux* over this range (see formula 5.19).

$$Flux(E_{max} > E > E_{min}) = \int_{E_{min}}^{E_{max}} \frac{dFlux}{dE}\, dE \tag{5.19}$$

The straight approach for the calculation of a *light curve* would be to divide the complete data interval in time bins, compute the *differential flux* for each time bin, then fit the obtained spectrum and compute from the fit's result the corresponding *integral flux*. This approach has the requirement of rather large time bins in order to be able to compute properly the spectrum.

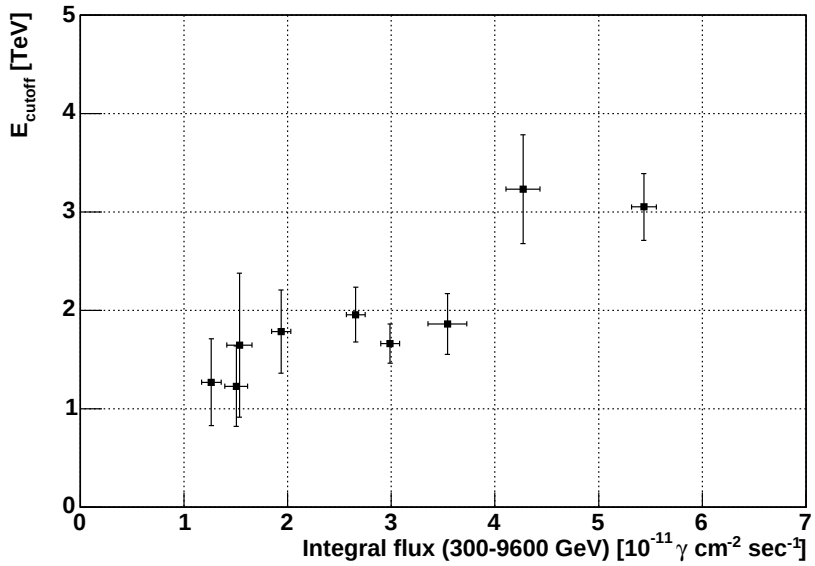

Figure 5.8: Correlation between flux state and spectrum energy cutoff for Mkn421 during the spring of 2004. Each of the points in the figure represents the spectrum results for one of the nights. In the fit performed to each daily spectrum the spectral index has been fixed to $\alpha = 1.85$. The χ^2 obtained assuming a constant energy cutoff for all flux levels is 23.7 (8 $d.o.f$), which corresponds to a probability of 0.13%.

In this Thesis a different approach has been adopted in order to reduce as much as possible the time bins in the *light curve* calculation. The method used consist on computing the rate of excesses for the given energy range for the different time bins. To convert each excess rate to *integral flux* they are divided by the average effective area over the integrated energy range, taking into account in the averaging the measured spectrum for the source. For a more accurate calculation of the *integral flux*, all the previous steps are split into different Zenith angle bins. This makes possible to take into account the change in the effective collection area during the time window due to the change of the ZA of the observation while the tracking of the source. The expressions used to calculate the *light curve* following this procedure are shown in equation 5.20.

$$Flux(t^l) = \sum_{\theta^j} \frac{Rate_{excess}(t^l,\theta^j)}{\langle A_{eff}(\theta^j)\rangle} \tag{5.20}$$

$$Rate_{excess}(t^l,\theta^j) = \frac{\Delta N^i_{Excess}(t^l,\theta^j)}{T_{eff}(t^l,\theta^j)} \tag{5.21}$$

$$\left\langle A_{eff}(\theta^j)\right\rangle = \sum_{E_{min}}^{E_{max}} \frac{A_{eff}(E^i,\theta^j)}{U^i(E^i,\theta^j)} \cdot \frac{\int_{E^i}^{E^{i+1}} \frac{dFlux}{dE}\Big)_{measured} dE}{\int_{E_{min}}^{E_{max}} \frac{dFlux}{dE}\Big)_{measured} dE} \tag{5.22}$$

In the previous formulation the same Monte Carlo derived magnitudes computed for the spectrum calculation has been used.

5.2.2 Time dependent studies

The calculation of *light curves* presented before is based on the assumption that the conditions of the analysis are stable during the window of data taking. These conditions include the atmosphere, the telescope response and the analysis behaviour itself. The stability of the analysis is necessary to guarantee that the possible changes in the measured *integral flux* are due to real changes in the source emission.

In next paragraphs a few tests performed to the data samples used in the *light curves* calculations are presented. These tests check the most plausible sources of time dependent biases which could affect the calculation of *light curves*.

1. **Hadronic cosmic rate**

   In the previous chapter it was explained the utility of the Hadronic cosmic rate as a good indicator of the atmospheric conditions as well as the telescope response. In the former chapter this magnitude was used for the rejection of bad runs. In an equivalent way, it is going to be used now to guarantee the stability of the atmosphere and the telescope during the *light curve*. The difference with the former hadronic rate calculation is that, in this case, the rate is computed using exactly the same time bins than the ones used in the *light curve*. This approach has two main advantages. First, it is a good tool to detect time bins in the *light curve* with remaining problems in a straight way. Second, it testes the goodness of the effective time calculation which is fundamental for a right *integral flux* calculation.

2. **Hillas distributions**

   The previous tests take into account things related with the general behaviour of the Telescope (including the atmosphere). However, even having a smooth hadronic rate, it could still exist hidden problems related with the behaviour of the analysis itself. Changes in the basic Hillas distributions for a particular time bin could give an apparent change in the emission of the source when it actually is related with a wrong calculation of the efficiency of the analysis with the Monte Carlo.

   To test this possibility, the stability of the mean and variance of some basic Hillas distributions (mainly *width* and *length*) are monitored for each of the time bins used in the *light curve* calculations.

3. ***alpha* distribution width**

   There is one final test performed before *light curve* calculation which checks the possible remaining mispointing for a particular time bin. One of the most important effects of the mispointing is the broadening of the *alpha* distribution. In other words, due to the wrong source position knowledge the *alpha* parameters for γ-showers is reconstructed larger than the actual value. In case of having an important mispointing, the net effect would be the reconstruction of lower excess rate due to the lost of γ-showers events badly selected as background candidates due to a large *alpha* parameter.

   To discard these possible source of error, in addition of making the *alpha* cut in the definition for the signal region large enough (see section 4.4.3), the width of the *alpha* parameter distribution is monitored for each time bin. The calculation of the width is done fitting the *alpha* plot for the excess events (i.e. *On- Off*) with a

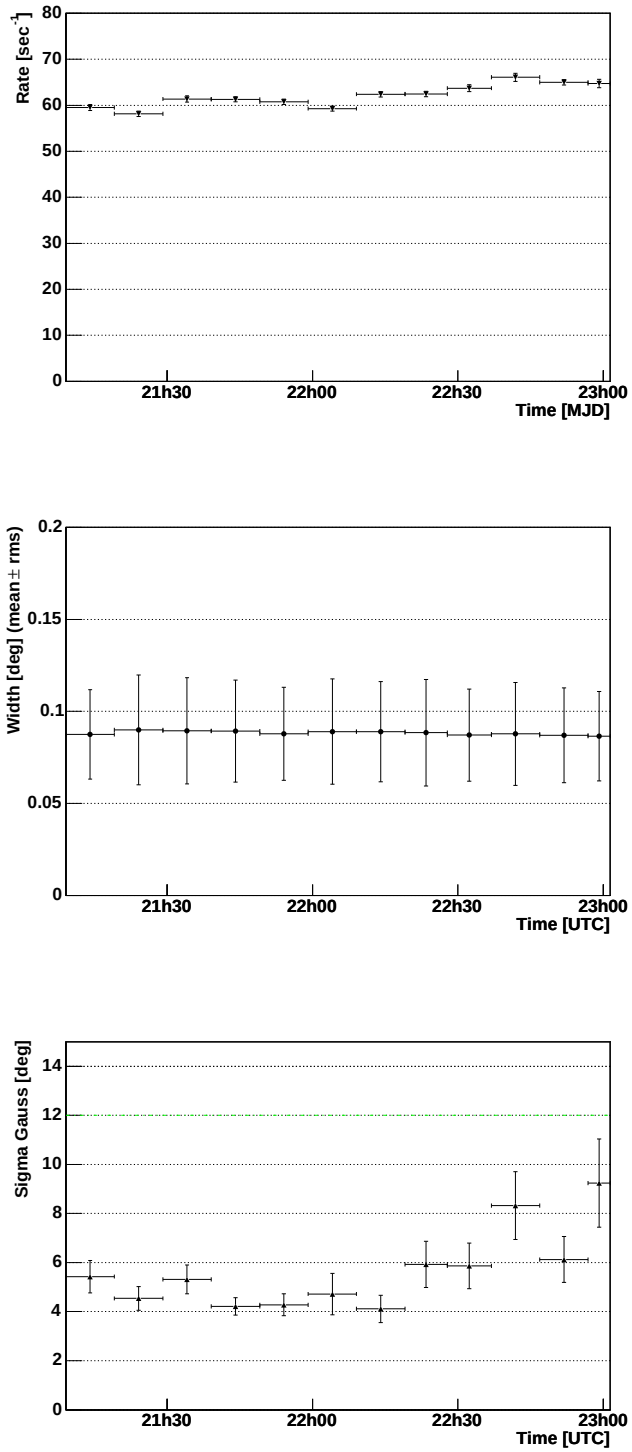

Figure 5.9: Time dependent test for Mkn421 during 19th April 2004. The figures shown represent the hadronic cosmic rate (top figure), the mean and standard deviation of the *width* distribution with time (medium figure) and the sigma of the *alpha* distribution for excess events (Bolton figure). The mean hadronic cosmic rate is 62 Hz with an RMS of 2.4 Hz which corresponds to a relative variability of less than 4%.

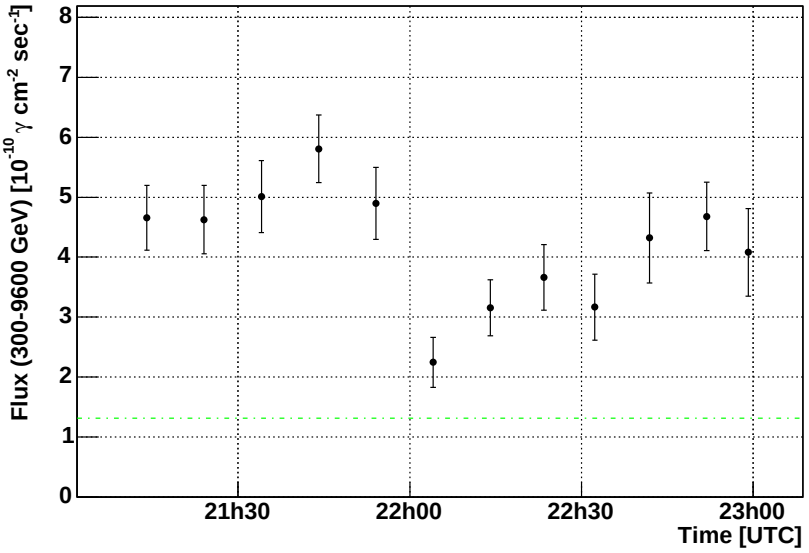

Figure 5.10: *Light curve* for Mkn21 during 19th of April 2004. The *integral flux* for each time bin has been computed in an energy range between 300 and 9600 GeV.

Gaussian function. The evolution of the sigma of the fit for each time bin is a good indicator of the stability of the mispointing of the telescope.

All these tests have been performed to each of the *light curves* computed in this Thesis, with the aim of looking for time bins with remaining problems. In figure 5.9 the results from the previous explained time dependent tests are shown for one of the nights, as an example.

5.2.3 Light Curve results

A *light curve* has been computed for each night in the spring of 2004 Mkn421 observation. The width of the time bins has been decided according to the activity state of each night. Time bins of 5, 10 and 15 minutes have been chosen for high, medium and low state nights. In figure 5.10 the *light curve* for the 19th of April, can be observed a clear time structure not compatible with a steady emission.

The complete set of *light curves* is shown in appendix B. Unfortunately for the purpose of this Thesis, altough the emission during many of the nights observed is very high, Mkn421 showed rather smooth light curves with the exception of the 19th of April night. In next chapter, it will be shown how the emission of Mkn421 during this night has been used for the measurement of the invariance of the speed of light.

5.3 Comparison between MAGIC and HESS Mkn421 observations

This high emission period shown by Mkn421 was observed not only by MAGIC but also by others IAC Telescopes. In particular, there are analysis published for that period by

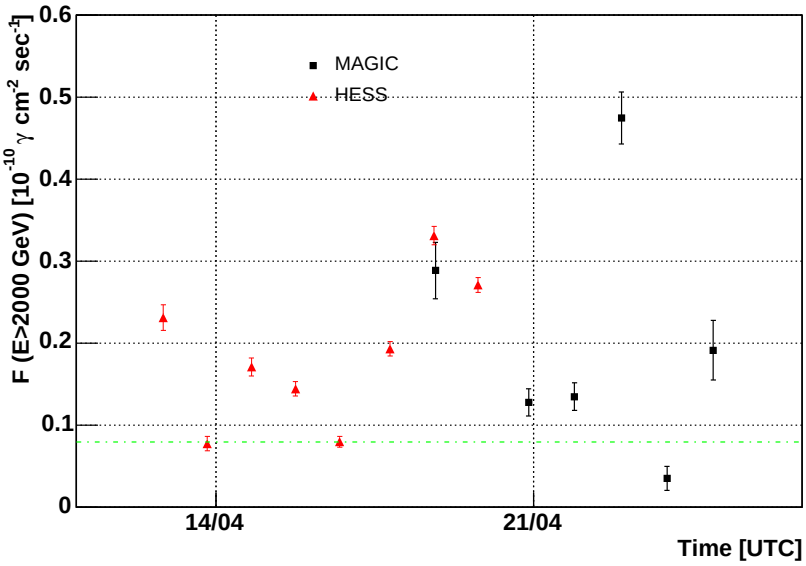

Figure 5.11: Daily average *integral flux* observed by MAGIC and HESS for Mkn421 during April of 2004. The (green) dashed line represents the *integral flux* for Crab Nebula. Notice the large statistical errors shown by the MAGIC results due to the smaller collection areas because the different zenith angle observations for both telescopes.

the Whipple [61] and HESS [62] telescopes.

Of special interest for the study presented in this Thesis is the observation done by HESS because their observation at a very different zenith angle range. This IACT is placed in Namibia, in the southern hemisphere, which makes the observation of Mkn421 for that period to be necessarily done at large zenith angles. The observation in these conditions benefits from the considerable increase of the collection area, which results in a better sensitivity in the measurement of the Mkn421 energy spectrum for very large energies. The trade-off for these large zenith angle observations are that the energy threshold is increased, in this particular case being in average of 1.5 TeV.

MAGIC, being in the northern hemisphere, made the observation of Mkn421 during the spring of 2004 for rather low zenith angles. This fact made possible to measure up to the lowest energies accessible with the analysis method presented in this Thesis. Joining the measurements from MAGIC and HESS in this situation produces a combined energy spectrum for almost 3 decades in energy.

Before the join of both measurements, we have produced the daily mean integral flux light curve for both observation samples (see figure 5.11). Due to the larger energy threshold for the HESS sample, the MAGIC daily integral fluxes have been recalculated above 2 TeV. Unfortunately, just one single night was observed almost simultaneously by both experiments. However, the emission level for the HESS data sample is comparable to the medium emission state observed by MAGIC. This makes possible to join the spectrum measured by HESS with the medium state energy spectrum measured by MAGIC (see figure 5.12). From this figure, it can be concluded that both observations coincide very well, either in emission level, and what is even more important, in the shape of the spectrum.

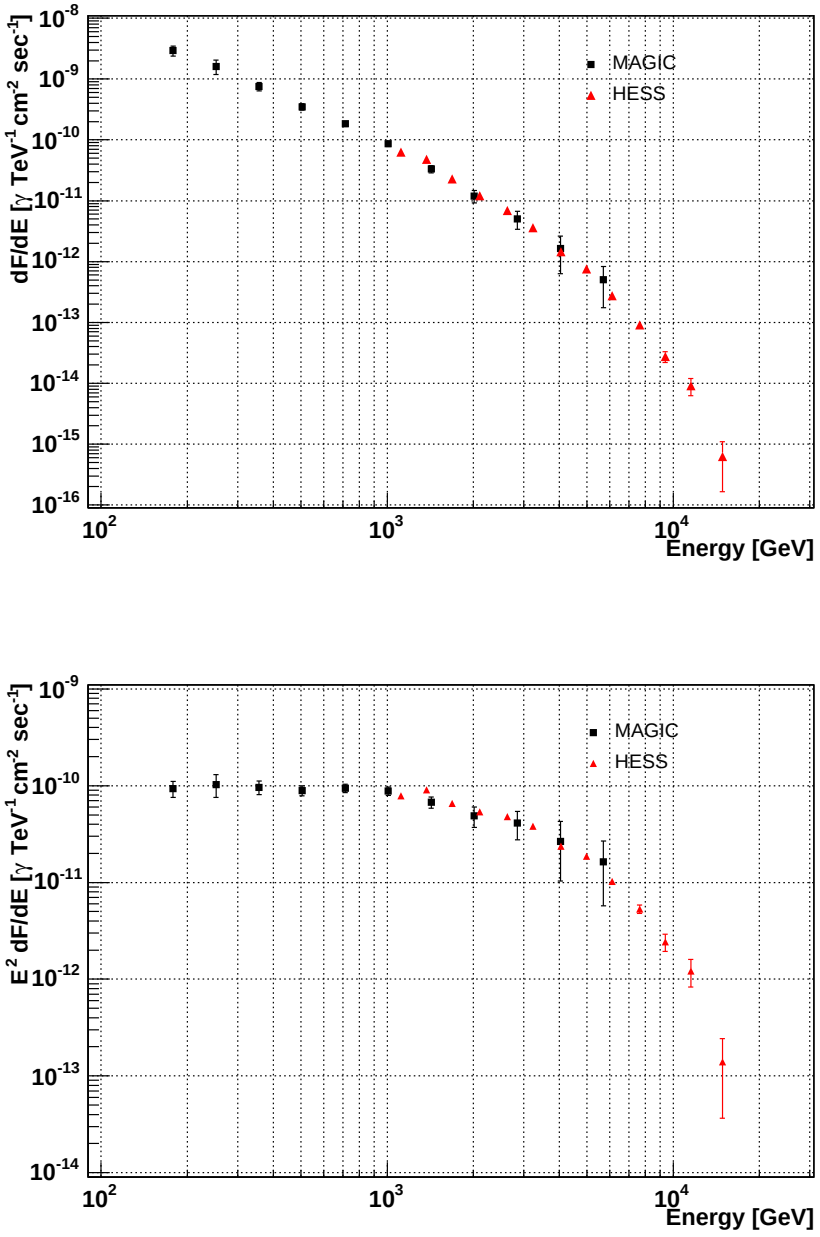

Figure 5.12: Joined *Differential flux* measurements for Mkn421 for MAGIC and HESS observations. The MAGIC measurement correspond to the medium state emission presented in this Thesis, whereas the HESS data has been obtained from the reference [62]. The top figure shows the *differential flux* while and the bottom one shows the SED.

5.4 Summary from Mkn421 Spectrum and Light Curve results

In this study two sources, Crab Nebula and Mkn421, have been analysed.

Crab Nebula has been used as a calibration source due to its strong and steady emission in the VHE domain. Limited data from this source, less than 2 hours, was available with equivalent conditions to the Mkn421 sample. Despite this limiting observational time, an energy spectrum for Crab has been measured for March of 2004 with compatible results with the ones already present in literature reported by other IACTs.

From the point of view of Mkn421, this source showed during the spring of 2004 one of the strongest activity period for the last years, with maximum *integral flux* values above 300 GeV up to $(6.6 \pm 0.6) \cdot 10^{-10} \gamma \cdot cm^{-2} sec^{-1}$ which is 5 times the *integral flux* of Crab Nebula.

Mkn421 showed during this period large variability in the mean daily integral flux above 300 GeV, with changes bigger than a factor two between consecutive nights. However, rather smooth light curves have been measured for each of the nights observed with the exception of the 19th of April, which shows a clear rapid time structure with a time scale of the order of tens of minutes.

From the study of the shape of Mkn421 spectrum presented in this Thesis, it has been possible to confirm previous observations of an energy cutoff in the energy spectrum. In addition, the measured energy spectra for Mkn421 shows a clear power law behaviour for low energies up to 180 GeV with no signs of curvature (i.e. Inverse Compton peak) for these energies.

In a deeper study, it has also been possible to confirm the change of the spectrum shape on Mkn421 with the flux level, showing harder spectrum for higher flux levels. The hardening of the spectrum has been proved through the observation of a clear correlation between the energy cutoff versus the average *integral flux*, calculated both in a daily basis. In previous studies about this effect (see reference [59]) it has been pointed out, as the possible explanation for it, the shift of the inverse Compton peak to higher energies, rather than just a change in the global luminosity of the source. This model should explain the changes in the spectrum shape observed.

The measurement done in this Thesis has been joined with the measurement done by HESS to Mkn421 during the same period. Even though the observations done by both telescopes are not simultaneously, it has been possible to compare the energy spectrum for equivalent emission levels, leading to a combined differential flux for almost 3 decades in energy in the VHE domain, from 180 GeV to 15 TeV, with good agreement in the spectral shape measured for Mkn421 by both experiments.

Finally, the presented results confirm the robustness of the analysis used in this Thesis for the calculation of the energy spectrum and the light curves. They also confirm the good overall performance shown by MAGIC during the spring of 2004, at the beginning of its commissioning phase. The telescope presented some technical problems, such as a sizeable mispointing or changes in the reflector focusing quality, which highly increased the complexity of the analysis. However, the condition of the telescope still made possible to perform competitive measurements for Mkn421 at the studied period.

Chapter 6

Lorentz Invariance Measurement

The aim of this chapter is the study of the invariance of the speed of light using the *Time of flight* measurement approach with the MAGIC Telescope observations. This kind of measurements are included in the Lorentz invariance violation (LIV) subject. Over the last decade there has been tremendous interest and progress in this field motivated from both theoretical and experimental new inputs. On the theoretical side, present theories for Quantum Gravity open the possibility for Lorentz invariance as a non exact symmetry for all energies. On the experimental side, the last advances in technology and observational techniques have dramatically increased the precision of experimental tests, leading to the level where they can be sensitive to small low energy residual effects due to Lorentz invariance violation.

In the first two sections of this chapter it is overviewed the present status of the Lorentz invariance test in the literature, making special emphasis on the contribution from VHE astrophysics and in particular the *Time of flight* observation approach. Before this overview, the theoretical/phenomenological framework necessary for the understanding of the experimental tests is briefly introduced. The overview presented in this chapter does not try to be exhaustive nor conclusive but simple enough to give a clear introduction to the subject. For a deeper overview see the references [63, 64, 65]. A final summary is included, justifying the relevance of the *Time of Flight* measurement that is studied in the next section.

The final section of the chapter deals with the *Time of Flight* measurement with MAGIC. To begin with, the best scenario for the most sensitive measurements of Lorentz invariance symmetry with the MAGIC Telescope is discussed. It follows a critical analysis of the present experimental approaches within VHE astrophysics to perform this test, leading to the development of an alternative, theoretically more sensitive way to do this measurement. This new procedure is then applied to the Mkn421 results shown in the previous chapter to obtain a measurement of the invariance of the speed of light. Finally, the obtained result is compared to previous measurements of this magnitude to illustrate the performance of the new approach.

6.1 Lorentz Invariance violation phenomenology

Quantum Gravity has been proposed as a possible source of LIV which it is a fundamental symmetry postulated by Special Relativity and by extension of General Relativity. For this reason any Lorentz invariance violation experimental evidence will be a clear signature

of new physics beyond General Relativity and probably the first measured effect of the quantum nature of gravity.

The different theoretical approaches to quantum gravity available nowadays are still far from being able to give clear predictions for guiding LIV experiments. For this reason, a phenomenological approach, also known as *test theories*, has been developed during the last years in the LIV field. These test theories have shown to be useful both as a guideline for testing new possible effects, as well as a framework to compare different kind of experiments which test the same effect.

In the following sections we show an introduction to both *Quantum Gravity* as the inspiration theory for the studied phenomena and the phenomenology of LIV as the basic framework for the experimentation in the subject.

6.1.1 Quantum Gravity

Quantum gravity is the field of physics which attempts to explain the quantum effects of gravity. From the theoretical point of view, quantum gravity is seen as the last piece left in the attempt to unify two fundamental and well-established theories: the theory of quantum mechanics and the theory of general relativity. This would provide a theory of everything that would explain in a reasonable and coherent way the four fundamental forces of nature: electromagnetism, weak and strong interaction (well explained in the quantum framework) and gravity.

Historically, quantum gravity has had different approaches regarding the role given to the geometric interpretation of gravity. For some of these, the geometric interpretation is not fundamental and it will only emerge as a semi-classical limit. The second approach, states that background independence is fundamental, thus implying quantum mechanics needs to be generalize to settings where there is not *a priori* specified time. The two most popular approaches to quantum gravity are based on *String theory* and *Loop Quantum Gravity*, despite many other representations of a quantum theory of gravity (e.g. non-commutative geometry, Twistor theory, etc.) also exist. For a complete review on the history of Quantum Gravity see reference [66].

A general expected feature of all these quantum-gravity scenarios is the appearance of new effects, often mediated by new fields. In particular, both *String theory* and *Loop Quantum Gravity* theory allow for the possibility that Lorentz symmetry might not hold exactly [67, 68]. Despite it is far beyond the scope of this Thesis to provide a detailed explanation of these theories, the following paragraphs show a brief description of the basics together with the motivations for the violation of Lorentz invariance for each of them.

1. **String theory**

   String theory was originally developed in the 60s to explain the behaviour of Hadrons. One of the largest problems faced by string theory was its prediction of the existence of a massless particle with spin two, being no experimental evidence of such a hadron. These inconsistencies among others finally led to QCD as the agreed theory for Hadrons while String theory lost most interest from the scientific community. Around the 70s, however, the problematic prediction of the spin-two hadron became extremely important because it fitted with the expected characteristics for the graviton, the quantum for the gravitational field. In this sense, String theory suffered a change of scope, being postulated as a possible quantum theory of Gravity

or even an aspiring *Theory of Everything*, which tries to explain all the fundamental interactions.

Basically, String theory is based on the idea that the fundamental particles are one-dimensional extended objects, the so-called strings, rather than the points-like objects in the Standard Model of particle physics. Due to this reason, String theory is able to avoid some of the problems of the Standard model which are associated to the presence of zero-dimensional particles. One basic postulate of string theory is that the plethora of possible oscillatory states of a string is responsible for the variety of the different elementary matter and force particles that occur within the standard model of particle physics. In other words, there is only one species of string, but depending on how this tiny string oscillates, it acquires the same properties as an electron, a photon, a specific kind of quark or some other elementary particle.

A particularity of String theory is that it predicts the number of space-time dimensions of the universe, while in previous theories (e.g. electromagnetism or relativity theory) the number of dimension needs to be introduced ad hoc. In String theory, for a different number of dimensions the theory presents a gauge anomaly, related to the necessity to predict a massless photon. However, the mass of the photon predicted in this framework depends on the energy of the string mode which represents the photon. This energy includes effects from quantum fluctuations in the string that obviously depend on the number of dimensions (for larger number of dimensions implies more possible fluctuations of the string). Therefore, a massless solution for the photon particle only occurs for a particular number of dimensions.

These early versions of String theory had the basic problem of predicting a spectrum of particles that contained only bosons, becoming just a bosonic theory. For bosonic theories, the dimensionality of the universe turned out to be 26. The investigation of how a String theory may include fermions in its spectrum led to Supersymmetry. String theories which include fermionic vibrations are now known as Superstring theories and several different kinds have been described, all predicting a universe of 10 dimensions.

There are five distinct superstring theories which in recent years it has been shown that they are not independent from each other but a special case of a single, more fundamental theory. These Superstring theories are related by transformations called dualities (S-duality, T-duality and U-duality). The existence of these relationships imply that each of the Superstring theories previously proposed is a different aspect of a single underlying theory, which has been named "M-theory" and predicts a universe of 11 dimensions.

For a more detailed String theory review see [69].

Motivations for Lorentz Invariance Violation in String theory

From the phenomenologist point of view, the low-energy limit of String theory is a special scenario. On the one hand, it predicts a variety of new effects beyond the Standard Model, including effects leading to violation of Lorentz invariance. On the other hand, the theory can be easily tuned to avoid all of these new effects. In this sense, it appears at present not possible to falsify String theory on the basis of low-energy phenomenology. However, it would be very interesting to find experimental

evidence of any of these new effects.

One of the most exciting effects mentioned in the literature is the possible violation of Lorentz invariance due to spontaneous symmetry breaking in the context of string theories [67]. In ordinary field theories, some requirements like renormalizability and gauge invariance make impossible spontaneous symmetry breaking of the Lorentz group. Unlike the conventional standard model, string theories typically involve interactions that could generate nonzero expectation values for Lorentz tensors in the vacuum state, leading to spontaneous symmetry breaking. In fact, some kind of spontaneous breaking of the higher-dimensional Lorentz symmetry is expected in any realistic Lorentz-covariant fundamental theory involving more than four spacetime dimensions, such as String theories.

Another new effect predicted by string theory which has an impact in Lorentz invariance violation is the appearance of modified energy-momentum Dispersion relation [70]. Due to the fact that in String theory the effective Maxwell and Dirac equations contain higher order derivatives than in standard equations, it leads to modified dispersion relations. The simplest and most studied modified dispersion relation is shown in 6.1.2, where the implications of this modified energy-momentum dispersion relation for Lorentz invariance violation is discussed.

2. **Loop Quantum Gravity**

The assumption that Einstein's classical theory of gravity can be quantized non-perturbatively is at the root of a wide variety of approaches to Quantum gravity. The general expectation in the Quantum gravity community is that at the very shortest distances the smooth geometry of Einstein's theory is replaced by some quantum space or spacetime, and the continuum becomes a discretum. Many different formulations have been done in the quantum gravity field around these ideas.

According to General Relativity, gravity is not a force but a property of space-time itself. This distinction between gravity and the rest of fundamental interactions between particles has been the reason why all attempts to treat gravity in the same quantum field formalism than the other three interactions have failed. Loop quantum gravity (among other Quantum gravity theories) attempts to develop a quantum theory of gravity based directly on Einstein's geometrical formulation of space-time [71]. Thus, the main idea beyond Loop quantum gravity is that a quantum theory of the gravitational field is a quantum theory of the space-time metric as well. It follows that loop quantum gravity cannot be formulated as a quantum field theory over a continuum metric, because the metric itself is a quantum variable.

Apart from their original assumptions and many other aspects related with the mathematics involved, the basic difference between String theory and Loop quantum gravity remains in their scope. String theory considers that Einstein-Hilbert action is only an effective low energy approximation to a more fundamental theory (i.e. String theory). On the other hand, Loop quantum gravity takes Einstein's theory as the basic starting point for a quantification of gravity. Despite its limited scope, Loop quantum gravity addresses several interesting aspects that are currently outside the main focus of String theory, in particular the question of background independence and the quantization of geometry.

For a more detailed Loop quantum gravity review see [72].

Motivations for Lorentz Invariance Violation in Loop quantum gravity

In loop quantum gravity the key difficulty is the fact that the techniques for obtaining the classical limit of the theory have not yet been developed. In other words, this candidate for quantum gravity has not been shown to actually contain classical gravity as a limit. Since our phenomenology will usually be structured as a search of corrections to the classical effects, this is a very serious issue. However, several authors (see, e.g. reference [68]) have proposed to start with the exploration of the properties of some candidate quasiclassical states, as a way to get some intuition for the type of effects that the theory might predict when the complete theory is fully understood. Introducing the so-called *weave states* leads to modified Maxwell and Dirac equations with higher order derivatives. As has been explained before in the framework of String theory, these higher order derivatives terms suggest a modified energy-momentum dispersion relation. But clearly these violations from Lorentz symmetry still cannot be viewed as a prediction of Loop Quantum Gravity because of the heuristic nature of the underlying arguments. In this sense, there are some authors (see, e.g. reference [73]) who have discussed arguments in favour of exact Lorentz symmetry for Loop Quantum Gravity.

6.1.2 Test theories

In ambitious attempts to describe a complete quantum theory of gravity, such as the ones introduced in the previous section (i.e. String theory or Loop quantum gravity), it has already been mentioned that the extremely complex and rich formalism open the potentiality to a plethora of new phenomena. However, none of these theories, at present, has been able to establish that any of this new effect is definitely present in the theoretical framework.

These sorts of not-fully developed theoretical frameworks provide a motivation for a general approach to describe deviations from standard theories. From the phenomenological point of view, it is natural to deal with this complex situation by developing a set of test theories that indeed describe the new effects via some new terms in the old theoretical framework. This approach makes simpler the experimental study of the new possible phenomena as well as introduces a common terminology to express the experimental results. Nevertheless, the phenomenology should also keep in mind that there have been cases in the history of physics where the description of the new physics really demanded a new formalism.

Test theories are used in this Thesis to study the Lorentz invariance violation problem. For testing this symmetry, a well defined set of parameters are introduced in the standard equations. These parameters are chosen in such a way that the symmetry is recovered for particular values of the parameters, while the other values represent a breakdown of the symmetry.

In the next paragraph two different kinds of test theories are explained. The first two are kinematical test theories. Most part of the Lorentz invariance violation study carried out in this Thesis is based on these first two formalisms. The last test theory presented is the most general dynamical test theory which includes Lorentz invariance violation within the Standard model. As it will be shown, this formalism is the standard framework for many LIV experiments, providing theoretical motivations for many experimental works as well as a common terminology to express the results from these different experiments.

Before going on with the explanation of the test theories, an important concept in Quantum Gravity theories is going to be briefly introduced: the Planck mass or energy (E_{Pl}). This mass appears as the unique way of defining an energy scale using the fundamental constants coming from general relativity (the speed of light c and Newton's gravitational constant G) and from quantum mechanics (Planck's constant $\hbar$).

$$E_{Pl} = \sqrt{\frac{\hbar c^5}{G}} \simeq 1.22 \cdot 10^{19}\ GeV. \tag{6.1}$$

It is reasonable to suspect that any theory reconciling general relativity and quantum theory will involve all three constants c, G, and $\hbar$, thus suggesting the Planck energy as the natural energy scale in a quantum formulation of gravity. An additional argument for this statement is that the Planck mass is the mass of a black hole whose Schwarzschild radius multiplied by π equals its Compton wavelength [1]. The radius of such a black hole is roughly the Planck length, which is believed to be the length scale at which both general relativity and quantum mechanics simultaneously become important.

Modified dispersion relation model

The modified dispersion model was proposed by Amelino-Camelia [74] for the possible observation of a LIV signature observing Gamma Ray Bursts (see section 6.4 for a detailed discussion).

This simple kinematical framework proposed the introduction of correction terms in the Lorentz invariant dispersion relation of the type $E^2 = m^2 + p^2 + \mathcal{O}(m,p)$. Since we live in an almost Lorentz invariant world the introduced corrections must reduce to the Lorentz invariant dispersion at small energies and momenta. Hence, it is natural to expand the dispersion relation about $\overrightarrow{p} = \overrightarrow{0}$, which leads to the expression,

$$E^2 = m^2 + p^2 - \sum f^{(n)} \frac{|\overrightarrow{p}|^n}{E_{Pl}^{(n-2)}} \simeq m^2 + p^2 - \sum f^{(n)} \frac{E^n}{E_{Pl}^{(n-2)}} \tag{6.2}$$

where $f^{(n)}$ are dimensionless constants that might be expected to be of order unity [2] if indeed quantum gravity does violate Lorentz symmetry. The order n of the first not-zero term in equation 6.2 depends on the underlying model of quantum gravity taken.

Since the underlying motivation for this Lorentz violation model is quantum gravity, the coefficients of the expression have been factorized using the Planck energy scale (E_{Pl}) in such a that way they become dimensionless.

There is no underlying reason for the coefficients in equation 6.2 to be universal for all particles. In fact, it is phenomenologically safest when investigating modified dispersion to assume that each particle has a different dispersion relation. For this reason the coefficients $f^{(n)}$ are labelled as $f_A^{(n)}$ where A represents the different particle species (e.g. $f_{e^-}^{(n)}$ for electrons).

A variation of the above dispersion relation is obtained assuming that different polarization states of the particle have different propagation velocities (i.e. $f_{\gamma_L}^{(n)} \neq f_{\gamma_R}^{(n)}$). For

[1] Quantum mechanics, in particular the uncertainty principle, postulates that any particle with a certain mass has an intrinsic uncertainty in its position equal to h/mc which can be thought of as a fundamental limitation on measuring the position of a particle. This length is defined as the Compton wavelength of a particle.

[2] This is actually true for $n > 2$ terms. The first two terms should be really small if not they were already being found.

photons this possibility introduces the birefringence (i.e different propagation speeds for different photon polarizations) in the modified dispersion framework.

To close this test theory, two prescriptions must be added to the above dispersion relation: the aforementioned validity of the standard law of energy-momentum conservation and the computation of the velocity of the particle from the standard expression 6.3.

$$v = \frac{\partial E}{\partial p} \tag{6.3}$$

These simple prescriptions suffice for analysing many Lorentz-violating phenomena, like energy-dependence speed of light, birefringence or modifications of the threshold of reactions in astrophysics. Actually, modified thresholds of reactions may require some dynamical model but many authors argue that standard Lorentz invariant dynamics could be used as long as they are assumed not to be drastically different from the physics including Lorentz invariant violation.

Doubly special relativity

In any quantum theory of gravity the quantification of space and time is an expected characteristic of the theory. This characteristic leads to the existence of an intrinsic length (or energy) scale, which in most cases is identified with the Planck scale l_{Pl} (or E_{Pl}). Furthermore, the resulting theory of Quantum Gravity is expected to agree with Special Relativity in the limit when the gravitational field is weak and the energies involved are much smaller than the intrinsic scale E_{Pl}. These two facts lead to the paradox that if the intrinsic length scale is l_{Pl} in one inertial reference frame, Special Relativity suggests it may be different in another observer's frame due to application of Lorentz-Fitzgerald contraction.

This paradox is the motivation for the development of Doubly Special Relativity (DSR) [75, 76]. DSR is constructed as a new version of Special Relativity based on two postulates. The first is the same than Special Relativity, which is the equivalence of all inertial observers. The second is the existence of two observer independent scales: the velocity c scale, identified with the maximum possible speed, and the dimension of mass E_{DSR} scale, identified with the Planck mass. In this new theory, by definition the transformation between inertial frames keeps invariant the intrinsic length scale $l_{DSR} = E_{DSR}^{-1}$. It is important to mention that Double Special Relativity, rather than being a theory that violates Lorentz invariance, is a nonlinear realization of the Lorentz group that exhibits both a limiting velocity and a limiting energy.

DSR is a very recent theory. In fact, it has been developed in the last few years. Nevertheless, there exists already quite a clear picture of the observable predictions which arise from this theory [3]. One of these observables is the possible energy-dependence of velocity for massless particles like the photon. This effect is based on the modification of the invariant dispersion relation in the DSR with respect to the Special Relativity (SR).

Doubly special relativity modifies not only particle dispersion relation but also the form of the energy conservation equations. The conservation equations change in such a way that they compensate for the modified dispersion relations. In this sense, all reactions

[3]DSR is not a finished theory. In fact, it is not settled yet if the theory is fully mathematically consistent [77]. Therefore, it is somehow premature to talk about robust predictions in DSR. Nevertheless, in case the theory became mathematically mature, the observational predictions are already quite well-known.

that are forbidden by conservation in ordinary Lorentz invariant physics are also forbidden in DSR.

DSR theories predict an energy-dependent speed of light, effectively given by an n = 3 type dispersion relation like the one presented in equation 6.2. On the other hand, it is not expected that DSR yields birefringence. In addition, DSR marginally affects threshold reactions, making the actual shift of threshold energies due to DSR negligible at the level of sensitivity we have with astrophysical observations. Hence DSR cannot be ruled out or confirmed by any present threshold type of analysis. The observational signature of DSR, or some similar model, would therefore be a possible energy dependence of the speed of light without birefringence and no appreciable change in particle thresholds.

For a deeper introduction to DSR and DSR phenomenology see the reviews [78, 79].

Standard Model Extension

Many Lorentz invariance tests are motivated and analysed in purely kinematical frameworks like the ones explained in the previous sections. This kind of models have the advantage of being independent of a dynamical theory, which simplifies the test theory. Nevertheless, only few observations like Doppler shift, interferometry, birefringence or time-of-flight are by construction insensitive to dynamics. For this reason, the implementation of general dynamical features in test theories is necessary to significantly increase the scope of Lorentz invariance tests.

The most general treatment of Lorentz invariance violations within the Standard Model is the dynamical model developed by Kostelecky and coworkers [70], the so-called Standard Model Extension (SME). This framework has been used to obtain a general extension of the Standard model that violates both Lorentz invariance and CPT. In addition to the desirable features of energy-momentum conservation, this model maintains gauge invariance and power-counting renormalizability. It would emerge from any fundamental theory (e.g. String theory) that generates the standard model and contains spontaneous Lorentz and CPT violation.

The SME contains all the possible interactions that could arise from spontaneous breaking of Lorentz symmetry. In this case the SME coefficients become the constant background fields that permeate the universe and lead to particle interactions that have preferred directions. This means that the physical properties of a particle, such as its energy and momentum, will change as the motion or spin orientation of the particle changes with respect to the background SME coefficients.

One of the most attractive features of the SME is that it can incorporate the different theoretical ideas involved in different types of experiments. For example, the SME includes terms that break CPT, making the observation of violation of this symmetry a test to the model. It also introduces the birefringence due to the behaviour of the spacetime as an anisotropic medium. This model has also been successfully used to design and analyse many experiments on Lorentz violation (some of these experiments are explained in section 6.2). Moreover, SME gives a common framework for all these different experiments providing a common terminology which enables to compare results from different types of experiments.

A final aspect to take into account about the SME is that certain limits of this framework correspond to classical kinematics test models. In particular, within the SME it is possible to verify that Lorentz violation typically modifies one-particle dispersion relations. As it has already being noted, this feature permits the prediction of possible

experimental signatures like the potentially observable threshold modifications for particle reactions or the energy dependence of the speed of light.

6.2 Present Lorentz Invariance Experimental tests

For a long time the search for experimental clues on the nature of quantum gravity was dismissed as impractical, based on the simplistic argument that those effects should appear only at energies of the order of Planck scale, far beyond present day experimental possibilities. Nevertheless, in the last decade there has been a tremendous progress in the so-called Quantum Gravity phenomenology field. Many experiments have been designed to test different possible Quantum Gravity signatures, like the Lorentz invariance violation, leading to so tight bounds in some test theory frameworks that they call into question the full scheme of Lorentz invariance violations induced by Quantum Gravity [4].

In discussing some of the recent experimental tests of Lorentz symmetry it is important to keep in mind that there is no single best test of Lorentz symmetry, due to the quite large phenomenology. Furthermore, since it is possible for one type of particle in the Standard Model to have interactions that violate Lorentz symmetry while another type does not, an exhaustive investigation of Lorentz violation involves a large number of experiments in order to probe every particle sector.

In the next paragraph the present status of the different experimental test of the Lorentz invariance are reviewed. Within these measurements, two sets can be differentiated. The first are the measurements carried out in laboratories, either ground-based or space-based ones (i.e. satellites). These measurements are also called Terrestrial measurements. The second type of measurements is done within astronomical observations. The main difference among both is that the first ones are controlled experiments. Both kinds of measurements are reported in this section.

6.2.1 Terrestrial measurements

Terrestrial experiments were the first sort of experiments performed to measure a possible Lorentz Invariant Violation. Actually, it can be considered that they started as long ago as the 19th century with the well-known Michelson-Morley experiment. In the present, some terrestrial experiments are based on the same ideas than those 'traditional' experiments, with the intention to test some basic special relativity postulates. Other terrestrial experiments, however, perform different kinds of measurements in which LIV is tested through CPT violation.

In the following paragraphs, a brief description of different possible experiments of LIV is presented. The aim is to show the large amount of possible signatures of LIV that has been studied in this field, together with the different principles in which those measurements are based on. In particular, the experiments will be classified among those based on 'traditional' special relativity tests and those based on CPT Symmetry violation tests. For the sake of brevity, this list has been chosen to be representative rather than exhaustive of both sorts of terrestrial experiments.

Some terrestrial experiments based on 'traditional' special relativity tests:

1. **Doppler shift experiment**

[4] At least with respect to terms linear in the Planck scale.

The Doppler effect of light is one of the classic tests of special relativity, in particular about the symmetry under Lorentz transformations. It consists in the measurement of the Doppler shift between two groups of atoms: one group at rest in the lab frame and the other forming a beam with velocity β in the lab frame. The same transition should be studied in each group and compare them within Special Relativity predictions. The best test to date comes from spectroscopy of lithium ions in a storage ring [80]. In this experiment, $^7Li^+$ ions are trapped in a storage ring at a velocity of 0.064c. The transition frequencies of the boosted ions are then measured and compared to the transition frequencies at rest, providing a bound on the deviation from the special relativistic Doppler shift.

2. **Cavity experiments**

   From the Michelson-Morley experiments onward, interferometry has been an excellent method of testing relativity. Modern-day versions of these laboratory experiments with light have recently been performed. The most sensitive of these measurements looks for small changes in the resonant frequency of a microwave cavity as it rotates and moves due to the Earth's orbit around the Sun. The signal for Lorentz violation in these experiments would be a difference between the two resonator frequencies that varies with the same periodicity as the Earth's motion. In this sense, cavity experiments are similar to clock comparison experiments. However, since the cavities involve photons, this kind of experiments constrains the electromagnetic sector of the SME.

Lorentz symmetry is intimately tied up with CPT symmetry in that the assumption of Lorentz invariance is required for the CPT theorem. Hence, CPT violation signals the breakdown of Lorentz symmetry altogether. The consequences of CPT invariance are well known: masses, magnetic moments and charge of particles and antiparticles must be equal in absolute value, as well as cross sections and decay rates. Any of these properties may be used to check the validity of CPT invariance and some of the most sensitive tests of Lorentz Invariance are based on them.

Some terrestrial experiments based on CPT symmetry violation tests:

1. **Penning traps**

   A Penning trap is a combination of static magnetic and electric fields that can keep a charged particle localized within the trap for extremely long periods of time. A trapped particle moves in a number of different ways. The two motions relevant for Lorentz violation tests are the cyclotron motion in the magnetic field and the Larmor precession due to the spin (spin-cyclotron). In this kind of experiments there are two ways to test for Lorentz violation. The first is to look for instantaneous CPT violation between electrons and positrons measuring the cyclotron and spin-cyclotron difference of frequencies [81]. The second approach is to track cyclotron and spin-cyclotron frequencies over time, looking for sidereal variations as the orientation of the experimental apparatus changes with respect to the background Lorentz violating SME tensors. Similar techniques have been used to measure CPT violations for proton/anti-proton and hydrogen ion systems.

2. **Neutral mesons**

Mesons have long been used to probe CPT violation in the standard model. Most of the work done in this approach is through the neutral kaon system [5], and in particular by measuring mass differences between K^0 and $\overline{K^0}$. Each of these neutral mesons is the antiparticle of the other, which by the CPT theorem implies that they should have the same mass. This situation leads the measurement of the mass difference between neutral kaons as a test of the CPT symmetry. This mass difference has been measured with extremely high precision by experiments such as KTeV [82, 83] at Fermilab.

6.2.2 Astrophysical observations

The test of LIV through astrophysical observations is a very recent field, initiated in the last decade. Compared with terrestrial experiments, the astronomical observations are much more precise, due to the high energies involved in the physical processes of the observed astronomic sources and the enormous distances to these sources. It is for this reason that in a very short time, a big quantity of different astronomical observation tests has been developed, such as a variety of Threshold measurements, Synchrotron radiation, Birefringence and Time of flight. In particular, the Time of flight approach is the one used in this Thesis, as shown in section 6.4.2.

Threshold measurements

When Lorentz invariance is broken, there are a number of changes that can occur with the threshold of reactions among particles. These changes include shifting existing reaction thresholds in energy, adding additional thresholds to existing reactions or introducing new reactions entirely. By demanding that the energy of these thresholds is inside or outside a certain range (so as to be compatible with observation) one can derive stringent constraints on Lorentz violation. In astronomical observations, the changes in the energy threshold are observed in the physical processes that occur in astronomical sources.

In the following paragraphs, different threshold reaction tests are described in some detail, classified into those that introduce new reactions and those that shift the standard threshold. It is necessary to mention that the threshold experimental tests are one of the most widely used approaches with the biggest precision results for LIV testing.

Some threshold measurements that introduce new reactions:

1. **Photon decay**

   The spontaneous decay of a photon into an electron-positron pair ($\gamma \rightarrow e^+ e^-$) is a reaction usually forbidden by energy-momentum conservation in ordinary Lorentz invariant physics. However, modifications of the dispersion relation of the form 6.2 allow this reaction to occur. To see this intuitively, it can be noted that the extra term in the dispersion relation acts as an effective mass. For large enough energies, the effective mass of the photon can allow its decay into the $e^+ e^-$ pair. Obviously, this decay can only happen above a certain energy which depend on the extra term introduced in the dispersion relation (i.e. $f^{(n)}$). The observation with IACTs of 50 TeV photons from Crab Nebula makes possible to constrain $f_\gamma^{(3)}$ slightly better than $\mathcal{O}(1)$ [84, 85].

[5] Although this situation is changing with the data produced by the new B mesons factories detectors (i.e. BaBar and Belle).

2. **Vacuum Cherenkov**

   Like in the case of photon decay, the spontaneous emission of photons by a charged particle in vacuum ($A^{\pm} \rightarrow A^{\pm}\,\gamma$) is forbidden since the sum of a timelike and null 4-momentum vectors cannot lie on the same mass shell as the timelike 4-momentum. Modifications of the dispersion relations can allow some phase space for this reaction to happen.

   The 50 TeV photons observed from the Crab Nebula are believed to be produced via inverse Compton (IC) scattering of charged particles off the ambient soft photon background. If one further assumes that the charged particles are electrons, it can then be inferred that 50 TeV electrons must propagate. Using this conclusion, similar constrains than in the photon decay observation can be obtained but for the electron dispersion relation (i.e. $f_e^{(3)} < \mathcal{O}(1)$) [84, 85].

It has been argued that technically, threshold constraints cannot truly be applicable to a kinematics model where only a modified energy dispersion relation is postulated and the dynamics elements of the model are not known. However in reference [63] it is argued that for rapid reactions, where rapid means reactions with rates faster than the time the messengers (i.e. photons) take to arrive to the Earth, even a quite large change in the dynamics is irrelevant for deriving a kinematic constraint. In general, under the assumption that the dynamics is not drastically different from that of Lorentz invariant effective field theory, one can effectively apply particle reaction constraints to kinematic theories since the decay times are extremely short above the threshold.

Some threshold measurements that shift the standard threshold:

1. **The GZK Cutoff**

   Ultra-high energy cosmic rays (UHECR) are supposed to be protons. If this is correct, they are expected to interact with the cosmic microwave background (CMB) and produce pions, losing energy in the process. As the energy of a proton increases, the pion production reaction can happen with lower energy CMB photons. The net effect of this reaction is the existence of a different mean interaction length for protons depending of their energy. This interaction length is the mean distance a given cosmic ray would travel before interacting with the CMB. To obtain it, the power spectrum of the interacting background photons (i.e. CMB) it is combined with the cross section of the reaction. At very high energies (above $10^{19} eV$), the interaction length becomes of order 50 Mpc. However, sources of cosmic rays with such an enormous energy are supposed to be at further distances. The Greisen-Zatsepin-Kuzmin limit (GZK cutoff) is a theoretical cutoff expected on the energy of cosmic rays from distant sources based on the pion production. The actual theoretical GZK cutoff occurs at $5 \cdot 10^{19} eV$. Cosmic rays with energies above this cutoff have very 'short' interaction lengths, losing rapidly their energy in every interaction with the CMB till their energy fell below the cutoff. Therefore, extragalactic cosmic rays with energies greater than this threshold energy should never be observed on Earth.

   A number of different experiments have looked for the GZK cutoff, with conflicting results. AGASA found trans-GZK events inconsistent with the GZK cutoff while Hi-Res has found evidence for the GZK cutoff, although both experiments lack enough statistics to have conclusive results. Due to the impossibility to answer the question of the existence of the GZK cutoff with the present experimental results,

a new experiment called AUGER is been build at present, expected to resolve this issue in the next few years.

In case of an absence of the GZK limit, the violation of the Lorentz invariance could be a possible explanation of the effect [86] [6]. Since LIV may produce shifts in the threshold of reactions, the location of the GZK cutoff, or even the inexistence of the cutoff, would give significant information about Lorentz violation. In reference [85] this argument, together with the present experimental results, was used to set limits to some modified dispersion parameters, achieving the conclusion that $|f_p^{(3)}| < \mathcal{O}(10^{-14})$. These results must be taken with some care due to the mentioned controversial results about the cutoff used. Nevertheless, several authors have argued that the precise measurement of the GZK cutoff with the next cosmic ray observatory AUGER could be one of the more precise tests to Lorentz invariance. If the cutoff is seen, then Lorentz violation will be severely constrained, while no cutoff or a shifted cutoff might be a positive signal. Before truly accurate constraints can be calculated from the GZK cutoff, a more detailed analysis of the dynamics in a Lorentz violating Effective Field Theory (EFT) must be done. This analysis should consider the particulars of the background photon distribution and the cross-section reaction.

2. **Photon annihilation**

   As it was shown in chapter 5, the Mkn 421 shows a clear cutoff in the energy spectrum. This well-known behaviour is a common characteristic of all extragalactic sources observed by IACTs (e.g. Mkn 501, 1ES1959, etc). The accepted explanation for this effect is the expected absorption by the diffuse background radiation fields, or Extragalactic Background Light (EBL), of the high energy gamma rays when traversing cosmological distances. This absorption process is based on the photon annihilation interaction $\gamma + \gamma \rightarrow e^+ + e$.

   Like in the case of the GZK cutoff, the threshold of this reaction could be affected by the presence of Lorentz invariance violation, which makes possible to use this EBL absorption to constrain LIV. Various authors have argued for different constraints on the n = 3 dispersion relation, based upon how far the threshold can move. The constraints vary from $f_\gamma^{(3)} < \mathcal{O}(1)$ *to* $\mathcal{O}(10)$. Nevertheless, these constrains may be taken with some care due to the present lack of information about the spectrum of the background IR photons, which is the most relevant EBL component for the absorption of the γ energy range observed by IACTs. Since there is so much uncertainty about the situation, we will not treat this constraint in more detail. For discussions see [84, 85].

Synchrotron radiation

One of the net effects of the existence of a modified dispersion relation with negative $f_e^{(n)}$ for electrons or positrons is that they have a maximal velocity less than the low energy

[6] There exist a set of proposed explanations for these observations which do not need the violation of Lorentz symmetry. First, the observations could be due to an instrumental error. Second, despite it is unclear what these sources could be, the cosmic rays could have local sources. It could also be the case that ultra-high energy neutrinos might be created at great distances and later react locally to give rise to the particles observed.

speed of light (i.e. c). Therefore, there is a maximal synchrotron frequency regardless the electron (or positron) energy.

In reference [87] the statement that the emission from Crab Nebula could be explained using *Synchrotron Self Compton* model is used to argue that the observed radiation from Crab Nebula at 100 MeV is produced by synchrotron emission from high energy electrons (and/or positrons). Deriving the velocity for these electrons from previous argument, it is possible to constrain the modified dispersion parameter for electrons to the level of $f_e^{(3)} < \mathcal{O}(10^{-8})$. [7]

Birefringence

As it was mention in 6.1.2, certain test theories (e.g. SME) include the possibility of birefringence. In the presence of birefringence, a linearly polarized wave rotates its direction of polarization during propagation. Hence the observation of linearly polarized radiation coming from far away can constrain Lorentz invariance violation. A number of distant astrophysical objects exhibit strong linear polarization in various low energy bands which can be used to constrain this kind of phenomenon. The strongest currently reliable constraint use UV light from distant galaxies, and is given by $|f_{\gamma_{R,L}}^{(3)}| < \mathcal{O}(10^{-4})$ [88]. An even stronger constraint $|f_{\gamma_{R,L}}^{(3)}| < \mathcal{O}(10^{-14})$ was derived in [89] using the measured polarization of MeV photons from GRB021206. However, the data has been reanalysed in different studies and no statistically significant polarization was found [90].

Time of flight

The time-of-flight (TOF) approach consists in the measurement of a possible dependence with energy of the speed of light, hence testing the possible existence of modified dispersion relation for photons. This test is based on the detection of a different time-of-flight for photons with different energies produced simultaneously in distant sources. This kind of measurement was firstly proposed by Amelino-Camelia and co-workers in [74]. In this pioneering work of Quantum Gravity phenomenology, the authors proposed the Gamma Ray Burst (GRB) observations as very sensitive tests to the invariance of the speed of light. They remarked the fine-scale time structure and hard spectra of GRB emissions together with their cosmological origin as a possible scenario where to constrain the modified dispersion models to the order of the Planck scale (i.e. f^3 of order 1).

After this proposal, several authors performed measurements using different kinds of astronomical sources, but none of them accomplished constrains up to the Planck scale. The best present limit are provided by observations of the most rapid flares from Mkn 421 observed by the Whipple telescope [91]. In that work, the Mkn 421 showed a strong correlation of flux at 1 TeV and 2 TeV on a time scale of 280 sec, leading

[7] In reference [63] it is argued that this result does not take into account the possibility that the high energy synchrotron emission could be due to positrons, which may also be generated near the pulsar. This is an important possibility, since in the EFT that gives rise to $f^{(3)}$ terms for electrons, the positron has an opposite dispersion modification. Hence there is always some charged particle in the Crab Nebula with a dispersion modification that evades the synchrotron constraint. The possibility that there are two different populations, one of electrons and one of positrons, both contributing to the overall spectrum would mean a departure from the *Synchrotron Self Compton* model, which presupposes only one population of particles injected into the nebula. However, such a possibility cannot be ruled out without more detailed modelling of the Crab Nebula and a better understanding of how the initial injection spectrum of particles from the pulsar is produced.

to a constrain of $|f_\gamma^{(3)}| < \mathcal{O}(300)$. The best result from the observation of GRBs was presented in reference [92, 93] with a constrain of $|f_\gamma^{(3)}| < \mathcal{O}(10^3)$ while the best constrain from Pulsars is of the level of $|f_\gamma^{(3)}| < \mathcal{O}(10^4)$ [94].

For a detailed discussion about this measurement see section 6.4.2.

6.3 Summary of the phenomenological framework

The present situation of Lorentz invariance experimental test results has change enormously in less than a decade. From the first experimental proposals sensitive to the Planck scale till the present constrains in many parameters beyond first order Planck scale modifications, there has been a big improvement. At present, the worst constrained sector is the photon sector, were not even first order Planck scale constrains have been achieved experimentally. This situation motivates the interest for new measurements of LIV by photons.

From the theoretical point of view, some authors argue that from the present experimental results it is hard to believe that Lorentz invariance could be violated in a manner that is theoretically natural. Nevertheless, there are theoretical proposals like Double Special Relativity which evades most of the threshold constraints from astrophysics (e.g. the photon decay and vacuum Cherenkov constrains), as well as any constraint from terrestrial experiments that look for sidereal variations, leading a modified energy dispersion relation (i.e. energy dependent velocity for photons) as the only signature able to rule out this theory.

In this scenario, we believe that the test of the invariance of the speed of light is the most favourable approach to constraint LIV in the photon sector. At present, time-of-flight is the only experimentally viable measurement able to constrain the modified energy dispersion up to the Planck scale. This will produce the last piece in this first generation of Quantum Gravity phenomenology experiments, leading to the first evidence of new physics beyond General Relativity or constraining very much the Lorentz invariance in the Quantum Gravity theories.

6.4 Time of flight measurement with MAGIC

In the introduction of this chapter it was pointed out that the violation of the Lorentz invariance may produce a modification of the energy dispersion relation. This would lead to a modification of the velocity of massless particles and in particular of the photon (see appendix C.1 for derivation of the modified velocity expression) like,

$$v = 1 - \frac{n-1}{2} \cdot f_\gamma^{(n)} \left(\frac{E}{E_{Pl}} \right)^{(n-2)} \tag{6.4}$$

In this expression some approximations have already been made, being the resulting expression a phenomenological approach for low energy photons (i.e. low energy compared to the Planck scale hence adequate for TeV γs). From this approximation n represents the first term of the phenomenological approach with non zero value. From this expression it can be derive that for the range of energies IACTs are able to observe the modification in the velocity of γs is extremely small (i.e. $\mathcal{O}(10^{-16})$ for TeV γs). However, the idea behind the observation of this kind of effects is to amplify this tiny energy dependence using the travel of γs from cosmological distances looking the energy dependence of the

γs time-of-flight. In such a way, the tiny effect in the velocity for TeV photons becomes an observable effect looking at the energy dependence of the gamma time-of-flight.

$$t = t^0 + \Delta t \sim t^0 + \frac{n-1}{2} \cdot f_\gamma^{(n)} \left(\frac{E}{E_{Pl}}\right)^{(n-2)} D \tag{6.5}$$

where t^0 represents the time-of-flight assuming photons travel at the 'classical' speed of light c, Δt is the time delay due to the LIV and D is the distance to the source.

This simple approximation has been already used in most of the measurements performed about this kind of effect. Those experiments exclude the possibility of terms below $n = 3$ which motivates the study of the cases $n \geq 3$. Nevertheless, $n = 4$ means an E_{Pl} suppression factor in the time delay. As it will be shown in next section, the expected time delay for the scenario $n = 3$ already puts very demanding observational requirements for IACTs. That means that in case of being the first term of the type $n = 4$ it would lead to a non measurable Δt ($\mathcal{O}(10^{-16}s)$) for the energy ranges of IACTs. Therefore we cannot exclude the possibility that the leading term of a possible underlying theory which violates LI goes as $(E/E_{Pl})^2$ but, if it was the case, the IAC Telescopes would not have any chance to test it with the gamma time-of-flights. That forces us to study only the most favourable case (potentially largest effects) hence $n = 3$.

In addition to this experimental argumentation, it has been already pointed out in the introduction of this chapter that there are present theories like the Doubly Special Relativity which specifically predicts a modified velocity with leading order $n = 3$ (see section 6.1.2). This fact adds to the study of the $n = 3$ scenario the potential of confirming or ruling out an already proposed theory.

The previous expressions in the scenario with leading order $n = 3$ produce the following expressions:

$$v = 1 - f_\gamma^{(3)} \frac{E}{E_{Pl}} \tag{6.6}$$

$$t = t^0 + f_\gamma^{(3)} \frac{E}{E_{Pl}} D \tag{6.7}$$

This energy dependence time delay should be one of the cleanest signatures that Cherenkov telescopes are able to study in order to spot Lorentz Invariance violation effects. Nevertheless, as it has already been pointed out in the literature, this signature might be mimicked by processes related to the source physics (internal production delays for higher energy γs) or propagation (time delay due to cascading in intergalactic magnetic fields [95]). Therefore it is mandatory to use the scaling of the effect with redshift to distinguish between energy dependence velocity of photons and any source-dependent phenomena [91] in case of observing an energy dependence time delay. It is important to remark that in case of not observing any effect the sensitivity achieve measuring the effect can be used to derive a limit in the phenomenology framework described above. This is correct except in the unrealistic scenario in which there exist both effects, a LIV effect and a propagation or source effect, of the same order of magnitude and with opposite effect in such a way they cancel out.

One of the main goals of this Thesis is the study of the invariance of the speed of light measuring an energy dependence time-of-flight for γs using the MAGIC Telescope observations. This study was motivated by previous works either in phenomenology and already existing experimental observations (see section 6.2.2). In this Thesis is stressed

the study in the advantages for an IAC Telescope like MAGIC may have to observe energy dependent time-of-flight effects. Moreover, the present experimental approaches to this measurement have been revised critically, proposing a new methodology which intends to extract the maximum information from the present observations.

6.4.1 Optimal LIV measurement scenario with present IACTs

The previous generation of IACTs was able to observe a handful of galactic and nearby extragalactic sources, all of them with modest redshift. The reason for the lack of further sources is the attenuation of the flux of high energy gamma rays by the interaction with the diffuse Extragalactic Background Light (EBL) through the pair production reaction (i.e. $\gamma_{VHE}\gamma_{EBL} \rightarrow e^+e^-$). From the practical point of view, the net effect for those γs is the existence of an interaction length when they travel cosmological distances.

A widely used concept to work with this idea is the *Gamma Ray Horizon* (GRH), which limits the feasibility of observing very high energy gamma rays coming from very far distances. The GRH gives the energy, for a given redshift, above which the observation of γ-rays becomes very difficult, due to the fact that they have been absorbed by their interaction with the EBL.

The new generation IACTs have a lower threshold than the previous Cherenkov telescopes. In fact, lowering the energy threshold is the first goal of MAGIC with the aim of observing more distant sources in the VHE energy domain. The discussion of the possible improvements in the observation of an energy dependent time-of-flight for γs due to this threshold reduction in the new IACTs was the maim point in our previous work on the topic of Lorentz invariance violation was published in [96]. In the paper we discussed fundamental aspects of the observation with the aim of setting the best scenario within the VHE astrophysics for the study of these effects. In the next paragraph the main discussion shown in the paper as well as the final conclusions are summarized.

Time delay evolution with redshift

In previous works before the mentioned paper, the expected time delay due to LIV was parametrized using a simple approximation of the type shown in equation 6.6. This expression is correct for the extragalactic nearby sources like the ones detected by the old IACTs. However, this approximation might be not appropriate for the present observation situation with the expectation of observing further sources. For this reason the proper derivation of the expected time delay expected for γs was done.

The first point to take into account in this derivation is the fact that γs detected at Earth with energy E have changed their energy during the cosmological travel due to the expansion of the universe. This changes the expression for the velocity of photons to,

$$v = 1 - \frac{n-1}{2} \cdot f^{(n)} \left(\frac{E\,(1+z)}{E_{Pl}} \right)^{(n-2)} \tag{6.8}$$

Once the velocity for the photon is known in every redshift, the lookback time expression can be used to compute the time the photon takes to arrive from a given redshift to the Earth [8].

[8] All the results presented in this section about our paper were computed using the best fit values for the fundamental cosmological parameters (i.e $H_0, \Omega_M, \Omega_K, \Omega_\Lambda$) following reference [97]. Those results after WMAP satellite are outdated, however the conclusions obtained in the paper and reproduced in this section still holds.

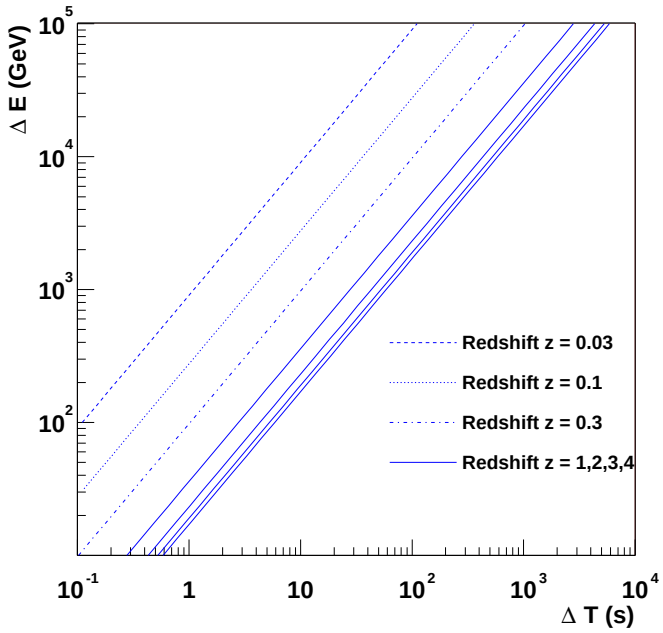

Figure 6.1: Expected time delay as a function of the γ-ray energy for different redshift sources for $f^{(3)} = 1$.

$$t = \int_0^z \frac{1}{v}\frac{dt}{dz}dz \tag{6.9}$$

$$t = t^0 + \Delta t = \int_0^z \frac{dt}{dz}dz + \frac{n-1}{2}\cdot f^{(n)}\left(\frac{E}{E_{Pl}}\right)^{(n-2)}\int_0^z (1+z)^{(n-2)}\frac{dt}{dz}dz \tag{6.10}$$

Finally, as it was pointed out before, time-of-flight experiments with IACTs are only sensitive to terms of type $n = 3$ in previous expression, leading the expected time delay as follows,

$$\Delta t = f^{(3)}\frac{E}{E_{Pl}}\int_0^z (1+z)\frac{dt}{dz}dz = f^{(3)}\frac{E}{E_{Pl}}D^* \tag{6.11}$$

where D^* corresponds to the lookback time integral and can be understood as an effective distance to the source although it is quantitative bigger than the distance travelled by the photon due to the extra $(1+z)$ term. In such a way, the time delay becomes again proportional to the energy of the gamma and to an effective distance to the source.

In figure 6.1, the lines in the plane E versus Δt provided by the above equation for a set of different source redshifts are shown. Each line represents the expected dependence between time delay and energy for a γ coming from a source at the corresponding redshift.

The aim of this study was to understand the role of observing distant sources in the time-of-flight analysis. For this reason the lines in this figure can be understood as the limits for the possible observation of energy dependent speed of light effect for a given time delay sensitivity (i.e. Δt), energy and redshift. In that interpretation, the region of the figure above the line (i.e lager energies and lower time delay sensitivities) would

make possible the observation (or constrain in case of absence of any effect) of the energy dependent time-of-flight above the Planck scale (i.e. $f^{(3)} \leq 1$). In that interpretation the lines represent the conditions where the experiment is sensitive exactly to the Planck scale.

From the last figure and the derived expression 6.11, within this new interpretation there could be deduced two conclusions. The first one is that the effective distance giving the z dependence of the time delay, see equation 6.11, has a correction of $(1+z)$ to the lookback time integrand which produces that the Δt saturates more quickly than in the absence of modified velocity of gammas. That point could be important when selecting the distance where to observe sources to maximize the sensitivity in the effect or when scaling the effect with redshift to disentangle between energy dependent speed of light effects from source or other propagation effects. A second conclusion could seem to be that for γs detected with a given energy, less demanding time delay sensitivities are needed to prove the Planck scale looking a further distant sources. Nevertheless, this conclusion should be checked carefully because the existence of the previous mentioned *Gamma Ray Horizon* which, as it will be shown in next paragraph, forbids some region in figure 6.1 due to the lack of γs absorbed by the EBL.

Gamma Ray Horizon

The interaction of high energy γs with the EBL leads to the existence of an *Gamma Ray Horizon* (see references [98, 40] and references therein). The GRH limits the observation of very high energy γ-rays coming from very far distances. The actual value of this horizon distance for γ-rays depends on the density of the diffuse background radiation (i.e. EBL). Moreover, due to the peaked cross-section of the responsible interaction (i.e. pair production) there is a specific relevant energy range for given γ energy. In the range of energies which can be effectively studied by present IACTs (from 50 GeV to 50 TeV), the most relevant EBL component is the ultraviolet (UV) to infrared (IR) contribution.

Due to the well known cross-section for the pair production reaction, the key ingredient in the calculation of the GRH is the EBL density. Different models have been developed to try to predict the EBL density for all redshifts. In these models a complex convolution of the measurements of star formation rate, initial mass function and dust and light recycling history is done. Using these models precise predictions of the GRH can be made, although there exist rather considerable systematic uncertainties between models which are nowadays not possible to rule out due to lack of a direct measurement of the EBL at some wavelengths (e.g. in the IR). The existence of the absorption of high energy gammas from the EBL is very likely the reason for the absence of observation of far sources in the VHE regime. However, so far, no clear confirmation of the value of the GRH can be drawn from the observations of the present data from IAC Telescopes.

The Gamma Ray Horizon used in our paper was derived using the EBL model from [99]. The results of this calculation are shown in figure 6.2. Although there exist model dependencies in the derivation of the GRH, they are mostly for low redshift, leading the results for medium-large shift almost model independent [40]. It will be shown and discussed in this section that low redshift predictions are not important for the conclusions derived in the paper. Therefore, the conclusion derived in the paper using the previous GRH calculation holds for any other EBL prediction.

The above GRH calculation has been obtained assuming purely Standard Model Physics. The existence of LIV should also affect the calculation of the Gamma Ray Hori-

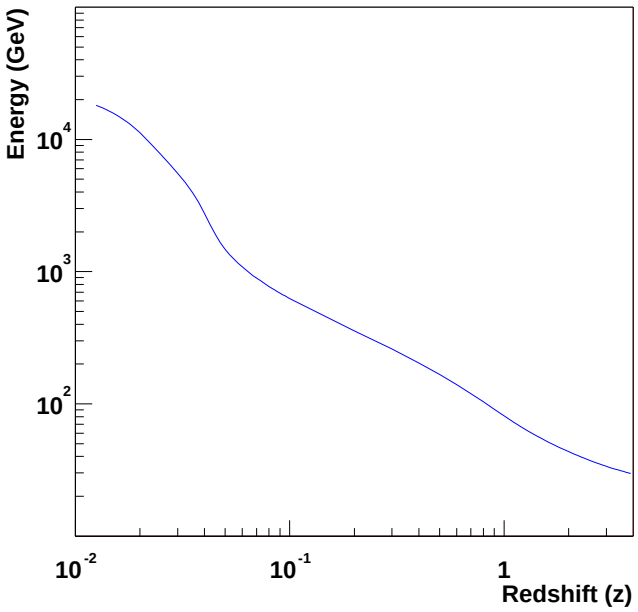

Figure 6.2: The Gamma Ray Horizon computed assuming purely Standard Model Physics.

zon, since the threshold energy of the pair production interaction is modified [100, 101] (see section 2). Therefore, to be consistent with the framework of the analysis, in the paper we implemented consistently the calculation of the GRH including the threshold-modifying effects coming from LIV inspired modified dispersion relations.

In the Standard Model calculation of the Gamma Ray Horizon the energy threshold for the electron-positron pair production is given by

$$\epsilon_{tr} = \frac{2m_e^2}{E_\gamma x(1+z')^2} \tag{6.12}$$

where $x \equiv 1 - cos\theta$ being θ the γ-γ scattering angle.

After including the modified dispersion relation, the threshold condition is modified leading the following expression,

$$\epsilon_{tr} = \frac{2m_e^2}{E_\gamma x(1+z')^2} - f^{(n)} \frac{2}{x(1+z')} \frac{[E_\gamma(1+z')]^{(n-1)}}{4E_{Pl}^{(n-2)}} \left(\frac{1}{2^{(n-2)}} - 1 \right) \tag{6.13}$$

where E_γ and ϵ_{tr} are the energies at the Earth and, therefore, we had to add some $(1+z')$ factors respect to previous equation. In figure 6.3 the resulting GRH for different values of $f^{(3)}$ are shown.

The net effect of the correction is to increase the threshold energy in such a way that, for any given gamma energy, EBL photons with lower wavelength are responsible for their absorption. The main consequence of the modification of the pair production threshold is the modification of the GRH for low redshift, arriving in the most extreme cases to make the universe become transparent again for large energy gammas. Nevertheless the results for the lower energy γs (i.e. medium-large redshifts) in the GRH remain basically unmodified.

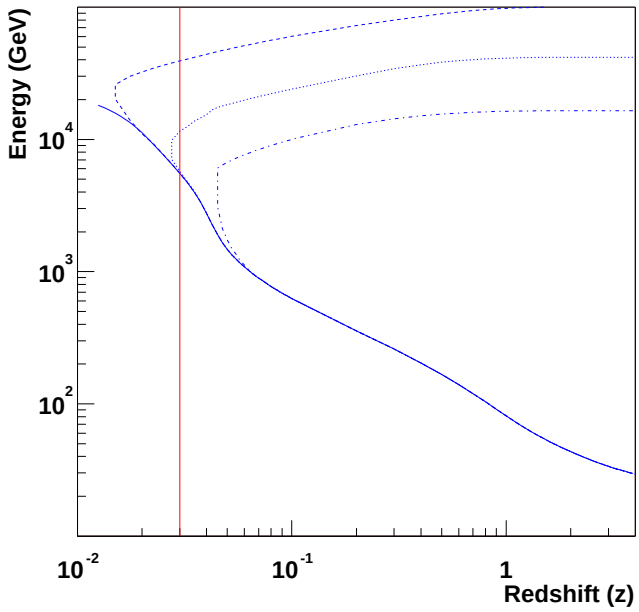

Figure 6.3: The Gamma Ray Horizon computed assuming LIV motivated modified pair production threshold. The continuous line is for a calculation without LIV whereas the dashed, dotted and dash-dotted lines are for values of $f^{(3)} = 1$, 10 and 100 respectively.

To arrive to the final conclusion it is necessary to put together the two ideas discussed in previous paragraphs: on the one hand, the capability of observing more distant sources should allow to explore stronger constrains in $f^{(3)}$ due to the direct relation between the expected time delay and the redshift of the source. Unfortunately, on the other hand, for more distant sources, the gamma absorption in the EBL is stronger and the Gamma Ray Horizon happens at smaller gamma energies. This forces the study in the time-of-flight to be done with lower energy gammas, leading to smaller time delays due to the direct relation between both quantities.

This trade-off is summarized in figure 6.4 where, on top of the E versus Δt lines predicting the propagation delays, one can see the parameter region beyond the Gamma Ray Horizon. It must be stressed here that the Gamma Ray Horizon does not mean a "hard boundary" since it just gives the condition for an e-fold reduction of the observed flux. Because of that, the shaded area given by the Gamma Ray Horizon has to be understood as the region in which the flux reduction due to the absorption starts being strong enough to make the source observation difficult.

From this figure it is clear that to explore above the Planck scale, time delay sensitivities on the scale of just few seconds will be mandatory quite independently on the actual source redshift and energy of the observed γ-rays. Moreover, taking into account that time delay goes linear with the energy scale of the modified dispersion relation (i.e. $f^{(3)}/E_{Pl}$) time delays sensitivities of tenths and hundreds of seconds are necessary to constrain $f^{(3)}$ to $\mathcal{O}(10)$ and $\mathcal{O}(100)$ respectively.

It could be considered that delay time sensitivities of the order of few seconds should not be difficult to achieve with present detection technologies. However, the delay sensitivity requested before is not related to the time measurement error of the telescope.

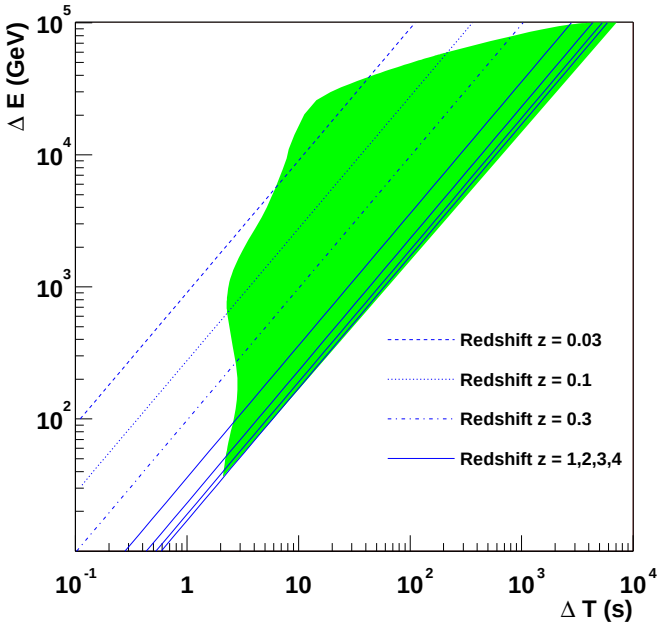

Figure 6.4: Expected time delay as a function of the γ-ray energy for different redshift sources for $f^{(3)} = 1$ and including the GRH. The shadow(green) area is a projection of the Gamma Ray Horizon in the ΔE v.s. Δt plane.

Instead, it is strongly related with the internal time structure of the gamma emission. In the kind of observations used for this measurement, there is no absolute time reference with which compare the arrival time of the γs and compute the possible time delay they suffer. In fact, any measurement of TOF is based on the idea of looking for a possible energy dependent shift in time of some variability in the emission. In most of the present approaches in the literature, the experimental method consists in comparing the time position for the maximum of some peak in the light curve in several energy ranges. The time delay sensitivity in such cases is related to the precision for the time position of the used peak, which is given by the intrinsic width of that peak and the total number gammas detected within the peak. This derivation of the relation between the time delay sensitivity with the time scales of the emission variability might seem very specific for the case of peak based measurements. However, it can be generalized to cases where some variability in the time structure of the emission could be used as a time reference.

In this context, IACTs with lower energy threshold like MAGIC have an advantage measuring time delays. Lowering the threshold opens the possibility to observe a new kind of cosmological VHE gamma emitters like the Gamma Ray Bursts. Time structures with peaks narrower than seconds have been observed by satellite in lower energy ranges than IACTs. Moreover, several models predict VHE emission for GRBs although no clear confirmation up to now has been found. Several problems explain the lack of observations. The first one is the cosmological origin of GRBs which make impossible their observation by old IACTs due to the Gamma Ray Horizon. The second, the rapid falling down of the emission after the beginning of the burst, makes the prompt observation of the GRBs essential for their detection. Nowadays, there exist a net of satellites which provides alerts about Gamma Ray Burst location when a burst is detected by some of them. Together

with this vital information, MAGIC has been designed to be able to point to any part of the sky in less than 100 sec and 40 sec in average moving from two random positions in the sky. This characteristic was introduced in the design of MAGIC with the aim of being able to detect GRBs. The detection of one of those GRBs in the VHE regime will be a milestone in the astrophysics field as well as a fantastic tool to test the invariance of the speed of light up to the Planck scale with the time-of-flight experimental approach.

In this Thesis we are interested in investigating the time-of-flight with AGN flares. The reason is that AGNs are the fastest variable source already observed in VHE regime at cosmological distances, hence leading to the maximum time delay effect being measured with IACTs. This situation might change if IACTs or the next γ-rays satellite generation (e.g. GLAST) detects GRBs. However, within the present observational capabilities, AGNs are the best experimental scenario for this kind of studies in the VHE regime.

6.4.2 Proposed measurement approach

The measurements already presented in the literature about TOF [91, 92, 93, 94] might seem very different among each other because they use different astronomical sources in their observations (e.g. AGNs, GRBs and pulsars); different time scale structures in the emission; different energy ranges and quite different mathematical algorithms in the measurement of a possible positive effect. Nevertheless, all of them are based in the same idea of looking for a time shift with energy of the position of a peak in the source emission. This makes necessary the integration of the number of γs in time bins, which averages the information from every event. The method presented in this work, on the contrary, is able to use the information from every single γ, thus increasing the sensitivity of the measurement.

Before introducing the new measurement method in detail, a brief review of the most significant measurements already performed about TOF is presented.

6.4.2.1 Present measurements

AGNs

The most successful measurement about TOF until now was presented by the Whipple collaboration in reference [91], shortly after the pioneering Amelino-Camelia paper proposing the whole method. In that work, the most rapid flare ever observed from Mkn421 in the VHE energy regime (see reference [102]) was used. The combination of the short time scale, of the order of minutes for that flare, together with the extragalactic origin of the TeV γ observed by the Whipple telescope, made that scenario very promising for the TOF measurement.

In the mentioned work, the method follows a quite simple but robust mathematical approach. The authors compare two light curves in different energy ranges for the same flare (see figure 6.5). These two histograms represent the observed number of γs below 1 TeV and above 2 TeV in time bins of 280 seconds. Both histograms show a maximum (i.e. peak) for the same time bin together with the absence of events in the two immediately adjacent bins to the maximum in the highest energy histogram. That particular situation let the authors the possibility of computing the probability of absence of time delay of the order of the time binning with a confidence level of more than 99%. From this time delay limit, it can be calculated a limit in $|f^{(3)}|$ of the order $\mathcal{O}(300)$, taking into account also both the energy difference between the two histograms and the distance to Mkn421.

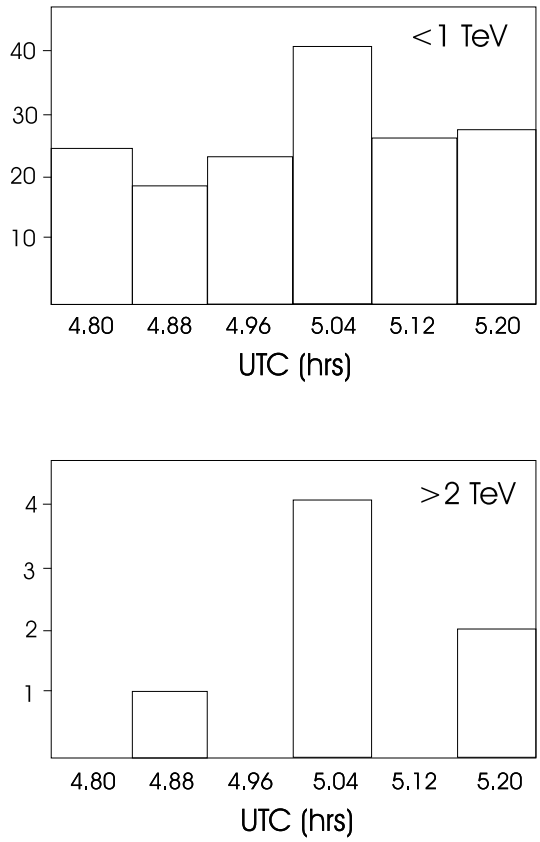

Figure 6.5: Number of γs observed by Whipple for the Mkn421 flare during 15th May 1996. The top plot represents the γs observed with less than 1 TeV, whereas the bottom plot is for energies above 2 TeV. Figure extracted from reference [91].

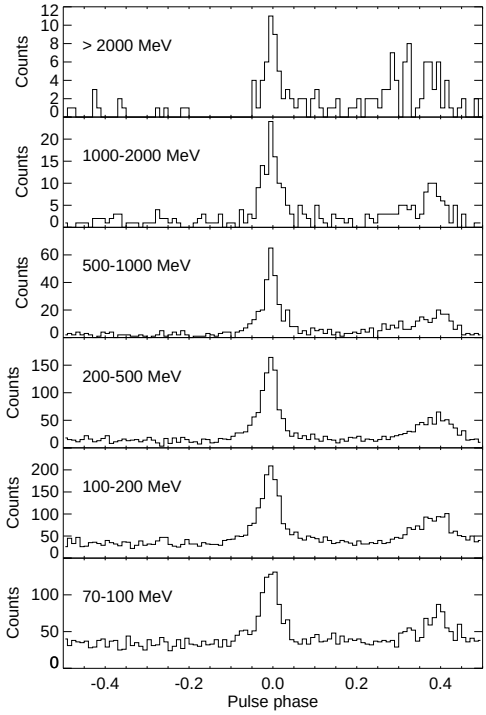

Figure 6.6: Crab Nebula phase histograms for various energy ranges using data from the EGRET detector. Figure extracted from reference [94].

This result was computed using a Hubble constant of 85 km/sec/Mpc. However, using the present best results for the cosmological constants (i.e. $H_0 = 71 \pm 4$ km/sec/Mpc), the actual result would be $|f^{(3)}| < \mathcal{O}(260)$.

Pulsars

There exist in the literature a measurement about TOF using the pulsed emission in soft γ-rays from Crab Nebula pulsar (see reference [94]). In that work, data from the EGRET detector placed in the *Compton Gamma-Ray Observatory* (CGRO) satellite was used. The possible time delay was studied by looking for an energy dependence shift in the pulsed γ-rays arrival time. For doing that, the pulse phase histograms for the detected γ-rays where produced for several energy ranges, from 70 MeV to 2 GeV (see figure 6.6). The position of the main peak was calculated fitting each histogram using a Lorentzian profile. From the result of those fits, no statistical significant variation with energy was found for the position of the peak. The authors used those results to put a limit in a possible modification of the speed of light based on the results that the peak position between the lowest energy range (i.e. 70-100 MeV) and the highest (above 2 GeV) was less than 0.35 ms with a 95% confidence. These values, together with the distance to Crab Nebula, lead to a limit in $|f^{(3)}|$ of $\mathcal{O}(10^4)$. Something important to remark about this particular result is that, in addition to be two orders of magnitude worse than the result using Mkn421 fastest flare, is calculated at 95% confidence level in comparison to the 99% confidence level of Mkn421 results.

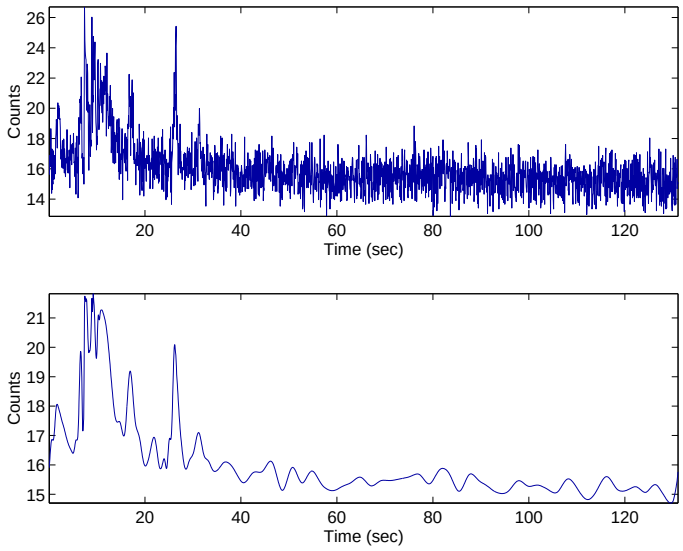

Figure 6.7: GRB990308 light curve observed by the BATSE satellite. The upper plot shows the direct measurement from the satellite whereas the bottom one shows the approximation given by the wavelet technique. Figure extracted from reference [92].

GRBs

The most sophisticated approach, from the mathematical point of view, about measuring energy dependent TOF was presented in references [92, 93]. In their paper, the authors use data from the observations of GRBs by a set of satellites composed by BATSE and OSSE detectors in the CGRO telescope, together with the new HETE and SWIFT satellites. One of the important differences between this work and the aforementioned ones is that in this paper the possible energy dependent time delay is studied for several objects covering a quite wide redshift range, whereas in the previous measurements just one object, either Mkn421 or Crab Nebula, was used. This peculiarity allows the authors of the paper to be independent of the possible source induced energy dependent time delay in case of observing a positive effect. In this work the evolution with the distance to the object is taken into account in the analysis, making a positive result just explainable due to propagation effects (e.g. energy dependent speed of light). The authors used GRBs light curves in different energy ranges going from 25 to 320 KeV.

The most important particularity of these measurements is that the authors used wavelet transformation for the selection of intrinsic peaks (i.e. not statistical fluctuations) in the analysis of GRBs light curves (to see an example look at figure 6.7). The wavelet analysis is similar conceptually to Fourier analysis, although making a scale (in our case, a time scale) analysis instead of a frequency analysis. That makes possible theoretically to 'clean' (i.e. filter) a signal from non intrinsic time structures, leaving just the intrinsic ones. Together with this noise filter, the wavelet analysis provide a mathematical technique to get the time position of the maximum for all the peaks that the wavelet transformation has selected as real signal peaks. The authors called that maximum positions *genuine variation points*. They combined the positions of all the *genuine variation points* present in the lowest (i.e. 25-55 KeV) and in the highest (above 320 KeV) energy bands to set a global time delay per GRBs. Putting together all the results for the set

of GRBs, they made a global fit to the time delay evolution with the distance to GRBs, finding no significant statistical delay. This led the authors to set a limit in $|f^{(3)}|$ of the order of $\mathcal{O}(10^3)$ at 95% confidence level.

Common Remarks about present TOF measurements

All the aforementioned measurements, despite using very different kind of sources and mathematical techniques to study the energy dependent time-of-flight, are based on the same concept: to use light curves (or histograms in time) to extract a possible time delay. This means that all these methods integrate the γs time information within a time bin. Moreover, comparison between light curves, which are themselves averaged quantities, are computed in energy ranges which makes nothing else than averaging the light curve within the corresponding energy range. In this sense, in all these methods each observed γ does not contribute directly to the global measurement of the time delay dependence, but through averaged quantities, losing by definition some of the information obtained when measuring the time and energy of individual γs.

Motivated by this limitation of the previous presented methods, we investigated the possibility of using the direct information of every observed γs (i.e. arrival time and energy) for the study of time delays. The aim of searching for this new method is to use the maximum information available, therefore to have the maximum sensitivity, when studying TOF for a given observation.

In the rest of this section, we present the new method to measure the time delay as well as all the mathematical and experimental studies we have performed related with this measurement.

6.4.2.2 Covariance analysis

The method we present is based on the idea that in case of existing a linear energy dependent time-of-flight for γs, there should exist a mathematical correlation between their arrival time and their energy. Mathematically, this can be straightforward derived from equation 6.11,

$$t = t^0 + f^{(3)} \frac{E}{E_{Pl}} D^* \equiv t^0 + \eta \cdot E \tag{6.14}$$

where η is the linear relation between the time delay Δt and the energy of the gamma E. Actually, η is just a redefinition of $f^{(3)}$ which is the magnitude pursuit in all the time-of-flight experimental measurements.

From the methological point of view it is possible to derive the value of η from the set of pairs formed by the measured arrival time t_i and measured energy E_i for each gamma (i.e. $\{t_i, E_i\}$ where i stands for each detected γ). Using the previous equation, we have derived an estimator of η based on first and second order momenta of the set of pairs $\{t_i, E_i\}$ (see appendix C.2 for the detailed derivation).

$$\eta \left(\equiv f^{(3)} \cdot \frac{D^*}{E_{Pl}} \right) = \frac{\langle tE \rangle - \langle t \rangle \cdot \langle E \rangle}{\langle E^2 \rangle - \langle E \rangle^2} = \frac{cov(t, E)}{\sigma_E^2} \tag{6.15}$$

In this method no averaging, neither in time nor energy, is necessary in the calculation of the time delay (i.e. η). Therefore, every single detected γ contribute to the calculation of the linear relation between time and energy in a direct way. In other words, the possible linear relation between time and energy for γs is measured individually for each of them,

and the final result is the 'addition' of the effect in all the γs and not in an averaged magnitude.

Before applying this method to the analysed Mkn421 data presented in this Thesis, it is important to understand its expected behaviour. This has been performed by applying the method to Monte Carlo simulated sample of γs. In the following paragraphs, the set of tests performed using this Monte Carlo sample is presented, with the aim of proving the viability as well as the possible limitations and best conditions to apply the proposed method.

Monte Carlo studies

For producing the necessary sample of γs, a simple Monte Carlo was developed. To use the full Monte Carlo of MAGIC was discarded because it was over dimensioned for the planned studies, which need quite a large sample of simulated γs, thus consuming enormous time and computing resources. Moreover, due to the fact that the aim of these studies is not making an accurate prediction of the expected behaviour of the MAGIC telescope, but to prove the first principles for the proposed method, a detailed description of MAGIC was not necessary. However, the simple Monte Carlo developed uses many results from the full Monte Carlo of MAGIC, such as the trigger collection area, selection efficiency, etc., in order to reproduce the behaviour of the telescope accurately enough.

In the next paragraph the core of the developed 'Simple' Monte Carlo is briefly explained.

1. **Production**.

   In the production phase the two basic magnitudes of the Monte Carlo which does not come from the full MAGIC MC are simulated. They are the emission time and energy for each of the γs. Those magnitudes are randomly simulated according to predefined probability density distributions. Due to the variability of Mkn421, a particular energy distribution and time emission has to be chosen. For the purposes of this thesis, results from a previous work (see reference [59]) have been used.

   For the energy distribution, the Mkn421 power-law with exponential cut-off shape is assumed:

$$dF/dE = 7 \cdot 10^{-11} \cdot \left(\frac{E}{TeV}\right)^{-2.0} \cdot e^{-\left(\frac{E}{3\ TeV}\right)} \cdot \gamma \cdot TeV^{-1} cm^{-2} sec^{-1} \qquad (6.16)$$

   This particular spectrum corresponds to an emission level of around two Crabs.

   From the point of view of the time emission, a simple flare model is used, with a non-symmetric peak structure of the type:

$$F(t) = a + \frac{b}{2^{-\left(\frac{t-t_0}{t_{doubling}}\right)} + 2^{\left(\frac{t-t_0}{t_{halving}}\right)}} \qquad (6.17)$$

   where a is a possible baseline in structure of the flare, $b/2$ is the height of the maximum of the peak to respect the baseline. The position of the peak is related with t_0 by the following expression,

$$t_{peak} = t_0 + \frac{t_{doubling} \cdot t_{halving}}{t_{doubling} + t_{halving}} \log_2 \left(\frac{t_{doubling}}{t_{halving}} \right) \tag{6.18}$$

Whereas $t_{doubling}$ and $t_{halving}$ are the doubling and halving times of the flare.

In the referenced work, it was found that the typical doubling (or halving) for Mkn421 has a distribution with two peaks, one around 20' and the second at 60'. These particular values have been used in most of the simulations although other values for the halving time of 40' and 20' where also simulated for studies related with the shape of the flare. It is important to remark that these used values for the doubling and halving times are not the fastest flare observed for Mkn421. However, for the study of the behaviour of the proposed method we have decided to use a representative scenario rather than an extreme one.

2. **Propagation**.

   The second step in the simulation is the energy dependent time delay motivated by the modified energy dispersion. For that purpose, the time delay from the expression 6.14 is used.

   For the simulation of this delay several quantities are necessary. First, the redshift of the studied source, which in the case of Mkn421 is $z = 0.031$. Second, the best fit values for the cosmological constants [103] necessary for the calculation of D^*. With these numbers, the D^* for Mkn421 has a value of $1.32 \cdot 10^{16}$ light-seconds.

   The golden parameter in this Monte Carlo simulation is the level of modification we introduce in the energy dispersion relation, or in other words, the value we set for $f^{(3)}$. We have set this value of $f^{(3)} = 100$, as a compromise between the actual best limits available in the literature and the lowest value is going to be possible to be measured with present conditions described in the 'Simple' Monte Carlo. However, in some places of the Monte Carlo study, this magnitude will be changed for higher and lower values in order to study dependencies of the method with the value of $f^{(3)}$.

   The relation between η and $f^{(3)}$ for the γs observed from Mkn421 is given by the following expression:

$$\eta = f^{(3)} \cdot \frac{1.32 \cdot 10^{16} \cdot sec}{1.22 \cdot 10^{19} \cdot GeV} = f^{(3)} \cdot 1.08 \cdot 10^{-3} \cdot sec\, GeV^{-1} \tag{6.19}$$

   then, with $f^{(3)}$ set to 100, the value for η is $0.108 \cdot sec\ GeV^{-1}$. From now on, in the Monte Carlo tests of the covariance analysis, η is the parameter actually being estimated. This has been done for mathematical simplicity: η is the linear relation between the time delay and the energy, which appears in all the formulation.

3. **Detection & Selection**.

   The last step in the simulation is the selection, from among all the simulated events, of the ones which are detected by the Telescope and, among these, the ones that pass the γ selection process. These two processes are done by using as probability density functions to be detected and selected the trigger collection area and the selection efficiency, respectively (see section 5.1.3.2). One extra thing performed in this part of the simulation is the calculation of the estimated energy for the γ. To

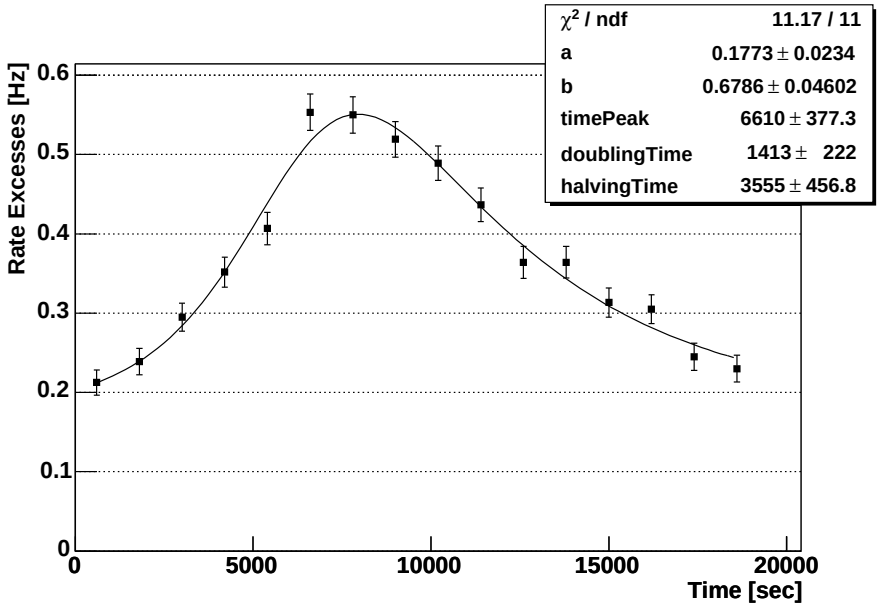

Figure 6.8: Mkn421 flare simulated with the 'Simple' Monte Carlo. This flare have been simulated using a doubling and halving times of 20' and 60' respectively and baseline equal to 1 and maximum to 3 in the time structure. The light curve have been computed for energies above 150 GeV.

do this, the energy resolution computed with the full MAGIC MC in section 5.1.1.3 has been used.

An example of the calculation of the light curve of the 'Simple' Monte Carlo simulation is shown in figure 6.8.

Bias produced by the energy resolution

There are two important things to investigate with the Monte Carlo described before. First, whether the 'covariance' method reconstructs correctly the value for η set in the Monte Carlo. Second, the calculation of the resolution of the method reconstructing the actual value, in order to see the power of the method.

To investigate these two points, η has been estimated with the 'covariance' method for a large number of independent equivalent flares, that is, flares with the same underlying MC parameters. With all these results, it is possible to make the distribution for the estimation of η, which is expected to be a Gaussian centred in the actual value of η with a sigma equal to the resolution of the estimation. Figure 6.9 shows the distribution for η computed for the kind of flare of figure 6.8.

From the previous figure it can be derived that the mean value obtained is not statistically compatible with the value set in the Monte Carlo (i.e $\eta = 0.108 \cdot sec\ \ GeV^{-1}$), in fact the mean reconstructed value is 4 sigmas to the one set in the 'Simple' Monte Carlo. After some investigation, it was observed that this bias in the estimation of η disappears if the previous distribution was computed using the actual MC energy of the γs and not the measured energy.

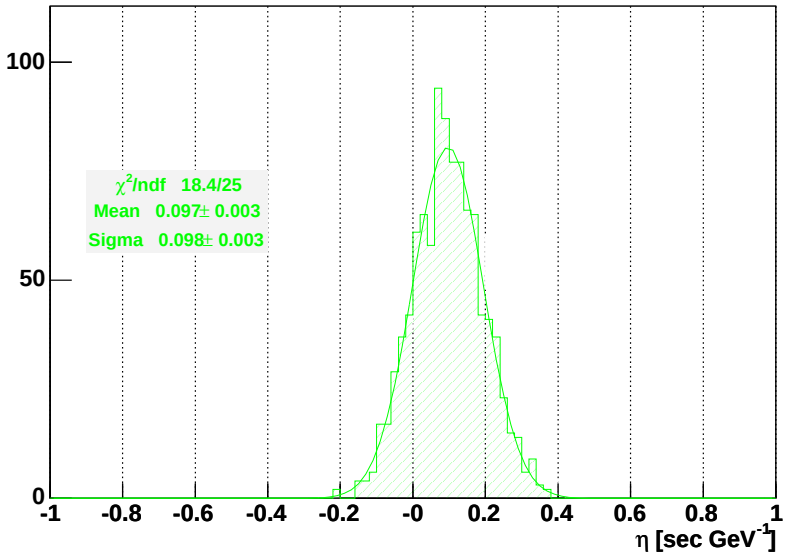

Figure 6.9: η distributions. The distribution is fitted using a gaussian and the results of the fit are shown in a label on the figure.

Therefore, the fact that the energy measured for the γs has a certain resolution produces a bias in the estimation of η with the 'covariance' method. The magnitude of this bias can be derived mathematically just rethinking the basic equations that describe the two magnitudes measured for γs.

$$t = t^0 + \eta \cdot E_{True} \tag{6.20}$$

$$E_{Reco} = E_{True} + Res(E_{True}) \tag{6.21}$$

where E_{True} represents the actual energy of the γ, E_{Reco} is the estimation of that energy [9] and $Res(E_{True})$ is the resolution in the estimation of the energy [10]. In this representation, the actual measured magnitudes for each γ are t and E_{Reco}, being all the rest unknown quantities.

In that scenario the equation 6.15 does not represent a good estimation of the real η parameter. This can be observed if that equation is calculated in the present formalism,

$$\eta_{Reco} = \frac{cov(t, E_{Reco})}{\sigma^2_{E_{Reco}}} \tag{6.22}$$

but in this formalism the actual η is calculated by,

$$\eta = \frac{cov(t, E_{True})}{\sigma^2_{E_{True}}} \tag{6.23}$$

[9] The resolution in the measurement of the arrival time is of the order of 1 μs which is much less than the relevant time scale in the observed light curves (above seconds). For this reason, any possible effect of this time resolution could be neglected.

[10] $Res(E_{True})$ is not a constant like η but a random variable with a probability density.

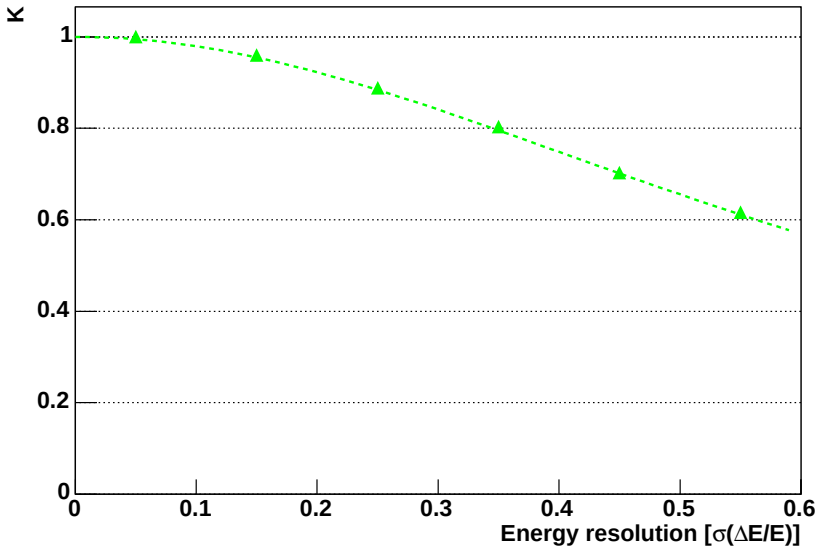

Figure 6.10: Bias produced by the energy resolution ($K \equiv \eta_{Reco}/\eta$) vs. the standard deviation of this resolution. The (green) triangles haven computed using Monte Carlo simulations whereas the dashed line was calculated using numerical methods.

It is possible to derive mathematically the relation between this two ηs leading to the following expression (for a detailed mathematical derivation see appendix C.3),

$$\eta_{Reco} = \eta \cdot K = \eta \cdot \left(\frac{1 + \dfrac{cov(E_{True}, Res(E_{True}))}{\sigma^2_{E_{True}}}}{1 + \dfrac{\sigma^2_{Res(E_{True})}}{\sigma^2_{E_{True}}}} \right) \tag{6.24}$$

where K is a factor that depends on the energy estimation bias (i.e. $cov(E_{True}, Res(E_{True}))$), the estimation resolution (i.e. $\sigma^2_{Res(E_{True})}$) and the observed energy spectrum (i.e. $\sigma^2_{E_{True}}$). In the more simple case where the energy estimation has no bias, all the linear terms in $Res(E_{True})$ become zero by definition in the previous equation, leading the expression for η_{Reco} in a more simply way,

$$\eta_{Reco} = \eta \cdot \frac{1}{1 + \dfrac{\langle Res(E_{True})^2 \rangle}{\sigma^2_{E_{True}}}} \tag{6.25}$$

After this mathematical discussion, it is clear that the estimation of η_{Reco} in the presence of a non zero energy resolution is biased. The correctness for this mathematical derivation can be confirmed using the 'Simple' Monte Carlo described before. For that purpose, the distributions for η and η_{Reco} for several energy resolution levels have been computed. The bias, understood as the ratio between this two ηs (i.e. $K \equiv \eta_{Reco}/\eta$), has been computed using these Monte Carlo simulations, and compared with the numerical calculation performed using the mathematically derived expression for K (see figure 6.10).

Even being the bias at the end of the order of less than 15% for the energy resolution levels expected for MAGIC, we made the effort to investigate the possibility of finding an unbiased estimator for η using higher order statistical momenta of the available information. We discover that under certain conditions for the energy estimation resolution, it was possible to find an unbiased estimator using momenta up to $\langle E^3 \rangle$. The conditions in the energy resolution were that it has no bias and is symmetric. Requiring these conditions leads to the following expression for the unbiased estimator (see appendix C.4 for more detailed derivation),

$$\eta_{Reco}^{Unbiased} = \frac{-B \pm \sqrt{B^2 - 4AC}}{2A} \tag{6.26}$$

where,

$$A = 2\langle E \rangle^3 - 3\langle E^2 \rangle \cdot \langle E \rangle + \langle E^3 \rangle \tag{6.27}$$

$$B = 6\langle E \rangle^2 \cdot \langle t \rangle - 3\langle E \rangle^2 \cdot \langle t \rangle - 6\langle E \rangle \cdot \langle tE \rangle + 3\langle tE^2 \rangle \tag{6.28}$$

$$C = 4\langle E \rangle \cdot \langle t \rangle^2 - 4\langle t \rangle \cdot \langle tE \rangle - 2\langle E \rangle \cdot \langle t^2 \rangle + 2\langle t^2 E \rangle \tag{6.29}$$

This expression comes from a second-order equation which provides the two traditional solutions. This unbiased estimator has been studied using the 'Simple' Monte Carlo in order to see their behaviour. Unfortunately, it has been observed that the quadratic nature of the expression for the unbiased estimator leads to a large number of imaginary solutions even with zero energy resolution. The responsible for these imaginary solutions are the statistical fluctuations produced in the calculated values of the different momenta used in the calculation of $\eta_{Reco}^{Unbiased}$ due to the finite number of γs in the flare. These imaginary solutions make the distributions of the remaining real solutions non able to reconstruct correctly the value for η.

The existence of these imaginary solutions discard this method to estimate η, leading the estimation of the bias (i.e. of the parameter K) as the most favourable solution. That parameter can be estimated either using numerical methods with the mathematical derived expression for K or by the utilization of the 'Simple' Monte Carlo. The K factor is a multiplicative bias, that means that it is independent of the actual value of η, just depending on the energy distribution and resolution. In figure 6.11 it can be observed the values for K computed using Monte Carlo for the actual value of the energy resolution estimated with the full Monte Carlo of MAGIC.

From now on in this chapter, the estimation of η is done using the energy resolution biased expression (see equation 6.15) but corrected by the K factor obtained using the Monte Carlo simulations. Then, the estimation of η is done with the following expression:

$$\eta_{Reco} = \frac{cov(t, E)}{\sigma_E^2} \; K^{-1} \tag{6.30}$$

Bias produced by the observational time window

In this paragraph we are going to explain one of the most important behaviours of the 'covariance' method which is the appearance of a bias in the estimation of η due to the limited observational time window. As it will be shown in the following paragraph, this behaviour is very important because it forces to select for that measurement only certain

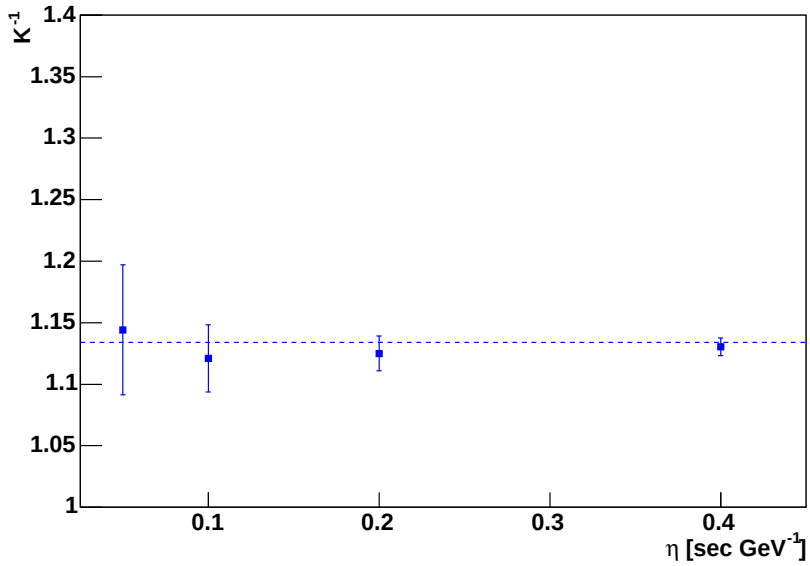

Figure 6.11: Energy resolution bias K vs. different values for η.

kind of light curves. Before explaining the reason for such bias, we will introduce some basic ideas necessary for the subsequent explanations.

The γs available for the measurement of the time-of-flight are the ones detected by the Telescope which represent a subsample of the whole set of γs arriving to the Earth from the source. In the 'covariance' method approach it is essential that the detected subsample keeps the same time-energy correlation than the whole emitted sample. That condition is fulfilled only if the selection produced in the detection depends independently on time and energy. That means that the time dependence of the selection is the same for all energies and vice versa. Therefore, any possible time-energy correlation present in the selection process would bias the original correlation motivated by LIV.

Unfortunately, the real observation of γs introduces a non zero time-energy dependence in the case of an existing LIV motivated time delay. The reason for this bias is based on the idea that any observation by definition is always limited to a time window: γs arriving sooner or later than this time window are not recorded. In case of no LIV time delay, the recorded γs correspond to an equivalent time window in the emission from the source. But in the case of a LIV time delay, high energy γs emitted just before the starting of the time window might be observed due to the time delay produced by the modified velocity of light. However, γs emitted at the same time but with lower energies will never be observed. Moreover, in an equivalent way, γs with high energy emitted just before the end of the time window might not be detected because they arrive outside the observational time window, whereas lower energy γs produced at the same time will be still caught.

The existence of this natural selection for non zero LIV time delays produces the effect of reducing the time-energy correlation within the γs which finally led inside the observational time window. Using the aforementioned phrasing: the observational time window produces a time-energy correlation which biases the actual LIV motivated correlation.

In order to illustrate why the time window produce that reduction in the correlation,

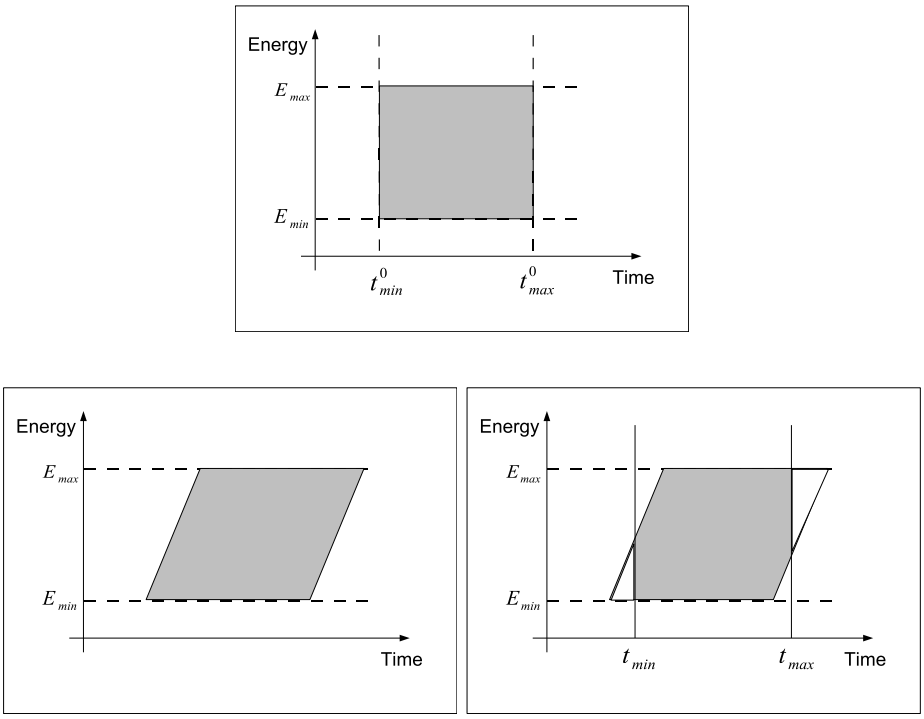

Figure 6.12: Simple graphical model to illustrate the bias produced by the observational time window. The shadowed area in all the figures represents the observed time-energy region. The top figure shows the area on the time-energy plane where γs are distributed at the source. The bottom drawings show the same time-energy plane but with the area where γs are expected to be observed at Earth. The left one shows the complete area as seen at the Earth whereas the right one shows the effect of making an observational time window.

a very simplistic graphical model is shown in figure 6.12. This model drawn in last figure is based on the following argument. Let us imagine an 'ideal' source which emits an steady flux starting and stopping at sharp times t^0_{min} and t^0_{max} respectively. Moreover, that 'ideal' source emits also with a flat energy spectrum between two energies E_{min} and E_{max}. In such an 'ideal' case, the shape representing the emission region in the time-energy plane at the source is a rectangle (see top drawing from last figure). In the case of LIV time delays, the area in the time-energy plane covered by the γs after the propagation (i.e. at Earth) becomes a trapezoid, due to the larger time delays suffered by the higher energy γs (see bottom-left drawing in last figure). If the complete trapezoid is observed, the 'covariance' method would reconstruct the correct η which, in this simplistic model, is the averaged slope of the trapezoid in the time-energy plane. Nevertheless, in the case that exists an observational time window smaller than the whole emission, the part of the trapezoid observed depends on time and energy. At the starting part of the observation, low energy γs are discarded, whereas at the end the large energy ones are the unobserved (see bottom-right drawing in last figure). In that scenario, the 'covariance' method would reconstruct a lower η than the actual one, because the averaged slope of the observed time-energy area is smaller than the one of the whole trapezoid.

Even being a very simple model, the previous explanation shows the fundamental

reasons why the existence of an observational time window might produce a bias in the 'covariance' method. Moreover, some general characteristics for this bias could be deduced from this model. First, the bias is produced only in case of non zero time delays. Second, the bias depends on the actual value for η. For the same observation time window, different value of η (in the model, different slopes for the trapezoid) have different biases. And third, in case of having an emission and time window such that the whole emission from the source is observed, no bias is produced. One final characteristic that is hard to see with this model but which will be shown in next paragraphs with the Monte Carlo is that, in case of existing a bias, it depends on the time emission shape (i.e. light curve) within the observational time window.

Based in all these characteristics, the estimated η_{Reco} with the 'covariance' method can be related with the actual value of η with the following expression.

$$\eta_{Reco} = \eta - \Delta\eta(\eta, F(time)) \tag{6.31}$$

where $\Delta\eta(\eta, F(time))$ is the window bias which depends on the actual value of η and the shape of the time emission.

The reason why in the Monte Carlo calculations on the previous paragraphs such a bias was not observable was because all the produced γs by the MC were used in the calculation of η. This is equivalent to not making any observational time window at all, which as it has been aforementioned would lead to a zero bias.

The window bias might be investigated in order to understand its magnitude and general behaviour. This investigation can be done using Monte Carlo studies following the same approach than in previous paragraphs. Additionally, this bias can be calculated numerically if the time and energy probability distributions (i.e. light curves and energy spectrum) are known. Let us assume that we know the time emission profile at the source which can be represented by $F(t^0)$ and the energy spectrum which can be written down as $\phi(E)$. With this information, any statistical magnitude can be computed just integrating these probability densities. One of the assumptions of the time-of-flight measurement is that both time and energy probability distributions are independent at the source emission. Assuming this makes possible to express the probability density as the multiplication of the two independent functions $F(t^0)$ and $\phi(E)$.

In that formalism, the effect of an energy dependence speed of light is a change of system of coordinates from emission time t^0 to observational time t. The probability density distributions stays the same but the magnitude observable at the Earth is t instead of t^0. These two magnitudes are related by the expression

$$t = t^0 + \eta \cdot E \rightarrow t^0 = t - \eta \cdot E \tag{6.32}$$

which introduces in the preceding time probability an energy dependence of the type $F(t-\eta\cdot E)$. With this new set of variables (i.e. t and E), the probability distributions are no longer independent. However, the probability density as a whole (i.e. $F(t-\eta\cdot E)\cdot\phi(E)$) is still correct, being possible to calculate any statistical magnitude in this new set of variables in the usual manner, for example,

$$\sigma_E^2 = \frac{\int\int (E^2 - \langle E\rangle^2)\cdot F(t-\eta\cdot E)\cdot\phi(E)\; dtdE}{\int\int F(t-\eta\cdot E)\cdot\phi(E)\; dtdE} \tag{6.33}$$

In that case it is not possible to cancel out the time terms, making necessary the integration in both time and energy variables to compute any statistical momentum,

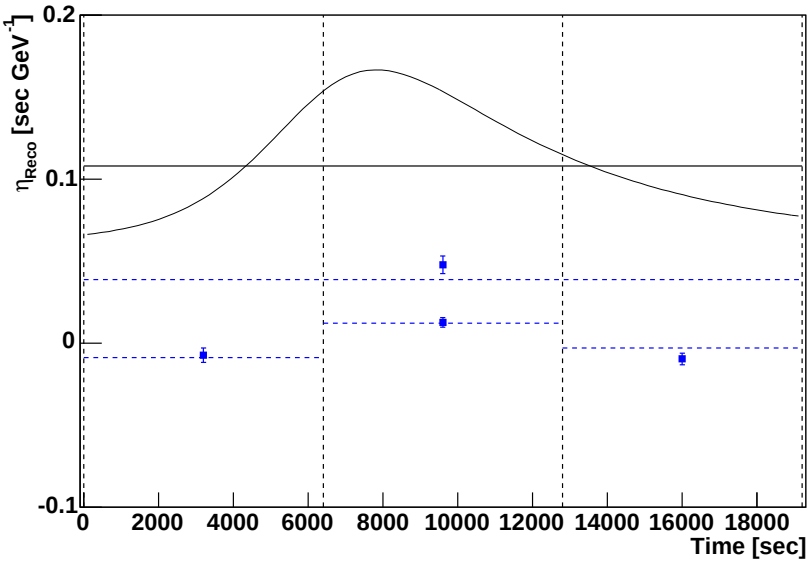

Figure 6.13: η estimation for different observation time windows. The (blue)squares represent the value for η_{Reco} measured for each of the time windows. Each of these squares lies in the center of its time window represented by two vertical (black)dashed lines. Within these time windows are drawn the numerical calculation for η_{Reco} as an horizontal (blue)dashed lines. The calculation of η_{Reco} for the complete flare is also drawn in the figure in an analogous way than the other time windows. A solid (black)line is drawn for the actual value of η set in the Monte Carlo and numerical calculations. Finally, the shape of the time emission used for all those calculations is drawn in the figure.

even the ones which just depend on one of the two variables (e.g. the energy variance).

Even assuming that the previous kind of expression could not be solved analytically for all kind of time and energy probability distributions, it is always possible to solve it numerically. The previously explained approach has been the one used in the numerical calculations of the expected results for η_{Reco} from the 'covariance' method. It is important to remark that for a given time and energy spectrum, actual value of η and observational time window the value of η_{Reco} is fixed.

The first step in the understanding of the bias $\Delta\eta$ is the observation of its possible evolution when different time emission profiles (i.e. light curves) are taken into account. For that purpose, in figure 6.13 it is shown the η_{Reco} estimation for different time windows within the Monte Carlo simulated light curve used in previous sections. The first thing that might surprise from these results is the large biases observed. It will be argued in next paragraphs that when dividing a flare like the one used in that study, it is expected a rather pathological behaviour in the case of using the 'covariance' method. The real conclusion that can be derived from this figure is that the bias produced by the observational time window depends strongly on the shape of the light curve.

In order to understand which are the characteristics for the previous flare which produce such a large bias, different flare morphologies have been used to compute the η_{Reco} (see figure 6.14). In fact, mainly two modifications over the Monte Carlo flare used in

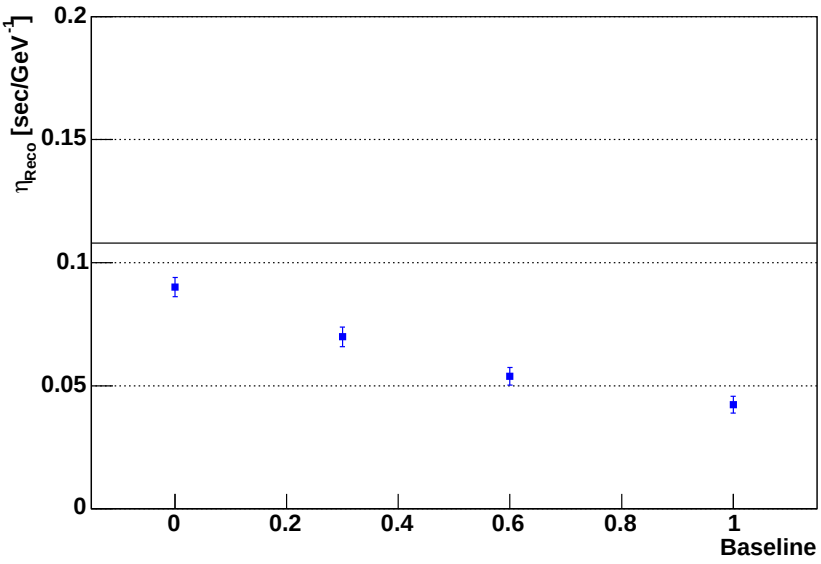

Figure a

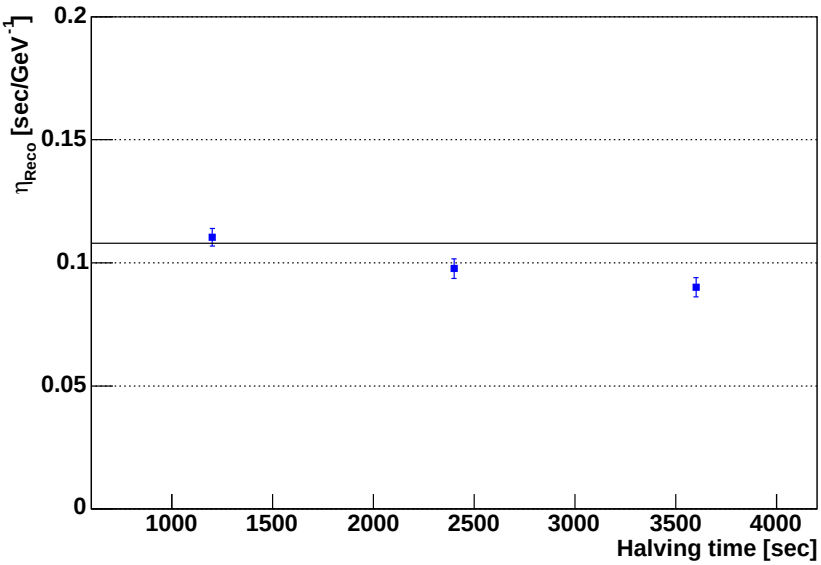

Figure b

Figure 6.14: η_{Reco} calculation for different flare morphologies. The figure **a** shows the evolution of the η_{Reco} calculation for the 'standard' light curve changing only the baseline parameter. Whereas in figure **b** it can be observed the evolution for η_{Reco} using in the simulation the 'standard' light curve with zero baseline and reducing the halving time of the flare remaining the rest of the parameters the same. In both figures a solid (black)line is drawn for the actual value of η set in the Monte Carlo.

previous studies have been simulated. First, the baseline for the 'standard' flare has been modified with values going from the initial used value (i.e. $baseline = 1$) till zero. From that simulation it can be derived that the baseline has a direct impact on the bias, showing that light curves with larger baselines show large biases when calculating η_{Reco}. Second, the 'standard' flare without baseline has been modified reducing the halving time. This test shows that sharper peak emissions, where sharpness is defined by comparison with the observational time window, shows lower biases, arriving to the point where sharp enough peaks show no bias.

Using the results from the aforementioned Monte Carlo test, it is possible to derive a general conclusion about the behaviour of the window bias. The higher the emission close to the borders of the time window, the higher the bias in the estimation of η with the 'covariance' method. That conclusion could have been predicted when the window bias was introduced, because this bias is produced by the γs that cross the time window due to the energy dependent time delays, either to enter through the starting point of the window or to leave the window through the ending point. In that situation, the higher the emission in that 'border' regions, the larger is the number of γs that cross the borders.

The existence of the window bias makes the most favourable scenario the one where all the emitted γs are observed. That situation happens when a peak emission is well contained within the observational window. Therefore, any other kind of flare observation will show some kind of bias. However, the existence of this window bias for a particular flare does not meant that this data is not suitable for the time-of-flight measurement with the 'covariance' method: it just makes the method less sensitive. In the following section about the analysis of the Mkn421 data, the approach used in this Thesis to apply the 'covariance' method for a clearly biased scenario is shown.

6.4.3 Lorentz Invariance test using Mkn421 flares

The first step in the analysis of the invariance of the speed of light using the Mkn421 data analysed in this Thesis is the selection of the best nights for the measurement. This selection should try to keep those nights which will show large sensitivities with the 'covariance' method. In previous sections it has been understood that the best scenario for applying the proposed method are flares with rapid and well contained peak emissions within the observation window. Unfortunately, during the period observed, Mkn421 shows a strong emission with large night-to-night changes in the flux level but not very significant variability within the same night. Just one of the nine observed nights, the 19th of April, shows a clear variable emission not compatible with the almost steady emission observed in the other analysed nights. The rest of the analysed nights are unsuitable for the energy dependence of TOF measurement, mainly by the large expected window bias in the proposed method due to the absence of variability within the observations.

Before using the data analysed from 19th of April flare, it is necessary to have a sample of γs as clean of hadrons as possible. The presence of hadrons in the analysed data sample would produce a similar effect to the one observed for large baselines in the flares. Hadrons are not expected to have any time-energy correlation, making any possible correlation in the sample of γs to be diluted in the hadrons background.

In section 4.4 it was explained how the γs were selected from the whole data sample. The main part of that selection was done cutting in the variable called *Hadronness* which contained all the information about the differences between the γs and the background. Different levels of hadron contamination were accessible by changing the cut in *Hadron-*

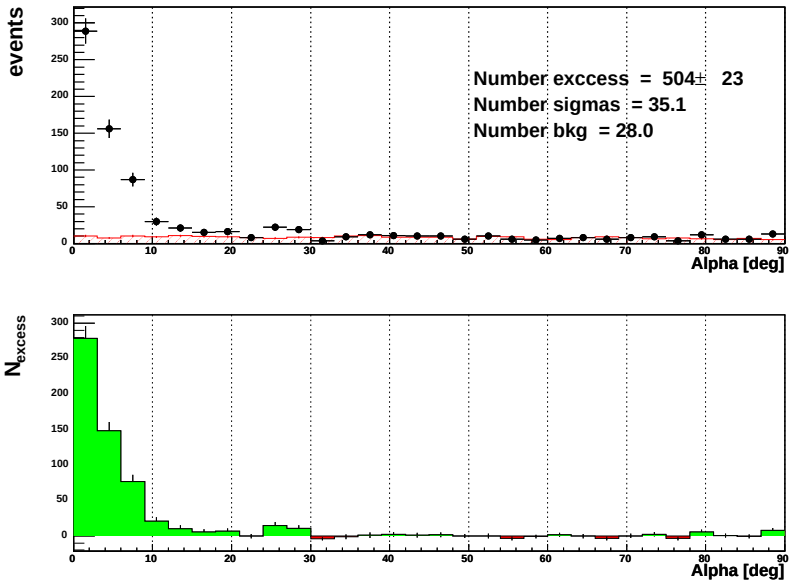

Figure 6.15: *Alpha* plot for Mkn421 during the 19th of April with a strong hadron rejection. The plot was produced for γs with an energy above 400 GeV.

ness. In the calculation of the spectrum and the light curves, the γ selection was based on setting a minimum efficiency for the γs to keep a large number of them. The idea in that approximation was that the hadron component in the sample can be estimated using a pure background sample (i.e *Off*). In this part of the analysis the approach is different. In order to reject most part of the hadrons, a minimum hadron rejection of 10^{-3} was set in the optimization of the *Hadronness* cut [11]. The result was an almost free γs sample which *alpha* distribution is shown in figure 6.15. From this figure it can be observed that hadron contamination in the remaining sample is of the order of 5%. Moreover, an energy dependent analysis of this sample shows that most of these hadrons belongs to low energies, which is the less sensitive part of the γ sample with respect to the time delays due to its linear relation with energy.

The drawback of this stronger selection is a loss of γs mostly for lower energy, leading a higher analysis energy threshold than the standard analysis. To see the net effect of the change in the selection, both γs efficiency curves for the standard and the more restrictive analysis are shown in figure 6.16. From that figure it can be observed that efficiencies above 600 GeV remain almost the same whereas larger reductions in the efficiency appear when lower energy γs are considered.

At that point, the most important remaining question is which level of window bias suffers that particular flare. To calculate this bias either numerically or using Monte Carlo, it is convenient to assume an expression that describes the observed light curve. That particular observation is not well fitted by the flare model proposed in section 6.4.2.2. However, it is perfectly well fitted by a simple extension of that model based on the introduction of an additionally falling peak to the previous rising one. The result for the fit of that function on the observed light curve for 19th of April is shown in figure 6.17.

[11] This 10^{-3} hadron rejection is obtained with the combination of the cuts in *Hadronness* and *alpha*.

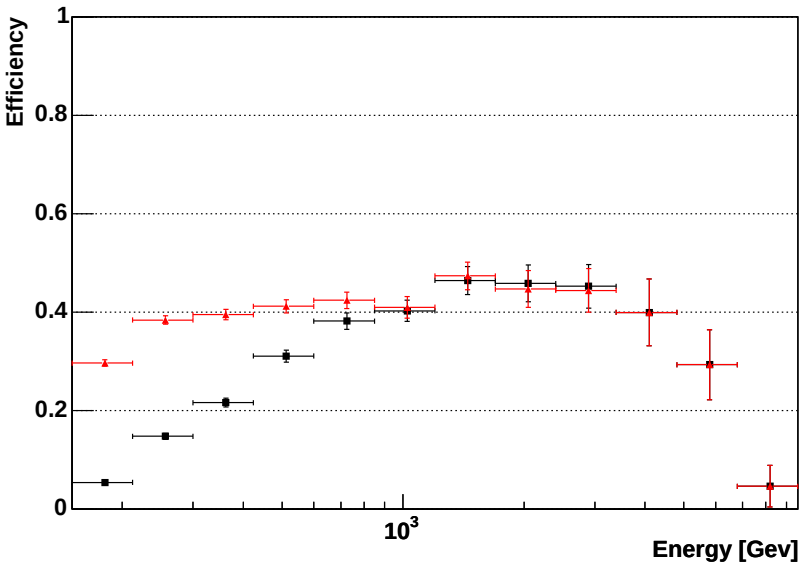

Figure 6.16: Selection efficiencies for the standard and 'covariance' analysis. The (black)squares represent the selection tuned for the 'covariance' method whereas the (red)triangles represent the standard analysis.

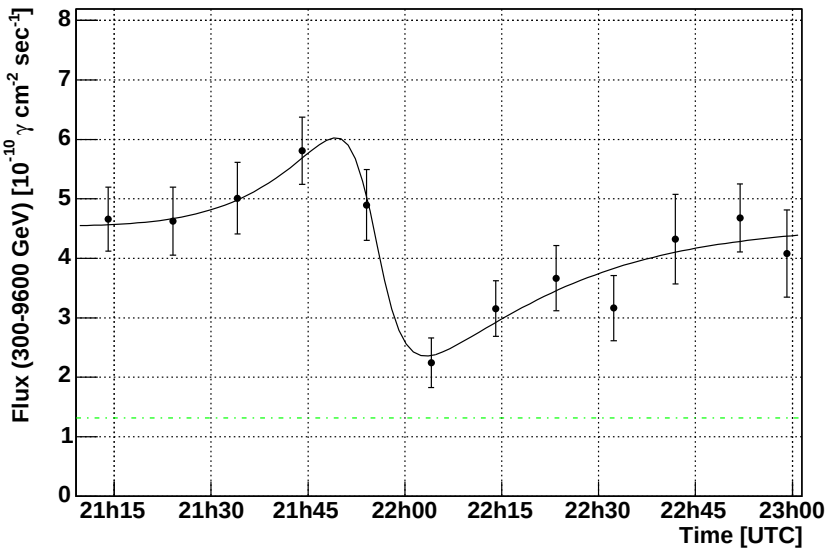

Figure 6.17: Fitted *light curve* for Mkn421 during the 19th of April 2004. The expression used in the fit is a straight extension of the flare model introduced in section 6.4.2.2.

Optimization of the sensitivity measuring η

The sensitivity for a given measurement is defined as the average upper limit one would get from an ensemble of equivalent experiments with no true signal. Due to the lack of that set of experiments, we are going to compute the sensitivity for the measurement of η using the Monte Carlo.

To compute this sensitivity, it is necessary to know on the one hand the resolution of the measurement for zero effect (from now on represented as $\delta\eta_{Reco}|_{\eta=0}$), and on the other, the correspondence between the expected measured value (i.e. η_{Reco}) with respect to the actual one (i.e. η). This second relationship is necessary because we will need to translate any measurement in η_{Reco} to the parameter that has physical meaning, that is, η. Once the resolution for zero effect in known and using the correspondence between η_{Reco} and η, obtained also from the Monte Carlo, it is possible to derive the sensitivity expressed in terms of η.

In the following paragraphs the possible changes in the measurement conditions to optimize the sensitivity are discussed. It is important to remark that at this point there is still some freedom in the setting of the measurement conditions which could be used for the optimization of the window bias. However, it has to be kept in mind that not only window bias but also $\delta\eta_{Reco}|_{\eta=0}$ have to be minimized in order to optimize the sensitivity.

Before introducing the optimization of the sensitivity for the 19th of April flare, it is necessary to remark an important point of the procedure that is going to be presented. There is a natural upper limit in the value of η that can be explored with the 'covariance' method. In fact, such a limit exists for any experimental method. For very large values of η, the high energy γs emitted within the time window are lost by the time delays. In a similar way, for this large η values, the observed high energy γs within the time window were actually emitted by the source before than the time window. Summarizing the previous ideas, for large values of η the 'covariance' method needs either large time windows or small maximum observed energies. In fact, for values of $\eta > \Delta t/E_{max} \equiv \eta_{max}$ the window bias effects are expected to become very large, making η_{max} the natural limit of the method.

Mainly two parameters can be tuned for that purpose, which are the used time window (Δt) and the maximum energy (E_{max}). The time window used in the measurement does not have to coincide with the whole observational window, but it can be smaller. In flares like the one observed, reducing the time window can be an advantage from the point of view of the bias because the central variability takes more importance with respect to the whole emission. The trade-off of this window reduction is that η_{max} becomes also smaller, making for some values of η_{Reco} impossible to reconstruct a corresponding η. The maximum energy used in the measurement can also be changed. The main advantage in reducing the maximum energy is the opposite effect than before, η_{max} becomes larger. However, this reduction has a negative impact in the uncertainty of η_{Reco} because high energy γs are the most sensitive to the time delays due to its linear dependence with energy.

In the previous paragraphs it has been shown that from the point of view of the sensitivity, the reduction of both Δt and E_{max} have positive and negative consequences. Therefore, it should exist a setting for these two parameters of the measurement which optimises the sensitivity measuring η. Using the Monte Carlo it is possible to find these optimum settings for Δt or E_{max}. Because the reduction of the time window has the intention of give more weight to the central time structure with respect to the whole

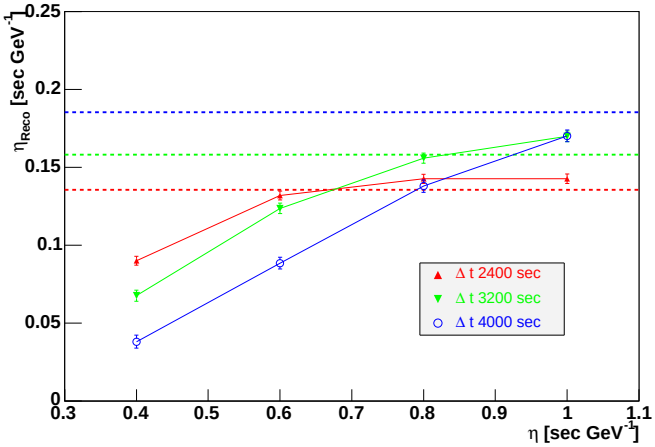

Figure a

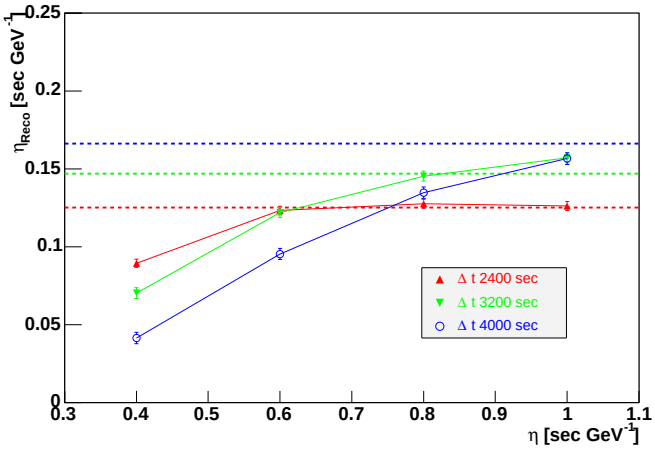

Figure b

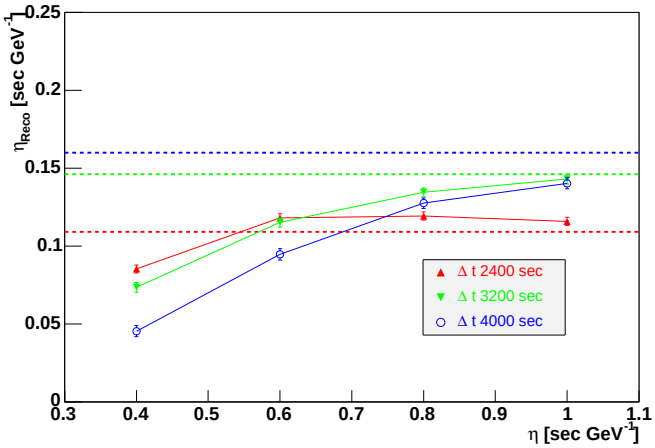

Figure c

Figure 6.18: Optimization of the sensitivity in the measurement of η. Figure **a**, **b** and **c** shows the results for maximum energies of $E_{max} = 3000, 3500, 4000\ GeV$ respectively. In each of these plots different time window results are shown, with values of $\Delta t = 2400, 3200, 4000\ sec$. Additionally, the value of the $\delta\eta_{Reco}|_{\eta=0}$ at 95% confidence level for each of these time window widths is drawn as horizontal dashed lines. In the previous plots the η_{Reco} vs η curve has been computed up to an $\eta_{max} = 1$, being that the value corresponding to the maximum of the E_{max}s and Δts used in the optimization.

emission, all the time windows used in this study has been chosen to contain this structure. In fact, the time window has been set centred in this structure with different window widths with values of $\Delta t = 2400, 3200, 4000$ *sec*. Additionally, all these time windows have been simulated for different maximum energies, $E_{max} = 3000, 3500, 4000$ GeV. Maximum energies around 3 TeV have been chosen because of the exponential cutoff of Mkn421 around that value. With that maximum energies, most of the γs emitted from Mkn421 are kept whereas the large window biases are still under control. For all this combination of parameters, it has been computed the η_{Reco} vs. η curve as well as the $\delta\eta_{Reco}|_{\eta=0}$. With this information, it is possible to calculate the expected sensitivity measuring η. The results from all these simulations are drawn in figure 6.18. Each of the plots in the figure represents the results for one of the maximum energies whereas for each plot the different simulated Δt results are represented by different (colour) point shapes.

From that study is possible to conclude that the best sensitivity at 95% confidence level for that particular flare are obtained for a time window (Δt) equal to 2400 sec and maximum energy of 4000 GeV, with a sensitivity measuring η of 0.55 $sec \cdot GeV^{-1}$ equivalent to a value of $f^{(3)}$ smaller than $\mathcal{O}(510)$.

Once the optimal Δt or E_{max} for the 19th of April flare are known, it is possible to perform the measurement with real data using these particular settings. The central value of the measurement of η_{Reco} can be obtained straightforward from the original 'covariance' method expression. However, knowing the uncertainty for that measurement is something more difficult. One of the possible approaches to estimate this uncertainty is to use the Monte Carlo simulations. A second approach using the same real data used for the measurement of η_{Reco} is possible. The idea behind this second approach is to repeat a large number of times the measurement of η_{Reco} with the same sample of real γs, but making pairs with their times and energies randomly. With that trick any possible time-energy correlation present in the data is lost, whereas all the rest of the characteristics of the flare are kept. The uncertainty in the measurement of η_{Reco} from this approach is obtained from the sigma of the obtained distribution for the values from the random time-energy pairings. In fact, this uncertainty is for the case of non LIV effect. Nevertheless, the uncertainty in the measurement of η_{Reco} just depend on the shape and level of the emission but not on the actual value of η.

From this study the central value of the measurement is found to be $\eta_{Reco} = -0.008$ $sec \cdot GeV^{-1}$ while the uncertainty estimated from the real data is $\delta\eta_{Reco}|^{data}_{\eta=0} = 0.051$ $sec \cdot GeV^{-1}$ which is compatible with the one obtained from the Monte Carlo simulation $\delta\eta_{Reco}|^{MC}_{\eta=0} = 0.056$ $sec \cdot GeV^{-1}$. Using the results obtained from the real measurement is possible to set limit at 95% confidence level for η of 0.50 $sec \cdot GeV^{-1}$ which for the distance of Mkn421 can be translated to a limit in $f^{(3)}$ smaller than $\mathcal{O}(460)$. This limit correspond to an energy scale of Quantum Gravity of $E_{QG} > 2.6 \cdot 10^{16}$ GeV.

Comparison of the 'covariance' method with present best results

In order to know the sensitivity of the 'covariance' method we are going to simulate the flare used in the present best limit measuring time-of-flight given by the Whipple collaboration. That limit was obtained using the most rapid flare observed for Mkn421 in the VHE regime. The light curve for that flare as reported by Whipple is shown in figure 6.19.

The simulation assumes that the central peak can be adjusted by a Gaussian which is extended till the regions with almost no emission at the borders of the observation.

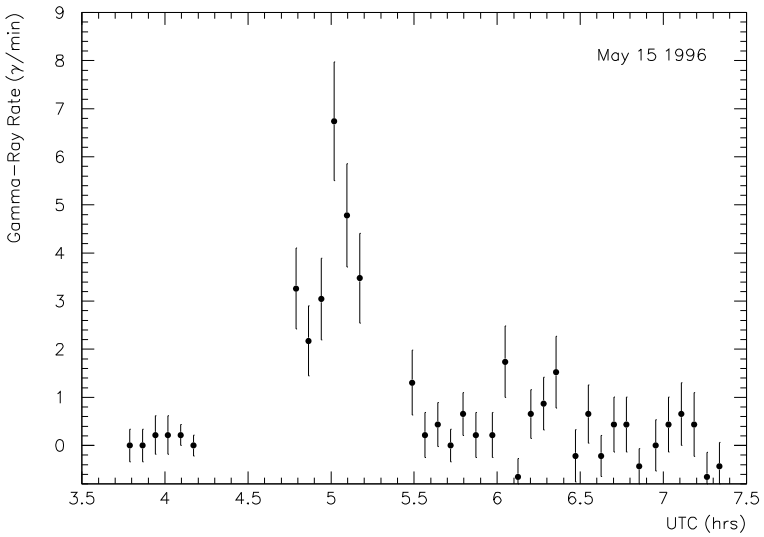

Figure 6.19: Flare observed by Whipple for the Mkn421 flare during 15th May 1996. Figure extracted from reference [91].

Moreover, no gaps are simulated during the observation in order to avoid possible biases produced by the time window. In that simulation, it is important to simulate correctly the emission level, because the number of γs detected under the peak time structure is as important as the width of the peak for the sensitivity of the TOF measurement. In the Whipple paper, together with the rate of γs for Mkn421, the rate for the Crab Nebula for the equivalent observational conditions is given. With that information is possible to know the flux for Mkn421 just inferred from the one of Crab Nebula. This scenario fulfils all the requirements to be a good candidate for the time-of-light measurements using the 'covariance' method: high emission level, sharp peak time structure and low emission levels at the borders of the observational time window.

Using the 'Simple' Monte Carlo simulation and assuming the MAGIC characteristics presented before, including the more restrictive γ selection, the Whipple flare is produced, providing as a mean value 210 γs above 400 GeV. The possible window bias has been checked by Monte Carlo and numerical calculations being the result negligible compared with the statistical errors involved.

The sensitivity of this measurement is defined as the resolution obtained by the method for zero effect (i.e. $\eta = 0$). In that case, the error for zero η effect has an uncertainty of $0.045\ sec \cdot GeV^{-1}$ which for the 'distance' of Mkn421 can be translated as a sensitivity in the $|f^{(3)}|$ parameter to be smaller than $\mathcal{O}(84)$ with 99% confidence level, or expressed as an energy scale of Quantum Gravity $E_{QG} > 1.5 \cdot 10^{17}\ GeV$. That sensitivity is more than 3 times better that the present best limit set by the Whipple collaboration.

6.5 Summary of the TOF measurement

In the last part of this chapter it has been presented the measurement of an energy dependent time-of-flight for γs by MAGIC, as a possible signature for the violation of the Lorentz symmetry. For this purpose, different aspects of this measurement have been investigated.

The first of these aspects has been the study of the role of the Gamma Ray Horizon in the sensitivity of the TOF measurement using distant sources. This study was motivated by the fact that new IACTs like MAGIC have within their goals the reduction of the energy threshold observed by previous Cherenkov telescopes. The aim behind this goal is the observation of farther sources not accessible with the previous telescopes due to the existence of the Gamma Ray Horizon (i.e the absorption of VHE gammas by the Extragalactic Background Light).

The magnitude of the time delay induced by LIV increases with both the energy and the distance travelled by the γs. The effect of the GRH in the sensitivity of the TOF measurement is a competition between the possibility of observing farther sources and the reduction of the maximum observable γ energies. In order to understand the situation after the combination of both effects, it has been performed the calculation of the expected energy dependent time delay as a function of redshift of the observed source. In addition, the Gamma Ray Horizon for these redshifts has been computed. These calculations have been done taking into account the modifications introduced by LIV in the energy threshold for the reactions responsible of the existence of the GRH.

Combining both calculations, the study concludes that time delay sensitivities on the scale of just few seconds will be mandatory to explore above the Planck scale, quite independently on the actual source redshift and energy of the observed γ-rays. In the context of this result, the observation of farther sources does not produce larger time delays, which are the ones that could be more easily measured. This leads to the nearby AGNs, already well-established VHE emitters, as the most comfortable sources to observe this phenomenon. However, the possibility of observing new further sources increases the available data for TOF studies. Among these further sources, there is the possibility of observing new VHE source categories like GRBs, which might provide very rapid time structures highly convenient for TOF measurements. In addition, the measurement of TOF for sources at different redshifts (e.g. farther sources) is mandatory in case of a positive observation of an energy dependant time delay. This is necessary in order to disentangle between LIV and internal source process induced time delays using the scaling of the TOF with the redshift.

After the previous study, a review of the present methodological approaches used in the literature has been discussed, finding a common limitation in all of them. This limitation is the use of light curves to measure a possible time delay, which means that all the existing methods integrate the time information within bins, degrading in this process the information available in the observation. Motivated by this, a new method to measure the TOF that uses the information for every single γ is developed in this Thesis. This new method, named 'covariance' method, is based on the idea that the arrival time and the energy for γs must be statistically correlated in case of existing a LIV motivated energy dependent TOF.

The 'covariance' method has been studied using Monte Carlo simulations. Along this study, a limitation for the method has been found. The method has a bias when computing the time-energy correlation which is produced by the fact of having a finite time window for any observation. This bias has been investigated using the Monte Carlo, reaching to the conclusion that for observations with large baselines in the time emission structure, the bias is bigger. In other words, the observations with small or none bias when using the 'covariance' method are those with light curves which show a well contained peak and with small baseline compared with respect to this 'central' peak.

The presented 'covariance' method has been used to measure the time-of-flight for

AUTHORS	f_γ^3 **limit**	E_{QG} **limit**	**Confidence level**
Kaaret *et al.*	$< 7\ 10^3$	$> 0.2\ \ 10^{16}\ GeV$	95%
Ellis *et al.*	$< 1.7\ 10^3$	$> 0.7\ \ 10^{16}\ GeV$	95%
Biller *et al.*	< 260	$> 4.7\ \ 10^{16}\ GeV$	99%
This Thesis	< 460	$> 2.6\ \ 10^{16}\ GeV$	95%

Table 6.1: Summary of the present measurements of an energy dependent TOF for gammas.

gammas using Mkn421 data from the night of the 19th of April, analysed in the previous chapter. The result is compared in table 6.1 with the present measurements already published in the literature. The result obtained in this Thesis is the second best result and confirms the conclusions for the rest of measurements.

The night of the 19th of April shows the best available flare in this Thesis for this measurement. Unfortunately, this flare does not fulfil the requirements mentioned before for having small or none bias in the 'covariance' method. For this reason, it has been computed the sensitivity of the new method in a most favourable scenario. It has been simulated using Monte Carlo the response of MAGIC for the most rapid flare ever observed for Mkn421, which is the one used in the Biller *et al.* TOF measurement. For this flare, the sensitivity at 99% confidence level of the 'covariance' method is of $E_{QG} > 1.5 \cdot 10^{17}\ GeV$, which is a factor 3 better than the Biller *et al.* measurement, thus showing that the proposed method is more sensitive.

Chapter 7

Summary and Conclusions

The MAGIC Telescope belongs to the group of new IACTs constructed in the last years with the aim of lowering both the sensitivity and the energy threshold of the previous generation of Cherenkov telescopes. MAGIC physics program is today a reality, with discoveries of new sources and contributions to the already well established VHE sources. The technical contribution done by the author to the common project that is the MAGIC Telescope has been presented in this Thesis. The best proof for the impact of this contribution is the daily operation of the Telescope, which is the first step in the science done by the MAGIC collaboration.

This Thesis has also contributed in the analysis of the data recorded by MAGIC. The most active period observed for the Active Galactic Nuclei Markarian 421 observed with the MAGIC Telescope, and one of the most active for that source in the last years, has been analysed in this Thesis. This active emission period took place during the Spring of 2004, being MAGIC in commissioning phase at that moment. Due to the non-nominal situation of the MAGIC Telescope for the analysed period, dedicated studies were necessary for the understanding of the Telescope performance. Among the dedicated studies, one of the most important for the analysis has been the calculation of the reflector Point Spread Function magnitude and stability during the complete data sample. The PSF of the reflector has become one of the key parameters of the MAGIC Telescope due to the innovative Active Mirror Control present in the telescope, becoming the knowledge of this parameter essential for the correct simulation of the Telescope, therefore, for the correct γ selection process. Additionally, due to the mentioned before non-nominal situation, the drive system of the Telescope showed a mispointing that made necessary the development in this Thesis of new tools for the correct interpretation of the data. The star field observed directly by the PMTs of the camera is used for the triangulation of the source position with an accuracy much better than the one obtained by the *disp* method. The conjunction of the high emission state for Markarian 421 with the sensitivity and lower energy threshold of MAGIC leads to the observation of more than thirteen thousand γs in around 10 hours, which is of the same order than the whole sample observed by HEGRA during the very large emission period for Markarian 421 during 2001, with almost 250 hours of observation.

For the analysed period, the energy spectrum and the light curves for each of the observed nights has been measured. The spectrum analysis has been performed for different emission levels, confirming the dependence of the Markarian 421 spectrum with activity state, already claimed in the literature. During the studied period, Markarian 421 showed variability between consecutive nights of a factor 2.5 reaching a maximum mean integral

flux over one night of $(5.4 \pm 0.1) \cdot 10^{-10}\ \gamma \cdot sec^{-1} \cdot m^{-2}$ above 300 GeV for the night of 23th of April, which is more than 4 times the integral flux for Crab Nebula. Rather smooth light curves have been measured for that period within each night, with the exception of the 19th of April, which showed a variability with halving times of the order of tens of minutes. Moreover, the nearly simultaneous observation of the source by the HESS Telescope made possible a join measurement of the source with completely compatible results.

This Thesis also has implications in the Quantum Gravity phenomenology field, a field of physics which has become a reality in the last decade through the measurement of the violation of Lorentz Invariance. From the scepticism about the possibility of ever measuring effects at the Planck mass scale of ten years ago, we are at present in a situation where experimental observations constrain very much the possibility of the existence of a violation of Lorentz Invariance symmetry. An important responsible for this new situation is the introduction of astrophysical observations in the LIV measurements. This Thesis contributes to this field in one of the sectors less constrained by the experimental measurements, which is the photon sector. This sector still needs better experimental data and measurement techniques in other to arrive to sensitivities up to the Planck scale. In this Thesis, it has been developed a new method to measure the invariance of the Speed of Light with the energy, which in case of a positive measurement would be a signature for Lorentz Invariance violation. This new method is motivated by the idea of being able to perform this measurement using the maximum available information from the experimental observations which, from our point of view, is not the case for previous approaches to this measurement. The method presented here is based in the idea that, if the speed of photons is energy dependent, the arrival time of photons from distant sources to the Earth must be statistically correlated with their energy. The proposed new method is based in simple concepts and is mathematically well grounded. The mathematical derivations as well as Monte Carlo simulations used for the understanding of the capabilities of the method has shown that the optimum scenario for its application corresponds to observations with peak structures with the lowest possible baseline emissions and well contained within the observational time window. In the rest of flare morphologies the method shows a bias in the estimation of the time-energy correlation which reduces its sensitivity.

The most rapid flare for the Markarian 421 analysed in the data has been used to make the invariance of the speed of light measurement. Even being this flare the most favorable for the measurement, unfortunately the flare shows a sizeable baseline in the emission. Nevertheless, in the Thesis it has been shown how to treat the method in these conditions. In a Quantum Gravity motivated LIV, using Markarian 421 data and this measurement, a limit at 95% confidence level corresponding to an energy scale of Quantum Gravity of $E_{QG} > 2.6 \cdot 10^{16}\ GeV = \frac{E_{Pl}}{460}$ has been obtained. This result is of the order of a factor 2 bigger than the best present limit of this kind. However, in order to compare the method potential and not the goodness of the observed flare, the method has been tested using a simulation of the same emission observed by Whipple to set the present best limit. In that situation, the method has shown a sensitivity at 99% confidence level of the order of $E_{QG} > 1.5 \cdot 10^{17}\ GeV = \frac{E_{Pl}}{84}$ which is more than 3 times smaller than the aforementioned best limit.

Our opinion is that this method could be exploited in the near future to achieve Planck mass scale sensitivities with the potential observation of GRBs emissions in the VHE domain, either by the present generation of IAC Telescopes like MAGIC or the next

generation γ-ray satellites like GLAST.

To conclude, this Thesis has tried to make three contributions to the field of Astrophysics: the technical contribution to the development of a new detector in the field, a complete analysis of one of the first observations done using this new Telescope, and the use of this analysis for a deeper understanding of the speed of light invariance measurement in the framework of the search of experimental evidences of a Quantum formulation of Gravity. All this contributions have been done with the aim of motivating further and future developments in the field.

Appendix A

Data Sample

In this Appendix, detailed information about the selected and excluded data for the analysis in this Thesis is presented. In the following tables the run number intervals selected or discarded for each of the nights are presented. In addition, the main reason that motivated the exclusion of some subsamples and the time of observation for the selected ones is shown. Moreover, for the *Off* observations, the celestial coordinates for dark patch in the sky observed are written down.

SAMPLE	SOURCE	DATE	RUNS SEL.	PROBLEM	OBS. TIME
Crab-I	Crab Nebula	2004-03-16	None	AMC problems	
		2004-03-17	None	AMC problems	
		2004-03-18	None	*On-Off* disagreement	
		2004-03-19	20663-20715		46 min
					46 min
Crab-II	Crab Nebula	2004-03-21	20924-20983		64 min
		2004-03-22	None	High extinction	
		2004-03-23	None	High extinction	
					64 min
OffCrab-I	OffCrab-9	2004-03-16	None	AMC problems	
		2004-03-17	None	AMC problems	
		2004-03-18	None	AMC problems	
		2004-03-19	20719-20778		65 min
					65 min
OffCrab-II	OffCrab-9	2004-03-21	20990-21074		65 min
		2004-03-22	None	High extinction	
		2004-03-23	None	High extinction	
		2004-03-24	None	High extinction	
					65 min

Table A.1: Summary of the selected and excluded samples for Crab Nebula data. The OffCrab-9 source has a celestial coordinates of $7^h\ 7'\ 42''$ right ascension and $25°\ 0'\ 51''$ declination.

SAMPLE	SOURCE	DATE	RUNS SEL.	PROBLEM	OBS. TIME
Mkn-I	Mkn421	2004-03-19	20781-20821		64 min
		2004-03-21	21078-21121		60 min
		2004-03-22	None	High extinction	
		2004-03-23	None	High extinction	
		2004-03-24	None	*On-Off* disagreement	
		2004-03-25	21961-22004		72 min
		2004-03-26	None	Low hadron rate	
					196 min
Mkn-II	Mkn421	2004-04-19	22388-22555		95 min
		2004-04-20	None	High extinction	
		2004-04-21	22962-23106		204 min
		2004-04-22	23210-23315		172 min
		2004-04-23	23428-23740		107 min
		2004-04-24	24130-24384		99 min
		2004-04-25	24787-24912		51 min
					728 min
OffMkn-I	OffMkn421-3	2004-03-16	20257-20646		52 min
	OffMkn421-5	2004-03-21	21157-21259		16 min
		2004-03-22	None	High extinction	
		2004-03-23	None	High extinction	
		2004-03-25	22047-22054		14 min
			22055-22065	Low hadron rate	
					82 min
OffMkn-II	OffMkn421-5	2004-04-20	22781-22811		57 min
	OffMkn421-6	2004-04-21	23117-23200		144 min
		2004-04-22	23321-23419		149 min
					350 min

Table A.2: Summary of the selected and excluded samples for Mkn421 data. The OffMkn421-3, OffMkn421-5 and OffMkn421-6 sources have a celestial coordinates of $12^h\ 34'\ 26''$, $13^h\ 40'\ 0''$ and $14^h\ 42'\ 0''$ right ascension and $38^\circ\ 12'\ 36''$, $38^\circ\ 30'\ 36''$ and $38^\circ\ 30'\ 36''$ declination respectively.

Appendix B

Mkn421 daily light curves

In this Appendix, the light curves for Mkn421 for every of the nine nights observed by MAGIC during spring of 2004 are shown. This observation includes the nights of 19,21 and 25 of March and the 19,21-25 of April. All the light curves have been computed integrating energies above 300 GeV. The green dashed horizontal line represents the Crab Nebula integral flux for the same energies.

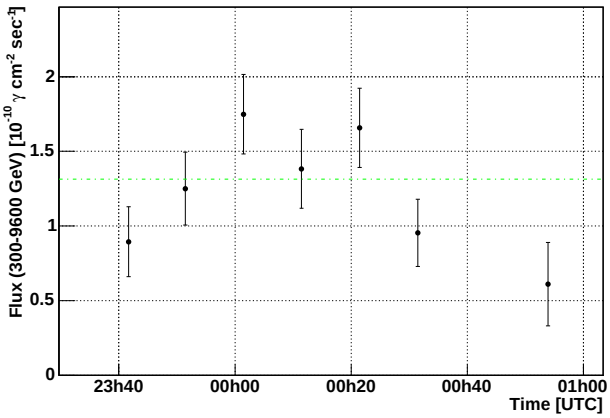

19th of March of 2004

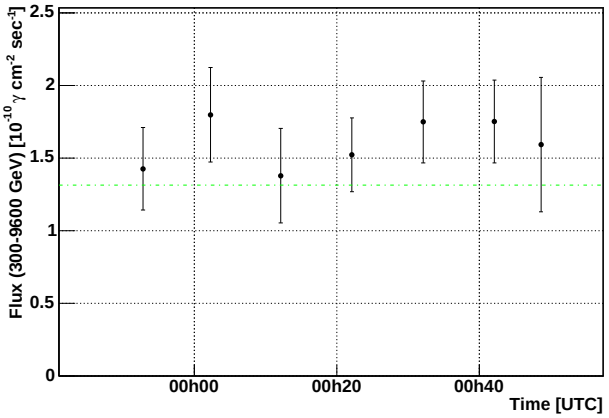

21th of March of 2004

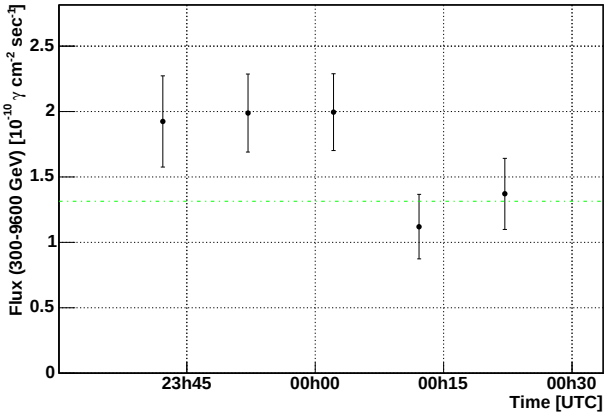

25th of March of 2004

Figure B.1: *Light curve* for Mkn421 during 19th, 21th and 25th of March 2004.

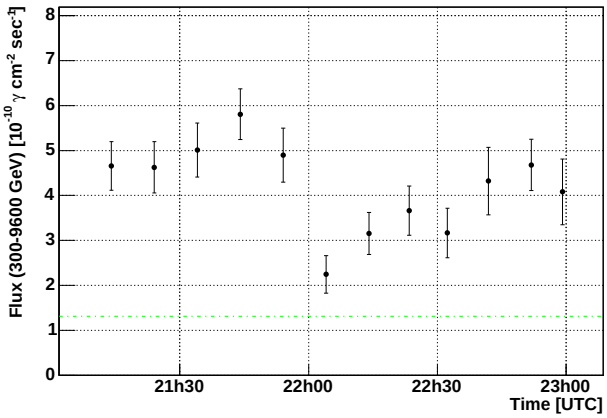

19th of April of 2004

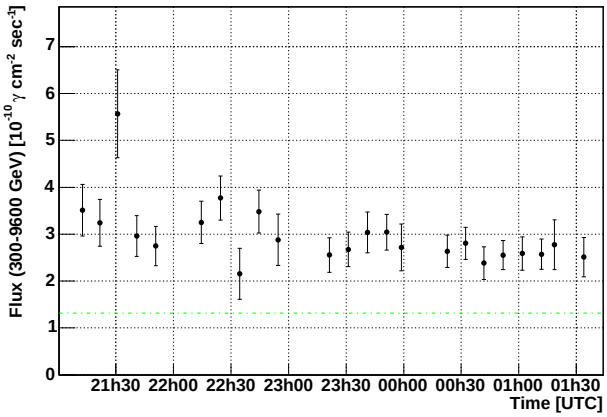

21th of April of 2004

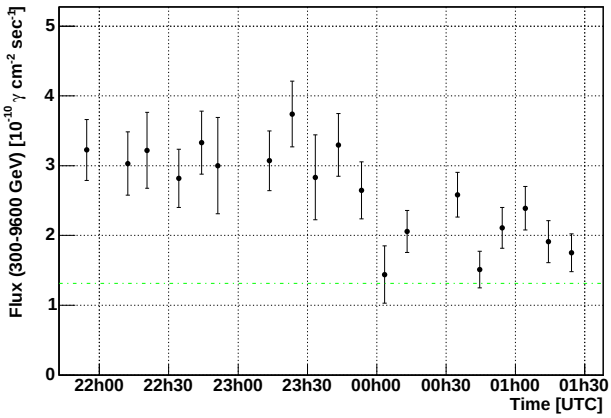

22th of April of 2004

Figure B.2: *Light curve* for Mkn421 during 19th, 21th and 22th of April 2004.

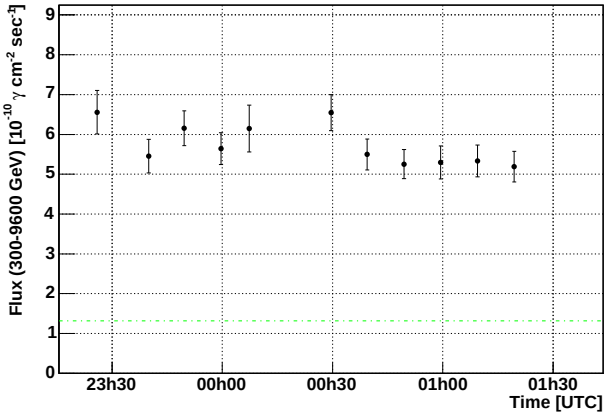

23th of April of 2004

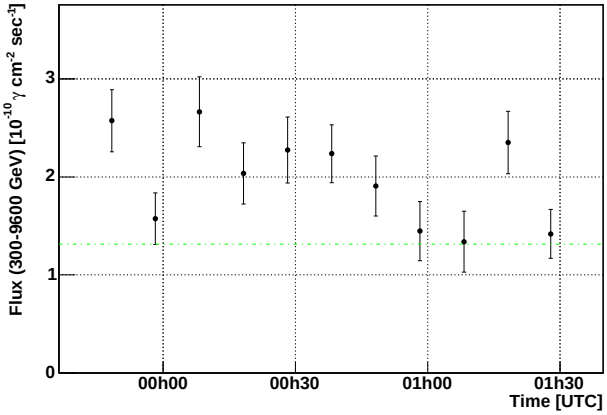

24th of April of 2004

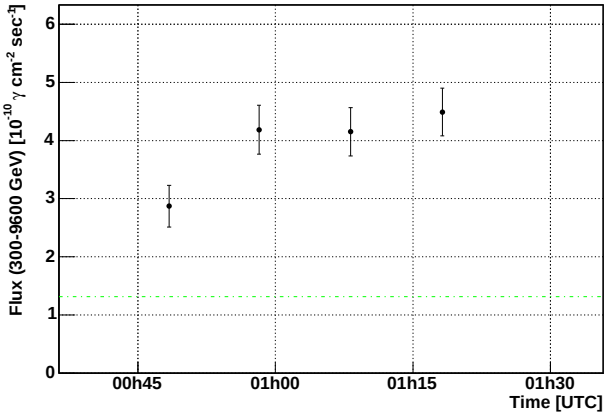

25th of April of 2004

Figure B.3: *Light curve* for Mkn421 during 23th, 24th and 25th of April 2004.

Appendix C

Mathematical derivations

In this Appendix, the mathematical derivations necessary to support several of the discusions and conclusions presented in this Thesis are written down.

C.1 Modified velocity derivation for massless particles

To compute the velocity for massless particles in the *Modified dispersion theory* framework (see section 6.1.2) the dispersion relation is differentiated.

$$E^2 = p^2 - \sum f^{(n)} \frac{E^n}{E_{Pl}^{(n-2)}} \tag{C.1}$$

$$2 \cdot E \cdot dE = 2 \cdot p \cdot dp - \sum f^{(n)} \cdot n \cdot \frac{E^{(n-1)}}{E_{Pl}^{(n-2)}} \cdot dE \tag{C.2}$$

$$p \cdot dp = E \cdot dE \cdot \left(1 + \sum f^{(n)} \cdot \frac{n}{2} \cdot \left(\frac{E}{E_{Pl}}\right)^{(n-2)}\right) \tag{C.3}$$

$$v\left(\equiv \frac{dE}{dp}\right) = \frac{p}{E} \cdot \left(1 + \sum \frac{n}{2} \cdot f^{(n)} \cdot \left(\frac{E}{E_{Pl}}\right)^{(n-2)}\right)^{-1} \tag{C.4}$$

$$v = \frac{\left(E^2 + \sum f^{(n)} \frac{E^n}{E_{Pl}^{(n-2)}}\right)^{\frac{1}{2}}}{E} \cdot \left(1 + \sum \frac{n}{2} \cdot f^{(n)} \cdot \left(\frac{E}{E_{Pl}}\right)^{(n-2)}\right)^{-1} \tag{C.5}$$

$$v = \left(1 + \sum f^{(n)} \left(\frac{E}{E_{Pl}}\right)^{(n-2)}\right)^{\frac{1}{2}} \left(1 + \sum \frac{n}{2} \cdot f^{(n)} \cdot \left(\frac{E}{E_{Pl}}\right)^{(n-2)}\right)^{-1} \tag{C.6}$$

At this point it is necessary to make some approximations to go further in the derivation of a simple expression for the speed of massless particles. The approximation is based in the fact that the energy range it is being investigated (around 1 TeV) is much less than the Planck scale (i.e. $\frac{E}{E_{Pl}} \gg 1$). This fact makes possible two approximations in the previous expressions. The first one is the fact that the relation $(1+x)^{\lambda} \sim (1+\lambda\, x)$ for $x \gg 1$ could be used to simplified the previous expression, leading the velocity as,

$$v \simeq \left(1 + \sum \frac{1}{2} \cdot f^{(n)} \left(\frac{E}{E_{Pl}}\right)^{(n-2)}\right) \left(1 - \sum \frac{n}{2} \cdot f^{(n)} \cdot \left(\frac{E}{E_{Pl}}\right)^{(n-2)}\right) \tag{C.7}$$

The second possible approximation is to express the velocity just as the leading order of the previous expression and lead the rest of term as corrections of extra order. This approximation is possible due to the fact that $\frac{E}{E_{Pl}} \gg 1$ and the factors $f^{(n)}$ are expected to be of the order unity (see section 6.1.2).

Finally the expression for the velocity of a massless particle is

$$v \simeq 1 - \frac{n-1}{2} \cdot f^{(n)} \left(\frac{E}{E_{Pl}}\right)^{(n-2)} + \mathcal{O}\left(\frac{E}{E_{Pl}}\right)^{(n-1)} \tag{C.8}$$

C.2 η calculation

From the arrival time expression $t = t^0 + \eta \cdot E$ it is possible to derive the mean values for several statistical momenta for the variables measured for the set of γs $\{t_i, E_i\}$.

$$\langle E \rangle \equiv \sum \frac{E_i}{N} \tag{C.9}$$

$$\langle t \rangle \equiv \sum \frac{t_i}{N} = \left\langle t^0 \right\rangle + \eta \cdot \langle E \rangle \tag{C.10}$$

$$\langle tE \rangle \equiv \sum \frac{t_i \cdot E_i}{N} = \left\langle t^0 \right\rangle \cdot \langle E \rangle + \eta \left\langle E^2 \right\rangle \tag{C.11}$$

This this system of equations have two unknown magnitudes (i.e. $\left\langle t^0 \right\rangle$ and η) and two independent equations, hence it is possible to resolve the system. Actually we are interested in calculating η.

$$\langle tE \rangle - \langle t \rangle \cdot \langle E \rangle = \left\langle t^0 \right\rangle \cdot \langle E \rangle + \eta \left\langle E^2 \right\rangle - \left\langle t^0 \right\rangle \cdot \langle E \rangle - \eta \cdot \langle E \rangle^2 \tag{C.12}$$

$$\langle tE \rangle - \langle t \rangle \cdot \langle E \rangle = \eta \cdot \left(\left\langle E^2 \right\rangle - \langle E \rangle^2\right) \tag{C.13}$$

Then finally η can be express like,

$$\eta = \frac{\langle tE \rangle - \langle t \rangle \cdot \langle E \rangle}{\langle E^2 \rangle - \langle E \rangle^2} = \frac{cov(t, E)}{\sigma_E^2} \tag{C.14}$$

C.3 η energy resolution bias calculation

Using the 'theoretically' expressions for the measured magnitudes for the γs,

$$t = t^0 + \eta \cdot E_{True} \tag{C.15}$$

$$E_{Reco} = E_{True} + Res(E_{True}) \tag{C.16}$$

is possible to found the relation between the calculation of η using the estimated energy (E_{Reco}),

$$\eta_{Reco} = \frac{cov(t, E_{Reco})}{\sigma^2_{E_{Reco}}} \tag{C.17}$$

with the actual η calculated using the real energy of the γ (E_{True})

$$\eta = \frac{cov(t, E_{True})}{\sigma^2_{E_{True}}} \tag{C.18}$$

To found this relation is important to notice, first the relation between the Reco and the True variances,

$$\sigma^2_{E_{Reco}} = \sigma^2_{E_{True}} + \sigma^2_{Res(E_{True})} \tag{C.19}$$

and second the relation between the Reco and True covariances,

$$cov(t, E_{Reco}) = cov(t, E_{True}) + \eta \cdot cov(E_{True}, Res(E_{True})) \tag{C.20}$$

$$cov(t, E_{Reco}) = \eta \cdot \left(\sigma^2_{E_{True}} + cov(E_{True}, Res(E_{True}))\right) \tag{C.21}$$

With this two previous expressions is possible to find the relation between the Reco and True ηs,

$$\eta_{Reco} = \eta \cdot \left(\frac{\sigma^2_{E_{True}} + cov(E_{True}, Res(E_{True}))}{\sigma^2_{E_{True}} + \sigma^2_{Res(E_{True})}}\right) \tag{C.22}$$

$$\eta_{Reco} = \eta \cdot K = \eta \cdot \left(\frac{1 + \frac{cov(E_{True}, Res(E_{True}))}{\sigma^2_{E_{True}}}}{1 + \frac{\sigma^2_{Res(E_{True})}}{\sigma^2_{E_{True}}}}\right) \tag{C.23}$$

where K is a factor that depends in the energy estimation bias (i.e. $cov(E_{True}, Res(E_{True}))$) and resolution (i.e. $\sigma^2_{Res(E_{True})}$). In the more simple case where the energy estimation has no bias all the linear terms in $Res(E_{True})$ becomes zero by definition (i.e. no bias means $\langle Res(E_{True})\rangle = 0$) in the previous equation, leading the expression for η_{Reco} like,

$$\eta_{Reco} = \eta \cdot \frac{1}{1 + \frac{\langle Res(E_{True})^2\rangle}{\sigma^2_{E_{True}}}} \tag{C.24}$$

C.4 Unbiased η calculation

It is possible to find an unbiased estimator of η using moments of higher order than $\langle E^2\rangle$ and assuming certain conditions for the energy estimation behavior. The first one is that the estimations has no bias (i.e. $\langle Res(E_{True})\rangle = 0$). If such a condition holds true is possible to derived that any expression of the type $\langle Res(E_{True}) \cdot E^n_{True}\rangle$ is also zero. The second condition is that the energy estimation is symmetric (i.e.$\langle Res(E_{True})^3\rangle = 0$). With a similar argumentation than before it can be derived that $\langle Res(E_{True})^3 \cdot E^n_{True}\rangle$ is also zero.

Based in the idea that the magnitudes measured for γs can be 'theoretically' expressed using the following equations,

$$t = t^0 + \eta \cdot E_{True} \tag{C.25}$$
$$E_{Reco} = E_{True} + Res(E_{True}) \tag{C.26}$$

From these relations for each γ is possible con construct system of equations using statistical moments which makes possible to construct un unbiased estimator of η. This system is formed by the following equations,

$$\langle E \rangle = \langle E_{True} \rangle \tag{C.27}$$
$$\langle t \rangle = \langle t^0 \rangle + \eta \cdot \langle E_{True} \rangle \tag{C.28}$$
$$\langle tE \rangle = \langle t^0 \rangle \cdot \langle E_{True} \rangle + \eta \cdot \langle E^2_{True} \rangle \tag{C.29}$$
$$\langle E^2 \rangle = \langle E^2_{True} \rangle + \langle Res(E_{True})^2 \rangle \tag{C.30}$$
$$\langle t^2 \rangle = \langle (t^0)^2 \rangle + \eta^2 \cdot \langle E^2_{True} \rangle + 2\eta \cdot \langle t^0 \rangle \cdot \langle E_{True} \rangle \tag{C.31}$$
$$\langle tE^2 \rangle = \langle t^0 \rangle \cdot \langle E^2_{True} \rangle + \eta \cdot \langle E^3_{True} \rangle + \langle t^0 \rangle \cdot \langle Res(E_{True})^2 \rangle + \eta \cdot \langle Res(E_{True})^2 \cdot E_{True} \rangle \tag{C.32}$$
$$\langle t^2 E \rangle = \langle (t^0)^2 \rangle \cdot \langle E_{True} \rangle + \eta^2 \cdot \langle E^3_{True} \rangle + 2\eta \cdot \langle t^0 \rangle \cdot \langle E^2_{True} \rangle \tag{C.33}$$
$$\langle E^3 \rangle = \langle E^3_{True} \rangle + 3 \langle Res(E_{True})^2 \cdot E_{True} \rangle \tag{C.34}$$

In this system of equation there are a number of known magnitudes which can be calculated from the measured γs ($\langle E \rangle$, $\langle t \rangle$, $\langle tE \rangle$, $\langle E^2 \rangle$, $\langle t^2 \rangle$, $\langle tE^2 \rangle$, $\langle t^2 E \rangle$ and $\langle E^3 \rangle$). Moreover, the system have 7 independent equations and 7 unknown magnitudes within which η is one of them. Arranging properly the previous set of equations is possible to construct a single equation where just the known magnitudes and η are present leading to,

$$\begin{aligned} \left(2\langle E \rangle^3 - 3\langle E^2 \rangle \cdot \langle E \rangle + \langle E^3 \rangle\right) \cdot \eta^2 \; + \\ \left(6\langle E \rangle^2 \cdot \langle t \rangle - 3\langle E \rangle^2 \cdot \langle t \rangle - 6\langle E \rangle \cdot \langle tE \rangle + 3\langle tE^2 \rangle\right) \cdot \eta \; + \\ \left(4\langle E \rangle \cdot \langle t \rangle^2 - 4\langle t \rangle \cdot \langle tE \rangle - 2\langle E \rangle \cdot \langle t^2 \rangle + 2\langle t^2 E \rangle\right) = 0 \end{aligned} \tag{C.35}$$

This resulting expression is a second-order equation of the type $A \cdot \eta^2 + B \cdot \eta + C = 0$ with the two traditional solutions.

Bibliography

[1] R. C. Hartman et al. The third EGRET catalog of high-energy gamma-ray sources. *Astrophys. J. Suppl.*, 123:79, 1999.

[2] N. Gehrels and P. Michelson. GLAST: The next-generation high energy gamma-ray astronomy mission. *Astropart. Phys.*, 11:277–282, 1999.

[3] http://glast.gsfc.nasa.gov/.

[4] T. C. Weekes et al. Observation of TeV gamma rays from the Crab Nebula using the atmospheric Cerenkov imaging technique. *Astrophys. J.*, 342:379–395, 1989.

[5] D. S. Hanna et al. The STACEE-32 ground based gamma-ray detector. *Nucl. Instrum. Meth.*, A491:126–151, 2002.

[6] J. E. McEnery et al. The MILAGRO gamma-ray observatory. *AIP Conf. Proc.*, 558:549–552, 2001.

[7] J. Holder et al. Status and performance of the first VERITAS telescope. 2005.

[8] R. Enomoto et al. Design study of CANGAROO-III, stereoscopic imaging atmospheric cherenkov telescopes for sub-TeV gamma-ray detection. *Astropart. Phys.*, 16:235–244, 2002.

[9] J. A. Hinton. The status of the HESS project. *New Astron. Rev.*, 48:331–337, 2004.

[10] J. Albert i Fort et al. The MAGIC project: Contributions to ICRC 2005, Pune, India. Part 3: MAGIC Detector and Analysis Details. 2005.

[11] Ong R. A. Rapporteur Talk OG 1 at the 29th ICRC, Pune, India. 2005.

[12] *High Energy Astronphysics. VOLUME 1. Particles, photons and their detection.* Cambridge University Press, 1997.

[13] M. Risse. Properties of extensive air showers. *Acta Phys. Polon.*, B35:1787–1797, 2004.

[14] A. Moralejo. *Búsqueda de fuentes cósmicas de radiación gamma de muy alta energía con el detector AIROBICC.* PhD thesis, 2001. PhD. thesis.

[15] D. Petry. *Beobachtung hochenergetischer gamma-Strahlung (E ¿ 1 TeV) aus Richtung der aktiven Galaxien Mkn 421 und Mkn 501.* PhD thesis, 1997. PhD. thesis.

[16] http://www.mpi-hd.mpg.de/hfm/hess/public/som/som_10_05.htm.

[17] S.M. Bradbury et al. A Project for a 17m Diameter Imaging Cherenkov Telescope. *Proceedings of the 24th ICRC, Rome*, vol.1:1051, 1995.

[18] J. Barrio et al. The MAGIC telescope. Technical report. 1998.

[19] N. Tonello. *Study of the VHE gamma-ray emission from the Active Galactic Nucleus 1ES 1959+650.* PhD thesis, 2005. PhD. thesis.

[20] B. Riegel, T. Bretz, D. Dorner, and R. M. Wagner. A tracking monitor for the MAGIC telescope. Prepared for 29th International Cosmic Ray Conference (ICRC 2005), Pune, India, 3-11 Aug 2005.

[21] A. Ostankov, D. Paneque, M. Martinez, E. Lorenz, and R. Mirzoian. A study of the new hemispherical 6-dynodes PMT from electron tubes. *Nucl. Instrum. Meth.*, A442:117–123, 2000.

[22] D. Paneque. *An optical properties study of the new hemispherical PMTs from electron tubes.* PhD thesis, 2005. Diploma thesis.

[23] D. Paneque et al. A method to enhance the sensitivity of photomultipliers for air Cherenkov telescopes. *Nucl. Instrum. Meth.*, A504:109–115, 2003.

[24] A. Karle et al. Analog optical transmission of fast photomultiplier pulses over distances of 2-km. *Nucl. Instrum. Meth.*, A387:274–277, 1997.

[25] D. Paneque. *The MAGIC Telescope: development of new technologies and first observations.* PhD thesis, 2004. PhD. thesis.

[26] J. Rose et al. Fast analog signal transmission for an air Cherenkov photomultiplier camera using optical fibers. *Nucl. Instrum. Meth.*, A442:113–116, 2000.

[27] *Design and performance of analog fiber optical links used on the Whipple 10 meter air Cherenkov telescope.* Proceedings of 27th International Cosmic Ray Conference, 2001.

[28] D. Bastieri et al. A two-level pattern trigger for the MAGIC telescope. *Nucl. Instrum. Meth.*, A461:521–523, 2001.

[29] T. Schweizer, E. Lorenz, M. Martinez, A. Ostankov, and D. Paneque. The optical calibration of the MAGIC telescope camera. *IEEE Trans. Nucl. Sci.*, 49:2497–2503, 2002.

[30] M. Gaug. *Calibration of the MAGIC Telescope and observations of Gamma Ray Bursts.* PhD thesis, 2006. PhD. thesis.

[31] J. Cortina et al. The control system of the magic telescope, in internal MAGIC document, MAGIC-TDAS 00-07, version 7.2. 2006.

[32] *Camera control and central control of the MAGIC telescope.* Prepared for 28th International Cosmic Ray Conference (ICRC 2003), Tsukuba, Japan, 31 Jul - 7 Aug 2003.

[33] *The control system of the MAGIC telescope.* Prepared for International Symposium: The Universe Viewed in Gamma Rays, Kashiwa, Chiba, Japan, 25-28 Sep 2002.

[34] E. Domingo. *gamma-ray emission from regions of star formation: Theory and observations with the MAGIC Telescope*. PhD thesis, 2006. PhD. thesis.

[35] J. Flix. *Observations of gamma-rays from the Galactic Center with the MAGIC Telescope: indirect searches of super-symmetric dark matter*. PhD thesis, 2006. PhD. thesis.

[36] Hendrik Bartko, M. Gaug, A. Moralejo, and N. Sidro. FADC pulse reconstruction using a digital filter for the MAGIC telescope. 2005.

[37] *Comparison of on-off and wobble mode observations for MAGIC*. Prepared for 29th International Cosmic Ray Conference (ICRC 2005), Pune, India, 3-11 Aug 2005.

[38] *MERCATOR Telescope*, volume 5492, 2004.

[39] D. L. King. RGO/La Palma technical note 31. 1995.

[40] O. Blanch. *Study of the Gamma Ray Horizon with MAGIC as a new method to perform cosmological measurements*. PhD thesis, 2004. PhD. thesis.

[41] D. Heck, G. Schatz, T. Thouw, J. Knapp, and J. N. Capdevielle. CORSIKA: A Monte Carlo code to simulate extensive air showers. FZKA-6019.

[42] J. Knapp and D. Heck. Extensive air shower simulations with the CORSIKA code. (In German). *Nachr. Forsch. zentr. Karlsruhe*, 30:27–37, 1998.

[43] J. Alcaraz et al. Cosmic protons. *Phys. Lett.*, B490:27–35, 2000.

[44] J. Alcaraz et al. Helium in near earth orbit. *Phys. Lett.*, B494:193202, 2000.

[45] L. Breiman. Random Forest. *Machine Learning*, 45:5–32, 2001.

[46] L. Zimmermann. *Statistical Learning in High Energy and Astrophysics*. PhD thesis, 2005. PhD. thesis.

[47] T. P. Li and Y. Q. Ma. Analysis methods for results in gamma-ray astronomy. *Astrophys. J.*, 272:317–324, 1983.

[48] P. T. Reynolds et al. Survey of candidate gamma-ray sources at TeV energies using a high resolution Cherenkov imaging system: 1988 - 1991. *Astrophys. J.*, 404:206–218, 1993.

[49] D. Kranich. *Temporal and spectral characteristics of the active galactic nucleus Mkn 501 during a phase of high activity in the TeV range*. PhD thesis, 2001. PhD. thesis.

[50] V. P. Fomin et al. New methods of atmospheric Cherenkov imaging for gamma-ray astronomy. 1: The False source method. *Astropart. Phys.*, 2:137–150, 1994.

[51] R. W. Lessard, J. H. Buckley, V. Connaughton, and S. Le Bohec. A new analysis method for reconstructing the arrival direction of TeV gamma-rays using a single imaging atmospheric Cherenkov telescope. *Astropart. Phys.*, 15:1–18, 2001.

[52] *The DISP analysis method for point-like or extended gamma source searches/studies with the MAGIC telescope*. Prepared for 29th International Cosmic Ray Conference (ICRC 2005), Pune, India, 3-11 Aug 2005.

[53] *A new method to determine the arrival direction of individual air showers with a single air Cherenkov telescope.* Prepared for 28th International Cosmic Ray Conferences (ICRC 2003), Tsukuba, Japan, 31 Jul - 7 Aug 2003.

[54] J. Albert et al. Observations of Mkn 421 with the MAGIC telescope. 2006.

[55] G. D. Lafferty and T. R. Wyatt. Where to stick your data points: The treatment of measurements within wide bins. *Nucl. Instrum. Meth.*, A355:541–547, 1995.

[56] F. Goebel et al. Absolute energy scale calibration of the MAGIC telescope using muon images. Prepared for 29th International Cosmic Ray Conference (ICRC 2005), Pune, India, 3-11 Aug 2005.

[57] A. M. Hillas et al. The Spectrum of TeV Gamma Rays from the Crab Nebula. *Astrophys. J.*, 503:744, 1998.

[58] F. Aharonian et al. The Crab Nebula and pulsar between 500-GeV and 80-TeV: Observations with the HEGRA stereoscopic air Cherenkov telescopes. *Astrophys. J.*, 614:897–913, 2004.

[59] T. Schweizer. *Analysis of the large gamma ray flares of Mkn 421 as obsered with HEGRA CT1 on the insland La Palma in 2001.* PhD thesis, 2002. PhD. thesis.

[60] F. Krennrich et al. Discovery of Spectral Variability of Markarian 421 at TeV Energies. *Astrophys. J.*, 575:L9–L14, 2002.

[61] M. Blazejowski et al. A Multi-wavelength View of the TeV Blazar Markarian 421: Correlated Variability, Flaring, and Spectral Evolution. *Astrophys. J.*, 630:130–141, 2005.

[62] F. Aharonian et al. Observations of Mkn 421 in 2004 with HESS at large zenith angles. *Astron. Astrophys.*, 95:437, 2005.

[63] D. Mattingly. Modern tests of Lorentz invariance. *Living Rev. Rel.*, 8:5, 2005.

[64] G. Amelino-Camelia, C. Lammerzahl, A. Macias, and H. Muller. The search for quantum gravity signals. *AIP Conf. Proc.*, 758:30–80, 2005.

[65] H. Vucetich. Testing Lorentz invariance violation in quantum gravity theories. 2005.

[66] C. Rovelli. Notes for a brief history of Quantum Gravity. 2000.

[67] V. A. Kostelecky and S. Samuel. Spontaneous breaking of lorentz symmetry in string theory. *Phys. Rev.*, D39:683, 1989.

[68] R. Gambini and J. Pullin. Nonstandard optics from quantum spacetime. *Phys. Rev.*, D59:124021, 1999.

[69] J. Polchinski. Lectures on D-branes. 1996.

[70] D. Colladay and V. A. Kostelecky. Lorentz-violating extension of the standard model. *Phys. Rev.*, D58:116002, 1998.

[71] C. Rovelli and L. Smolin. Loop representation of quantum general relativity. *Nucl. Phys.*, B331:80, 1990.

[72] H. Nicolai and K. Peeters. Loop and spin foam quantum gravity: A brief guide for beginners. 2006.

[73] C. N. Kozameh and M. F. Parisi. Lorentz invariance and the semiclassical approximation of loop quantum gravity. *Class. Quant. Grav.*, 21:2617–2621, 2004.

[74] G. Amelino-Camelia, John R. Ellis, N. E. Mavromatos, D. V. Nanopoulos, and Subir Sarkar. Potential Sensitivity of Gamma-Ray Burster Observations to Wave Dispersion in Vacuo. *Nature*, 393:763–765, 1998.

[75] G. Amelino-Camelia. Relativity in space-times with short-distance structure governed by an observer-independent (Planckian) length scale. *Int. J. Mod. Phys.*, D11:35–60, 2002.

[76] J. Magueijo and L. Smolin. Lorentz invariance with an invariant energy scale. *Phys. Rev. Lett.*, 88:190403, 2002.

[77] N. Jafari and A. Shariati. Doubly special relativity: A new relativity or not? 2006.

[78] G. Amelino-Camelia, J. Kowalski-Glikman, G. Mandanici, and A. Procaccini. Phenomenology of doubly special relativity. *Int. J. Mod. Phys.*, A20:6007–6038, 2005.

[79] J. Kowalski-Glikman. Introduction to doubly special relativity. *Lect. Notes Phys.*, 669:131–159, 2005.

[80] C. D. Lane. Probing lorentz violation with Doppler-shift experiments. *Phys. Rev.*, D72:016005, 2005.

[81] H. Dehmelt, R. Mittleman, Jr. van Dyck, R. S., and P. Schwinberg. Past electron positron g-2 experiments yielded sharpest bound on CPT violation. *Phys. Rev. Lett.*, 83:4694–4696, 1999.

[82] Hogan Nguyen. CPT results from KTeV. 2001.

[83] A. Alavi-Harati et al. Measurements of direct CP violation, CPT symmetry, and other parameters in the neutral kaon system. *Phys. Rev.*, D67:012005, 2003.

[84] T. Jacobson, S. Liberati, and D. Mattingly. TeV astrophysics constraints on Planck scale Lorentz violation. *Phys. Rev.*, D66:081302, 2002.

[85] T. Jacobson, S. Liberati, and D. Mattingly. Threshold effects and Planck scale Lorentz violation: Combined constraints from high energy astrophysics. *Phys. Rev.*, D67:124011, 2003.

[86] S. R. Coleman and S. L. Glashow. High-energy tests of Lorentz invariance. *Phys. Rev.*, D59:116008, 1999.

[87] T. Jacobson, Stefano Liberati, and D. Mattingly. Lorentz violation and Crab synchrotron emission: A new constraint far beyond the Planck scale. *Nature*, 424:1019–1021, 2003.

[88] R. J. Gleiser and C. N. Kozameh. Astrophysical limits on quantum gravity motivated birefringence. *Phys. Rev.*, D64:083007, 2001.

[89] T. A. Jacobson, S. Liberati, D. Mattingly, and F. W. Stecker. New limits on Planck scale lorentz violation in QED. *Phys. Rev. Lett.*, 93:021101, 2004.

[90] R. E. Rutledge and D. B. Fox. Re-Analysis of Polarization in the Gamma-ray flux of GRB021206. *Mon. Not. Roy. Astron. Soc.*, 350:1272, 2004.

[91] S. D. Biller et al. Limits to quantum gravity effects from observations of TeV flares in active galaxies. *Phys. Rev. Lett.*, 83:2108–2111, 1999.

[92] J. R. Ellis, N. E. Mavromatos, D. V. Nanopoulos, and A. S. Sakharov. Quantum-gravity analysis of gamma-ray bursts using wavelets. *Astron. Astrophys.*, 402:409–424, 2003.

[93] J. R. Ellis, Nick E. Mavromatos, D. V. Nanopoulos, A. S. Sakharov, and E. K. G. Sarkisyan. Robust limits on Lorentz Violation from Gamma-Ray Bursts. 2005.

[94] P. Kaaret. Pulsar radiation and quantum gravity. 1999.

[95] R. Plaga. Detecting intergalactic magnetic fields using time delays in pulses of gamma-rays. *Nature*, 374:430–432, 1995.

[96] O. Blanch, J. Lopez, and M. Martinez. Testing the effective scale of quantum gravity with the next generation of gamma ray telescopes. *Astropart. Phys.*, 19:245–252, 2003.

[97] L. M. Krauss. Space, Time, and Matter: Cosmological Parameters 2001. 2001.

[98] O. Blanch and M. Martinez. Exploring the Gamma Ray Horizon with the next generation of Gamma Ray Telescopes. Part 1: Theoretical predictions. *Astropart. Phys.*, 23:588–597, 2005.

[99] T. M. Kneiske, K. Mannheim, and D. H. Hartmann. Implications of Cosmological Gamma-Ray Absorption - i. Evolution of the Metagalactic Radiation Field. 2002.

[100] T. Kifune. Invariance violation extends the cosmic ray horizon? *Astrophys. J.*, 518:L21–L24, 1999.

[101] G. Amelino-Camelia and T. Piran. Planck-scale deformation of Lorentz symmetry as a solution to the UHECR and the TeV-gamma paradoxes. *Phys. Rev.*, D64:036005, 2001.

[102] J. A. Gaidos et al. Extremely rapid bursts of TeV photons from the active galaxy Markarian 421. *Nature*, 383:319, 1996.

[103] D. N. Spergel et al. First Year Wilkinson Microwave Anisotropy Probe (wmap) Observations: Determination of Cosmological Parameters. *Astrophys. J. Suppl.*, 148:175, 2003.